UNIVERSITÀ DEGLI STUDI DI PADOVA

Dipartimento di Fisica e Astronomia "Galileo Galilei"
Scuola di dottorato di ricerca in Astronomia
Ciclo XXV

X-ray spectral states and metallicity of Ultra Luminous X-ray sources: a deeper insight into their spectral properties

Direttore della Scuola: Ch.mo Prof. Giampaolo Piotto
Supervisore: Dr. Luca Zampieri

Dottorando: Fabio Pintore

Padova, 31 Gennaio 2013

Abstract

Ultraluminous X-ray sources (ULXs) are a class of extragalactic, off nuclear and point-like sources with isotropic X-ray luminosities higher than 10^{39} erg s^{-1}. They are supposed to be accreting Black Hole binaries systems but the accretion mechanisms at the basis of their extremely high X-ray luminosity are still matter of debate.

We carried out a detailed spectral analysis of all the available *XMM-Newton* observations of two ULXs in NGC 1313, adopting a common model based on a multicolor disc plus a comptonizing component. We were able to describe the spectral evolution of the two sources within such a common framework. Furthermore, we investigated the chemical abundances of their local environments making use of both EPIC and RGS data. The results appear to indicate sub-solar metallicity for both sources.

The possible existence of two spectral states in NGC 1313 X-1 and X-2 suggested to look for similar behaviours also in other ULXs. We then studied a larger sample of sources, including IC 342 X-1, NGC 5204 X-1, NGC 5408 X-1, Holmberg IX X-1, Holmberg II X-1, NGC 55 ULX1 and NGC 253 X-1. These sources were selected because they have a luminosity $\geq 2.0 \cdot 10^{39}$ erg s^{-1}, are nearby, have one long observation and at least three other observations. The high quality observations provide at least 10000 counts in the EPIC instruments allowing us to constrain the curvature at high energy and to perform

an analysis of the abundances of the material along the line of sight. We found that, in most of the spectra of the sources of our sample, the high energy component has a low temperature and is optically thick. However, because of the poor quality of some observations, the spectral fits are sometimes affected by a degeneracy between the spectral parameters and the roll-over of the spectrum at high energy is not easy to detect. For these reasons, similarly to what has been done for low counting statistics spectra of Galactic X-ray binaries (XRBs), we adopted the method of the *hardness ratios* that has also the advantage to allow us to study the spectral variability in a way completely independent of the spectral models. This analysis suggests the existence of possible characteristic evolutionary patterns on the *color-color* and *intensity-color* diagrams linking at least two different spectral states. This behaviour can be explained in terms of a non-standard accretion disc in which the increment of the accretion rate produces outflows that become more and more important at the highest luminosities.

We tested the scenario of the ejection of a wind jointly analyzing the spectral and timing properties of the source NGC 55 ULX1 which shows a puzzling flux variability. In fact, fast drops in the flux are observed on time scales of minutes to hours that may be produced by optically thick blobs of matter that from time to time encounter our line of sight. We compared its variability properties with those of a Galactic accreting systems, EXO 0748-676, which is powered by a neutron star and is a known dipping source. We characterised the nature of the variability observed in the power density spectrum and, in particular, we checked the presence of a linear relation between the Root Mean Square (RMS) variability and the flux in several energy bands. We found that, in EXO 0748-676, the predominance of an (ionised) absorber strongly affects the RMS-flux relation which may anticorrelate when the absorption lines are unsaturated. On the other hand, no further variability is introduced when they are saturated and the variability is dominated by the accretion flow. In this case the source shows a positive correlation between RMS and flux. Since we found

an anticorrelation in NGC ULX1, we suggest that at the highest flux levels, massive and unsaturated turbulent outflows are ejected.

Finally, persistent ULXs, as those discussed above, do not allow us an easy comparison with the behaviour of Galactic XRBs. Transient ULXs are much more promising in this respect as they span different accretion regimes. Till now, only a handful of transient ULXs has been discovered and the link between them and the persistent sources is still unclear. We monitored the evolution of a new ULX (XMMU J004243.6+41251) discovered in January, 2012 in M31 by *XMM-Newton*. Its outburst showed that, at maximum luminosity, it entered in the ULX regime. It was then extensively followed by *Swift* during the flux decay. The source has experienced a fast rise in flux after discovery during which the *XMM-Newton* spectra changed from a powerlaw-like to a disk-like shape in the *Swift* spectra, suggesting a transition between the canonical *low/hard* and *high/soft* states. Its luminosity remained fairly constant for at least 40 days and then it faded below 10^{38} erg s^{-1}. During the decay the disc emission softened and the temperature decreased from $\sim$ 0.9 keV to $\sim$ 0.5 keV. An optical follow-up and the UVOT images failed to provide evidence of a counterpart down to 22 mag in the optical band and to 23$-$24 mag in the near Ultraviolet. We compared the properties of XMMU J004243.6+412519 with those of other known ULXs and Galactic black hole transients, finding more similarities with the latter.

Abstract

Le *Ultraluminous X-ray sources* (ULXs) sono una classe di sorgenti extragalattiche, lontane dal nucleo della galassia ospite e puntiformi, con una luminosità isotropica maggiore di 10^{39} erg s^{-1}. Si pensa siano buchi neri in accrescimento in sistemi binari ma i meccanismi di accrescimento alla base della loro estrema luminosità X sono ancora lontani dall'essere totalmente compresi.

In questo lavoro è stata svolta una dettagliata analisi spettrale di tutte le osservazioni disponibili di *XMM-Newton* di due ULXs in NGC 1313, adottando un modello comune basato su un disco multicolore più una componente di comptonizzazione. Noi siamo stati capaci di descrivere l'evoluzione spettrale delle due sorgenti all'interno di tale scenario. Inoltre, è stato possibile determinare le abbondanze chimiche dei loro ambienti locali facendo uso sia di dati EPIC che di dati RGS. I risultati sembrano indicare metallicità sub-solare per entrambe le sorgenti.

La possibile esistenza di due stati spettrali in NGC 1313 X-1 e X-1 hanno suggerito di cercare comportamenti simili anche in altre ULXs. Per questo motivo, un campione più vasto di sorgenti, il quale include IC 342 X-1, NGC 5204 X-1, NGC 5408 X-1, Holmberg IX X-1, Holmberg II X-1, NGC 55 ULX1 e NGC 253 X-1, è stato studiato. Queste sorgenti sono state selezionate poichè la loro luminosità è $\geq 2.0 \cdot 10^{39}$ erg s^{-1}, sono sorgenti vicine

e posseggono un'osservazione lunga e almeno altre tre ulteriori osservazioni. L'alta qualità delle osservazioni fornisce almeno 10000 conteggi nello strumento EPIC, consentendoci di determinare con più precisione la curvatura ad alta energia e di svolgere un'analisi delle abbondanze del materiale presente lungo la linea di vista. È stato trovato che, nella maggior parte degli spettri delle sorgenti del nostro campione, la componente ad alta energia mostra una bassa temperatura ed è otticamente spessa. Ad ogni modo, a causa della bassa qualità di alcune osservazioni, i fit spettrali sono a volte influenzati da una degenerazione fra i parametri spettrali e la curvatura ad alta energia dello spettro non è facilmente individuata. Per queste ragioni, in modo simile a ciò che è stato ampiamente fatto per gli spettri di sorgenti binarie Galattiche di raggi X, abbiamo adottato il metodo degli *hardness ratios* che hanno anche il vantaggio di consentirci di studiare la variabilità spettrale in un modo completamente indipendente dal modello spettrale. Questa analisi suggerisce l'esistenza di un possibile caratteristico cammino evolutivo sui diagrammi *colore-colore* and *intensità-colore* collegando almeno due differenti stati spettrali. Questo comportamento può essere spiegato in termini di un disco di accrescimento non standard in cui l'aumento del tasso di accrescimento produce fuoriuscite di materiale che diventano via via più importanti alle più alte luminosità.

Lo scenario di emissione di vento è stato ulteriormente studiato analizzando le proprietà spettrali e temporali della sorgente NGC 55 ULX1 che mostra un'enigmatica variabilità nel flusso. Infatti, rapide diminuzioni del flusso emesso sono osservate su tempi scala di minuti od ore che potrebbero essere prodotti da nuvole di materiale otticamente spesso che di tanto in tanto entrano all'interno della nostra linea di vista, oscurando le regioni centrali della sorgente. È stata fatta un'analisi comparativa fra le proprietà della sua variabilità con quelle di un sistema Galattico in accrescimento, EXO 0748-676, conosciuto per ospitare una stella di neutroni e per essere una sorgente con "dips". Abbiamo caratterizzato la natura della variabilità osservata negli spettri di potenza e, in particolare, abbiamo testato la presenza

di una relazione lineare tra la variabilità quadratica media (RMS) e il flusso in diverse bande di energia. È stato trovato che, in EXO 0748-676, la predominanza di un mezzo assorbente (ionizzato) influenza fortemente la relazione fra RMS e flusso che potrebbero anti-correlare qualora le linee in assorbimento fossero non sature. D'altra parte, nessuna variabilità ulteriore è introdotta quando esse sono sature e la variabilità è dominata dal flusso d'accrescimento. In questo caso la sorgente mostra una correlazione positiva tra flusso ed RMS. Poichè noi abbiamo individuato un'anti-correlazione in NGC 55 ULX1, proponiamo che ai livelli di flusso più alti, imponenti venti, non saturi e turbolenti, siano eiettati.

Infine, ULX persistenti come quelle discusse sopra, non consentono una facile comparazione con il comportameno delle sorgenti binarie Galattiche. ULX transienti sono molto più promettenti sotto questo punto di vista poichè esse attraversano differenti regimi di accrescimento. Fino ad ora, solo una manciata di ULX transienti sono state scoperte e la connessione tra loro e le sorgenti persistenti è ancora poco chiara. Noi abbiamo monitorato l'evoluzione di una nuova ULX (XMMU J004243.6+41251) scoperta nel Gennaio 2012 nella galassia M31 da *XMM-Newton*. La sua accensione ha mostrato che, alla luminosità di picco, la sorgente è entrata nel regime ULX. È stata poi ampiamente seguita da *Swift* durante la sua fase di decadimento in flusso. La sorgente ha sperimentato un veloce incremento del flusso dopo la sua scoperta, durante il quale gli spettri ottenuti da *XMM-Newton* si sono evoluti da un semplice andamento a legge di potenza fino ad una forma tipica per un disco d'accrescimento in tutti gli spettri *Swift*, suggerendo una transizione tra gli stati canonici *low/hard* and *high/soft*. La sua luminosità è rimasta abbastanza costante per almeno 40 giorni, per poi scendere al di sotto di 10^{38} erg s^{-1}. Durante il decadimento, l'emissione del disco è diventata più soft e la temperatura è diminuita da ~ 0.9 keV fino a ~ 0.5 keV. Un follow-up ottico e immagini UVOT non sono riuscite a fornire evidenze di una controparte fino a 22 mag in banda ottica e fino a $23-24$ mag nel vicino Ultravioletto. Noi abbiamo

comparato le proprietà di XMMU J004243.6+41251 con quelle di altre ULX transienti e buchi neri Galattici, trovando più similitudini con le ultime.

Contents

1 Introduction to Ultra Luminous X-ray sources **1**

1.1 Intermediate mass, stellar mass or massive stellar Black Holes 5

1.2 X-ray spectral properties 7

1.3 Super Eddington accretion 11

1.3.1 Slim disc 11

1.3.2 Ultra Luminous State 12

1.4 Short-term Variability 13

1.5 Stellar environment and emission nebulae 15

2 The sample and the spectral models **19**

2.1 Selection criteria 21

2.2 Properties of the sources and their host galaxies 23

2.3 Adopted spectral models 30

2.4 *XMM-Newton* data reduction 36

2.5 Overview 38

3 X-ray spectral states and metallicity in the ULXs NGC 1313 X-1 and X-2 41

3.1 Introduction . . . 41

3.2 Preliminary X-ray spectral fits . . . 43

3.2.1 Comptt . . . 44

3.2.2 Eqtherm . . . 51

3.3 Preliminary discussion . . . 51

3.4 Comptonization plus multicolor blackbody disc . . . 52

3.4.1 Effects of varying the ratio of seed photons temperature to the disc temperature . . . 60

3.5 Chemical abundance estimates . . . 63

3.6 Discussion . . . 65

4 ULXs: a deeper insight into their X-ray spectral evolution 71

4.1 Introduction . . . 71

4.2 Analysis . . . 72

4.2.1 Spectral analysis . . . 72

4.2.2 Temporal analysis . . . 72

4.3 Spectral fits . . . 74

4.3.1 IC 342 X-1 . . . 74

4.3.2 NGC 253 X-1 . . . 79

4.3.3 NGC 5204 X-1 . . . 87

4.3.4 NGC 5408 X-1 . . . 92

4.3.5 Ho II X-1 . . . 97

4.3.6 Holmberg IX X-1 . . . 102

4.4 Colors . . . 108

4.5 Discussion . . . 115

5 Investigating the variability of ULX1 in NGC 55 **119**

5.1 Introduction . . . 119

5.2 EXO 0748-676 . . . 121

5.2.1 X-ray spectra . . . 121

5.2.2 Power Density Spectra . . . 126

5.2.3 Flux dependent variability . . . 129

5.2.4 Lag and Covariance spectra . . . 134

5.3 Predictions for wind induced variability in ULXs . . . 137

5.4 NGC 55 ULX1 . . . 138

5.4.1 X-ray Spectra . . . 138

5.4.2 Flux dependent variability . . . 144

5.4.3 Lag and Covariance spectra . . . 150

5.5 Discussion . . . 155

6 *Swift* observations of the transient ULX XMMU J004243.6+412519 in M31 **159**

6.1 Introduction . . . 159

6.2 *Swift* observations and data reduction . . . 160

6.3 X-ray data analysis . . . 161

6.4 Optical and ultraviolet observations . . . 173

6.5 Pre outburst observations . . . 175

6.5.1 *CHANDRA* . . . 176

6.5.2 *Swift* . . . 176

6.6 Discussion: spectral states in transient ULXs . . . 178

7 Conclusions **183**

7.1 Spectral states 183

7.2 Wind 187

7.3 Transient sources 188

7.4 Some future perspectives 189

Bibliography **190**

Chapter 1

Introduction to Ultra Luminous X-ray sources

Ultra Luminous X-ray sources (ULXs) are a peculiar class of extragalactic, point like and off-nuclear X-ray sources with isotropic luminosity higher than 10^{39} erg s^{-1} and up to 10^{41-42} erg s^{-1}. Although they were discovered more than 30 years ago and nowadays more than 450 ULXs are known and catalogued (e.g. Roberts & Warwick 2000; Colbert & Ptak 2002; Swartz et al. 2004; Liu & Bregman 2005; Walton et al. 2011; Swartz et al. 2011), their nature is still matter of debate and their observational properties are still puzzling. Few ULXs are now known to be supernova remnants interacting with the interstellar medium (Immler et al., 2007) while a larger fraction ($\sim 25\%$) of them are identified as background Active Galactic Nuclei (AGN) (Swartz et al. 2004; Foschini et al. 2002b, Masetti et al. 2003; Wong et al. 2008). The contamination is lower in spiral galaxies ($\sim 15\%$ of the total number of ULXs) than in elliptical galaxies ($\sim 44\%$; Swartz et al. 2011). In general ULXs are detached from the nucleus of their host galaxies, excluding the possibility of association with supermassive Black Holes (BHs).

Einstein was the first X-ray satellite to reveal the existence of X-ray sources in external galaxies (Long & van Speybroeck 1983; Helfand & Becker 1984; Fabbiano 1989; Stocke

et al. 1991). The brightest sources showed isotropic X-ray luminosities $> 10^{39}$ erg s^{-1}, higher than those of X-ray binaries in our Galaxy. Initially, these sources were named in several ways, as extraluminous, superluminous or intermediate X-ray sources. The name Ultraluminous X-ray sources (ULXs) was introduced for the first time by the Japanese ASCA team. The imaging and sensitivity capabilities of *Einstein* were considerable at that time but not sufficient to resolve groups of sources in compact and dense star forming extragalactic regions and to study the long-term variability of their X-ray fluxes. Many ULXs were confused with background AGNs or supernovae. Only with the advent of *ROSAT* was it possible to make order between the different objects and resolve the emission of groups of sources. Moreover, with *ROSAT* it was possible to compile the first catalogues of ULXs (i.e. Colbert & Mushotzky 1999, Roberts & Warwick 2000, Colbert & Ptak 2002). It became soon clear that most of them were not associated to supernovae since they were often persistent sources. Thanks to the Japanese mission *ASCA*, the first physical models were applied to the spectra of ULXs showing that several of them could be well fitted by a single thermal component with a temperature of $\sim 1 - 2$ keV (Makishima et al., 2000). Such high disc temperatures were explained in terms of highly spinning stellar mass BHs. In such a case, the inner disc radius can be 6 times smaller than that of a non-rotating BH, making the inner disc temperature higher (Makishima et al., 2000). Another proposed scenario was that the emission is produced by an advection dominated disc (slim disc) whose temperature is higher than a standard disc (Mizuno et al., 2001; Ebisawa et al., 2003). In some cases, the data were good enough to describe the spectra also with the combination of two components, usually a cold thermal disc and a *power-law*.

The high luminosities of ULXs can be explained assuming bigger BH masses or considering beaming effects and/or super-Eddington accretion. A combination of the two latter effects may, in principle, account for ULXs with luminosities up to 10^{40} erg s^{-1}. For solar abundance, the three effects can be taken into account using the following expressions:

$$L \approx \frac{1.3 \cdot 10^{38}}{b} \dot{m} \left(\frac{M}{M_{\odot}} \right) \text{ erg s}^{-1}, \tag{1.1}$$

$$L \approx \frac{1.3 \cdot 10^{38}}{b} \dot{m} \left(1 + \frac{3}{5} \ln \dot{m} \right) \left(\frac{M}{M_{\odot}} \right) \text{ erg s}^{-1} \tag{1.2}$$

in which b is the beaming factor ($b = \Omega/4\pi$ where Ω is the solid angle of the emitted flux and $\dot{m}$ is the average accretion rate normalized to the Eddington accretion rate ($\dot{M}/\dot{M}_{Edd}$). The first equation applies to standard discs (Shakura & Sunyaev, 1973) and is valid only for $\dot{m} \leq 1$ while the second equation applies at super-Eddington accretion rates for $1 \leq \dot{m} \leq 100$ (Poutanen et al., 2007).

- *Strong beaming ($1/b \gg 1$)* - In a large number of objects like Blazars or Galactic binary systems strong beaming is observed in the form of relativistic jets originating from the central regions. The observed flux is mainly produced by synchrotron emission from relativistic electrons. This scenario was proposed to explain also the emission of ULXs (Körding et al., 2002). However, it is strongly disfavoured. First of all, only few ULXs have shown radio counterparts or fast X-ray variability typical of beamed emission. Secondly, Davis & Mushotzky (2004) showed that in such a scenario for every ULX at 10^{40} erg s^{-1} there should be ~ 30 sources at 10^{39} erg s^{-1}. This is in strong contrast with the luminosity functions estimated by Swartz et al. (2004) and Walton et al. (2011) in which for each source at 10^{40} erg s^{-1} only $\sim 5-10$ sources at 10^{39} erg s^{-1} are found within 100 Mpc. Finally, a number of ULXs is surrounded by optical nebulae (e.g. Pakull & Mirioni 2002, Kaaret et al. 2004) which are illuminated by a quasi-isotropic flux of 10^{39} erg s^{-1}.

- *Beaming - Super-Eddington accretion ($1/b \geq 10$, $\dot{m} \gg 1$)* - It was suggested that, when accretion rates higher than the Eddington limit are reached, the inner regions

of the disc can start to expel matter inside the spherization radius. This is the region in which the disc becomes geometrically thick and the its structure is no longer described by that of a standard disc (e.g. Poutanen et al. 2007; King 2009). In these conditions, an equatorial outflow that channels the high energy photons emitted in the inner regions may originate. Luminosities up to 10^{40} erg s^{-1}, for a 10-20 $M_{\odot}$ BH may be explained considering accretion rates $\sim 10 \div 30$ times the Eddington limit and mild beaming effects (King et al., 2001; King, 2009). Recently Ohsuga & Mineshige (2007) and Ohsuga et al. (2009) carried out magneto-hydrodynamical simulations showing that at accretion rates ~ 5 times higher than the Eddington limit the disc can reach ULX luminosities.

However, Begelman (2002); Begelman et al. (2006) suggested that high accretion rates in pressure-dominated discs modify how the system releases the energy, trapping it inside bubbles. Another example of modified accretion disc structure is the two-phase super-Eddington, radiatively efficient disc model proposed by Socrates & Davis (2006). In these cases, beaming is not significant.

- *Isotropic Eddington luminosity* ($1/b \sim 1,\ L_{Edd} \sim 1$) - BHs with masses bigger than stellar-mass BHs, but smaller than $\sim 100\ M_{\odot}$ (which is the upper limit of the BHs formed by massive stars, e.g. Belczynski et al. 2010) can explain luminosities up to 10^{40} erg s^{-1} or even higher in presence of some beaming (Zampieri & Roberts, 2009; Mapelli et al., 2009). Only the most luminous sources well above 10^{40} erg s^{-1} (or Hyperluminous sources, HLXs) are difficult to explain in any of the aforementioned scenarios and are then good candidates for being powered by Intermediate Mass BHs (IMBHs). Remarkable examples of such sources are ESO243-49 HLX-1, M82 X-1 and the source 2XMM J134404.1-271410 (if confirmed) in the galaxy IC 4320 (Farrell et al. 2009; Feng et al. 2010; Sutton et al. 2012 and reference therein).

- *Isotropic sub-Eddington luminosity (*$1/b \sim 1,\ \dot{m} < 1$) - This is the standard scenario in which ULXs are similar to BH binary systems of our Galaxy. This woud require the presence of an IMBH. In such a case, canonical spectral state transitions similar to those in the Galactic BHs should be observed but, with the exception of a handful of sources (e.g. ESO243-49 HLX-1, Servillat et al. 2011), this is usually not the case.

1.1 Intermediate mass, stellar mass or massive stellar Black Holes

The general aspects regarding the formation of stellar-mass BHs in stars are reasonably well understood. They are believed to form through fallback after a supernova explosion from stars with initial masses above $\sim 25\ M_{\odot}$. At the end of the life of these stars, the inner core collapses and bounces, forming a proto-neutron star and producing a shock wave that starts to propagate through the stellar envelope (e.g. Arnett, 1996).

If the convective pressure induced by neutrino reheating below the shock overcomes the ram pressure of the infalling stellar envelope, the supernova explosion is inevitable and most of the stellar envelope is ejected (e.g. José & Iliadis, 2011). However during and after the explosion, the inner layers of the star can have a velocity below the escape velocity of the proto-neutron star and start to fall onto it. If the infalling matter brings the core mass over the Chandrasekar limit, a BH will form with a mass in the range $\sim 5 - 20\ M_{\odot}$ (e.g Heger & Woosley, 2002; Heger et al., 2003). This is the expected formation path for stellar-mass BHs at solar metallicity, like those in Galactic BH X-ray binaries. If the BHs in ULXs form in this way and are then of a similar size, they have to be significantly beamed and accreting at largely super-Eddington rates to account for their (apparent) isotropic luminosity.

Indeed the ULXs for a long time appeared to be the best candidates for a new class of

IMBHs as their high luminosities can be easily explained assuming a large BH mass. Since IMBHs cannot form in the same way as stellar mass BHs (sMBH), three alternative scenarios were proposed. In compact and dense star clusters, because of dynamical interactions, very massive stars sink towards the center and undergo mergers and runaway collisions on timescales of $\leq 10^6$ years. Numerical simulations have shown that in such conditions, a super-massive star (800-3000 $M_\odot$) may form that can then collapses to an IMBH (e.g. Portegies Zwart & McMillan 2002; Portegies Zwart et al. 2004). Another scenario involves wandering seeds of sMBHs inside compact and massive globular clusters. Such BHs may effectively merge because of dynamical interaction (Miller & Hamilton, 2002) or grow in mass up to a hundred times, capturing the gas expelled by the first generation of cluster stars during the red-giant phase (Vesperini et al., 2010). Finally, another scenario entails the evolution of very massive stars in the metal poor early Universe.Indeed, it is generally believed that the most massive stars ($\sim 100 - 300\ M_\odot$) at solar metallicity do not collapse into BHs since the electron-positron pairs instability leads to the complete disruption of the star. However, at very low metallicity, stars with $\geq 260\ M_\odot$ (helium core of $\sim 130\ M_\odot$) may exist and form IMBHs through direct collapse (Heger & Woosley, 2002; Heger et al., 2003). Therefore Population III stars, which are expected to be metal-free, are good candidates to be the progenitors of IMBHs (Madau & Rees, 2001) since their initial mass could exceed several hundreds solar masses.

As discussed in Zampieri & Roberts (2009), the existence of IMBHs is not required to explain the large majority of the ULX population. In fact, a combination of slightly super-Eddington accretion and beaming effects may explain the bulk of the ULX population up 10^{40} erg s^{-1} with compact objects smaller than IMBHs, but more massive than "standard" sMBH. Such BHs may originate from the direct collapse of massive stars (above $\sim 40\ M_\odot$) formed in low metallicity environments ($\sim 0.1\ Z_\odot$; Zampieri & Roberts 2009; Mapelli et al. 2009, 2010). In these stars the collapse into a BH occurs without a supernova

explosion becuase the convective pressure below the shock is smaller than the ram pressure of the infalling stellar envelope (Fryer, 1999), in contrast to sMBH in which there may be rapid fallback after the ejection of the outer layers of the star. This is a consequence of the decreased efficiency of mass loss in low metallicity environments, that leads to more massive envelopes at the end of the star life. These massive stellar BHs (MsBHs) are in the range $\sim$ 40-100 $M_{\odot}$ (Belczynski et al., 2010).

1.2 X-ray spectral properties

The advent of *XMM-Newton* and *CHANDRA*, the two high spectral resolution X-ray missions launched by ESA and NASA respectively, led to a dramatic improvement of the quality of the X-ray spectra of ULXs and to a better understanding of their time variability on short timescales. The spatial resolution of the detectors onboard these two satellites confirmed also the non-nuclear nature of the ULXs, definitely ruling out in the large majority of the cases an identification with a low luminosity AGN. The data and, in particular, X-ray spectra provided by such telescopes are the best available and yielded a substantial contribution to the physical understanding of ULXs.

Most of the observations were focussed on bright objects ($f_X \geq 10^{-12}$ erg s^{-1} cm^{-2}) in the local universe (within $\sim$ 10 Mpc). Their spectra show a wide variety of properties that in general appear not to correlate with the total luminosity. Even though they can be well described by canonical models as *power-laws* or *multicolor discs*, their physical interpretation poses several questions about the properties of the BHs and of their accretion regimes.

In general, the X-ray spectra of ULXs are *powerlaw-like*, often with *high energy curvature* (above 2-3 keV) and a soft excess (at $\sim 0.2 - 0.4$ keV). The powerlaw-like sources show a wide range of photon indexes between 1 and 3, but usually centered around 1.7-2

(Swartz et al. 2004; Winter et al. 2006; Berghea et al. 2008; Sutton et al. 2012). Berghea et al. (2008) found that the sources with the steeper photon index are harder at higher luminosities ($L_x > 10^{40}$ erg s^{-1}). If the *power-law* spectrum corresponds to the hard state of Galactic BHs, the inferred BH mass is $\approx 10^3\ M_\odot$. An indication of such a state is the presence of radio jets which are commonly observed in AGNs and X-ray binaries (XRBs). IC 342 X-1 shows compact radio emission. Assuming that this emission come from a jet in the hard state and using the fundamental plane of accreting BHs (Merloni et al., 2003), Cseh et al. (2012) estimated a BH mass of $1.2 - 13.6 \cdot 10^3\ M_\odot$.

Several proposals have been put forward to explain the low-hard state of XRBs (that may possibly apply also to those ULXs that show a similar spectral and timing behavior), such as an advection dominated flow (Esin et al. 1997), a luminous hot accretion flow (Yuan, 2001), a combination of synchroton and inverse Compton emission at the basis of a jet (Markoff et al. 2001) and a hot corona above the accretion disc (Liang & Price 1977). If ULXs are powered by sub-Eddington accretion onto IMBHs, they should show a similar spectral evolution from a low/hard to a high/soft spectral state, as Galactic X-ray binary systems (*hysteresis cycle*). Till now only one source, ESO 243-49 HLX-1 (e.g. Farrell et al. 2010; Servillat et al. 2011; Webb et al. 2012), has shown the clearest lines of evidence of XRB spectral states. For this and other reasons (including the detection of transient compact radio emission; Webb et al. 2012), this source is indeed considered a good candidate for an IMBH.

On the other hand, a large number of sources can be well modelled by the combination of a soft component (described by a multicolor black body disc below 2 keV) and a *power-law*. In low counting statistic XMM-Newton spectra, the temperature of the soft component is significantly lower than that observed in Galactic BH binary systems. Such temperatures are mainly in the range $0.1 - 0.4$ keV (e.g. Fabian & Ward 1993; Miller et al. 2003, 2004; Roberts et al. 2004; Feng & Kaaret 2005) and, since the disc temperature (and

normalization) scale with the BH mass, this was considered as evidence for the existence of IMBHs of $10^3 - 10^4\ M_\odot$.

When high quality *XMM-Newton* observations ($\sim$ 100 ks) started to become available, people realized that the spectral properties of ULXs are in fact markedly different from those of Galactic XRBs. In particular, Gonçalves & Soria (2006) questioned the interpretation of the soft component in terms of a cold disc since they proved that the temperature of such a component is strongly dependent on the energy range in which the *power-law* component fits the spectrum. In the same year, Stobbart et al. (2006) analyzed a sample of ULXs showing that most of them present a degeneracy between the two components, the *power-law* and the disc. In fact in some sources the *power-law* component could equally well fit the high as well as the low energy part of the spectra: however, as the *power-law* is expected to be inverse Compton scattering by an optically thin corona of seed photons from the disc, if the *power-law* fits the low energy part of the spectrum, the seed photons are hotter than the corona, making this model physically inconsistent. However, the ULXs of the sample of Stobbart et al. (2006) could be well described also by a combination of two blackbody components, which was an important indication of the existence of curvature at high energy never observed in the Galactic systems accreting at sub-Eddington rates. The curvature or roll-over is presented at energies of 3-5 keV in most of the spectra (although in some cases the detection was marginal) and points towards an intrinsically different accretion mechanism. Such a roll-over can be well fitted by a comptonization component, characterised by an optical thickness larger than one and a low electron temperature. This component is interpreted as an optically thick corona atop the inner regions of the disc.

The increasing number of observations of ULXs that became available in the last years favoured a deep investigation of their spectral state transitions. Even though flux variability is a common property of ULXs, they are usually persistent sources. The spectral transitions of some sources like NGC 1313 X-1 and X-2 (see Feng & Kaaret 2006), modeled with a

cold disc plus a *power-law*, show similarities with the canonical states of Galactic XRBs: at high luminosity X-1 seems to enter into a *very high* state but never in the *high/soft* state; on the other hand the X-ray spectrum of X-2 may appear more similar to a *low/hard* state in many observations but a different slope is found at higher fluxes. IC 342 X-1 and X-2 are the first two ULXs in which transitions from a *low/hard* to a *high/soft* spectral state were reported (Kubota et al., 2001). However, the behaviour of the soft component is puzzling: in fact, although in IC 342 X-2 there is a $L_{disc} \propto T_{disc}^4$ correlation typical of a standard accretion disc, IC 342 X-1 shows an anticorrelation (Feng & Kaaret, 2009) between the disc temperature and the total luminosity. An anticorrelation of the form $L_{disc} \propto T_{disc}^{-3.5}$, was observed also in other sources and may indicate an increment of the visible inner disc radius (and hence a decrement of its temperature) when the luminosity increases (Kajava & Poutanen, 2009). In this case, the soft component may be the emission from the photosphere of a wind (whose radius increases with luminosity, Poutanen et al., 2007; Soria, 2007). We note, however, that such conclusions depend on the model (*power-law*) adopted to describe the high energy X-ray spectrum. As found by Stobbart et al. (2006) and later by Gladstone et al. (2009) there is an almost ubiquitous roll-over between 3 and 5 keV in high quality *XMM-Newton* observations and hence the spectral variability needs to be properly reconsidered on the basis of more adequate spectral models.

Finally, we briefly mention also the *supersoft* ULXs that emit mostly at energies below 2 keV, in contrast with the bulk of the ULX population for which the flux peaks above this energy. Their spectral shapes can be well fitted by a single, cold disc component with temperatures of tens to hundreds of eV, making them a different class of ULXs. The fluxes of a certain number of supersoft ULXs showed large variations without changes in the temperature of the soft component. Amongst them, we recall M81 ULX1 (Swartz et al. 2002; Liu 2008), Antennae X-13 (Fabbiano et al. 2003), NGC 247 ULX1 (Jin et al. 2011), NGC 4631 X-1 (Carpano et al. 2007; Soria & Ghosh 2009) and M101 ULX1 (Pence et al.

2001; Kong & Di Stefano 2005; Mukai et al. 2005). Some of these sources displayed also dips and periodic obscuration which may be due to orbital motion. They show also short-term variability on timescales of ~ 100 s which excludes an association with AGNs. Finally, the changes in the luminosity without corresponding variations in the temperature of the soft component, excludes accretion via standard disc around an IMBH. It has been suggested that some supersoft ULXs are white dwarfs in super-Eddington outbursts and/or white dwarfs with beamed emission (e.g Di Stefano et al., 2010).

1.3 Super Eddington accretion

In this section we summarise two of the proposed explanations for the roll-over and the soft excess observed in high quality spectra of several ULXs.

1.3.1 Slim disc

Accretion at or above the Eddington limit can be described in terms of an advection dominated disc or slim disc (Abramowicz et al. 1988, Watarai et al. 2001; Ebisawa et al. 2003). This accretion disc does not show the same properties of the standard accretion disc of Shakura & Sunyaev since it is geometrically thick ($H/R \sim 1$, where H and R are the scale height and radial coordinate, respectively) and the transport of energy via advection dominates over the radiative cooling. As a consequence, the radial profile of the disc temperature changes from $T \sim R^{3/4}$ (standard disc) to $T \sim R^{1/2}$. A simplified spectral model for a slim disc is the *p-free* model in which the index of the temperature profile is free to vary while the spectrum emitted from each annulus is a blackbody at the local gas temperature. Some sources are satisfactorily described by this model with values of the p index of ~ 0.5, consistent with the expected emission of a slim disc (for example NGC 1313 X-2, NGC 5204 X-1, IC 342 X-1; see e.g. Vierdayanti et al. 2006; Gladstone et al. 2009).

This suggests that ULXs may be stellar or massive stellar BHs accreting marginally above the Eddington limit.

However, this model may fail from a theoretical and observational point of view and in fact the temperatures inferred for some ULX spectra are too high (see Gladstone et al. 2009). Moreover, numerical simulations clearly showed that warm outflows are expected to set in at supercritical regimes (Ohsuga & Mineshige 2007; Ohsuga et al. 2009), obscuring the emission of the underlying disc.

1.3.2 Ultra Luminous State

A roll-over at energies of $2 - 5$ KeV is usually not observed in Galactic XRBs, in which spectral curvature is seen at energies of tens to hundreds keV. Gladstone et al. (2009) suggested that the rollover detected in ULX spectra may be produced by an optically thick and warm corona atop the inner regions of the disc. Therefore, the soft component found in these objects are representative of the outer part of the disc, i.e. the region which is not covered by the corona. Gladstone et al. (2009) fitted the spectra of a sample of ULXs using the same model adopted to describe the coupling between disc and corona in the *very high* state of Galactic BH binary systems (Svensson & Zdziarski 1994; Done & Kubota 2006), and found that the coronae of ULXs are rather compact. This model accounts for the exchange of energy between the accretion disc and the corona and allows one to estimate what would be the temperature of the disc without the thermal coupling with the corona. The disc temperatures inferred by the model are consistent with accretion onto sMBHs or MsBHs. Furthermore, Gladstone et al. (2009) identified a spectral sequence in their sample of ULXs in which the soft component becomes progressively more important as the total luminosity increases.

This effect was associated to the onset of an optically thick wind whose photosphere produces the soft component observed at the upper end of the Gladstone et al. (2009)

sequence, supporting again the picture of super-Eddington accretion. Since this spectral state appears to occur only in ULXs and never in Galactic XRBs, Gladstone et al. (2009) called it the *Ultraluminous state*.

1.4 Short-term Variability

Although the physical understanding of the rapid variability of Galactic XRBs is still matter of debate, however it is a powerful tool to classify their spectral states (e.g. Belloni 2010). Also the properties of the short-term variability of ULXs are still poorly understood. In fact, sources with similar X-ray spectra may show different temporal variability. Heil et al. (2009) analyzed the Power Density Spectra (PDS) of a sample of 16 bright ULXs and found that, irrespectively of their X-ray spectra, there are two groups of sources: a smaller group displays a well defined variability at about the same level while in the other the variability is almost absent. This behaviour appears different from that of Galactic XRBs, in which the variability is usually observed in the *low/hard* state while the absence of variability is a distinctive property of the *high/soft* state (e.g. Belloni 2010).

In particular, only in a handful of ULXs, QPOs were found in the PDS: M82 X-1, NGC 5408 X-1 and M82 X42.3+59. The first identification of a QPO in M82 X-1 at a frequency of 54 mHz was obtained with *RXTE* and *XMM-Newton* (Strohmayer & Mushotzky 2003). By means of a joint analysis of CHANDRA and XMM-Newton observations, Feng & Kaaret (2007) were able to confirm that the QPO is indeed produced by the ULX X-1. In a following *XMM-Newton* observation the QPO centroid frequency was different (114 mHz; (Dewangan et al. 2006; Mucciarelli et al. 2006). Variations in the QPO frequency from ~ 50 to ~ 170 mHz, with a possible 1:2:3 ratio, and were observed in RXTE data (Mucciarelli et al. 2006).

The QPO in NGC 5408 X-1 was discovered in a *XMM-Netwon* observation by Strohmayer

et al. (2007). It had a centroid frequency of ~ 20 mHz and was associated to a band-limited noise with a break in the PDS at 2.5 mHz (also detected by Soria et al. 2004). In subsequent *XMM-Newton* observations, the QPO was detected at 10 mHz while the spectral shape of the source was varied. Strohmayer et al. (2007) reported that the QPO frequency scales with the disc flux and the *power-law* photon index. On the basis of these spectral and temporal properties they suggested that the QPO frequency could be similar to the type C QPOs observed in Galactic BH binaries (Casella et al., 2005). Assuming that the QPO frequency is inversely proportional to the BH mass, NGC 5408 X-1 may host a BH of 600-5000 $M_{\odot}$. However, Middleton et al. (2011) challenged this conclusion claiming that, at variance with Galactic BH binaries, the low frequency break is not proportional to the centroid frequency. They further suggested that the high level of variability is associated to extrinsic variability of the Comptonizing medium and produced by optically thick blobs of matter ejected by the inner regions of the disc. In addition, they proposed that this QPO may be associated to the Ultra-low frequency QPO observed from time to time in the Galactic source GRS 1915+105. We note finally tha, this is the first source in which a positive trend between Root Mean Square (RMS) variability and flux was reported (Heil et al. 2012).

M82 X42.3+59 (Matsumoto et al. 2001) showed a broad low frequency QPO at $\sim 3-4$ mHz, observed only when the source is more luminous than $\sim 10^{40}$ erg s^{-1} (Feng et al. 2010). The properties of the QPOs are consistent with those of a type A or B QPO.

Finally a tentative identification of a QPO at 3 mHz was reported also in NGC 6946 X-1, which is the ULX with the highest short-term variability (fractional RMS variability of $\sim 60\%$ over the frequency band $1-100$ mHz; Rao et al. 2010).

QPO frequencies have been used to try to estimate BH masses in ULXs using a variety of methods. One of these approaches has made use of the so called "variability plane" of Galactic BH binaries and AGNs. The variability plane is defined by the BH mass, the

accretion rate and the low frequency break in the PDS. The latter cannot be detected by *XMM-Newton* but it can be inferred from the observed QPO frequency, assuming it is a type C. Using this approach Casella et al. (2008) found that the BH masses of M82 X-1 and NGC 5408 X-1 were $\sim 95 - 1300\ M_{\odot}$ and $\sim 115 - 1300\ M_{\odot}$, respectively.

The problem with using timing properties of ULXs to directly infer masses is that it remains to date unclear how exactly these quantities are related. All the estimates are based upon tentative identifications of the timing features and the use of scaling laws that are known to hold only for a limited number of objects, and are therefore highly uncertain (Zampieri & Roberts, 2009). In addition, low values of the QPO frequency in ULXs may not be necessarily a clue of larger BH masses but simply reflect the fact that they originate in the observable outer disc (i.e. the part not covered by the optically thick corona; Soria 2007).

1.5 Stellar environment and emission nebulae

A number of ULXs are associated to stellar optical counterparts and for some of them the spectral type is known (e.g. Liu et al. 2002; Kaaret et al. 2004; Mucciarelli et al. 2005, 2007; Soria et al. 2005; Tao et al. 2011). The counterparts appear almost ubiquitously hosted in young stellar environments (e.g. Pakull et al. 2006; Liu et al. 2007). However, a few ULXs appear to be associated to older stellar populations (Roberts et al., 2008) and at least one possible later-type stellar counterpart is now known (IC 342 X-1; Feng & Kaaret 2008), although its spectral classification may be affected by significant galactic and extra-galactic reddening (Grisé et al., 2008). The identification of ULX optical counterparts makes possible, in principle, to measure the mass function of the system, that will provide direct constraints on the BH masses of individual sources. Attempts were made to determine radial velocity shifts in the spectral lines of NGC 1313 X-2 (Pakull et al. 2006),

but the claimed detections are highly uncertain. A recent Gemini spectroscopy campaign conducted on two ULXs failed to reveal regular modulations. Although radial velocity variations are observed, they are not sinusoidal (Roberts et al., 2011). Determining the orbital period in the optical band appears comparatively easier, although the expected amplitude of the modulation is small and contamination from X-ray irradiation is significant, making such measurements feasible only with Hubble Space Telescope (*HST*) or from ground with optimal seeing conditions for the brightest counterparts. Only one measurement for NGC 1313 X-2 has been reported to date (Liu et al., 2009), which is however uncertain (Impiombato et al., 2011; Zampieri et al., 2012). Although the precise identification of a single object is not possible, the stellar environment of ULXs can still provide interesting constraints on the properties of ULX binary systems. Several ULXs are located in groups or clusters of OB stars. Isochrone fitting of the cluster colour-magnitude diagram has been attempted and provides cluster ages of tens of millions of years, although there is some disagreement among different authors (Pakull et al. 2006; Ramsey et al. 2006; Liu et al. 2007; Grisé et al. 2008). Comparison of stellar evolutionary tracks of ULXs with the photometric properties of their optical counterparts on the colour-magnitude diagram may also be used to constrain the masses of their donor stars (e.g. Madhusudhan et al. 2006; Patruno & Zampieri 2008a). Population synthesis calculations show that the mass-transfer rates needed to supply the majority of the ULX binaries can be attained over a significant fraction of the life time of the systems for both stellar-mass and intermediate-mass BHs (Madhusudhan et al., 2008, and references therein).

In addition, several ULXs are found in very extended optical emission nebulae, that may provide important information on the energetics and lifetime of these systems (e.g. Pakull & Mirioni 2002; Abolmasov et al. 2007; Kaaret et al. 2010; Figure 1.1). From the He II λ4686 line it is possible to determine the source flux since the line "counts" the photons in the energy range 54-200 eV (Pakull & Angebault 1986). This value is then compared

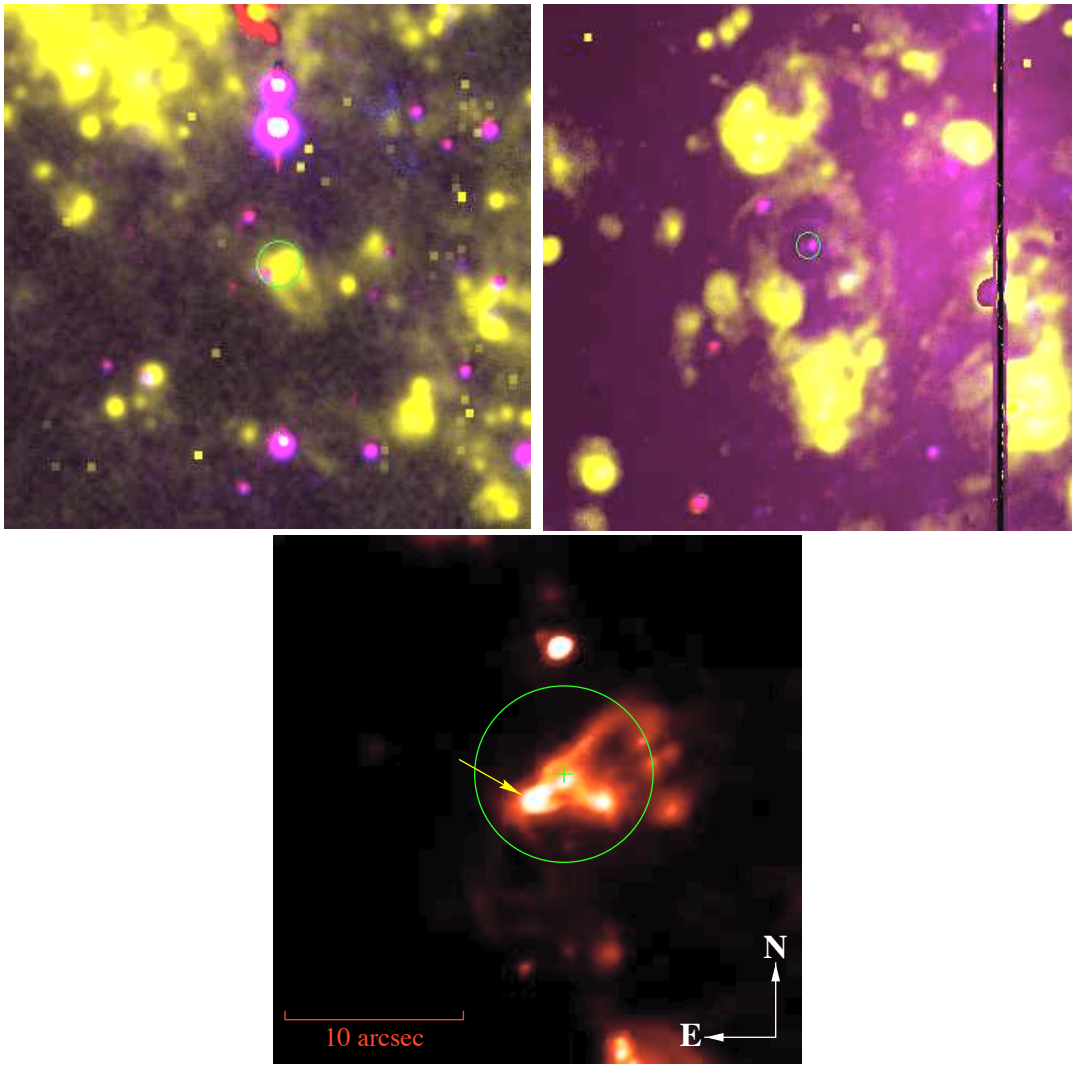

Figure 1.1: The *tooth* nebula surrounding IC 342 X-1 (*top-left* - the X-ray error circe includes the brightest part of the Tooth nebula), NGC 5204 X-1 (*top-right*) and the *foot* nebula of Holmberg II X-1 (*bottom*); images taken from Pakull & Mirioni (2002).

with the source flux inferred at energies > 0.3 keV in the *XMM-Newton* and *CHANDRA* data. With this method, some sources (NGC 5408 X-1, Holmberg II X-1) showed evidence of almost isotropic source emission (e.g. Kaaret & Corbel 2009), suggesting accretion onto massive stellar BHs.

The ULX nebulae have characteristic diameters of $\sim 200 - 400$ pc, radial velocities of $100 - 200$ km s^{-1}, and kinematic ages of $0.5 - 1$ Myr (e.g Roberts et al. 2003; Grisé et al. 2006a; Pakull & Grisé 2008; Kaaret et al. 2010). Their properties are different from those of typical SN remnants. Some of them may be powered by continuos emission of material from outflows or jets (Pakull et al. 2006; Pakull & Grisé 2008). Furthermore, radio counterparts to a few of these nebulae have also been reported (Miller et al. 2005; Lang et al. 2007).

Chapter 2

The sample and the spectral models

It is well known that Galactic BH XRB (BHB) transients show a typical evolutionary path on the hardness-intensity diagram, the *hysteresis cycle* (e.g. Belloni, 2010). During these outbursts, the sources experience several spectral transitions usually characterised in terms of two spectral components, a standard disc and a *power-law* tail. Each spectral state (*high/soft, low/hard, very high state*, etc.) is characterised by specific spectral and timing properties. If ULXs were in an accretion regime similar to those of Galactic BHB systems, we should observe similar spectral and temporal properties: however ULX systems show rather peculiar spectral changes, often different from source to source. In any case, if the Galactic sources follow an ordered path on the hardness-intensity diagram, it is not so unlikely that also ULXs may do something comparable.

Detailed spectral analyses were carried out by several authors on significant number of ULXs showing that the major part of their spectral variability could be well modeled by a soft component plus a *power-law*/comptonizing corona (see amongst the others Feng & Kaaret 2006, 2009; Vierdayanti et al. 2010; Kajava & Poutanen 2009). However, hints of a spectral curvature at high energy were noticed by Stobbart et al. (2006), and, later on, Gladstone et al. (2009) suggested it was almost ubiquitous in the highest quality ULX spec-

tra and only limitations in the exposure times may hide its presence. They suggested that the curvature is a characteristic feature of a new spectral state, the *Ultraluminous state*, and found a likely spectral sequence (*Fig. 8* of their paper) in which the soft component becomes more important when the luminosity increases. This is probably produced by strong outflows from the disc as expected at high accretion rates (Poutanen et al., 2007). The spectra show also a hard component which may be an optically thick corona coupled to the inner regions of the accretion disc or the disc itself (see Section 1.3.2). It seems reasonable to study the spectral variations of ULXs adopting such a model for all the observations even if in several low quality spectra the curvature is not statistically detectable. This allows to have a consistent spectral comparison between poor quality and high quality observations and a more reliable physical interpretation of the spectral properties than a simple *power-law*.

The aim of this work is to investigate the spectral properties of the ULXs in order to increase our understanding on the behaviour of the accretion flow in these "anomalous" X-ray sources and, possibly, put constraints on the scenarios proposed to explain them. Here we focus our attention mainly on *XMM-Newton* data, paying particular attention to those observations with high counting statistics. Our goal is to characterise the spectral variability of ULXs and to check the consistency of the spectral models on the basis of the variability patterns of their parameters. Considering the relevance of the metallicity for one of the proposed scenarios for the formation of ULXs, we also put a significant effort in using X-ray spectroscopy to investigate the chemical abundance in the environment of ULXs.

2.1 Selection criteria

The location of ULXs in external galaxies makes their observation intrinsically harder than that of Galactic sources. Indeed, although their fluxes are 10-100 times brighter than Galactic BHBs, their distances do not allow to obtain spectra of comparable quality in a few ks of observation because the counting statistics is severely limited. On the other hand, in most cases the foreground absorption is low, because our line of sight intersects only a small fraction of the Galactic disc and then the obscuration of the interstellar medium affects only marginally the observations. In addition, the extragalactic position of ULXs allows us to better constrain their distances than the sources in the Galaxy. Till now, the best observations are mostly provided by the *XMM-Newton*, *CHANDRA* and *Swift* satellites since they have the sensitivity to collect conspicuous number of counts from extragalactic sources.

The highest quality *XMM-Newton* observations have shown that the ULX emission is characterised by properties not commonly observed in the Galactic BHBs accreting at sub-Eddington rates. In particular, as already mentioned, a roll-over or a curvature at high energy, usually at 3-5 keV (Stobbart et al., 2006), is typically seen in bright persistent ULXs which cannot be observed with poor quality observations. Stobbart et al. (2006) developed a method to identify such a curvature, from fits of the spectra in the 2-10 keV energy band. They adopted an unabsorbed *power-law* and a broken *power-law*, and if the latter model is statistically more significant in the selected energy range, they conclude that there is evidence of curvature. In addition, Gladstone et al. (2009) found that such a curvature can be clearly seen in the *XMM-Newton* EPIC instruments only if a total of at least ~ 10000 counts are collected, providing a spectrum with at least ~ 500 independent spectral bins.

Since the observed count rates of the closest ULXs in the EPIC-*pn* detector are in

the range $\sim 0.1 - 1.5$ count s^{-1}, only long exposure times of $\sim 50 - 100$ ks (at least for the faintest sources) can provide the necessary amount of total counts. As mentioned above, we studied the spectral evolution of the curvature during time adopting a common spectral model, i.e a multicolor blackbody disc plus a comptonizing component, for both the shortest and the longest *XMM-Newton* observations because it appears particularly suitable to describe the shape of ULX spectra.

However, some ULX spectra appear to be properly described also by a slim disc and, whenever appropriate, in this work we will investigate if the evolution of the spectral parameters of this model provides a physically consistent scenario for the sources of our sample.

It is important to note also that the physical interpretation obtained from the spectral models must be consistent with the temporal properties. Indeed, Middleton et al. (2011, 2012) showed that the analysis of the temporal variability of ULXs as a function of energy can be a powerful tool in order to discriminate among different spectral models, providing further support to the need of long exposure observations with high counting statistics.

The same is true for the analysis of the chemical abundances. Indeed, Winter et al. (2006) pointed out that with the counting statistics achieved in the longest observations, it is possible to clearly detect the K-shell edges of Oxygen and Iron. In particular, they proved that these two chemical elements can be detected only if a *XMM-Newton* observation collects at least 5000 and 40000 counts in the EPIC instrument for the Oxygen and Iron edges, respectively.

Therefore, in order to study systematically the spectral variability and, at the same time, the chemical abundances of ULXs, we selected a sample of sources that have long *XMM-Newton* observations. We made use of the ULX catalogues of Liu & Bregman (2005) and Walton et al. (2011) and selected sources with luminosity $\geq 2 \cdot 10^{39}$ erg s^{-1}, nearby (no more than 20 Mpc away), having one long observation (~ 20 to ~ 100 ks) and at least

three other observations. The list of sources may not be fully representative of the ULX properties but these criteria allow us to sample a rather large range of luminosities.

We note that in the two aforementioned catalogues there is a large number of sources that only partially satisfy these requirements. For example, sources with more than 4 observations may not have in any of them the necessary amount of total counts in order to statistically constrain the spectral curvature. Therefore they were excluded from our sample.

We selected nine sources, two in the galaxy NGC 1313 and one in the galaxies NGC 55, NGC 5204, IC 342, NGC 5408, Holmberg II, Holmberg IX and NGC 253. In the next section we will describe briefly their properties and those of their host galaxies.

2.2 Properties of the sources and their host galaxies

- **NGC 1313** is a late-type barred spiral galaxy with an irregular shape, classified by de Vaucouleurs et al. (1992) as *SBd*. It is a nearby galaxy in the local Universe, at a distance of 3.7 Mpc (Tully & Fisher, 1988). It hosts several star forming regions, mainly concentrated in the spiral arms and in particular in the southern spiral arm. Multi-wavelength observations of the central regions of the galaxy indicate the possible presence of an active nucleus or a luminous nuclear starburst. This galaxy hosts three ULXs (X-1, X-2 and X-3) and one of them is a known supernova (X-3 or SN 1978K) interacting with the circumstellar medium. X-1 and X-2 were observed many times by *ROSAT* (e.g. Colbert & Ptak 2002) and *ASCA* (e.g. Colbert & Mushotzky 1999), showing variability in their X-ray fluxes. NGC 1313 X-1 is located close to the nucleus (at about 50″) while NGC 1313 X-2 is placed at the outskirts of the galaxy (at about 6').

  – **NGC 1313 X-1** is one of the most luminous nearby ULXs with a luminosity

of $\sim 10^{40}$ erg s^{-1}. It shows flux variability up to a factor of 3. It was observed many times by *XMM-Newton* and was originally used as a proof of the existence of IMBHs (Miller et al., 2003) because its low counting statistics spectra can be well described by a *power-law* plus a cold disc with a temperature of ~ 0.2 keV. X-1 is surrounded by a H_α nebula with a diameter of about 250 pc and a more extended region of ~ 800 pc with an Oxygen line emission ($O_{\lambda_{6300}}/H_\alpha > 0.1$). The latter region seems to indicate the presence of ionised gas with a temperature of 10^4 K (Pakull & Mirioni, 2002).

– **NGC 1313 X-2** is slightly less luminous than the companion ULX ($\sim 5 \cdot 10^{39}$ erg s^{-1}) but has bigger flux variations up to a factor of 5. Zampieri et al. (2004) identified a potential optical counterpart for this source. Follow-up investigations found that the bluer of the two objects inside the error circle had an absolute magnitude (corrected for extinction) of $M_B = -4.5$ mag, color $(B-V)_0 = -0.15$ mag and $(V-I)_0 = -0.16$ mag (Mucciarelli et al. 2007; Grisé et al. 2008). Pakull et al. (2006) showed that the optical spectrum of this object contains a He II 4686A emission line, suggestive of X-ray reprocessing. The colors of this star are consistent with those of a B spectral type star, as found also for several other ULXs with optical counterparts (e.g. Liu et al. 2002; Soria et al. 2005). A possible periodicity flux of 6.12 ± 0.16 days was found in the B band light curve (Liu et al. 2009; Impiombato et al. 2011; Zampieri & Patruno 2011; Zampieri et al. 2012) that may be possibly related to the orbital modulation of the system. In addition, the source is surrounded by a bubble nebula with a diameter of 400 pc, confirming that the source is associated to the host galaxy (Pakull & Mirioni, 2002; Zampieri et al., 2004). The nebula is expanding inside the interstellar medium at a speed of ~ 80 km s^{-1} estimated

from the emission lines of S II and O I and has a kinematic age of about 1 Myr.

- **NGC 55** is a Magellanic type galaxy, SB(s)m type, viewed almost edge-on with an inclination angle of $\sim 80°$, at a distance of 1.78 Mpc (Karachentsev et al., 2003)). It is one of the members of the Sculptor group and it hosts only one ULX. NGC 55 ULX1 is coincident with one of the biggest radio emission regions of the galaxy, therefore it seems more likely associated to it (Read et al., 1997). This particular object was observed for the first time by *ROSAT* and it is located $\sim 7'$ to the east of the main bar complex of the galaxy. It is one of the closest ULXs in the local universe with a luminosity of $\sim 1 - 2 \cdot 10^{39}$ erg s^{-1} and has intriguing temporal properties that show strong decrements in the flux on timescale of minutes/hours. Stobbart et al. (2004) related these decrements to dipping phases that become more important at higher energy. Heil et al. (2009) found a strong variability in the PDS but no further analysis have been done in terms of energy dependence of the variability. In the same year, in the spectral sequence of Gladstone et al. (2009), the spectrum of NGC 55 ULX1 showed the most extreme wind-dominated regime although its luminosity was lower than other ULXs of the sequence. This conclusion was supported by the position of the source in the galaxy, ULX1 is almost buried inside NGC 55.

- **NGC 5204** is a Magellanic type galaxy classified as SA(s)m and is a member of the M101 group. It hosts an X-ray source located at 17.3" from the nucleus (403 pc, see Colbert & Mushotzky 1999). This is the only ULX in the galaxy and it was observed for the first time by *EINSTEIN* (Fabbiano et al., 1992) and later on by *ROSAT*. Several *CHANDRA* and *XMM-Newton* observations were obtained, showing flux variations up to a factor of five on a time-scale of few-days but with no evidence of flux variability on timescales less than an hour (Roberts et al. 2005, 2006). Its luminosity, assuming a distance of 4.5 Mpc (Stobbart et al., 2006), is $\sim 7 \cdot 10^{39}$ erg

s^{-1}, making this source a genuine ULX. A H_α emitting bubble, firstly reported by Roberts et al. (2001), with a diameter of $\sim$ 400 pc, is centered around the X-ray source (Pakull & Mirioni, 2002). However the relation of the nebula with the ULX is still controversial because of inconsistencies in the determination of the extinction (see Tao et al. 2011).

Roberts et al. (2001) found a bright stellar counterpart ($m_V = 19.7$ mag) which was then resolved in *HST* images (Goad et al. 2002). Pakull & Mirioni (2002) proposed a $m_B = 21.9$ *mag* star as a major candidate for the optical counterpart. Finally, aligning *CHANDRA* and *HST* images, Liu et al. (2004) identified a single optical counterpart with colors consistent with those of a *B0 Ib* star.

- **IC 342** is a nearby starburst spiral galaxy of the type *SAB(rs)cd* in the *Maffei* group as classified by de Vaucouleurs et al. (1992). This galaxy hosts two ULXs (X-1 and X-2) which have shown spectral transitions noticed for the first time in *ASCA* data (Kubota et al., 2002) and subsequently in *XMM-Newton* data (Feng & Kaaret, 2009). Such spectral changes are reminiscent of the *high/soft - low/hard* state transitions. In our work we focused our attention only on X-1, located $\sim 5'$ away from the center of the galaxy (Bregman et al., 1993). The luminosity of X-1 has varied of at least a factor of 2 in the last 10 years, largely exceeding the luminosity of 10^{40} erg s^{-1}. The source is located inside a bubble, called the tooth-bubble (Pakull & Mirioni 2002) because of its peculiar shape. It has a diameter of $\sim$ 110 pc and shows Supernova remnant-like emission line ratios $S[II]/H = 1.2$ and $[OI]6300/H = 0.4$. Roberts et al. (2003) found that the energy needed to form the nebula was at least 2-3 times larger than the mean explosion energy of most supernovae. The nebula shows two very bright regions in the $[O\ III]$ λ5007 emission line which may be an indication of X-ray reprocessed emission.

- **Holmberg II** is an irregular dwarf galaxy (*Im*) of the M81 group (Karachentsev et al., 2003), at a distance of 4.5 Mpc. There are no indications of interactions with the closest galaxies Kar 52 and UGC 4483, so it can be definitely considered as an isolated system. The galaxy is characterised by having a very gas-rich reservoir (Puche et al. 1992; Stewart et al. 2000; Bureau & Carignan 2002) and a mass of $\sim 6 \cdot 10^9\ M_\odot$. It hosts 31 X-ray sources with luminosities higher than 10^{37} erg s^{-1} but only one of them can be considered a true ULX source (X-1 hereafter). X-1 reached a luminosity of $4 \cdot 10^{40}$ erg s^{-1} making it one of the most luminous ULX and certainly the most luminous of our sample. Its flux varied up to an order of magnitude (Zezas et al. 1999; Miyaji et al. 2001; Goad et al. 2006; Grisé et al. 2010; Caballero-García & Fabian 2010) but it seems that its spectral states are not directly correlated with its luminosity (see for example Grisé et al. 2010 and reference therein). The source is embedded in an ionised nebula (the *foot* nebula, Pakull & Mirioni 2003; Kaaret et al. 2004; Lehmann et al. 2005; Miller et al. 2005) with a luminosity in the He II 4686 emission line of $\sim 3 \cdot 10^{36}$ erg s^{-1}. Its degree of ionization strongly suggests that the nebula is photoionised by an isotropic flux corresponding to a luminosity of at least $4 \cdot 10^{39}$ erg s^{-1}. In addition, it shows diffuse radio emission, probably optically thin synchrotron emission (see Feng & Soria 2011 and references therein).

- **NGC 5408** is a dwarf irregular galaxy of the *IB(s)m* type as determined by de Vaucouleurs et al. (1992), at a distance of 4.8 Mpc (Karachentsev et al., 2003). It hosts one of the most powerful ULX, characterised by a dominant soft X-ray spectral component. A tentative periodicity of 115 days was found by Strohmayer & Mushotzky (2009) in a *Swift* monitoring campaign of the source. This was initially interpreted as an orbital period or super-orbital periodicity (Foster et al., 2010), but its existence has been recently questioned (Albert Kong, private communication).

NGC 5408 X-1 displays significant short-term variability and has a QPO at 10-20 mHz (Strohmayer et al. 2007; Strohmayer & Mushotzky 2009) whose nature is still unclear. Its properties may be consistent with a type C QPO. In particular, its frequency suggests the possibility that NGC 5408 X-1 may host an IMBH (see Section 1.4). However, the type-C QPO association was questioned by Middleton et al. (2011), arguing that the frequency break in the power spectrum is not proportional to the frequency of the QPO. In addition, the X-ray spectrum shows a significant soft excess that dominates the total flux and the fractional variability reaches values up to $\sim 40\%$ at high energy, suggesting that the soft component may be referred to a massive and turbulent outflow ejected by the accretion disc. This scenario is quite different from the standard accretion regime of Galactic BH binaries in which Type-C QPOs are detected. However, the existence of an IMBH in NGC 5408 X-1 is still debated (e.g. Dheeraj & Strohmayer, 2012). We note also that NGC 5408 X-1 is the first ULX in which a RMS-flux relation was observed. The correlation is strong in the energy range $0.3 - 1$ keV while it is poorly constrained between 1 and 10 keV (Heil & Vaughan, 2010).

The source is associated to a photoionised nebula which is probably isotropically illuminated. The inferred ionizing luminosity is $3.0 \cdot 10^{39}$ erg s^{-1} (see Lang et al. 2007; Kaaret & Corbel 2009).

- **NGC 253** is a barred spiral galaxy of the Sculptor group characterised by an intense nuclear starburst activity. With the exception of the nuclear regions where strong and extended infrared and radio emission was found, the rest of the galaxy does not display peculiar properties (Read et al., 1997). It is located ~ 3.1 Mpc away and it shows diffuse X-ray emission and a number of X-ray sources, included three ULXs (X-1, X-2 and X-3). In this work we focus our analysis on X-1 because the

diffuse emission around this source is less significant than that around the other two. NGC 253 X-1 is a transient source observed for the first time by *ROSAT* during an outburst in 1991. It has shown high variability in the X-ray luminosity up to a factor of 500, reaching a value of $\sim 2 \cdot 10^{39}$ erg s^{-1}. *XMM-Newton* observed it at luminosities consistent with those of Galactic BHBs (few 10^{38} erg s^{-1}) and also in the Ultraluminous regime ($> 10^{39}$ erg s^{-1}). The first, short *XMM-Newton* observation provided poor quality spectra which were described by a simple bremsstrahlung with a temperature of 1.74 keV (Bauer & Pietsch 2005). However the subsequent higher quality *XMM-Newton* observations were modelled with a multicolor black body disc with an average temperature around 1.3 keV (Kajava & Poutanen 2009). The disc temperature follows the $L \propto T^4$ relation, typical of a standard accretion disc, when the source has a luminosity lower than 10^{39} erg s^{-1} but then it shifts towards lower temperatures at higher luminosities, showing a behaviour similar to that observed in the spectra of XTE J1550-564 when it is in the *very high state* (Kubota & Done 2004).

- **Holmberg IX** is an irregular dwarf galaxy of the M81 group (Holmberg et al., 1974) at a distance of about 3.6 Mpc (Freedman et al. 1994). It may be the result of a tidal interaction between the galaxies M81, M82 and NGC 3077 (Sabbi et al. 2008). It hosts one ULX, Ho IX X-1, whose luminosity is $\sim 10^{40}$ erg s^{-1} in the 0.3-10 keV energy band. It is located $2'$ in the north direction of the center of the galaxy and $\sim 1'$ outside the stellar envelope of the galaxy. The source is placed into a loose cluster ($m_V \sim 22.6$) with an age ≤ 20 Myr (Grisé et al., 2011) and in a region in which the star formation is low. It is surrounded by an ionised shell-like nebula (Miller, 1995; Grisé et al., 2006b, 2011), with a diameter of 250 pc. The properties of the optical counterpart, the UV emission and the existence of a broad He II 4686 emission line

identified in the optical spectrum of the ULX, suggest reprocessing from the accretion disc (Grisé et al., 2011). It has been shown that its luminosity increases with the *power-law* photon index (if the spectra are fitted with a single *power-law* model), meaning that the observed spectrum softens as the luminosity increases (Kajava & Poutanen, 2009). The source is highly variable (La Parola et al. 2001) up to a factor of 14 and has shown spectral transitions from a *low/hard* to a *high/soft* state. However, using recent *Swift* and *XMM-Newton* observations, Vierdayanti et al. (2010) showed that such transitions appear more complex than previously thought. Kaaret & Feng (2009) found a possible periodicity of ~ 56 days in *Swift* data that, however, was not confirmed by Kong et al. (2010).

2.3 Adopted spectral models

In this section we summarize the properties and main physical parameters of the models used to analise the X-ray spectra of the ULXs of our sample. We work in the *XSPEC* environment and describe the soft component adopting a multicolor blackbody disc, i.e *diskbb* or *diskpn*. Some spectra can be well described introducing a slim disc component that we approximate using the simplified *diskpbb* model. Finally, the high energy component is described by the *comptt*, *EQPAIR*, *nthcomp* and *DKBBFTH* models.

- The **diskbb** model (see e.g. Mitsuda et al. 1984; Makishima et al. 1986) represents an approximation of the spectrum emitted by a standard accretion disc (Shakura & Sunyaev, 1973). It is obtained from the sum of the fluxes of all the annuli of the disc assuming that each of them emits as a blackbody. It shows differences from the standard disc in particular in the adopted temperature profile, in which the viscous torque at the inner boundary of the disc is not set to zero. For the Shakura & Sunyaev disc, the temperature profile is:

$$T(r) = \left(\frac{3GM\dot{M}}{8\pi\sigma R_{in}^3}\right)^{1/4} \cdot \left(\frac{r}{R_{in}}\right)^{-3/4} \left[1 - \left(\frac{R_{in}}{r}\right)^{1/2}\right]^{1/4} \tag{2.1}$$

where M is the BH mass, $\dot{M}$ is the accretion rate, r is the radial coordinate, R_{in} is the inner disc radius, G is the gravitational constant and σ is the Thompson cross-section. Instead in the *diskbb* model, it is modified as:

$$T(r) = \left(\frac{3GM\dot{M}}{8\pi\sigma R_{in,BB}^3}\right)^{1/4} \cdot \left(\frac{r}{R_{in,BB}}\right)^{-3/4} = T_{in} \cdot \left(\frac{r}{R_{in,BB}}\right)^{-3/4} \tag{2.2}$$

where $R_{in,BB}$ is the inner radius of the multicolor blackbody disc and T_{in} is the temperature at $R_{in,BB}$. The true inner disc radius is related to that of the *diskbb* model by the expression $R_{in,BB} = 2.6 \cdot R_{in}$ (Kubota et al., 1998).

The local emission in each annulus is assumed to be a blackbody which is a good approximation only if the disc is entirely optically thick to true emission-absorption and if the radiative properties of the atmosphere of the disc are not taken into account. The effects of radiative transfer at the surface of the disc can be estimated introducing a hardening factor, *f*, defined as the ratio of the colour to the effective temperature[1] (e.g. Shimura & Takahara 1995).

The emitted spectrum can be evaluated adopting the expression:

$$L_\nu = 4\pi D^2 F_\nu = 8\pi^2 \cos\theta \int_{R_{in}}^{R_{out}} I_\nu(T) r dr \tag{2.3}$$

where D is the distance to the observer, θ is the inclination angle under which the disc is seen, R_{in} and R_{out} are the inner and outer radius of the disc, respectively, and $I_\nu(T)$

[1]The colour temperature is defined as the temperature of the Planckian that best fits the emitted spectrum while the effective temperature is defined as $T_{eff} = (F/\sigma_{SB})^{1/4}$, where F and σ_{SB} are the emitted flux per unit disc area and the Stephan-Boltzmann constant, respectively.

is the specific intensity (in case of Local Termodinamic Equilibrium $I_\nu(T) = B_\nu(T)$, which is the Planck function).

Finally we note that this model does not take into account the special and general relativistic effects that influence the emission of each single annulus because the matter is in rapid rotation inside a strong gravitational field. In fact, if relativistic effects are considered, the X-ray spectrum is correctly reproduced assuming that the inner radius of the *diskbb* model is $R_{in,BB} = 19.2 - 25\ R_g$ (Lorenzin & Zampieri, 2009).

The *diskbb* model has two parameters: the inner disc temperature T_{in} (measured in keV) and the normalization, N, defined as:

$$N = \frac{(R_{in}/km)}{(D/10\ kpc)} \cdot \cos\theta. \tag{2.4}$$

- **diskpbb**: this model was introduced in order to test if sufficiently far out from the inner radius the temperature profile of the accretion disc follows that of a standard disc (Mineshige et al. 1994; Hirano et al. 1995; Watarai et al. 2000; Kubota & Done 2004; Kubota et al. 2005). A flattening of the temperature profile is expected if cooling becomes inefficient so that part of the accretion energy released at a given radius may be advected inward. Also in the *diskpbb* model the radiation emitted from each annulus is a blackbody, but the temperature profile is $T(r) = T_{in}(r/R_{in})^{-p}$, where p is a positive parameter. For a standard disc, $p = 0.75$ (see Eq. 2.1) whereas, for a slim disc, $p = 0.55$.

  The parameters of the *diskpbb* model are the inner temperature of disc T_{in}, the p-index and the normalization of the disc N (see Eq. 2.4).

- **comptt**: this model describes the Comptonization of an input spectrum of soft

photons into a hot plasma (Titarchuk, 1994). It includes relativistic effects related to the motion of the electrons and the photons are allowed to have up-scattering and down-scattering. The input spectrum is described by a Wien law. The model is valid both in optically thin and optically thick regimes and the plasma temperature may range between 2-500 keV. However, it is not valid for low optical depths and low temperatures or high optical depths and large temperatures.

The model depends in total on 6 parameters:

- Redshift of the source;
- Temperature of the soft photons input in keV;
- Temperature of the electrons in the plasma (keV);
- Optical depth of the plasma;
- Geometry of the system: it is possible to choose between negative and positive values. If the value is higher than 1 the geometry is supposed to be spherical while for values ≤ 1 the geometry is that of a disc. In general this parameter must be frozen.
- The normalization;

- **nthcomp**: developed by Zdziarski et al. (1996) and extended by Życki et al. (1999) this model provides an improved description of thermal comptonization. The high energy roll-over of the emergent spectrum is described in terms of the electron temperature and the model takes into account also the soft energy roll-over below the characteristic seed photon energy.

  The seed photons spectrum can be a blackbody or multicolor blackbody disc, the latter possibility being more consistent with the scenario of accretion via a disc. The optical depth is not a parameter in this model but it can be evaluated by a

combination of the electron temperature and the low energy asymptotic photon index of the *power-law*, which describes the part of the spectrum between the low and high temperature roll-over, as:

$$\Gamma_{thcomp} = \left\{ \frac{9}{4} + \frac{1}{[(kT_e/m_e c^2)\tau(1+\tau/3)]} \right\}^{1/2} - \frac{1}{2} \tag{2.5}$$

The model depends in total on 6 parameters:

- The asymptotic photon index at low energies;
- The electron temperature (keV);
- The temperature of the seed photons distribution in keV;
- The properties of the input distribution, i.e. blackbody or disc blackbody;
- The redshift of the source;
- The normalization;

For the high counting statistics spectra of some sources, we adopted more advanced models for the high energy component (*EQPAIR* and *DKBBFTH*) with an improvement in the estimation of the physical parameters. However, for the great majority of the observations the counting statistics is not sufficient to apply them. For the sake of completeness we summarise their properties below.

- ***EQPAIR*** is a comptonization model developed by Paolo Coppi[2] including a hybrid thermal/not thermal electron population. Since the non thermal effects are assumed to be negligible in ULXs, we used a simplified version, *Eqtherm*, in which also the photon-photon pair production is removed. This model works also in the regime in which the electrons are marginally relativistic and takes into account reflection

[2]http://www.astro.yale.edu/coppi/*EQPAIR*/eqpap4.ps

effects.

The free parameters of the model are listed below:

- l_h/l_s: the ratio of the power supplied to the accelerated electrons in the source to the luminosity of soft photons injected into the source region;
- l_{bb}: the value of the soft photon compactness. This parameters is important for the photon-photon pair production and cooling processes for the electrons/pairs;
- kT_{bb}: it determines the soft photon distribution; for positive values, the distribution is that of a *diskbb* and, for negative values, is that of the *diskpn*. This temperature is defined in keV;
- l_{nt}/l_h: the fraction of the total power supplied to energetic particles that goes into accelerating non-thermal particles; if this ratio is 1, the regime is of pure non-thermal particle acceleration, while if it is equal to 0 the power is used to heat up the region of the thermal particles;
- τ_p: Thomson scattering optical depth;
- R: radius of the spherical scattering region evaluated in centimeter;

- **DKBBFTH**: developed by Done & Kubota (2006), this model makes use of the disc-corona coupling model of Svensson & Zdziarski (1994); assuming that the major part of the mass-accretion rate is carried by the disc, this model considers that a fraction f of the accretion energy is exchanged with the corona and dissipated by it. In this model the disc temperature is a function of $(1 - f)$. The relevant parameters are:

  - kT_{disc}: the true temperature of the underlying disc for $f = 0$. The inner disc temperature used in making the model is $(1 - f)^{1/4} \cdot T_{disc}$; the temperature is defined in keV;

- r_c: this parameter represents the transition radius between the disc and the coupled disc-corona region; it is defined in units of the gravitational radius R_g;
- Γ: the asymptotic photon index of the *nthcomp* model;
- kT_e: temperature of the electrons in the corona measured in keV;

2.4 *XMM-Newton* data reduction

In this section we present the general treatment for the extraction of the *XMM-Newton* data. We adopted the standard software *Science Analysis System* (SAS) which is composed by tasks, scripts and libraries, suitable for this kind of analysis.

The results of this analysis are presented in the following chapters. We considered all the available *XMM-Newton* observations of the sources NGC 1313 X-1 and X-2, IC 342 X-1, NGC 253 X-1, NGC 5204 X-1, NGC 5408 X-1, Ho IX X-1, Ho II X-1 and NGC 55 ULX1 and adopted the standard procedure suggested by the official website.

NGC 1313 X-1 and X-2 data were reduced using v9.0.0 of SAS and EPIC-MOS and EPIC-pn spectra were extracted selecting the good time intervals (GTI) with a background count rate not higher than 0.45 count s^{-1} in the energy range $10-12$ keV. For the remaining sources we reduced the data using v11.0.0 of SAS and EPIC-MOS and EPIC-pn spectra were extracted selecting GTI with a background count rate not higher than 0.7 count s^{-1} in the $10 - 12$ keV energy range. In general, we removed from the analysis all the observations in which the sources were on or too close CCD gaps. We discarded also some observations of NGC 1313 X-1, X-2 and NGC 253 X-1 taken in the year 2000 because the calibration before December 2000 may be incomplete. In the first available observation of NGC 253 X-1 the source is on the CCD gap but a dithering applied to the pointing reduces its influence. We then included it in the analysis. Finally, some other observations were excluded as they were empty or too affected by background flare contamination.

In order to exclude the events at the CCD edge and the bad pixels, the parameter FLAG was set to zero. Spectra were extracted from events with $PATTERN \leq 4$ for EPIC-pn (which allows for single and double pixel events) and $PATTERN \leq 12$ for EPIC-MOS (which allows for single, double, triple and quadruple pixel events). In the extraction of spectra and lightcurves, we used 35" circular extraction regions for NGC 1313 X-1 and IC 342 X-1 and $30''$ circular extraction regions for NGC 1313 X-2, NGC 253 X-1, Ho II X-1, Ho IX X-1 and NGC 5408 X-1. For the background we chose a 65" circular extraction region usually on the same CCD chip where the source is located. However, NGC 5204 X-1 was often very close to the CCD gap, therefore the extraction region was different from observation to observation. In general, we used circular extraction regions of $24" - 31"$ for the source and 65" for the background, respectively.

Another exception was NGC 55 ULX1. For the first and second observation, we used 52" circular extraction regions for the source and background, respectively, for consistency with Stobbart et al. (2004), while in the third observation the source is close to the CCD gap and, to minimize its influence, 40" extraction regions were chosen. In the second observation, NGC 55 ULX1 was on the EPIC-pn CCD gap and strongly off-axis ($\sim$ 12') and, therefore, particular care was taken in analyzing it.

All the EPIC spectra were grouped with 25 counts per channel, except for the third observation of NGC 55 ULX1 in which we applied a rebinning factor of 3 in order to avoid oversampling the data.

RGS spectra were extracted using the *rgsproc* task with the option *spectrumbinning=lambda*. In this way it turns out to be possible to combine the spectra of different observations.

All the spectral fits were performed using *XSPEC* v.12.5.1. To improve the counting statistics, whenever possible, we fitted the EPIC-pn and EPIC-MOS spectra simultaneously. EPIC spectral fits were performed in the $0.3 - 10.0$ keV energy range, while RGS fits were limited at most at $0.3 - 2.2$ keV energy range. For each instrument, a multiplica-

tive constant was introduced to account for possible residual differences in the instrument calibrations. The constant of the EPIC-pn data set was fixed equal to 1, while the other two are allowed to vary. In general, the differences among the three instruments are not higher than 10%.

In Chapter 5 we compare the properties of NGC 55 ULX1 with a Galactic source, EXO 0748-676. We extracted two observations of this source taken in 2003 and 2005. The 2003 observation was taken in *small-window* mode but it was affected by pile-up. Applying the standard correction procedure[1], we excised the core of the PSF selecting an annular region of 8.5" for the inner radius and 35" for the outer radius. A similar region close to the source was chosen for the background. The observation of 2005 was in *Timing* mode, making pile-up effects negligible. In this case, we selected a rectangular region between RAWX=[20,56] for the source and RAWX=[1,7] for the background.

2.5 Overview

In the next chapters, we will study the spectral and temporal properties of the sources of our sample trying to describe them within a common picture that may account for the manifold properties of ULXs. We first surmise the possible existence of spectral states in NGC 1313 X-1 and X-2 on the basis of *diskbb+comptt* spectral fits. The spectral properties of these two sources are then looked for in all the other sources of the sample, investigating also how the temporal properties are connected with the spectral states. A complementary color analysis is also presented and used to characterise the spectral evolution of ULXs. We tested that the soft component and the variability may be the imprint of strong outflows and we tested these predictions on the closest source of our sample, NGC 55 ULX1, that shows very intriguing features in the lightcurve. In the last chapter, we present a study

[1] *http://xmm.esa.int/sas/current/documentation/threads/epatplot.shtml*

of the recently discovered transient ULX in M31, finding that it is consistent with the properties of a soft X-ray transients hosting a stellar mass BH.

Chapter 3

X-ray spectral states and metallicity in the ULXs NGC 1313 X-1 and X-2

3.1 Introduction

In order to increase our understanding of ULXs and shed light on the mechanism at the origin of their powerful emission, it is crucial to investigate the evolution of their accretion flow through the variability of their X-ray spectra. In this chapter we present a systematic analysis of the X-ray spectra of two ULXs in the galaxy NGC 1313, using three years of *XMM-Newton* observations. NGC 1313 has been observed several times over the years by *XMM-Newton* and a sufficient number of X-ray spectra are now available to attempt a characterization of the spectral variability of the sources hosted in it.

Feng & Kaaret (2006) fitted a sequence of 12 *XMM-Newton* observations of X-1 and X-2 with a power-law plus multicolor disc blackbody model and found an anti-correlation between the luminosity and the inner temperature of the *diskbb* component. For this reason they concluded that such component does not originate in a standard accretion disc. The optical and X-ray variability of X-2 was also investigated by Mucciarelli et al. (2007) to constrain the properties of the donor star and the binary system. They found that the

Table 3.1: Log of the observations.

No.	Obs ID	Date	Exp[a] (ks)	Instr. (X-1)[b]	Instr. (X-2)[b]	Net counts(X-1)	Net counts(X-2)
1	0150280101	11/25/2003	1	M1/M2	M1/M2/pn	651, 637	578, 643, 734
2	0150280301	12/21/2003	7.4	pn	M1/M2/pn	7648	2960, 2874, 6304
3	0150280401	12/23/2003	3.2	pn	M1/M2/pn	2223	2215, 2151, 3030
4	0150280501	12/25/2003	1.7	pn	M1/M2/pn	484	1379, 1378, 904
5	0150280601	01/08/2004	6.5	pn	M1/M2/pn	5524	2714, 1694, 1690
6	0150281101	01/16/2004	2.7	M1/M2/pn	M1/M2/pn	1770, 1993, 2366	887, 713, 1013
7	0205230201	05/01/2004	7.8[c]	M1/M2	M1/M2	1310, 1489	700, 783
8	0205230301	06/05/2004	8.7	M1/M2/pn	M1/M2/pn	5446, 5151, 8685	3800, 3798, 819
9	0205230401	08/23/2004	3.8	M1/M2/pn	M1/M2/pn	2397, 2643, 2323	1252, 1316, 1173
10	0205230501	11/23/2004	12.5	M1/M2	M1/M2/pn	3013, 3179	1523, 1594, 4164
11	0205230601	02/07/2005	9.0	M1/M2/pn	M1/M2/pn	5025, 2435, 2187	3702,3697, 8224
12	0301860101	03/06/2006	17.2	pn	M1/M2/pn	3980	4043, 4374, 11426
13	0405090101	10/16/2006	78.6	M1/M2/pn	pn	24277, 25141, 58116	53271

[a] GTI of EPIC-pn
[b] pn = EPIC-pn camera; M1/M2 = EPIC-MOS1/MOS2 camera
[c] GTI of EPIC-MOS

power-law component hardens as the flux increases, opposite to what usually shown by Galactic BH XRBs.

Another crucial issue related to ULX formation are the properties of the environment in which ULXs are embedded. Claims regarding the correlation of ULXs with low metallicity environments have been recently reported. Swartz et al. (2008) and Walton et al. (2011) found that within the Local Volume the specific ULX frequency decreases with host galaxy mass above $\sim 10^{8.5} M_{\odot}$, meaning that smaller, lower metallicity systems have more ULXs per unit mass than larger galaxies. Mapelli et al. (2009) and Zampieri & Roberts (2009) suggested that at least a fraction of ULXs may be powered by massive stellar BHs formed from the direct collapse of low-metallicity massive stars. Using binary synthesis calculations, Linden et al. (2010) proposed another interpretation, in which the number, the lifetime and (to a less extent) the luminosity of high mass XRBs are enhanced at low metallicities. Only few measurements of the metallicity in the ULX environment are available, and results are not conclusive (see e.g. Zampieri & Roberts 2009 and references

therein). While optical observations provide probably the best means to perform such measurements, also the abundances inferred from the detection of K-shell photoionization edges of intermediate mass or heavy elements in the X-ray absorption spectrum of ULXs can be a viable tool, if high signal-to-noise spectra are available. This was already attempted by Winter et al. (2007) for a sample of 14 ULXs with *XMM-Newton* spectra, obtaining values that match the solar abundance, but no further investigation, especially using the high resolution RGS spectra, has been attempted since then.

In this Chapter we try to characterise the spectral variability of X-1 and X-2 using all the available *XMM-Newton* data. We will try to constrain also the metallicity of the absorbing gas towards X-1 and X-2 using the RGS and EPIC spectra of the longest observation, and stacking together all the RGS observations.

3.2 Preliminary X-ray spectral fits

We analyzed 14 out of the 17 (since three observations were affected by high flares contamination) *XMM-Newton* observations of X-1 and X-2. For X-1 the off-axis angle is quite similar for most of the observations ($\sim$ 5'$-$8' for all but one observation in which it is $\sim$1'). For X-2, 10 observations have off-axis angles that differ no more than 1', while the remaining three show a more significant variation. However, their spectra do not seem to present any peculiarity possibly associated to variations in the fraction of encircled energy. We adopted an absorbed Comptonization (*EQPAIR* or *comptt* model in XSPEC) plus a multicolor blackbody disc component, when needed. The latter was added if a single comptonization model was not statistically adequate to reproduce the spectrum or if the column density converged towards values significantly lower than the average. The interstellar absorption was modelled with the *tbabs* model in *XSPEC*. We fixed the Galaxy column density, along the line of sight, at $0.39 \cdot 10^{21}$ cm^{-2} (Dickey & Lockman, 1990) and added

a free absorption component to model local absorption near the source. We found that the X-1 column density is significantly variable during time and goes from a minimum of $1.1 \cdot 10^{21}$ cm^{-2} to a maximum value of about $3.0 \cdot 10^{21}$ cm^{-2} for both *comptt* and *EQPAIR* models. On the other hand, 12 out of 14 observations of X-2 have values of the column density clustering around $1.4 \cdot 10^{21}$ cm^{-2}. The other two observations have $N_H = 0.3 \cdot 10^{21}$ cm^{-2} and $N_H = 0.5 \cdot 10^{21}$ cm^{-2}. If we fix the column density of these two observations equal to $1.4 \cdot 10^{21}$ cm^{-2}, the spectral parameters remain essentially unchanged.

3.2.1 Comptt

The best fitting parameters of the corona for X-1 and X-2, obtained modelling Comptonization with *comptt*, are reported in Figure 3.1 (see also Table 3.2). All errors are at the 90% confidence level for one interesting parameter. The position of the observations of X-1 on the $kT_{cor} - \tau$ plot does not appear to show a clear correlation with the presence or absence of a soft component. The temperature of the soft component is in the range $0.21 - 0.35$ keV. On the other hand X-2 appears to show a well defined behaviour in the $kT_{cor} - \tau$ plane that, apart from a single observation, is correlated with the presence of a *diskbb* component. The temperature of this component lies in the range $0.25 - 0.38$ keV. When the soft component is present, the corona temperature is low ($\leq$ 2 kev) and the optical depth is high ($\tau \geq 7$). When the soft component is not needed, $T_{cor} \sim 3$ keV and $\tau \sim 5$.

The spectra in these two different states are shown in Figure 3.2. The only 'anomalous' observation without a soft component located in the region of high $\tau-$ low kT_{cor} in Figure 3.1 (*bottom*) is one of the two with low N_H mentioned above. However, fixing the column density equal to $1.4 \cdot 10^{21}$ cm^{-2} and adding a soft component, the fit of this observation is statistically equivalent to that obtained applying only the *comptt* model (with the N_H fixed at $1.4 \cdot 10^{21}$ cm^{-2}). Moreover we found that the normalization of the soft

Table 3.2: Best Fit Spectral Parameters of NGC1313 X-1 and X-2 in different observations with the absorbed *comptt+diskbb* model.

NGC1313 X-1							
Date Obs.	N_H [a] (10^{22} cm^{-2})	kT_{disc} [b] (keV)	kT_{cor} [c] (keV)	τ [d]	L_x [e] (10^{39} erg s^{-1})	L_{disc} [f] (10^{39} erg s^{-1})	χ^2/dof
10/17/2000	$0.232^{+0.009}_{-0.009}$	$0.231^{+0.002}_{-0.002}$	$2.2^{+0.5}_{-0.3}$	$8.2^{+0.1}_{-0.1}$	$7.3^{+2.3}_{-1.5}$	$2.00^{0.2}_{0.2}$	689.86/698
11/25/2003	$0.17^{+0.03}_{-0.03}$	$0.111^{+0.007}_{-0.007}$	$2.67^{+0.07}_{-0.07}$	$5.6^{+0.2}_{-0.2}$	10.9^{+2}_{-3}	...	23.12/39
12/21/2003	$0.186^{+0.01}_{-0.009}$	$0.198^{+0.005}_{-0.004}$	$1.83^{+0.02}_{-0.02}$	$6.7^{+0.1}_{-0.1}$	$11.5^{+0.9}_{-0.9}$	...	195.47/227
12/23/2003	$0.25^{+0.02}_{-0.02}$	$0.177^{+0.007}_{-0.007}$	$2.42^{+0.06}_{-0.06}$	$5.8^{+0.2}_{-0.2}$	11^{+2}_{-2}	...	66.93/76
12/25/2003	$0.16^{+0.04}_{-0.04}$	$0.16^{+0.02}_{-0.02}$	$3.3^{+0.2}_{-0.2}$	$5.1^{+0.5}_{-0.5}$	$8.4^{+3.6}_{-2.7}$	...	14.49/13
01/08/2004	$0.27^{+0.02}_{-0.02}$	$0.244^{+0.005}_{-0.005}$	$4.4^{+0.1}_{-0.1}$	$4.3^{+0.2}_{-0.2}$	10.8^{+4}_{-28}	$2.7^{0.5}_{0.4}$	184.56/176
01/16/2004	$0.14^{+0.01}_{-0.01}$	$0.219^{+0.006}_{-0.006}$	$1.98^{+0.03}_{-0.03}$	$6.4^{+0.1}_{-0.1}$	$9.3^{+0.7}_{-1}$	...	195.10/198
05/01/2004	$0.12^{+0.02}_{-0.02}$	$0.175^{+0.008}_{-0.007}$	$3.19^{+0.08}_{-0.08}$	$5.6^{+0.2}_{-0.2}$	$5.8^{+1.1}_{-0.8}$	...	106.03/92
06/05/2004	$0.128^{+0.007}_{-0.007}$	$0.231^{+0.004}_{-0.004}$	$1.72^{+0.01}_{-0.01}$	$7.2^{+0.1}_{-0.1}$	14.0^{+1}_{-1}	...	512.21/544
08/23/2004	$0.24^{+0.01}_{-0.01}$	$0.154^{+0.002}_{-0.002}$	$2.56^{+0.03}_{-0.03}$	$3.72^{+0.07}_{-0.07}$	$5.5^{+0.5}_{-0.5}$	...	234.06/233
11/23/2004	$0.11^{+0.01}_{-0.01}$	$0.181^{+0.005}_{-0.005}$	$3.23^{+0.06}_{-0.06}$	$5.5^{+0.1}_{-0.1}$	$7.1^{+0.8}_{-0.7}$	...	181.82/185
02/07/2005	$0.29^{+0.03}_{-0.03}$	$0.208^{+0.002}_{-0.002}$	$2.7^{+0.5}_{-0.5}$	$7.0^{+0.2}_{-0.2}$	$8.9^{+1.1}_{-1.2}$	$2.7^{+0.7}_{-0.7}$	313.10/305
03/06/2006	$0.24^{+0.02}_{-0.02}$	$0.346^{+0.007}_{-0.007}$	$1.09^{+0.03}_{-0.03}$	$15.6^{+0.9}_{-0.9}$	$4.7^{+0.7}_{-0.6}$	$1.8^{+0.2}_{-0.3}$	169.35/139
10/16/2006	$0.249^{+0.001}_{-0.001}$	$0.230^{+0.001}_{-0.001}$	$2.09^{+0.06}_{-0.01}$	$8.65^{+0.06}_{-0.06}$	$6.9^{+0.3}_{-0.2}$	$2.0^{+0.05}_{-0.1}$	1624.29/1481
NGC1313 X-2							
Date Obs.	N_H [a] (10^{22} cm^{-2})	kT_{disc} [b] (keV)	kT_{cor} [c] (keV)	τ [d]	L_x [e] (10^{39} erg s^{-1})	L_{disc} [f] (10^{38} erg s^{-1})	χ^2/dof
10/17/2000	$0.14^{+0.01}_{-0.01}$	$0.169^{+0.005}_{-0.005}$	$3.33^{+0.06}_{-0.06}$	$4.4^{+0.1}_{-0.1}$	$1.7^{+0.1}_{-0.2}$	...	141.40/146
11/25/2003	$0.03^{+0.02}_{-0.02}$	$0.26^{+0.02}_{-0.02}$	$1.18^{+0.03}_{-0.03}$	$12.7^{+0.6}_{-0.6}$	$5.1^{+1.4}_{-1.1}$	$1.9^{+2.9}_{-1.4}$	59.60/62
12/21/2003	$0.13^{+0.01}_{-0.01}$	$0.286^{+0.009}_{-0.009}$	$1.58^{+0.02}_{-0.02}$	$10.5^{+0.2}_{-0.2}$	$7.1^{+0.8}_{-0.6}$	$5.2^{+3}_{-0.1}$	386.29/395
12/23/2003	$0.05^{+0.01}_{-0.01}$	$0.26^{+0.01}_{-0.01}$	$1.72^{+0.03}_{-0.03}$	$10.1^{+0.2}_{-0.2}$	$7.7^{+0.9}_{-0.8}$	...	245.35/249
12/25/2003	$0.12^{+0.03}_{-0.02}$	$0.32^{+0.01}_{-0.01}$	$1.96^{+0.06}_{-0.06}$	$7.2^{+0.3}_{-0.3}$	$3.5^{+0.8}_{-0.6}$	$7.2^{+2.1}_{-1.7}$	101.36/120
01/08/2004	$0.13^{+0.01}_{-0.01}$	$0.254^{+0.007}_{-0.007}$	$1.91^{+0.03}_{-0.03}$	$6.5^{+0.2}_{-0.2}$	$2.7^{+0.5}_{-0.3}$	$3.6^{+1}_{-0.9}$	175.30/201
01/16/2004	$0.13^{+0.02}_{-0.02}$	$0.173^{+0.007}_{-0.007}$	$2.61^{+0.06}_{-0.06}$	$5.5^{+0.2}_{-0.2}$	$2.5^{+0.5}_{-0.4}$	...	85.33/86
05/01/2004	$0.10^{+0.05}_{-0.04}$	$0.38^{+0.01}_{-0.01}$	$1.44^{+0.07}_{-0.07}$	$7.2^{+0.7}_{-0.7}$	$1.8^{+0.5}_{-0.5}$	$6.3^{+2.1}_{-1.7}$	55.41/46
06/05/2004	$0.14^{+0.009}_{-0.008}$	$0.235^{+0.006}_{-0.006}$	$1.48^{+0.01}_{-0.01}$	$11.0^{+0.2}_{-0.2}$	$8.2^{+0.7}_{-0.6}$	$1.4^{+0.7}_{-0.7}$	515.23/507
08/23/2004	$0.14^{+0.01}_{-0.01}$	$0.151^{+0.005}_{-0.005}$	$3.36^{+0.07}_{-0.07}$	$4.6^{+0.1}_{-0.1}$	$2.0^{+0.3}_{-0.3}$	...	162.21/132
11/23/2004	$0.143^{+0.01}_{-0.009}$	$0.169^{+0.004}_{-0.004}$	$2.98^{+0.04}_{-0.04}$	$4.9^{+0.1}_{-0.1}$	$2.1^{+0.3}_{-0.2}$	...	215.02/238
02/07/2005	$0.104^{+0.009}_{-0.009}$	$0.268^{+0.009}_{-0.008}$	$1.53^{+0.02}_{-0.02}$	$11.4^{+0.2}_{-0.2}$	$7.7^{+0.7}_{-0.6}$	$2.4^{+1}_{-0.6}$	491.14/486
03/06/2006	$0.15^{+0.01}_{-0.01}$	$0.288^{+0.007}_{-0.007}$	$1.42^{+0.01}_{-0.01}$	$11.5^{+0.2}_{-0.2}$	$7.5^{+0.6}_{-0.6}$	$5.1^{+1.2}_{-1}$	577.03/603
10/16/2006	$0.133^{+0.004}_{-0.004}$	$0.258^{+0.004}_{-0.004}$	$1.63^{+0.01}_{-0.01}$	$9.94^{+0.08}_{-0.08}$	$6.8^{+0.3}_{-0.2}$	$2.5^{+0.4}_{-0.4}$	843.58/854

[a] Column density; [b] Inner disc temperature; the seed photons temperature T_0 is assumed to be equal to T_{disc}. [c] Temperature of the corona; [d] Optical depth of the corona; [e] Unabsorbed total x-ray luminosity in the 0.3 -10 keV range; [f] Unabsorbed disc luminosity in the 0.3-10 keV range.

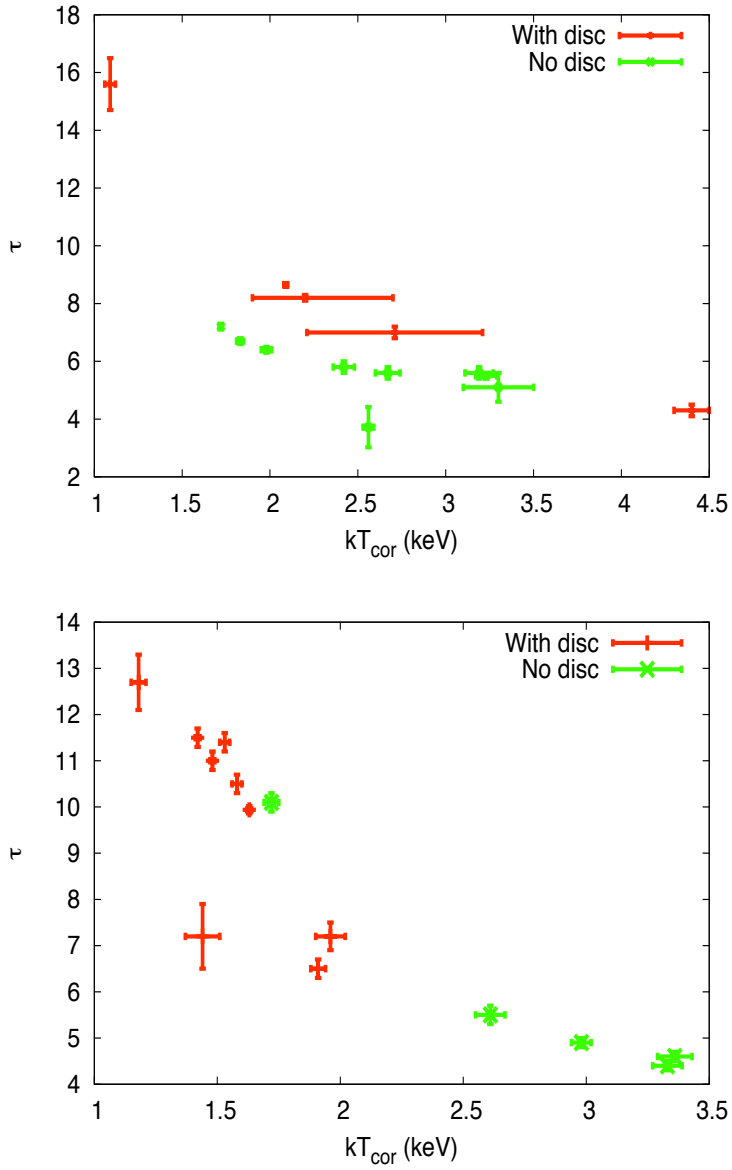

Figure 3.1: Optical depth versus temperature of the corona for the X-ray spectral fits of X-1 (*top*) and X-2 (*bottom*) with a *diskbb+comptt* model.

component is comparable to that obtained from the other spectra that show the presence of a disc. Therefore, it is unclear if this observation is really anomalous or if there is not sufficient statistics at low energies to pinpoint the soft component.

Letting aside this observation, when the disc component is present the total luminosity of X-2 may vary significantly, reaching $\sim 8 \cdot 10^{39}$ erg s^{-1}. However, at low luminosity the source appears to show spectra with and without a soft component, likely reflecting the lack of one-to-one correspondence between spectral shape and luminosity observed in Galactic BH binaries.

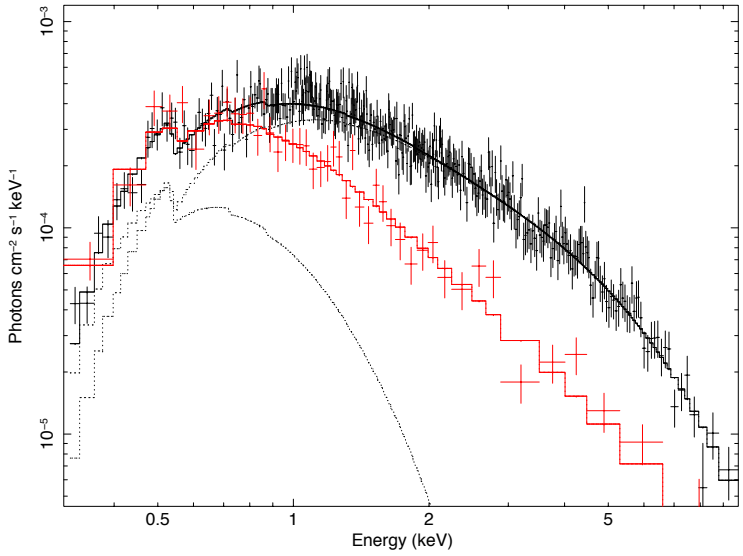

Figure 3.2: X-ray spectra of X-2 for a low luminosity state *without* disc (*red*) [$\tau = 3.4$ and $kT_{cor} = 4.6$] and a high luminosity state *with* disc (*black*) [$\tau = 11.5$ and $kT_{cor} = 1.4$].

Figure 3.3 shows the light curves of X-1 and X-2 computed from the best fitting *diskbb+comptt* models (a distance of 3.7 Mpc was assumed; Tully & Fisher 1988). On average, X-1 has a luminosity ($\sim 10^{40}$ erg s^{-1}), higher than that of X-2 ($\sim 5 \cdot 10^{39}$ erg s^{-1}). Variability of a factor ~ 3 and ~ 5 is observed for X-1 and X-2, respectively.

We further investigated the behaviour of the soft component in both sources. X-1

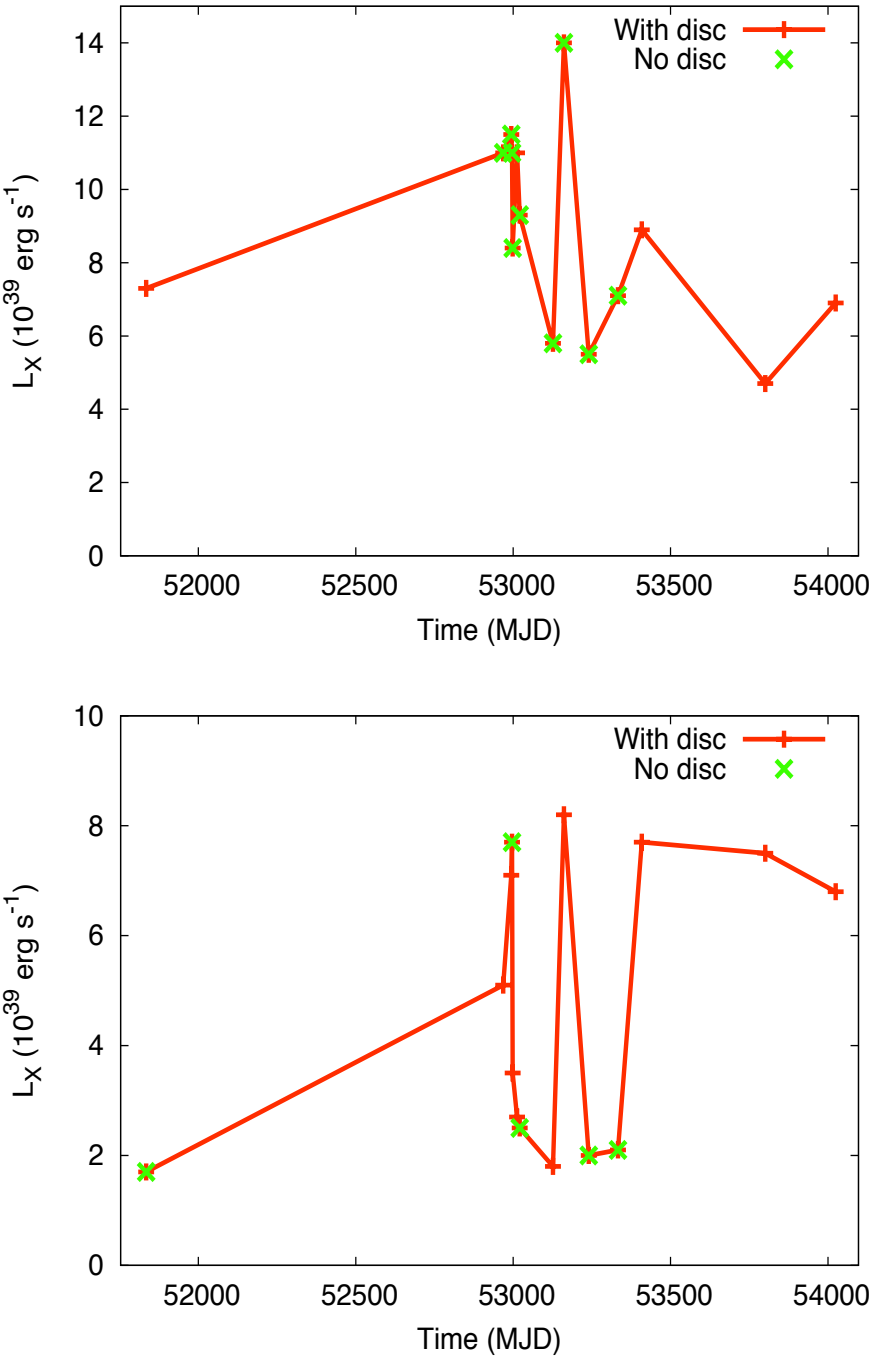

Figure 3.3: *Top*: X-ray light curve of X-1 (*top*) and X-2 (*bottom*). Unabsorbed luminosities evaluated in the 0.3-10 keV energy band.

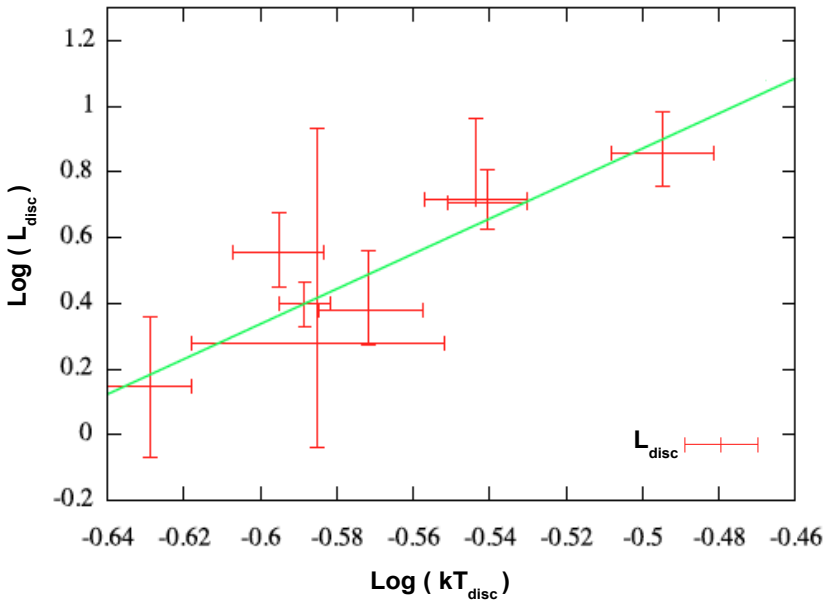

Figure 3.4: Inner disc temperature vs disc luminosity for X-2. The solid line is the best fit obtained with a power-law (see text). All the (unabsorbed) luminosities are evaluated in the 0.3-10 KeV energy band.

shows the disc component only in 5 observations while X-2 in 9 observations. In X-1 the luminosity of the soft component is $\sim 10^{39}$ erg s^{-1} and it represents a significant part of the total flux. There is essentially no correlation between the luminosity of the disc component and the inner disc temperature. The same holds true also for the total luminosity. On the other hand, for X-2 the luminosity of the soft component is only a small fraction of the total luminosity and the disc luminosity (L_{disc}) appears to show a power-law correlation with the inner temperature (T_{in}): $L_{\rm disc} \propto T_{in}^{5.3\pm1.1}$ (see Figure 3.4). In this fit we neglected the observation with kT$_{cor}$ = 1.7 keV and $\tau = 10$ because it has a very low statistics and the disc parameters inferred from it are not well constrained.

Table 3.3: Best Fit Spectral Parameters of NGC1313 X-1 and X-2 in different observations with the absorbed *Eqtherm+diskbb* model.

NGC1313 X-1							
Date Obs.	N_H [a]	kT_{disc} [b]	l_h/l_s [c]	τ [d]	L_x [d]	L_{disc} [e]	χ^2/dof
	(10^{22} cm^{-2})	(keV)			(10^{39} erg s^{-1})	(10^{39} erg s^{-1})	
10/17/2000	$0.212^{+0.005}_{-0.005}$	$0.2720^{+0.0007}_{-0.0007}$	$2.16^{+0.08}_{-0.04}$	$16.7^{+0.7}_{-0.7}$	$6.8^{+0.7}_{-0.2}$	$2.0^{+0.2}_{-0.1}$	691.25/697
11/25/2003	$0.17^{+0.03}_{-0.02}$	$0.118^{+0.01}_{-0.01}$	$2.3^{+0.3}_{-0.3}$	4^{+1}_{-1}	$11.0^{+0.3}_{-0.2}$	...	22.99/38
12/21/2003	$0.211^{+0.009}_{-0.009}$	$0.200^{+0.001}_{-0.001}$	$1.08^{+0.05}_{-0.05}$	10.6^{+1}_{-1}	$12.0^{+0.2}_{-0.2}$	...	198.04/226
12/23/2003	$0.24^{+0.02}_{-0.02}$	$0.200^{+0.002}_{-0.002}$	$1.4^{+0.2}_{-0.1}$	8.2^{+2}_{-3}	$11.0^{+0.2}_{-0.2}$	...	69.25/75
12/25/2003	$0.11^{+0.03}_{-0.04}$	$0.30^{+0.006}_{-0.007}$	7.3^{+9}_{-4}	$0.9^{+0.3}_{-0.2}$	$8.8^{+1.2}_{-1.9}$	...	15.50/13
01/08/2004	$0.20^{+0.01}_{-0.01}$	$0.236^{+0.001}_{-0.001}$	$2.2^{+0.3}_{-0.2}$	$1.1^{+0.1}_{-0.1}$	$9.7^{+0.3}_{-0.8}$	$1.3^{+1.3}_{-1.3}$	183.05/175
01/16/2004	$0.21^{+0.01}_{-0.01}$	$0.200^{+0.001}_{-0.001}$	$1.18^{+0.07}_{-0.07}$	9.4^{+1}_{-1}	$9.1^{+0.9}_{-1.1}$	...	194.96/197
05/01/2004	–	–	–	–	–	–	..
06/05/2004	$0.215^{+0.007}_{-0.007}$	$0.20^{+0.0006}_{-0.0006}$	$1.19^{+0.04}_{-0.03}$	$11.1^{+0.9}_{-0.6}$	$14^{+0.1}_{-0.1}$	...	513.78/543
08/23/2004	$0.229^{+0.009}_{-0.009}$	$0.1642^{+0.0007}_{-0.0007}$	$0.56^{+0.03}_{-0.02}$	$5.7^{+1}_{-0.8}$	$4.3^{+0.6}_{-0.4}$	...	242.40/232
11/23/2004	$0.18^{+0.01}_{-0.01}$	$0.232^{+0.001}_{-0.001}$	$4.0^{+0.8}_{-0.7}$	$0.89^{+0.1}_{-0.07}$	$8.0^{+0.7}_{-0.7}$	...	167.41/184
02/07/2005	$0.306^{+0.009}_{-0.008}$	$0.208^{+0.0009}_{-0.0009}$	$2.5^{+0.2}_{-0.1}$	$11.3^{+1}_{-0.5}$	$8.8^{+1.2}_{-1.2}$	$2.9^{+0.3}_{-0.3}$	313.44/304
03/06/2006	$0.25^{+0.01}_{-0.01}$	$0.312^{+0.003}_{-0.003}$	$1.29^{+0.09}_{-0.09}$	32.8^{+8}_{-6}	$4.8^{+0.6}_{-0.6}$	$1.5^{+0.2}_{-0.2}$	171.43/138
10/16/2006	$0.253^{+0.002}_{-0.002}$	$0.2399^{+0.0003}_{-0.0003}$	$2.21^{+0.04}_{-0.03}$	$15.8^{+0.2}_{-0.3}$	$6.7^{+0.6}_{-0.1}$	$2.0^{+0.1}_{-0.1}$	1625.67/1480
NGC1313 X-2							
Date Obs.	N_H [a]	kT_{disc} [b]	l_h/l_s [c]	τ [d]	L_x [d]	L_{disc} [e]	χ^2/dof
	(10^{22} cm^{-2})	(keV)			(10^{39} erg s^{-1})	(10^{39} erg s^{-1})	
10/17/2000	$0.16^{+0.01}_{-0.01}$	$0.205^{+0.002}_{-0.002}$	$1.5^{+0.2}_{-0.2}$	$1.2^{+0.2}_{-0.2}$	$1.7^{-}_{-0.1}$	...	139.38/145
11/25/2003	$0.10^{+0.03}_{-0.03}$	$0.199^{+0.002}_{-0.002}$	$1.9^{+0.1}_{+0.1}$	26.5^{+4}_{-3}	5.1^{+1}_{-1}	...	58.86/62
12/21/2003	$0.15^{+0.01}_{-0.01}$	$0.32^{+0.01}_{-0.01}$	$1.49^{+0.07}_{-0.06}$	19^{+1}_{-1}	$6.9^{+6.1}_{-3.3}$	$6.1^{+3.6}_{-2.4}$	385.68/394
12/23/2003	$0.13^{+0.02}_{-0.02}$	$0.230^{+0.001}_{-0.001}$	$2.08^{+0.1}_{-0.09}$	18^{+1}_{-1}	$7.8^{+0.9}_{-0.8}$	...	245.73/248
12/25/2003	$0.15^{+0.02}_{-0.02}$	$0.198^{+0.002}_{-0.002}$	$1.4^{+0.1}_{-0.1}$	13^{+2}_{-2}	$3.4^{+2}_{-1.5}$	$1.0^{+0.9}_{-1.2}$	101.48/119
01/08/2004	$0.18^{+0.01}_{-0.01}$	$0.22^{+0.02}_{-0.02}$	$1.04^{+0.08}_{-0.07}$	11^{+2}_{-2}	$2.7^{+7.3}_{-2.1}$	$2.8^{+6.0}_{-2.0}$	252.41/200
01/16/2004	$0.16^{+0.02}_{-0.02}$	$0.171^{+0.002}_{-0.002}$	$1.51^{+0.1}_{-0.08}$	7.5^{+1}_{-2}	$2.8^{+0.7}_{-0.6}$	...	85.49/85
05/01/2004	–	–	–	–	–	–	..
06/05/2004	$0.22^{+0.01}_{-0.01}$	$0.238^{+0.001}_{-0.001}$	$1.84^{+0.05}_{-0.06}$	$20.6^{+0.9}_{-0.9}$	$8.5^{+9.5}_{-2.7}$	$5.0^{+1.4}_{-1.4}$	287.60/270
08/23/2004	$0.21^{+0.02}_{-0.02}$	$0.191^{+0.002}_{-0.002}$	$1.7^{+0.3}_{-0.3}$	$0.6^{+0.09}_{-0.06}$	$1.3^{+0.2}_{-0.2}$	...	150.99/131
11/23/2004	$0.16^{+0.01}_{-0.01}$	$0.211^{+0.01}_{-0.01}$	$1.6^{+0.2}_{-0.2}$	$1.2^{+0.2}_{-0.1}$	$1.4^{+0.2}_{-0.2}$	...	211.11/237
02/07/2005	$0.14^{+0.01}_{-0.01}$	$0.251^{+0.001}_{-0.001}$	$1.98^{+0.07}_{-0.07}$	22^{+1}_{-1}	$7.7^{+2.2}_{-1.7}$	$1.7^{+0.8}_{-0.9}$	489.36/485
03/06/2006	$0.191^{+0.009}_{-0.009}$	$0.327^{+0.001}_{-0.001}$	$1.42^{+0.04}_{-0.04}$	$23.7^{+0.9}_{-1}$	$7.4^{+2.1}_{-1.7}$	$7.6^{+1.2}_{-1.2}$	578.54/602
10/16/2006	$0.180^{+0.005}_{-0.005}$	$0.2841^{+0.0007}_{-0.0007}$	$1.60^{+0.03}_{-0.03}$	$17.9^{+0.5}_{-0.5}$	$7.1^{+0.2}_{-0.2}$	$4.3^{+0.3}_{-0.3}$	827.48/853

[a] Column density; [b] Inner disc temperature; [c] Compactness ratio, i.e. the ratio of the power of the hard photons and the power of input photons target; [d] Optical depth of the corona; [e] Unabsorbed total x-ray luminosity in the 0.3 -10 keV range; [f] Unabsorbed disc luminosity in the 0.3-10 keV range.

3.2.2 Eqtherm

The *EQPAIR* model allows for a 'hybrid' (thermal and non-thermal) plasma and computes the resulting comptonized spectrum without assuming that the electrons are non relativistic. The seed photons may have a disc or blackbody spectral distribution. For ULXs, non-thermal processes are not likely to be important, so we decided to adopt a simplified version of *EQPAIR*, dubbed *eqtherm*, that neglects them. The results obtained modelling Comptonization with the *eqtherm* model are similar to those obtained with the *comptt* model for both sources (see Table 3.3). The soft component is needed in 5 spectra for X-1 and 7 for X-2. Also in this case X-2 displays a dependence of the disc luminosity on the disc inner temperature, that follows the relation $L_{\rm disc} \propto T_{in}^{2.1\pm0.5}$.

3.3 Preliminary discussion

The analysis of all the *XMM-Newton* observations shows that the spectra of X-1 and X-2 can be well reproduced by a Comptonization model plus a soft component. X-2 appears to show a well defined spectral behaviour in the optical depth (τ) versus corona temperature (T_{cor}) plane that, apart possibly for one observation, correlates with the presence of a soft component.

As already suggested by Gladstone et al. (2009), it is likely that X-1 and X-2 are in different regimes. X-1 shows higher average isotropic luminosity ($\sim 10^{40}$ erg s^{-1}) and smaller variability during the six years of observation. From time to time it shows the presence of a soft component that emits a significant fraction of the total flux and does not correlate with the disc temperature. As Gladstone et al. (2009) proposed, X-1 could be in the Ultraluminous regime, accreting at super-Eddington rates and launching powerful winds from the disc/corona (Poutanen et al. 2007). The accretion disc may be there, but covered by the wind/corona, while the soft component may actually represent emission

from the wind itself.

On the other hand, X-2 could be in a different regime, in which the average accretion rate is at around the Eddington limit. The disc may be still partly visible. This hypothesis is enforced by the correlation that we found between the disc luminosity and inner temperature, consistent with that of a standard disc ($L \propto T^4$) when adopting the *comptt* model. The correlation disappears using a simple power-law to describe the spectrum of the corona, as found by Feng & Kaaret (2006), because it does not take into account the spectral curvature at high energies. The corona may become more expanded in the low-luminosity no-disc state, when it covers the entire disc and no disc component is visible in the spectrum. Clearly, as the corona is always optically thick, it is not possible to use the disc parameters for estimating the BH mass. We found also that for X-2 the corona temperature decreases and the optical depth increases as the total luminosity goes up, in agreement with the recent analysis of Vierdayanti et al. (2010) for Ho IX X-1, although such a relation was questioned by Kong et al. (2010). So X-2 could be in a state similar to that of Ho IX X-1, with the corona becoming progressively mass loaded as the luminosity increases (Gladstone et al., 2009).

3.4 Comptonization plus multicolor blackbody disc

Although several of our observations show acceptable fits using only the *comptt* component, in some cases adding the *diskbb* component leads to a significant improvement in the fit. Therefore, in order to perform a comparison within the framework of a unique spectral model, here we assume the *diskbb+comptt* as reference model for all the observations and check its consistency on the basis of the variability patterns of its spectral parameters.

The results of the spectral fits with the *diskbb+comptt* model for the 13 *XMM-Newton* observations of X-1 and X-2 are reported in Table 3.4.

Table 3.4: Best fitting spectral parameters of NGC1313 X-1 and X-2 obtained with the absorbed *diskbb+comptt* model.

NGC1313 X-1								
No.	Date	N_H [a] (10^{21} cm^{-2})	kT_{disc} [b,c] (keV)	kT_{cor} [d] (keV)	τ [e]	L_X [0.3-10 keV] [f] (10^{39} erg s^{-1})	L_{disc} [0.3-10 keV] [g] (10^{39} erg s^{-1})	χ^2/dof
1	11/25/2003	$0.2^{+0.2}_{-0.2}$	$0.80^{+0.01}_{-0.01}$	9.03^{+400}_{-5}	16.2^{+2}_{-2}	$10.0^{+0.3}_{-0.3}$	$5.0^{1.2}_{0.4}$.	21.33/38
2	12/21/2003	$1.9^{+0.1}_{-0.1}$	$0.199^{+0.005}_{-0.005}$	$1.83^{+0.02}_{-0.02}$	$6.7^{+0.1}_{-0.1}$	$11.5^{+0.9}_{-0.9}$	0^{+3e36}_{0}	195.47/226
3	12/23/2003	$4.0^{+0.2}_{-0.2}$	$0.229^{+0.004}_{-0.004}$	$2.41^{+0.08}_{-0.08}$	$6.2^{+0.3}_{-0.3}$	$14.2^{+2.5}_{-2.2}$	$4.6^{0.8}_{0.9}$.	64.38/75
4	12/25/2003	$4.3^{+0.4}_{-0.4}$	$0.179^{+0.005}_{-0.006}$	$2.7^{+0.2}_{-0.2}$	$6.2^{+0.7}_{-0.7}$	$14.9^{+5.9}_{-4.8}$	$6.6^{2.4}_{2}$	12.88/12
5	01/08/2004	$2.7^{+0.1}_{-0.1}$	$0.244^{+0.003}_{-0.003}$	$4.5^{+0.1}_{-0.1}$	$4.3^{+0.2}_{-0.2}$	$10.8^{+1.3}_{-1.1}$	$2.7^{+0.4}_{-0.3}$	184.56/176
6	01/16/2004	$1.3^{+0.1}_{-0.1}$	$0.226^{+0.006}_{-0.006}$	$2.28^{+0.04}_{-0.04}$	$5.8^{+0.1}_{-0.1}$	$9.3^{+1.8}_{-0.6}$	$0^{1.6e38}_{0}$	194.71/197
7	05/01/2004	$3.2^{+0.2}_{-0.2}$	$0.216^{+0.003}_{-0.003}$	$4.8^{+0.2}_{-0.2}$	$4.8^{+0.3}_{-0.3}$	$8.0^{+1.8}_{-1.3}$	$2.4^{0.6}_{0.4}$	100.97/91
8	06/05/2004	$1.87^{+0.07}_{-0.07}$	$0.242^{+0.003}_{-0.003}$	$1.78^{+0.02}_{-0.02}$	$7.1^{+0.1}_{-0.1}$	15.0^{+1}_{-1}	$1.3^{0.2}_{0.2}$	511.38/543
9	08/23/2004	$2.3^{+0.1}_{-0.1}$	$0.158^{+0.002}_{-0.002}$	$2.59^{+0.03}_{-0.03}$	$3.70^{+0.07}_{-0.07}$	$5.4^{+0.6}_{-0.5}$	$0^{1.4e38}_{0}$	233.91/232
10	11/23/2004	$2.2^{+0.1}_{-0.1}$	$0.367^{+0.003}_{-0.003}$	$1.48^{+0.04}_{-0.04}$	$14.6^{+0.8}_{-0.8}$	$8.2^{+1}_{-0.9}$	$3.7^{0.3}_{0.3}$	165.41/184
11	02/07/2005	$2.91^{+0.09}_{-0.08}$	$0.208^{+0.002}_{-0.002}$	$2.71^{+0.05}_{-0.05}$	$7.0^{+0.2}_{-0.2}$	$8.9^{+1}_{-0.9}$	$2.7^{+0.3}_{-0.3}$	313.10/305
12	03/06/2006	$2.3^{+0.1}_{-0.1}$	$0.459^{+0.004}_{-0.004}$	$1.01^{+0.03}_{-0.03}$	15^{+17}_{-9}	$4.6^{+0.6}_{-0.5}$	$2.5^{+0.1}_{-0.2}$	168.29/139
13	10/16/2006	$2.67^{+0.002}_{-0.002}$	$0.222^{+0.001}_{-0.001}$	$2.14^{+0.01}_{-0.01}$	$8.44^{+0.06}_{-0.06}$	$7.1^{+0.2}_{-0.2}$	$2.1^{+0.1}_{-0.1}$	1490.95/1420
NGC1313 X-2								
No.	Date	N_H [a] (10^{21} cm^{-2})	kT_{disc} [b] (keV)	kT_{cor} [c] (keV)	τ [d]	L_X [0.3-10 keV] [e] (10^{39} erg s^{-1})	L_{disc} [0.3-10 keV] [f] (10^{38} erg s^{-1})	χ^2/dof
1	11/25/2003	$0.6^{+0.2}_{-0.2}$	$0.44^{+0.01}_{-0.01}$	$1.35^{+0.05}_{-0.05}$	$10.8^{+0.8}_{-0.7}$	$5.4^{+1.4}_{-1.2}$	12^{+3}_{-4}	58.72/62
2	12/21/2003	$1.6^{+0.1}_{-0.1}$	$0.380^{+0.004}_{-0.004}$	$1.56^{+0.02}_{-0.02}$	$11.0^{+0.3}_{-0.3}$	$7.3^{+0.7}_{-0.6}$	14^{+1}_{-2}	386.05/395
3	12/23/2003	$0.5^{+0.1}_{-0.1}$	$0.27^{+0.01}_{-0.01}$	$1.74^{+0.03}_{-0.03}$	$10.0^{+0.2}_{-0.2}$	$7.7^{+1}_{-0.8}$	$0^{6.4e+37}_{0}$	245.35/248
4	12/25/2003	$1.2^{+0.2}_{-0.2}$	$0.469^{+0.006}_{-0.006}$	$3.02^{+0.2}_{-0.2}$	$6.3^{+0.6}_{-0.6}$	$3.7^{+0.8}_{-0.6}$	14.4^{+2}_{-8}	99.68/120
5	01/08/2004	$1.4^{+0.1}_{-0.1}$	$0.266^{+0.005}_{-0.005}$	$1.89^{+0.04}_{-0.04}$	$6.6^{+0.2}_{-0.2}$	$2.8^{+0.4}_{-0.4}$	$4.5^{+1}_{-0.9}$	175.27/201
6	01/16/2004	$2.1^{+0.2}_{-0.2}$	$0.186^{+0.005}_{-0.005}$	$5.93^{+0.2}_{-0.2}$	$3.3^{+0.2}_{-0.2}$	$3.5^{+0.9}_{-0.7}$	$4.7^{+2.3}_{-1.7}$	84.94/85
7	05/01/2004	$1.0^{+0.3}_{-0.3}$	$0.38^{+0.01}_{-0.01}$	$1.44^{+0.07}_{-0.07}$	$7.2^{+0.7}_{-0.7}$	$1.8^{+0.5}_{-0.4}$	$6.3^{+1.7}_{-1.4}$	55.41/46
8	06/05/2004	$1.1^{+0.1}_{-0.1}$	$0.238^{+0.006}_{-0.006}$	$1.48^{+0.01}_{-0.01}$	$11.0^{+0.2}_{-0.2}$	$8.0^{+0.7}_{-0.5}$	$0^{+4.8e39}_{0}$	514.96/507
9	08/23/2004	$3.0^{+0.1}_{-0.1}$	$0.208^{+0.002}_{-0.002}$	$1.96^{+0.05}_{-0.05}$	$7.4^{+0.3}_{-0.3}$	$2.8^{+0.4}_{-0.4}$	12^{2}_{2}	150.72/131
10	11/23/2004	$2.3^{+0.1}_{-0.09}$	$0.226^{+0.002}_{-0.002}$	$3.84^{+0.08}_{-0.08}$	$4.4^{+0.1}_{-0.1}$	$2.6^{0+.3}_{-0.3}$	$7.0^{1.1}_{0.9}$	210.89/237
11	02/07/2005	$1.69^{+0.09}_{-0.08}$	$0.633^{+0.004}_{-0.004}$	$1.55^{+0.02}_{-0.02}$	$13.0^{+0.5}_{-0.5}$	$8.1^{+0.4}_{-0.6}$	28^{+2}_{-1}	490.92/486
12	03/06/2006	$1.54^{+0.08}_{-0.08}$	$0.288^{+0.006}_{-0.006}$	$1.42^{+0.01}_{-0.01}$	$11.5^{+0.2}_{-0.2}$	$7.5^{+0.6}_{-0.6}$	$5.1^{+1}_{-0.9}$	577.03/603
13	10/16/2006	$1.89^{+0.04}_{-0.04}$	$0.61^{+0.02}_{-0.02}$	$1.61^{+0.01}_{-0.01}$	$12.3^{+0.3}_{-0.3}$	$7.2^{+0.2}_{-0.3}$	$28^{+1.1}_{-0.2}$	841.83/854

[a] Column density; [b] Inner disc temperature; [c] The seed photons temperature T_0 is assumed to be equal to T_{disc}. [d] Temperature of the corona; [e] Optical depth of the corona; [f] Unabsorbed total x-ray luminosity in the 0.3 -10 keV range; [g] Unabsorbed disc luminosity in the 0.3-10 keV range.

We tied the temperature of the disc (T_{disc}) to that of the seed photons (T_0) for comptonization. We will comment on this choice at the end of this Section. The reported errors are at the 90% confidence level for one interesting parameter. We note that there are often several local minima with close values of the χ^2, sometimes with evidence for both a strong/warm and a weak/cool (or no) disc. After a careful inspection of the χ^2 surface, we found the absolute minima for each observation reported in Table 3.4. However, one should be aware that the actual uncertainty on the disc parameters caused by the topology of the χ^2 surface may be a few times larger than the formal error reported in the Table. We tried to adopt also more physical models, such as the *eqtherm* (Coppi, 2000) and the *DKBBFTH* (Done & Kubota, 2006). We found that the counting statistics of most of the spectra is inadequate to constrain the parameters of *eqtherm* and *DKBBFTH* (see also below).

The longest observation of X-1 has a short segment of ~ 3.5 ks within the first 13 ks that shows some intrinsic variability (a slight systematic hardening at high energies) and was then removed from the analysis. We note also that observation #1 has a very low value of N_H compared to the other observations and a low counting statistics. It converges towards a local minimum with a very strong disc component and with parameters unlike those of all the other spectra. For this reason, we excluded it from the following analysis.

Figure 3.5 shows a plot of the optical depth τ versus the temperature of the corona kT_{cor} obtained from the best fits of both sources. There appears to be well defined locii in the $kT_{cor} - \tau$ plane, indicating the existence of a somewhat ordered behaviour in the spectral variability of the corona. The spectra of X-2 populate two distinct regions characterised by very large optical depths ($\tau > 10$) and low temperatures ($kT_{cor} \sim 1.5$ keV), on one side, and smaller optical depths ($\tau < 8$) and a range of temperatures ($kT_{cor} \sim 1.5 - 6$ keV), on the other side. In both cases the corona turns out to be optically thick. In the following we refer to these two regions as "very-thick" and "thick" corona states, respectively.

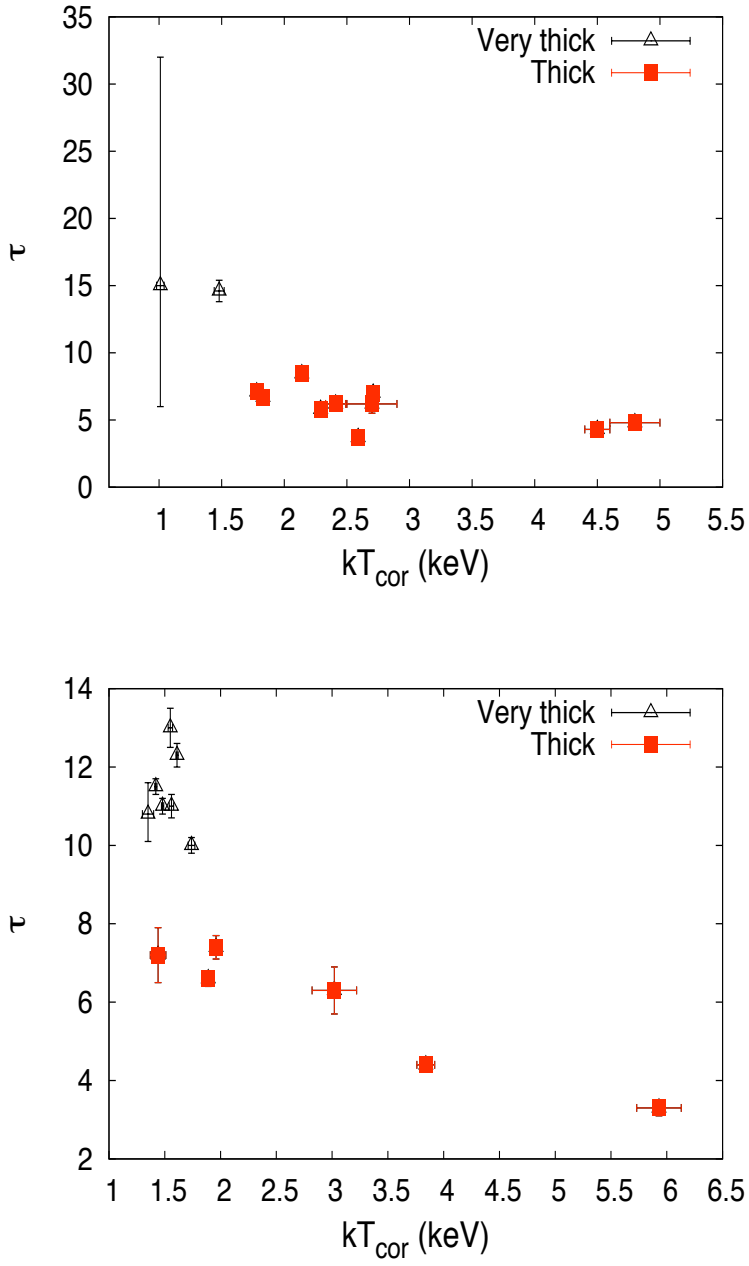

Figure 3.5: Optical depth τ versus temperature of the corona kT_{cor} for the X-ray spectral fits of X-1 (*top*) and X-2 (*bottom*) with a *diskbb+comptt* model. Observations that have a very thick corona are represented with *black* triangles while observations with a thick corona are represented as *red* squares.

X-1 may also be interpreted within the same framework. However, the clustering of the observations in the $kT_{cor} - \tau$ plane of X-1 is not so well defined and the region with high optical depths is populated by only two observations. Furthermore, although not included in Figure 3.5 because of the low counting statistics, our interpretation is not consistent with the spectral parameters inferred from observation #1. So, present data are not sufficient to establish whether X-1 has indeed a bimodal behaviour similar to that shown by X-2 or the changes in the optical depth should be interpreted in a different way (e.g. as due to different variability patterns or accretion geometries; Feng & Kaaret 2006; Dewangan et al. 2010). In the following we will continue to distinguish between the observations of X-1 with a very thick corona ($\tau > 10$) and a thick corona ($\tau < 8$), being aware that they may represent physically different states with respect to those of X-2.

An example of the spectral shapes when the two sources are in different positions on the $kT_{cor} - \tau$ plane is shown in Figure 3.6. Again there are analogies and differences between X-1 and X-2. In both cases the spectra for very high coronal depths are bell-shaped, with a clear turn-over at $> 3 - 4$ keV (e.g. Stobbart et al. 2006), whereas the spectra in the low-τ region are steeper and do not show strong evidence of curvature at high energies. Only for X-2 the two spectral states appear to correlate with total luminosity, the very-thick corona state being more luminous (see Figure 3.7). In X-1 there is no significant dependence of the spectral shape on L_X. This is evident also from the behaviour of the spectra shown in Figure 3.6. While for X-2 the thick corona spectra stay always below those in the very thick corona state, for X-1 there is a sort of crossing/pivoting point of the observed spectra (see also Kajava & Poutanen 2009) at ~ 2 keV. Therefore, the total counts in the thick corona state of X-2 are clearly smaller than those in the very thick corona state, while in X-1 the deficit of photons observed at low energies in spectra with larger optical depths is compensated by the excess of photons at high energies.

For both sources, we estimated the fractional variability amplitude (F_{var}) which is a

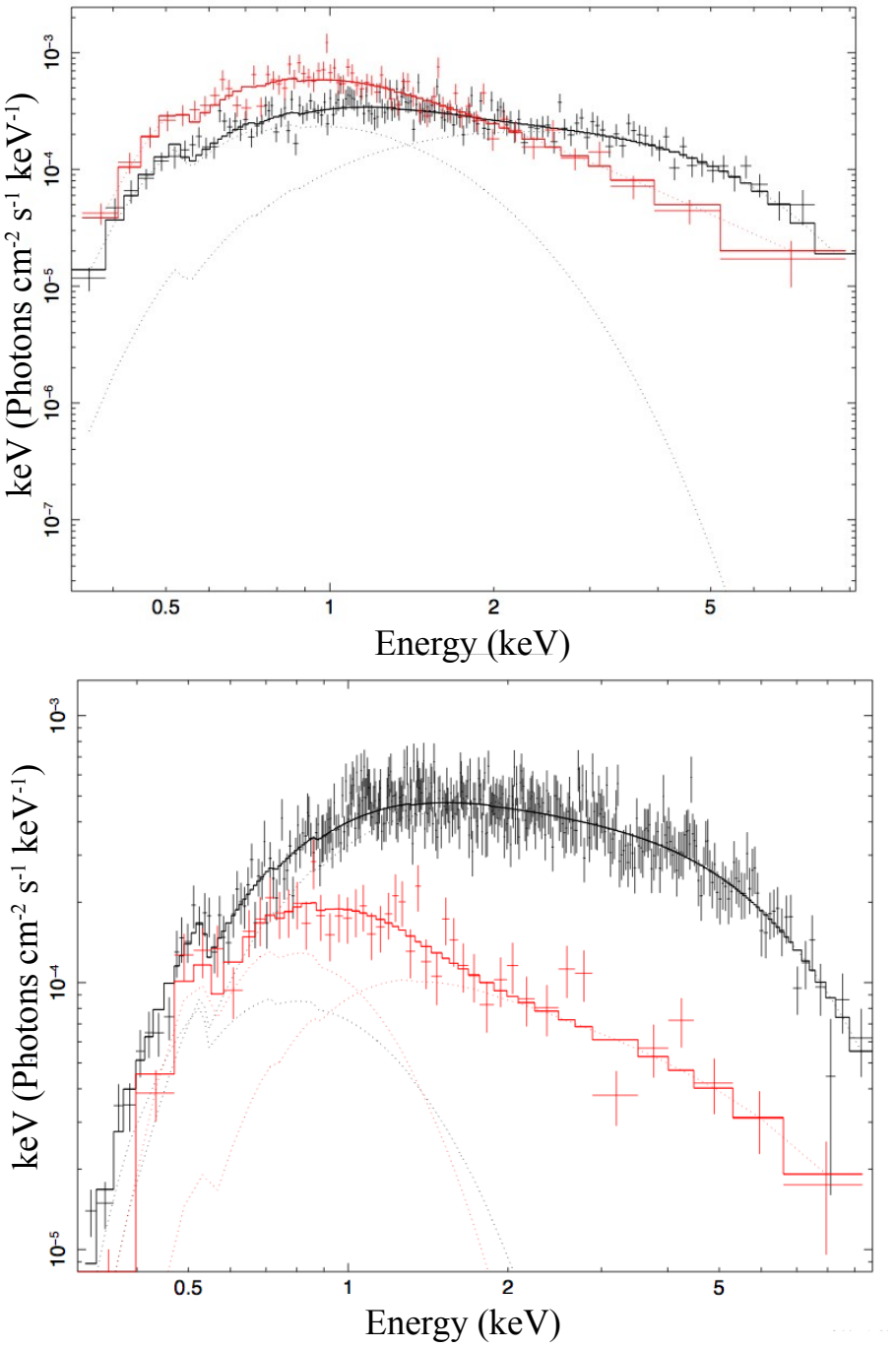

Figure 3.6: X-ray spectra (energy×photons) of X-1 (top) and X-2 (bottom) for observations that have a very thick corona (*black*) and a thick corona (*red*). In both cases the comparison is between observations #9 (*red*) and #12 (*black*), respectively.

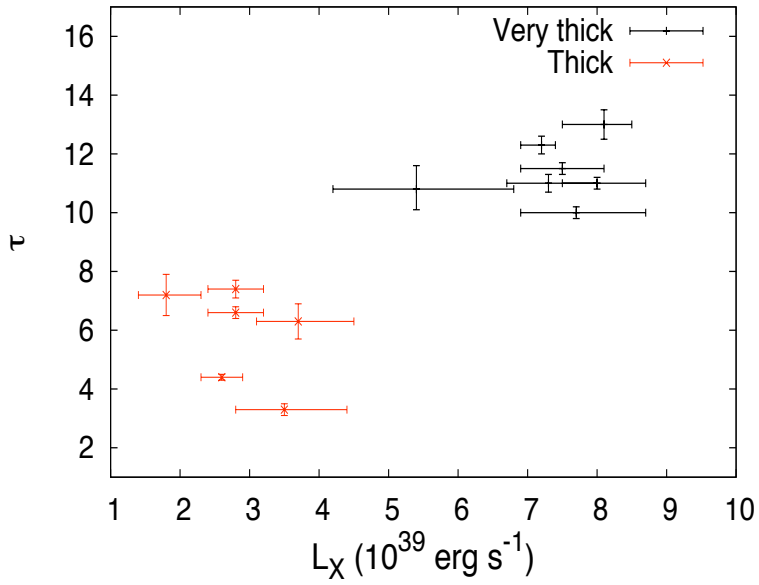

Figure 3.7: Optical depth τ versus unabsorbed total luminosity (in the 0.3-10 keV range) for X-2. The *black* points represent the very thick corona state while the *red* crosses are the thick corona state.

Table 3.5: Fractional variability of NGC 1313 X-1 and X-2.

		X-1		X-2	
	Energy band[a]	counts s^{-1}	F_{var}(per cent)[b]	counts s^{-1}	F_{var}(per cent)[b]
Obs.1	0.2-10 keV	–	–	0.82 ± 0.04	0.17[c,e]
Obs.2	0.2-10 keV	2.08 ± 0.03	4.0 ± 2	0.99 ± 0.01	7.0 ± 2
Obs.3	0.2-10 keV	2.01 ± 0.04	9.1[c,e]	1.11 ± 0.02	4 ± 3[e]
Obs.4	0.2-10 keV	2.0 ± 0.1	18 ± 6[c,e]	0.653 ± 0.04	28[c,e]
Obs.5	0.2-10 keV	1.53 ± 0.03	11[c]	0.49 ± 0.01	6.0 ± 3
Obs.6	0.2-10 keV	1.62 ± 0.04	12.1[c]	0.44 ± 0.02	14 ± 6
Obs.7	0.2-10 keV	–	–	–	–
Obs.8	0.2-10 keV	2.36 ± 0.02	4.0 ± 2	1.16 ± 0.01	7.1[c]
Obs.9	0.2-10 keV	0.97 ± 0.03	14.8[c]	0.34 ± 0.01	14 ± 5
Obs.10	0.2-10 keV	–	–	0.377 ± 0.006	6 ± 3
Obs.11	0.2-10 keV	1.05 ± 0.02	9.4[c]	1.06 ± 0.01	7.8[c]
Obs.12	0.2-10 keV	1.29 ± 0.03	13 ± 4	1.05 ± 0.02	8[c]
Obs.13	0.2-10 keV	0.841 ± 0.004[d]	1 ± 3[d]	0.978 ± 0.005	9.8 ± 0.7

[a] The adopted energy band is for a direct comparison with Dewangan et al. (2010). [b] Calculated from the background subtracted EPIC-pn light curve, with 200 s time bins. [c] 3 σ upper limit. [d] Fractional variability computed for the whole observation, including the short segment of 3.5 ks that we left out from the spectral analysis. [e] Number of useful bins lower than 20.

measure of the variance of the source over the Poissonian noise normalized to the average count-rate (Edelson et al. 2002; Vaughan et al. 2003). The fractional variability can be used to study the energy dependence of the short-term variability and it is a powerful tool in order to characterise the properties of the spectral components. The X-ray fractional variability shows that both sources present a variability of $\sim 6-14\%$, which may be slightly higher when the coronae are thicker (see Table 3.5). This strengthens the analogies between the behaviours of the two sources.

Figure 3.8 shows the light curves of X-1 and X-2 computed from the best fitting *diskbb+comptt* model (a distance of 3.7 Mpc was assumed; Tully & Fisher 1988). On average, X-1 has a luminosity ($\sim 10^{40}$ erg s^{-1}) higher than that of X-2 ($\sim 5 \times 10^{39}$ erg

s^{-1}).

We further investigated the behaviour of the soft component in both sources. The discs are soft or warm, with temperatures of $\sim 0.2 - 0.5$ keV for X-1 and $\sim 0.2 - 0.6$ keV for X-2. Three spectra of X-1 are consistent with zero normalization (or absence) of the soft component. In eight observations the luminosity of the soft component is $\sim 10^{39}$ erg s^{-1} and it represents a significant fraction of the total flux ($> 30\%$). Excluding the spectral fits that return zero normalization of the soft component, there is no evidence of correlation or anti-correlation between the disc (or total) luminosity and the inner disc temperature. In X-2 the luminosity of the soft component is a significant fraction ($> 30\%$) of the total luminosity in six observations. Two observations have normalization consistent with zero. Excluding them, the disc luminosity appears to show a weak power-law correlation with the inner temperature, $L_{\rm disc} \propto T_{disc}^{1.2\pm0.3}$. However, the correlation is uncertain, as the two observations that substantiate it (those with higher kT_{disc}) have also rather shallow minima in χ^2, admitting both a strong/warm and a weak/cool disc fit with close values of the χ^2. No correlation is found using the total luminosity.

3.4.1 Effects of varying the ratio of seed photons temperature to the disc temperature

The comptonizing coronae of the *comptt* model turn out to be optically thick. This poses a problem, as in these physical conditions the disc underneath the corona is masked by it. Therefore, the temperature of the disc component refers to the outer visible part of the disc, while the temperature of the seed photons T_0 is not necessarily equal to T_{disc}. For this reason, Gladstone et al. (2009) adopted the *DKBBFTH* model in which the corona is assumed to cover the inner disc. We tried to apply the same model to our spectral sequence, but found that it converges to plausible physical values of the parameters only for the highest quality spectra. We then tried to repeat our analysis with the *diskbb+comptt*

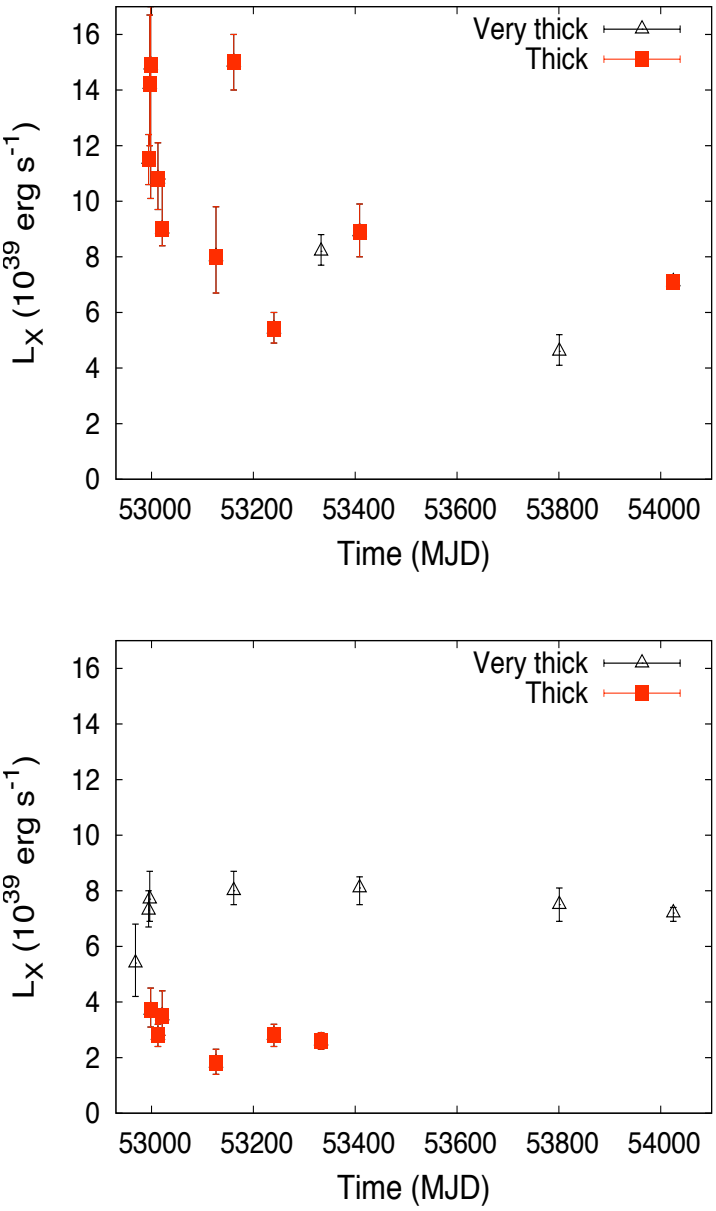

Figure 3.8: X-ray unabsorbed luminosity evaluated in the 0.3-10 keV energy band (a distance of 3.7 Mpc was assumed; Tully & Fisher 1988) for all the *XMM-Newton* observations of X-1 (*top*) and X-2 (*bottom*). Observations with a very thick corona are represented with *black* triangles while observations with thick corona are represented as *red* squares. All the (unabsorbed) luminosities are evaluated in the 0.3-10 keV energy band.

model and disconnecting the two temperatures, but this leads to difficulties in finding a global minimum (see also the analysis of NGC 5204 X-1 in Feng & Kaaret 2009). Finally, we decided to test our results tying the two temperatures with a fixed proportionality constant.

If the corona is optically thick and is absorbing a constant fraction f of the accretion power, the actual inner disc temperature $T_1^{'}$ is lower than the inner temperature of the disc in absence of the corona T_1, as $T_1^{'} = T_1(1-f)^{1/4}$ (e.g. Gladstone et al. 2009). If R_1 and R_T are the inner disc radius and the truncation radius of the corona respectively, from the relation $T(R) \approx T_1(R/R_1)^{-3/4}$, valid for a disc in absence of the corona, we obtain $T_1 \approx T_T(R_T/R_1)^{3/4}$. Thus, we have $T_1^{'} \approx T_T(R_T/R_1)^{3/4}(1-f)^{1/4}$. Assuming that $f < 90\%$ and that the corona is compact ($R_T < 4R_1$), the inner disc temperature $T_1^{'}$, which is also the seed photons temperature, is larger than the temperature of the outer visible disc T_T, and $1 < T_1^{'}/T_T = T_0/T_{disc} < 2.5$. We then attempted to perform some additional fits with two fixed values (1.5, 2) of the ratio $\delta = T_0/T_{disc}$ as representative of this situation.

We found that the spectral fits with a *diskbb+comptt* model and $\delta = 1.5, 2$ are statistically acceptable and the coronae are still optically thick, with the inferred optical depth weakly depending on T_0/T_{disc}. The parameters of the corona change by no more than $\sim 60\%$, with typical variations of $< 20-30\%$. However, the dependence of spectral states on the total luminosity that characterises the behaviour of X-2 for equal temperatures is lost. For X-1, the temperature of the disc continues not to correlate with the luminosity, as found for equal temperatures. For X-2, varying δ the very-thick state becomes less populated, as some observations previously in that state move to the thick corona state. For $\delta = 1.5$ there is a weak correlation between disc luminosity and temperature ($L_{disc} \propto T_{in}^{1.4\pm0.4}$), while if $\delta = 2$ the correlation disappears. At variance with the correlation found for equal temperatures, the correlation for $\delta = 1.5$ is not critically dependent only on two observations.

These results do not change significantly for slightly more extended coronae. On the other hand, if the corona is very extended and optically thick, the value of δ may become so large that the disc component falls essentially outside the *XMM-Newton* bandpass (unless the disc-corona coupling is very strong). In these conditions some spectra are no longer well fitted by the model.

However, these assumptions may fail if the soft component is actually the emission of an outflow ejected by the disc. In these conditions the soft photons do not seed the corona, which is fed by photons from the underlying disc, making the existence of a relation between the two temperatures unlikely.

3.5 Chemical abundance estimates

We analyzed the EPIC-pn and RGS data of all the *XMM-Newton* observations of X-1 and X-2 in an attempt to use them for determining the chemical abundances in the local source environment. Following Winter et al. (2007), for the EPIC-pn 5000 and 40000 counts are necessary to observe the Oxygen K-shell and Iron L-shell absorption edges at 0.538 keV and 0.851 keV, respectively. Observation #13 has $\sim$ 58000 (53000) EPIC-pn counts for X-1 (X-2), and hence we can perform a chemical abundance analysis on the EPIC-pn spectrum similar to that presented in Winter et al. (2007). In the spectral fits the *tbabs* absorption model is replaced with *tbvarabs* that allows to vary the chemical abundances (and grain composition). We set alternatively the abundance of Oxygen or Iron to zero. The spectrum was then fitted with the EPIC continuum model in Table 3.4 (keeping all parameters, but normalizations, fixed) plus an absorption edge, that accounts for the observed absorption feature. The parameters of the edge are then used to compute the abundance.

Using this approach, we found that the O and Fe abundances inferred from the EPIC-pn spectrum of X-1 are consistent with a sub-solar metallicity environment ($Z \sim 0.6 Z_{\odot}$ from

Table 3.6: Abundances inferred from the Oxygen K-shell photoionization edge (0.538 keV) from the X-ray spectral fits of NGC 1313 X-1 and X-2.

NGC 1313 X-1		
	τ^a	$12 + \log(O/H)^b$
RGS (observation 13)	$0.75^{+0.29}_{-0.25}$	$8.7^{+0.1}_{-0.2}$
EPIC (observation 13)	$0.75^{0.03}_{-0.03}$	$8.72^{+0.02}_{-0.02}$
RGS (stacked)	$0.53^{+0.26}_{-0.23}$	$8.7^{+0.3}_{-0.2}$
NGC 1313 X-2		
	τ^a	$12 + \log(O/H)$
EPIC (observation 13)	$0.46^{+0.05}_{-0.04}$	$8.64^{+0.06}_{-0.05}$

[a] Absorption depth at the threshold energy.
[b] For the solar abundance we assume $12 + \log(O/H) = 8.92$.

the O edge; Table 3.6). The χ^2 of the fit with the absorption edge is 1488 for 1423 d.o.f., while that without the edge is 1759 for 1424 dof. For X-2 we find a subsolar abundance for Oxygen ($Z \sim 0.5 Z_\odot$; see again Table 3.6) and an Iron abundance consistent with zero. The fits returns $\chi^2 = 839$ (857 dof) with the O edge and $\chi^2 = 953$ (858 dof) without it.

We tried to analyze also the RGS data of X-1 and X-2 using the same technique. As the sources are faint, the RGS net count rate is quite low ($\sim 1.5 \times 10^{-2}$ count s^{-1}). Therefore, only the last observation (observation #13, 122 ks) reached a reasonable counting statistics in the RGS for the brightest ULX (X-1), while no useful analysis could be performed on X-2. We tentatively identified two features in absorption in the RGS spectrum of X-1, associated to O I (0.535 keV) and Fe I (0.709 keV). There may be also two other lines in emission at the characteristic energy of O VIII K_α (0.653 keV) and Si K_α (1.748 keV), but their significance is very low. From the Oxygen edge we found an abundance below solar ($Z \sim 0.6 Z_\odot$) for the absorbing material towards X-1 (see Table 3.6), although the statistical improvement obtained including the absorption edge is small.

We tried to improve the analysis stacking together the RGS spectra in such a way to increase the counting statistics. We used only the RGS1 spectra, because our best

diagnostic is the Oxygen K-shell photoionization edge at 0.538 keV and the response of the RGS2 has some problems precisely in this energy range (0.5-0.6 keV). The stacked spectra of X-2 have not enough counting statistics for a meaningful analysis. For X-1, we combined spectra together using the *rgscombine* command, that appropriately accounts for the response matrices and backgrounds of the different observations. We had to exclude several observations ($\#2, 3, 4, 5, 6, 7, 11, 12$) that caused technical problems in the processing with *XSPEC*. Observation #1 was also excluded for the reason explained in the previous Section. The final combined RGS spectrum of X-1 has a total exposure time of 168 ks and $\sim$ 2861 net counts. We fitted it with a *diskbb+comptt* model with parameters fixed and equal to the mean values obtained from the EPIC spectral fits of X-1, setting the Oxygen abundance to zero and adding an absorption edge (Figure 3.9). We found that the Oxygen abundance is again sub-solar (Table 3.6) although we cannot claim the existence of the Oxygen edge only from RGS data. In fact, the χ^2 of the best fit with the absorption edge is 139 for 103 d.o.f., while that without the edge is 146 for 104 dof. The difference is small and hence the detection is marginal. In addition, the actual abundance is rather sensitive to the temperature of the soft component and its uncertainty becomes large if kT_{disc} is included in the spectral fit.

3.6 Discussion

The analysis of all the *XMM-Newton* observations shows that the spectra of X-1 and X-2 can be well reproduced by a Comptonization model plus a soft disc component in which the coronae are always optically thick. Both sources appear to show a well defined behaviour in the optical depth (τ) versus corona temperature (kT_{cor}) plane. For X-2 we clearly identified two states that characterise the spectral variability and appear to have also different short term variability properties: a "very-thick" (possibly more variable) corona state in which

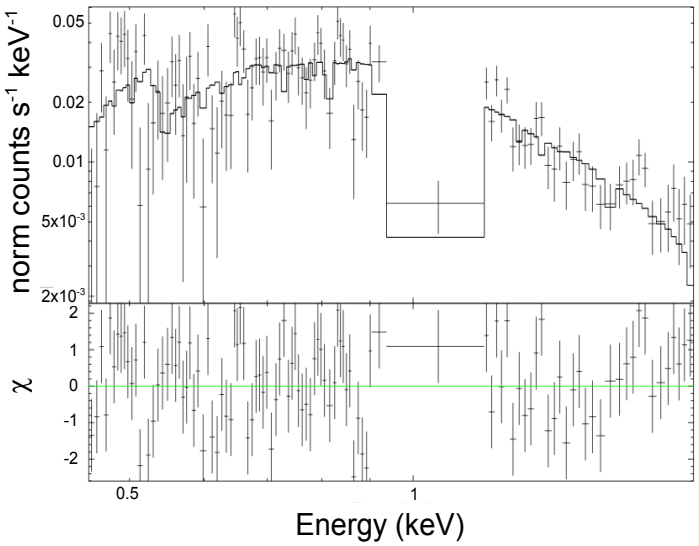

Figure 3.9: Stacked RGS1 spectrum of X-1, along with its best fitting model (see text for details).

$\tau > 10$ and $kT_{cor} \sim 1.5$ keV, and a "thick-corona" state in which $\tau < 8$ and $kT_{cor} \sim 1.5 - 6$ keV. We note that a morphological classification in terms of a harder brighter state and a softer dimmer state, based on a single power-law fit, has already been proposed for X-2 Feng & Kaaret (2006). Here we offer a physical explanation of these two states in terms of varying parameters of an optically thick corona. The behaviour of X-1 may be interpreted within the same framework but, with presently available data, the observed changes in the coronal optical depth could be explained also in a different way (e.g. as due to different variability patterns or accretion geometries; Feng & Kaaret 2006; Dewangan et al. 2010).

For X-2, which is on average less luminous than X-1, the two spectral states of the corona appear to correlate with luminosity. The optical depth of the corona increases as the total luminosity goes up, as expected if the corona responds rapidly to an increment in the instantaneous accretion rate. The behaviour of the disc component is also different in the two sources. While in X-1 the luminosity and temperature of this component do not

correlate, for X-2 we find that $L_{disc} \propto T_{disc}^{1.2\pm0.3}$. However, as already mentioned, this result is uncertain as the two spectra that substantiate the correlation admit both a strong/warm and a weak/cool disc fit with close values of the χ^2.

A spectral analysis based on the assumption that the seed photon temperature (T_0) is equal to the disc temperature (T_{disc}) has some inconsistencies because, if the corona is optically thick, the innermost part of the accretion disc is actually not visible and, hence, it is not necessarily true that $T_0 = T_{disc}$. For this reason, we repeated our analysis with the *diskbb+comptt* model tying the two temperatures with a proportionality constant, that was fixed assuming a compact corona energetically coupled to the disc (disconnecting the two temperatures leads to difficulties in finding a global minimum because of the low counting statistics of several observations). We find changes in the corona parameters of $< 60\%$, with typical variations of $< 20 - 30\%$. However, the dependence of spectral states on the total luminosity that characterises the behaviour of X-2 for equal temperatures is lost. While for X-1 the temperature of the disc continues not to correlate with the luminosity, for X-2 the correlation persists up to values of $T_0/T_{disc} < 1.5$, consistent with strong disc-corona coupling ($f \sim 90\%$).

We emphasize that the model adopted in the present investigation is not entirely physically consistent. Besides the issues of the relation between T_0 and T_{disc} that we tried to address as described above, there may be other caveats, such as the input photons not being a mono-temperature Wien distribution (as assumed in *comptt*), or the disc structure being different from a standard one at high accretion rates, or the origin and precise location of the thick corona/wind being unknown. However, our purpose was not to adopt the most physically consistent spectral model for ULXs, which does not exists yet, but a simplified one that can reflect the underlying physics and can be tested on the basis of the observed spectral variability patterns, limited by the current data quality.

A full explanation of the observed spectral variability patterns of X-1 and X-2 is beyond

the scope of the present investigation and appears not easy. Here we simply propose some interpretations within the framework of recent work on the subject (e.g. Feng & Kaaret 2009; Gladstone et al. 2009; Dewangan et al. 2010; Vierdayanti et al. 2010). X-1 shows higher average isotropic luminosity ($\sim 10^{40}$ erg s^{-1}) and smaller variability. The different spectral shapes do not correlate with luminosity, and the temperature and luminosity of the soft component do not vary together. These findings are consistent with X-1 being in the Ultraluminous regime (Gladstone et al., 2009), accreting at super-Eddington rates and launching powerful winds from a disc embedded in an optically thick corona. The accretion disc may be there, but in a different physical regime and covered by a wind/corona, while the soft component may actually represent emission from the wind itself. The probable larger X-ray fractional variability observed when the wind/corona is optically thicker may be consistent with increasing obscuration of the source caused by the turbulent wind itself at higher accretion rates (Middleton et al., 2011).

As far as X-2 is concerned, it behaves in a way similar to X-1 on the τ-kT_{cor} plane and also the fractional X-ray variability of the two sources appears to be comparable. Hence the corona may be in a similar physical state. Again, this may be consistent with the picture in which we are seeing the two sources under a high inclination angle and the temporal variability may be produced by blobs in the wind that intersect our line of sight to the hottest central regions of the source (Middleton et al., 2011). However, as noted above, X-2 has a lower average luminosity and, for $T_0 < 1.5T_{disc}$, it shows a weak correlation between the luminosity and inner temperature of the disc component. This may be interpreted as X-2 being in a less extreme regime, in which the average accretion rate is at around or slightly above the Eddington limit. The soft spectral component may then physically represent a true accretion disc which is partly visible and has a characteristic temperature in the range 0.2-0.6 keV. Clearly, some time-dependent interaction between the disc and the corona is likely to occur (e.g. a slight expansion on a dynamical timescale of the

corona as the accretion rate increases) and may be responsible for the observed slope of the temperature-luminosity relation ($L_{disc} \propto T_{disc}^{1.2}$), which is different from that of a standard disc with fixed inner radius ($L_{disc} \propto T_{disc}^{4}$). Clearly, as the corona is always optically thick, it is not possible to use the disc parameters for estimating the BH mass.

We note that the disc temperature-luminosity correlation in X-2 disappears using a simple power-law to describe the spectrum of the corona, as found by Feng & Kaaret (2006) (and by Feng & Kaaret 2009 for IC 342 X-1), probably because the power-law does not take into account the spectral curvature at high energies. The correlation of the optical depth of the corona with luminosity that we found for X-2 (assuming $T_0 = T_{disc}$) is in agreement with the results obtained for Ho IX X-1 by Vierdayanti et al. (2010). However, Kong et al. (2010) argued against the statistical significance of this correlation in Ho IX X-1. Also IC 342 X-1 shows some hint of an increase in the coronal depth as the X-ray luminosity increases (Feng & Kaaret, 2009). These similarities in spectral variability patterns appear to be consistent with the proximity of these three ULXs in the spectral sequence proposed by Gladstone et al. (2009).

We used the RGS high spectral resolution to attempt an estimate of the metallicities of the local environments of X-1 and X-2. Because of the low signal-to-noise ratio, only the last, longest observation of X-1 could be used. The analysis was performed also on the EPIC spectrum. The metallicity in the X-1 environment is consistent with being below solar. The last EPIC spectrum of X-2 was also analyzed with the same method and suggests sub-solar metallicity. In an attempt to increase the significance of our results we also stacked together the RGS spectra of some observations of X-1 and performed measurements of the metallicity on the stacked spectrum. Also in this case the Oxygen abundance turns out to be below solar, although it is rather sensitive to the temperature of the soft component. Our estimates are in agreement with the abundance measurements from HII regions in NGC 1313 that give values that are all sub-solar (Pilyugin 2001; Hadfield & Crowther

2007; Ripamonti et al. 2011), but are smaller than the slightly supersolar metallicity of the X-1 environment found by Winter et al. (2007). The difference with the latter Authors may be due to the fact that we analyzed an observation with higher counting statistics and adopted a different spectral model.

For these reasons, the acquisition of new, high quality spectra through a dedicated X-ray monitoring programme is definitely needed.

Chapter 4

ULXs: a deeper insight into their X-ray spectral evolution

4.1 Introduction

The existence of spectral state transitions in NGC 1313 X-1 and X-2 led us to further investigate if other ULXs can display a similar behaviour. In this chapter we focus on the other sources listed in Chapter 2.1. We continue to adopt as reference model the *diskbb+comptt*, trying to find a global picture into which we can describe the properties of the ULXs of our sample. In several low counting statistics observations the parameters of the spectral fits are sometimes degenerate or not so well constrained. Therefore, we tried to study the spectral evolution of our sample of ULXs using also a more model-independent approach, that of the hardness ratios. We suggest that a possible variability pattern may be identified on the hardness-intensity diagram and we tried to explain its physical origin on the basis of the results of the spectral analysis. We complemented this study with an analysis of the temporal properties of the source of our sample because, as for Galactic XRBs, they can be used to characterise their spectral states. Throughout this and the following chapters the distances of the ULX host galaxies adopted to compute their

luminosity are those reported in Chapter 2.

4.2 Analysis

A detailed description of the data reduction and analysis has been reported in Section 2.4. Here we give only a few additional information specific to this Chapter.

4.2.1 Spectral analysis

We carried out a complete spectral analysis on all the available *XMM-Newton* observations of the sources IC 342 X-1, NGC 253 X-1, NGC 5204 X-1, NGC 5408 X-1, Ho IX X-1 and Ho II X-1 (see Table 4.1). We made use also of the *XMM-Newton* observations of NGC 55 ULX1 which will be discussed in detail in Chapter 5.

Only 6 observations of NGC 5408 X-1 and 2 of Ho II X-1 were excluded from the analysis because the quality of the data was strongly limited by solar flares or the event list was empty. Two absorption components (*tbabs* in XSPEC) were always considered: one fixed at the Galactic column density along the direction of the source and another variable for the local absorption.

We note that, as for NGC 1313 X-1 and X-2, the spectral fits of some sources often have several local minima with close values of the χ^2, sometimes with evidence for both a strong/warm and a weak/cool (or no) disc. After a careful inspection of the χ^2 surface, we selected the absolute minima for each observation reported in the tables of this chapter. However, one should be aware that the actual uncertainty on the spectral parameters caused by the topology of the χ^2 surface may be a few times larger than the formal error reported in the tables.

4.2.2 Temporal analysis

For each source we computed the fractional variability amplitude (F_{var}) from background

Table 4.1: Log of the observations of the ULXs analyzed in this chapter.

No.	Obs. ID	Date	Exp[a] (ks)	Instr. (X-1)[b] count s^{-1}	EPIC-pn	Net counts	Off-axis angle
				IC 342 X-1			
1	0093640901	2001-02-11	4.826	pn	0.37	1768,1194,1164	5.084'
2	0206890101	2004-02-20	17.060	pn/M1/M2	0.42	7153,3366,3323	2.493'
3	0206890201	2004-08-17	14.360	pn/M1/M2	0.90	12946,7791,8162	4.271'
4	0206890401	2005-02-10	5.918	pn/M1/M2	1.157	68473911,4469	2.627'
				NGC 253 X-1			
1	0110900101	2000-12-13	10.97	pn/M1/M2	0.105	1154,802, 893	4.565'
2	0152020101	2003-06-19	61.37	pn/M1/M2	0.271	16625,6978,7201	5.304'
3	0304851101	2005-02-10	10.93	pn/M1/M2	0.097	1057,727,694	3.128'
4	0304850901	2006-01-02	8.815	pn/M1/M2	0.141	1241,458,488	3.137'
5	0304851001	2006-01-06	8.754	pn/M1/M2	0.155	1359,530,549	3.167'
6	0304851201	2006-01-09	15.96	pn/M1/M2	0.158	2525,994,965	3.186'
7	0304851301	2006-01-11	4.338	pn/M1/M2	0.162	703,338,373	3.224'
				NGC 5204 X-1			
1	0142770101	2003-01-06	15.33	pn/M1/M2	0.6236	9560,3121,3211	1.135'
2	0142770301	2003-04-25	4.020	pn/M1/M2	0.862	3465,1903,1868	1.121'
3	0150650301	2003-05-01	5.262	pn/M1/M2	1.018	5357,2213,2327	1.296'
4	0405690101	2006-11-15	10.050	pn/M1/M2	1.228	12600,7752,7752	1.097'
5	0405690201	2006-11-19	31.250	pn/M1/M2	1.031	32219,11791,11957	1.080'
6	0405690501	2006-11-25	22.420	pn/M1/M2	0.7745	17364,6906,7174	1.132'
				NGC 5408 X-1			
1	0112290501	2001-07-31	3.680	pn/M1/M2	1.441	5303,2530,2642	1.255'
2	0112290601	2001-08-08	4.504	pn/M1/M2	1.337	6023,2024,2140	1.265'
3	0112290701	2001-08-24	7.498 (MOS1)	M1/M2	1.018 (MOS1)	2405,2482	1.226'
4	0112291201	2003-01-27	2.793	pn/M1/M2	1.228	2354,920,935	0.990'
5	0302900101	2006-01-13	92.540	pn/M1/M2	1.031	94298,25437,25331	1.094'
6	0500750101	2008-01-13	46.090	pn/M1/M2	0.7745	43753,18471,17782	1.069'
7	0653380201	2010-07-17	92.680	pn/M1/M2	1.137	26034,33154,105377	1.112'
8	0653380301	2010-07-19	96.860	pn/M1/M2	1.113	30145,30188,107805	1.116'
9	0653380401	2011-01-26	87.380	pn/M1/M2	1.061	29307,29126,92710	1.116'
10	0653380501	2011-01-28	88.510	pn/M1/M2	1.024	27952,27822,90634	1.119'
				Ho II X-1			
1	0112520601	2002-04-10	4.638	pn/M1/M2	3.054	14164, 8316, 8886	1.127'
2	0112520701	2002-04-16	3.772	pn/M1/M2	2.751	10377, 4796, 4994	1.105'
3	0112520901	2002-09-18	4.325	pn/M1/M2	0.8154	3527, 1317, 1434	1.113'
4	0200470101	2004-04-15	40.75	pn/M1/M2	3.056	124532, 49487, 50578	1.135'
5	0561580401	2010-03-26	23.19	pn/M1/M2	1.238	28709, 14098, 13993	1.135'
				Ho IX X-1			
1	0112521001	2002-04-10	7.045	pn/M1/M2	1.895	13350	1.105'
2	0112521101	2002-04-16	7644	pn/M1/M2	2.173	16610	1.125'
3	0200980101	2004-09-26	83.17	pn/M1/M2	1.495	124339	1.130'
4	0657801601	2011-04-17	0.964	pn/M1/M2	0.76	733	7.404'
5	0657801801	2011-09-26	7.4	pn/M1/M2	2.477	13830	5.286'
6	0657802001	2011-03-24	3.2	pn/M1/M2	1.369	4381	7.319'
7	0657802201	2011-11-23	13.1	pn/M1/M2	2.211	28964	5.209'

[a] GTI of EPIC-pn; [b] pn = EPIC-pn camera; M1/M2 = EPIC-MOS1/MOS2 camera;

subtracted lightcurves in several energy bands: 0.3-10 keV, 0.3-2.0 keV and 2.0-10 keV. In addition, for the observations in which the counting statistics is adequate, we evaluated also the fractional variability spectrum selecting background subtracted EPIC-pn lightcurves in the energy ranges 0.3-0.5, 0.5-0.7, 0.7-1.0, 1.0-1.3, 1.3-1.6, 1.6-2.1, 2.1-4.0, 4.0-10 keV.

4.3 Spectral fits

4.3.1 IC 342 X-1

According to the work of Gladstone et al. (2009), this source is the most disc-like in our sample. Therefore, we initially tried to describe its spectral properties using a *slim disc* model (*diskpbb* in XSPEC). We set the Galactic absorption to $3.1 \cdot 10^{20}$ cm^{-2} (Dickey & Lockman 1990).

Apart from the longest observation (#3), the others can be described by an advection dominated disc with a p-index of ~ 0.55 and a disc temperature in the range $\sim 2.5 - 4$ keV. However, the temperature of the disc is rather high and it decreases when the total luminosity increases, the opposite of what is expected in such a scenario. Indeed if the luminosity increases, the disc should become more advection dominated and its temperature should raise. Hence this behaviour is not physically plausible and we can reject this spectral model as a coherent description of the source.

We then tried with our reference two component model, *diskbb+comptt*. The results of the spectral fits are reported in Table 4.2. We note that sometimes a certain degeneracy between a cold and a warm disc solution was found (see also Stobbart et al. 2006). Gladstone et al. (2009) associated the high energy component of IC 342 X-1 to a compact corona coupled to the inner regions of the disc and, indeed, the former is always optically thick and cold ($kT_{cor} \sim 1.8 - 2$ keV and $\tau \sim 8 - 11$, see Table 4.2 and Figure 4.1). In fact, although the X-ray spectra of IC 342 X-1 may be well described also by a single *comptt*

Table 4.2: Best fitting spectral parameters of IC 342 X-1 obtained with the absorbed *diskbb+comptt* model.

IC 342 X-1								
No.	Date	N_H [a] (10^{21} cm^2)	kT_{disc} [b,c] (keV)	kT_{cor} [d] (keV)	τ [e]	L_X [0.3-10 keV] [f] (10^{39} erg s^{-1})	L_{disc} [0.3-10 keV] [g] (10^{39} erg s^{-1})	χ^2/dof
1	2001-02-11	$6.1^{+0.2}_{-0.2}$	$0.23^{+0.01}_{-0.01}$	2.24^{+400}_{-5}	8.38^{+2}_{-2}	$5.2^{+1.1}_{-1.0}$	$1.1^{+0.2}_{-0.4}$.	55.5/60
2	2004-08-17	$6.2^{+0.1}_{-0.1}$	$0.50^{+0.005}_{-0.005}$	$1.71^{+0.02}_{-0.02}$	$10.1^{+0.1}_{-0.1}$	$11.0^{+1.0}_{-0.6}$	$3.8^{+0.2}_{-0.2}$	764.88/811
3	2004-02-20	$5.8^{+0.2}_{-0.2}$	$0.356^{+0.004}_{-0.004}$	$2.18^{+0.08}_{-0.08}$	$8.95^{+0.3}_{-0.3}$	$5.9^{+1.0}_{-0.6}$	$1.6^{+0.3}_{-0.3}$.	456.28/432
4	2005-02-10	$6.0^{+0.2}_{-0.2}$	$0.697^{+0.004}_{-0.004}$	$1.81^{+0.03}_{-0.03}$	$11.5^{+0.5}_{-0.5}$	14.0^{+1}_{-1}	$6.1^{+0.4}_{-0.4}$	485.83/496

[a] Column density; [b] Inner disc temperature; [c] The seed photons temperature T_0 is assumed to be equal to T_{disc}. [d] Temperature of the corona; [e] Optical depth of the corona; [f] Unabsorbed total X-ray luminosity in the 0.3 -10 keV range; [g] Unabsorbed disc luminosity in the 0.3-10 keV range.

model (Feng & Kaaret, 2009; Gladstone et al., 2009), the parameters of the corona are similar both introducing a soft component and without introducing it.

In the previous chapter, we defined these spectral parameters as indication of the *very thick* state that was heavily populated by NGC 1313 X-2 (Pintore & Zampieri, 2012). In this state the optical depth follows a correlation with the luminosity (see Figure 4.1-*bottom-right*). IC 342 X-1 is therefore another source with similar spectral properties. On the other hand, using a *diskbb+power-law* spectral model, Feng & Kaaret (2009) found that the source stays preferentially in two "spectral states" defined as *high/soft* and *low/hard*. A similar behaviour may be seen also using our reference spectral model although the corona remains always very thick. In addition, the variability of the source in the 0.3-10 keV band is usually $\leq 10\%$ (when the statistics is sufficient to have good constraints; see Table 4.3). We conclude that it is unlikely that the two spectral states may be associated to the canonical states observed in Galactic BHBs. Indeed in the *low/hard* state, the variability should be higher than 10%, not consistent with what observed in the corresponding low flux state of IC 342 X-1.

We note that the total luminosity of IC 342 X-1 has shown variations up to a factor of 3, from $5.2 \cdot 10^{39}$ erg s^{-1} to $1.4 \cdot 10^{40}$ erg s^{-1} (assuming a distance of 3.3 Mpc, Saha et al. 2002; see Figure 4.1-*top-right*). Interestingly, the flux of the soft component becomes progressively more important as the total luminosity increases (see Figure 4.2). At low luminosities the soft component carries $\sim 25\%$ of the total flux in the 0.3-10 keV energy range and this value increases to $\sim 40\%$ at the highest luminosities. In addition, there is a correlation between the temperature and the luminosity of the disc component ($L_{disc} \propto T_{disc}^{1.0\pm0.1}$), and the temperature of the disc component and the total luminosity ($L_X \propto T_{disc}^{1.3\pm0.1}$; see Figure 4.1-*bottom-left*).

The four observations have different temporal properties: as already mentioned above, the first three have short-term variability around $\sim 10\%$ in both the soft and hard band

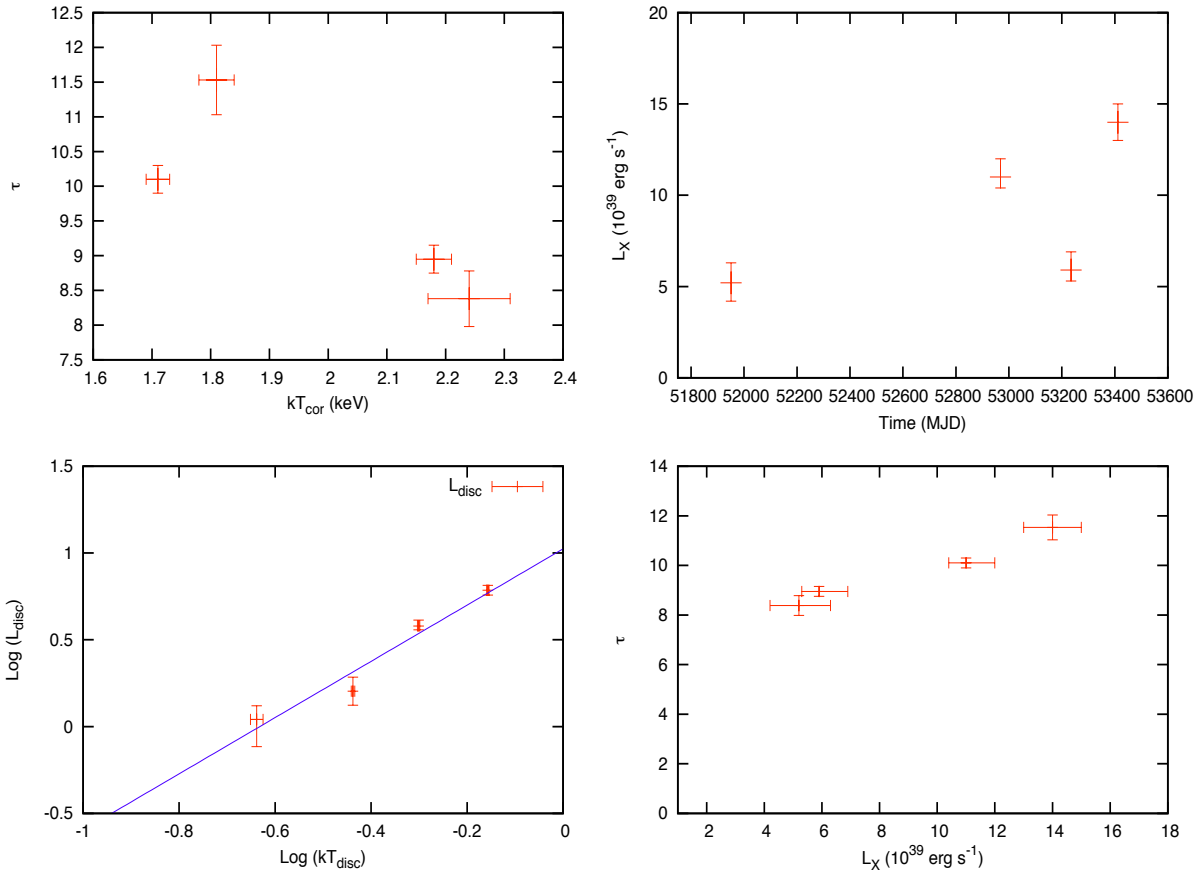

Figure 4.1: IC 342 X-1: *top-left*: optical depth τ versus temperature of the corona kT_{cor} (*diskbb+comptt* model); *top-right*: unabsorbed total luminosity in the 0.3-10 keV; *bottom-left*: unabsorbed luminosity vs temperature of the soft (disc) component in the 0.3-10 keV band; *bottom-right*: optical depth vs unabsorbed luminosity in the 0.3-10 keV band.

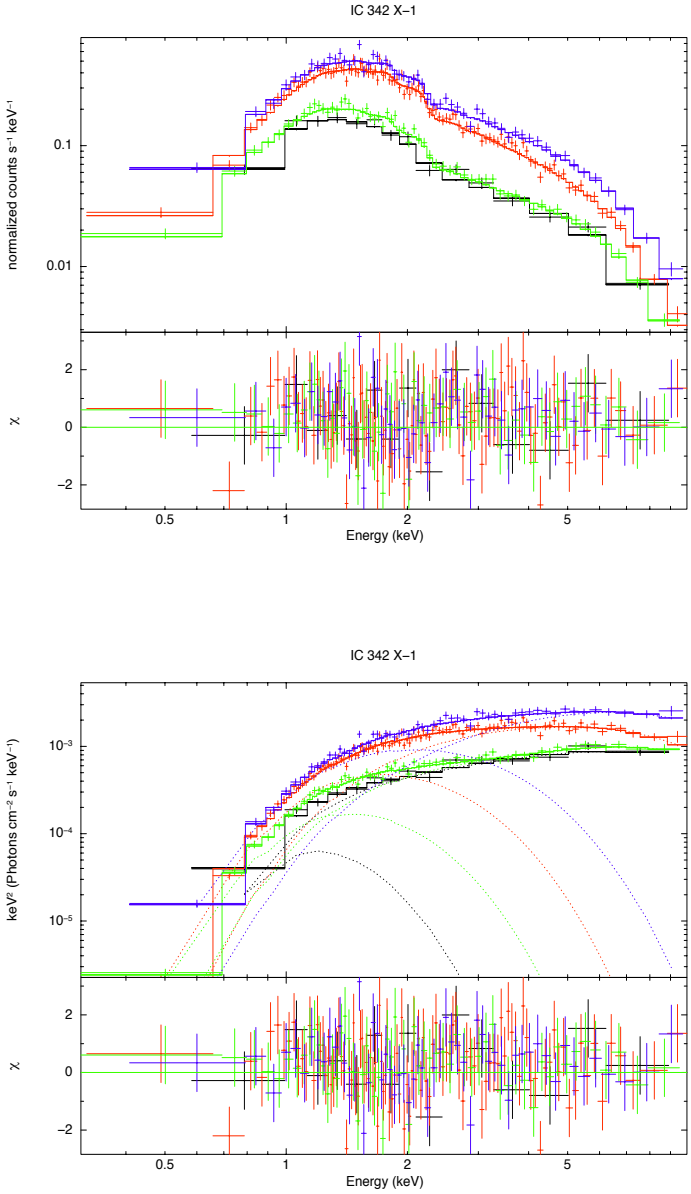

Figure 4.2: IC 342 X-1: comparison of all EPIC-pn spectra of IC 342 X-1 fitted with a *diskbb+comptt* model; folded (*top*) and unfolded ($E^2 f(E)$; *bottom*) spectra. For display purposes, the spectra are rebinned at 10σ.

Table 4.3: Fractional variability of IC 342 X-1.

	0093640901		**0206890101**	
Energy band	counts s^{-1}	F_{var}(per cent)[a]	counts s^{-1}	F_{var}(per cent)[a]
0.3-10 keV	0.49 ± 0.01	13[b]	1.09 ± 0.01	7 ± 2
0.3-2 keV	0.248 ± 0.009	19[b]	0.548 ± 0.009	13[b]
2.0-10 keV	0.252 ± 0.009	18[b]	0.550 ± 0.009	8 ± 3
	0206890201		**0206890401**	
Energy band	counts s^{-1}	F_{var}(per cent)[a]	counts s^{-1}	F_{var}(per cent)[a]
0.3-10 keV	0.561 ± 0.007	6 ± 2	1.43 ± 0.02	21 ± 2
0.3-2 keV	0.294 ± 0.005	2 ± 13	0.67 ± 0.01	12 ± 3
2.0-10 keV	0.276 ± 0.005	8 ± 3	0.77 ± 0.02	29 ± 2

[a] Calculated from the background subtracted EPIC-pn light curves, with 200 s time bins.
[b] Upper limit at 3σ

and they are consistent with a constant level of variability. Instead in the last one the variability is stronger and more variability is seen at higher energies ($\sim$12% at $0.3 - 2.0$ keV against $\sim$ 29% at $2.0 - 10.0$ keV, see Table 4.3) but it is probably produced by a significant drop in flux occurring during the observation.

As suggested in Winter et al. (2007), only EPIC-pn spectra with more than 5000 counts can be used to detect the Oxygen K-shell edge and IC 342 X-1 has at least 3 observations which reached the requested statistics. We fitted these observations using the best fit *diskbb+comptt* model, setting the Oxygen abundance at 0 and fitting again after adding a multiplicative *edge* component at 0.538 keV. This model gives an improvement in the fit with respect to a simple *diskbb+comptt* model. For example, in observation #2, $\Delta\chi^2 = 154.24$ for 1 additional dof. The abundance computed with this model is in the range 8.65-8.75 dex, consistent with sub-solar. We searched also for Iron K-shell features but found no evidence for them.

4.3.2 NGC 253 X-1

A single *comptt* model fits all the observations of this source but, in the spectrum with the highest counting statistics (#2), adding a disc component improves significantly the fit

(χ^2/dof = 854.226/810 against χ^2/dof=869.72/811). Furthermore, when this spectrum is fitted with a single *comptt*, the local N_H assumes a value close to 0 that seems rather unreasonable if compared with the average value attained in the other observations.

Often, the spectral fits of ULXs show a degeneracy between a cold and a warm disc solution when fitted with a *diskbb* plus a *power-law* (see Barnard 2010 and references therein for more details). We found a similar degeneracy using our reference model. In Table 4.4 and Figure 4.3, we show the best fits obtained adopting the absorbed *diskbb+comptt*, including the observation of January 2006 (Obs.Id. 0304851301) which is unpublished. We fixed the Galactic extinction at $1.3 \cdot 10^{20}$ cm^{-2} (Dickey & Lockman, 1990).

The spectral analysis shows that, even if the temperature of the soft component spans a larger range of values (from 0.1 to 0.8 keV), the high energy component is always optically thick and cold (see Figure 4.4-*top-left*). The temperature of the corona is in the range $1 - 2.5$ keV while the optical depth hardly becomes lower than 10 and it does not correlate with the flux (see Figure 4.4-*top-right, bottom*). The source occupies both the *very thick* and *thick* regions of the $\tau - kT_{cor}$ plane, but it stays most of the time in the former.

We estimated the chemical abundance in the local environment of NGC 253 X-1 from the Oxygen K-shell edge using the same procedure previously described. We used the longest observation (#2) as it provides the best counting statistics, adopting the best fit *diskbb+comptt* model. From the depth of the edge we found that the metallicity of its local environment is $8.8^{+0.09}_{-0.14}$ dex that is consistent within 3σ with the value of the solar metallicity we are assuming (8.92 dex).

We studied also the short-term variability of NGC 253 X-1, trying to understand which spectral component is driving it. As shown in table 4.5, the RMS fractional variability in the highest quality observation is $\sim 20\%$ in the $0.3 - 10$ keV energy band and there are indications that it is higher at high energy. However the error bars are large and the differences between the two bands remain below 3σ. The high variability allows us to

Table 4.4: Best fitting spectral parameters of NGC 253 X-1 obtained with the absorbed *diskbb+comptt* model.

NGC 253 X-1								
No.	Date	N_H [a] (10^{21} cm^2)	$^*kT_{disc}$ [b,c] (keV)	kT_{cor} [d] (keV)	τ [e]	L_X [0.3-10 keV] [f] (10^{38} erg s^{-1})	L_{disc} [0.3-10 keV] [g] (10^{38} erg s^{-1})	χ^2/dof
1	2000-12-13	$0.33^{+0.02}_{-0.02}$	$0.134^{+0.003}_{-0.003}$	$1.08^{+0.03}_{-0.03}$	$12.5^{+0.5}_{-0.5}$	25^{+7}_{-6}	$9.4^{+3.6}_{-3.2}$.	48.44/55
2	2003-06-19	$0.82^{+0.04}_{-0.04}$	$0.794^{+0.002}_{-0.002}$	$1.25^{+0.03}_{-0.03}$	27^{+5}_{-4}	24^{+1}_{-1}	17^{-2}_{-5}	852.44/810
3	2005-02-10	$0.20^{+0.02}_{-0.02}$	$0.464^{+0.009}_{-0.009}$	$0.97^{+0.04}_{-0.04}$	20^{+3}_{-2}	$9.9^{+3.1}_{-1.1}$	$3.3^{+1.1}_{-0.7}$	75.117/73
4	2006-01-02	$0.45^{+0.02}_{-0.02}$	$0.35^{+0.01}_{-0.01}$	$1.62^{+0.06}_{-0.06}$	$9.5^{+0.6}_{-0.6}$	$12^{+3}_{-2.3}$	$2.1^{+0.6}_{-0.6}$	88.229/83
5	2006-01-06	$0.64^{+0.01}_{-0.01}$	$0.104^{+0.007}_{-0.007}$	$0.94^{+0.02}_{-0.02}$	$13.8^{+0.4}_{-0.4}$	$7.2^{+1.9}_{-1.4}$	$(1.2e^{-4})^{+2.6}_{-1.2e^{-4}}$	88.57/91
6	2006-01-09	$0.49^{+0.01}_{-0.01}$	$0.715^{+0.008}_{-0.008}$	$1.61^{+0.08}_{-0.08}$	10^{+1}_{-1}	13.0^{+3}_{-2}	$6.4^{+0.8}_{-0.7}$	174.57/161
7	2006-01-11	$0.40^{+0.03}_{-0.03}$	$0.79^{+0.002}_{-0.002}$	$1.80^{+0.02}_{-0.02}$	9^{+3}_{-3}	$13.0^{+5}_{-4.4}$	$6.8^{+1.6}_{-1.3}$	44.325/45

[a] Column density; [b] Inner disc temperature; [c] The seed photons temperature T_0 is assumed to be equal to T_{disc}. [d] Temperature of the corona; [e] Optical depth of the corona; [f] Unabsorbed total X-ray luminosity in the 0.3 -10 keV range; [g] Unabsorbed disc luminosity in the 0.3-10 keV range.

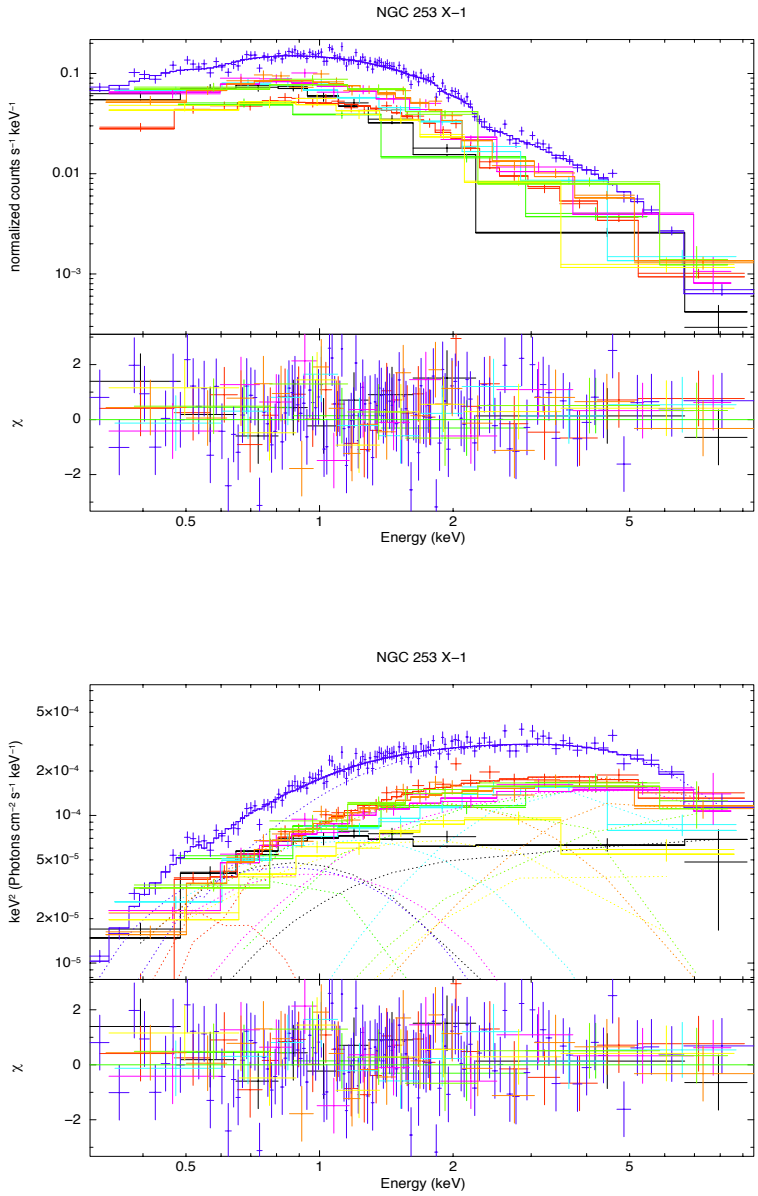

Figure 4.3: NGC 253 X-1: comparison of all EPIC-pn spectra of NGC 253 X-1 fitted with a *diskbb+comptt* model; folded (*top*) and unfolded ($E^2 f(E)$; *bottom*) spectra. For display purposes, the spectra are rebinned at 10σ.

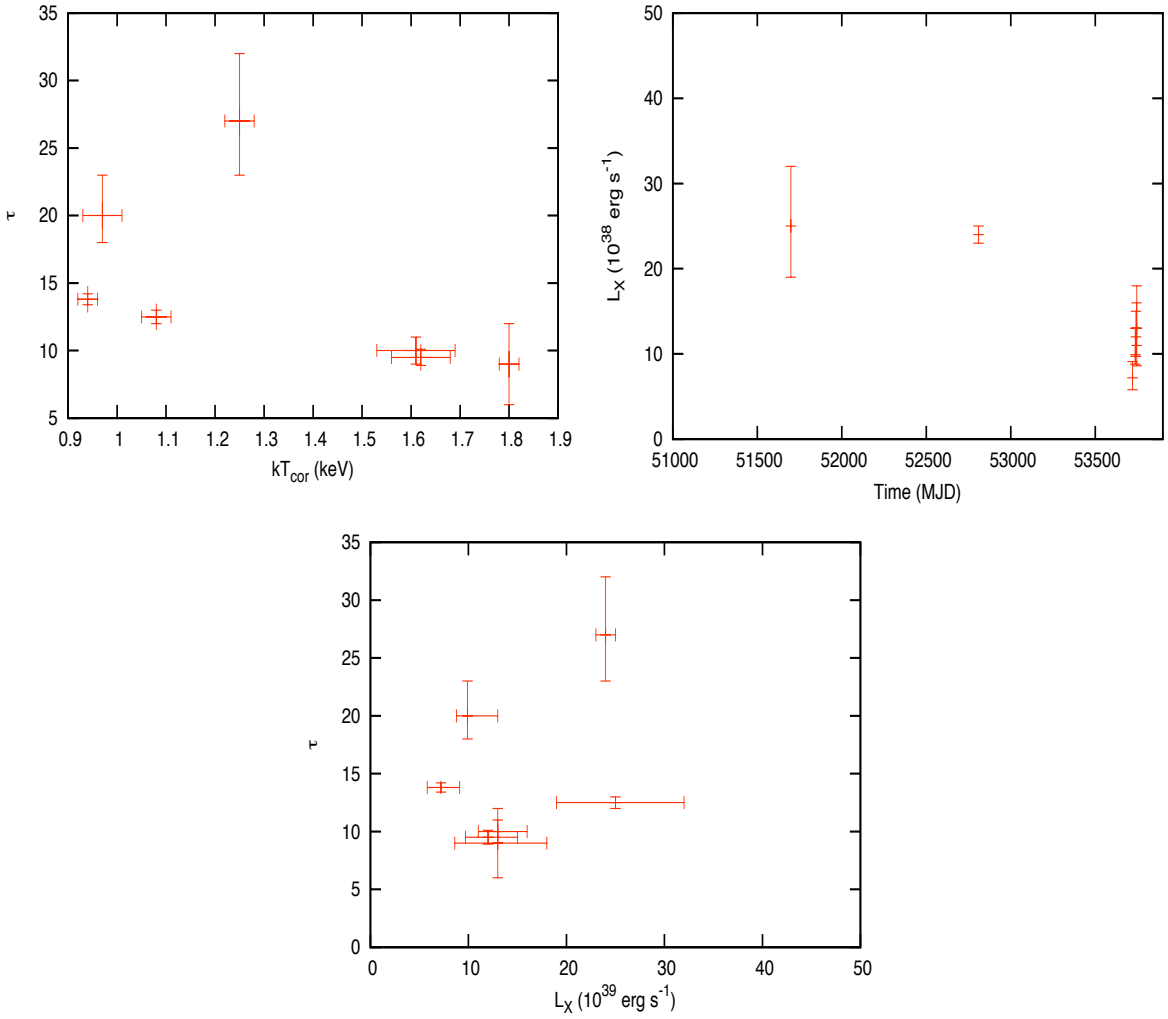

Figure 4.4: NGC 253 X-1:*top-left*: optical depth τ versus temperature of the corona kT_{cor} (*diskbb+comptt* model); *top-right*: unabsorbed total luminosity in the 0.3-10 keV; *bottom*: optical depth vs unabsorbed luminosity evaluated in the range 0.3-10 keV.

Table 4.5: Fractional variability of NGC 253 X-1.

	0110900101		**0152020101**		**0304851101**	
Energy band	counts s^{-1}	F_{var}(per cent)[a]	counts s^{-1}	F_{var}(per cent)[a]	counts s^{-1}	F_{var}(per cent)[a]
0.3-10 keV	0.146 ± 0.007	40[b]	0.408 ± 0.004	28 ± 1	0.148 ± 0.006	27[b]
0.3-2 keV	0.132 ± 0.006	39[b]	0.416 ± 0.004	28 ± 1	0.121 ± 0.006	40[b]
2.0-10 keV	0.066 ± 0.007	96[b]	0.137 ± 0.003	22 ± 3	0.070 ± 0.005	65[b]
	0304850901		**0304851001**		**0304851201**	
Energy band	counts s^{-1}	F_{var}(per cent)[a]	counts s^{-1}	F_{var}(per cent)[a]	counts s^{-1}	F_{var}(per cent)[a]
0.3-10 keV	0.180 ± 0.006	11 ± 5	0.199 ± 0.006	5 ± 8	0.205 ± 0.005	18[b]
0.3-2 keV	0.137 ± 0.005	23[b]	0.152 ± 0.005	21[b]	157 ± 0.004	20[b]
2.0-10 keV	0.077 ± 0.005	48[b]	0.082 ± 0.005	46[b]	0.077 ± 0.003	41[b]
	0304851301					
Energy band	counts s^{-1}	F_{var}(per cent)[a]				
0.3-10 keV	0.209 ± 0.009	28[b]				
0.3-2 keV	0.157 ± 0.008	31[b]				
2.0-10 keV	0.085 ± 0.007	54[b]				

[a] Calculated from the background subtracted EPIC-pn light curves, with 200 s time bins.
[b] Upper limit at 3σ

exclude a canonical *soft* state for which the variability is less than 10%. These values may be more consistent with a *very high state*. We studied the RMS spectrum in the highest quality observations ($\#2, 4$) in which the counting statistics is adequate. In figure 4.5, we can see that the variability is consistent with a constant within 3σ and may thus be produced by a single spectral component.

We tested also a modified single component disc model, the slim disc, suitable to describe the advection dominated regime that may set in at slightly super-Eddington rates. We fitted the data using the simplified model *diskpbb* in XSPEC. Notably all the spectra can be well described by this model (see Table 4.6). Although the fits are generally statistically acceptable, we found one observations ($\#3$) in which the column density pegged at 0 indicating that the absorption was anomalously low. The variation of the p value with the total unabsorbed 0.3-10 keV luminosity and with the disc temperature kT_{disc} is shown in Figure 4.6-*top* and 4.6-*bottom*, respectively. There is a tendency for the p-index to decrease with increasing disc temperature and luminosity. Therefore, we suggest that

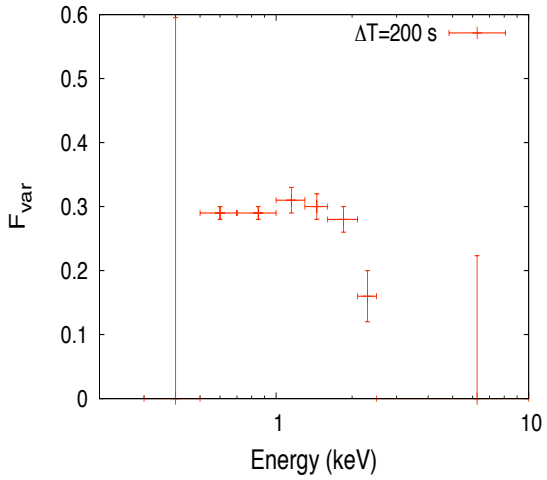

Figure 4.5: NGC 253 X-1: RMS fractional variability spectrum evaluated on background subtracted EPIC-pn lightcurves of observation 0152020101, sampled with time bins of 200 s.

Table 4.6: Best fitting spectral parameters of NGC 253 X-1 obtained with the absorbed *diskpbb* model.

NGC 253 X-1						
No.	Date	N_H [a] (10^{21} cm^2)	p [b] (keV)	kT_{disc} [c]	L_X [0.3-10 keV] [d] (10^{38} erg s^{-1})	χ^2/dof
1	2000-12-13	$0.7^{+0.2}_{-0.2}$	$0.625^{+0.01}_{-0.01}$	$1.60^{+0.02}_{-0.02}$	15^{+2}_{-2}	52.02/57
2	2003-06-19	$1.46^{+0.04}_{-0.04}$	$0.588^{+0.001}_{-0.001}$	$1.521^{+0.004}_{-0.004}$	27^{+1}_{-1}	856.21/812
3	2005-02-10	$0^{+0.2}_{-0}$	$0.703^{+0.01}_{-0.01}$	$1.42^{+0.02}_{-0.02}$	10^{+1}_{-1}	75.88/75
4	2006-01-02	$1.2^{+0.2}_{-0.2}$	$0.581^{+0.003}_{-0.003}$	$1.98^{+0.02}_{-0.02}$	13^{+2}_{-9}	88.97/85
5	2006-01-06	$0.4^{+0.1}_{-0.1}$	$0.652^{+0.01}_{-0.01}$	$1.25^{+0.01}_{-0.01}$	$7.0^{+0.7}_{-0.6}$	90/93
6	2006-01-09	$1.0^{+0.1}_{-0.1}$	$0.620^{+0.003}_{-0.003}$	$1.66^{+0.01}_{-0.01}$	13.0^{+1}_{-1}	174.94/163
7	2006-01-11	$0.9^{+0.2}_{-0.2}$	$0.635^{+0.01}_{-0.01}$	$1.59^{+0.02}_{-0.02}$	13.0^{+2}_{-2}	44.38/47

[a] Column density; [b] exponent of the radial dependence of the disc temperature; [c] disc temperature; [d] unabsorbed total X-ray luminosity in the 0.3 -10 keV range;

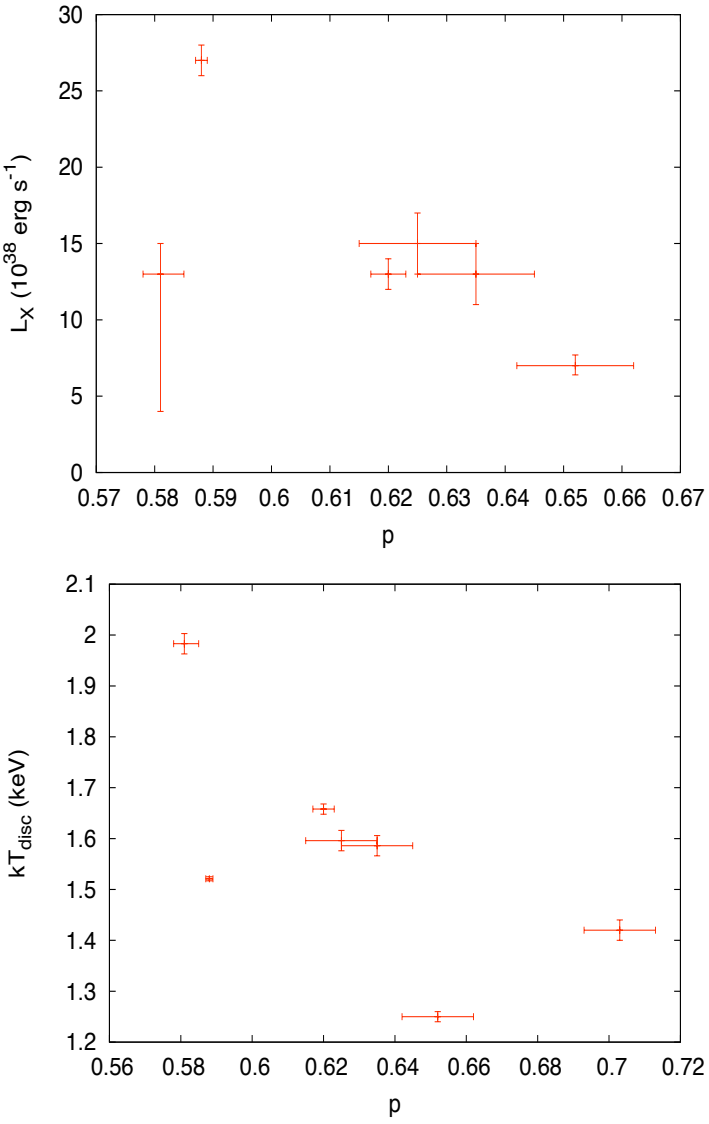

Figure 4.6: NGC 253 X-1: unabsorbed total X-ray luminosity in the 0.3-10 keV energy band (*top*) and disc temperature (*bottom*) versus the p-index (diskpbb model).

a slim disc may provide a reasonable description of the behaviour of NGC 253 X-1, which appears to marginally enter the ULX regime. In fact, at low fluxes, the spectrum may also be well described in terms of a canonical *soft* state and modeled by a *diskbb* (Kajava & Poutanen, 2009). This source may then be marginally entering the ULX regime only at high luminosity and may not be able to produce powerful outflows.

4.3.3 NGC 5204 X-1

The spectral properties of NGC 5204 X-1 have been analysed in several papers (Roberts et al. 2005; Stobbart et al. 2006; Kajava & Poutanen 2009; Feng & Kaaret 2009; Gladstone et al. 2009). It was observed six times by *XMM-Newton* and its spectra can be well fitted by a *power-law* plus a cold disc ($\sim 0.2-0.3$ keV). The X-ray flux variability that does not exceed a factor of 2-3. Amongst the sources of this sample, it is the only one that does not show strong evidence for curvature at high energy. Following Stobbart et al. (2006), we fitted the $2-10$ keV energy band with a *power-law* or a broken *power-law*. We found that only in the first observation a broken *power-law* is favourite with respect to a simple *power-law* ($\Delta\chi^2 = 29.76$ for 2 additional d.o.f.) while in the remaining we do not find statistical evidence of it, (although this may be due to the low counting statistics). Feng & Kaaret (2009) fitted all the six *XMM-Newton* observations using a *power-law* or a *comptt* model, plus a *diskbb* component, and found that the *diskbb+power-law* model provides the best fit. There is a correlation between the temperature of the disc and the total luminosity. This is consistent with that of a standard disc, but is not observed adopting a *diskbb+comptt* model (see Feng & Kaaret 2009 for a more detailed discussion). The ratio of the fluxes of the disc and the *power-law* component seems consistent with the *very-high* state of Galactic BHB. However, from a temporal analysis on the highest quality *XMM-Newton* observation, Heil et al. (2009) found that the variability is consistent with zero, the opposite of what is expected for the *very-high* state.

Table 4.7: Best fitting spectral parameters of NGC 5204 X-1 obtained with the absorbed *diskbb+comptt* model.

NGC 5204 X-1								
No.	Date	N_H [a] (10^{21} cm^2)	kT_{disc} [b,c] (keV)	kT_{cor} [d] (keV)	τ [e]	L_X [0.3-10 keV] [f] (10^{39} erg s^{-1})	L_{disc} [0.3-10 keV] [g] (10^{39} erg s^{-1})	χ^2/dof
1	2003-01-06	$0.04^{+0.04}_{-0.04}$	$0.306^{+0.002}_{-0.002}$	$1.39^{+0.02}_{-0.02}$	$12.7^{+0.4}_{-0.4}$	$5.1^{+0.3}_{-0.3}$	$1.90^{+1.2}_{-0.4}$.	398.56/453
2	2003-04-25	$0.67^{+0.06}_{-0.06}$	$0.203^{+0.002}_{-0.002}$	$6.2^{+0.2}_{-0.2}$	$3.5^{+0.2}_{-0.1}$	$7.7^{+1}_{-0.9}$	$2.3^{+0.3}_{0.3}$	238.66/221
3	2003-05-01	$0.31^{+0.05}_{-0.05}$	$0.283^{+0.002}_{-0.002}$	$1.55^{+0.03}_{-0.03}$	$8.8^{+0.3}_{-0.3}$	$7.7^{+0.9}_{-0.8}$	$3.1^{+0.3}_{-0.2}$.	301.49/271
4	2006-11-15	$0.33^{+0.03}_{-0.03}$	$0.216^{+0.001}_{-0.001}$	$1.44^{+0.01}_{-0.01}$	$7.2^{+0.1}_{-0.1}$	$8.7^{+0.6}_{-0.6}$	$2.3^{+0.2}_{-0.2}$	717.93/722
5	2006-11-19	$0.47^{+0.02}_{-0.02}$	$0.265^{+0.001}_{-0.001}$	$2.35^{+0.02}_{-0.02}$	$5.72^{+0.08}_{-0.02}$	$8.1^{+0.4}_{-0.4}$	$2.9^{+0.1}_{-0.1}$	839.02/822
6	2006-11-25	$0.32^{+0.03}_{-0.03}$	$0.231^{+0.001}_{-0.001}$	$4.31^{+0.05}_{-0.05}$	$4.6^{+0.09}_{-0.05}$	$6.6^{+0.4}_{-0.4}$	$1.8^{+0.1}_{-0.1}$	642.82/676

[a] Column density; [b] Inner disc temperature; [c] The seed photons temperature T_0 is assumed to be equal to T_{disc}. [d] Temperature of the corona; [e] Optical depth of the corona; [f] Unabsorbed total X-ray luminosity in the 0.3 -10 keV range; [g] Unabsorbed disc luminosity in the 0.3-10 keV range.

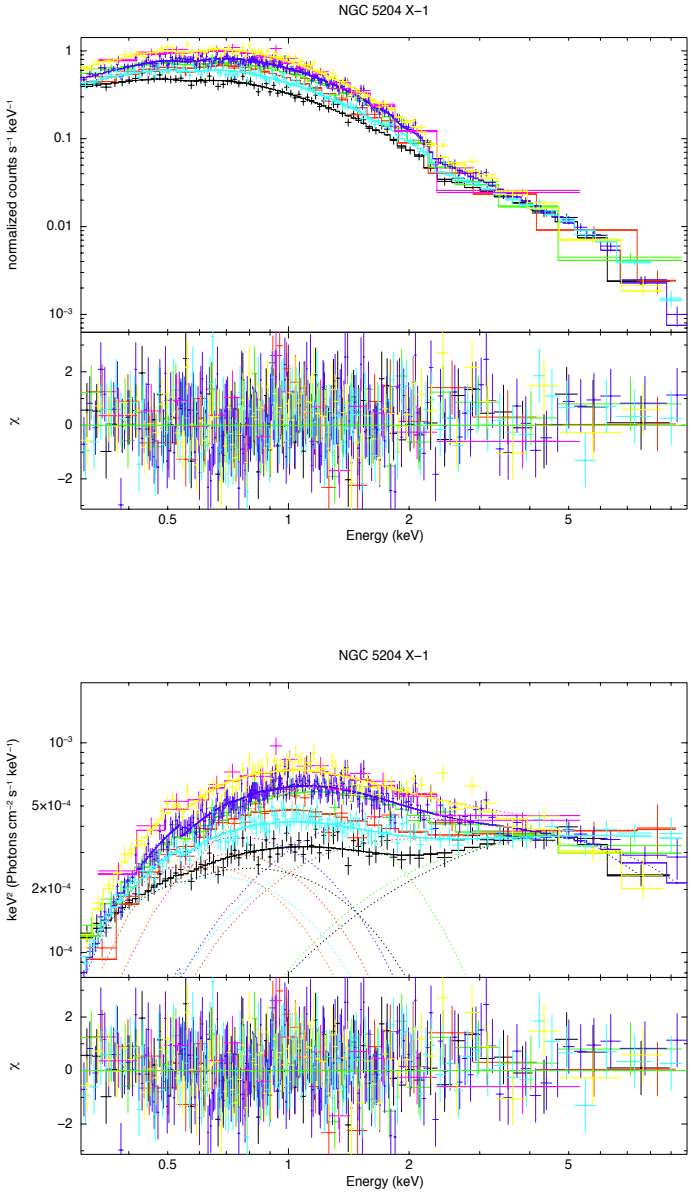

Figure 4.7: NGC5204 X-1: comparison of all EPIC-pn spectra of NGC5204 X-1 fitted with a *diskbb+comptt* model; folded (*top*) and unfolded ($E^2 f(E)$; *bottom*) spectra. For display purposes, the spectra are rebinned at 10σ.

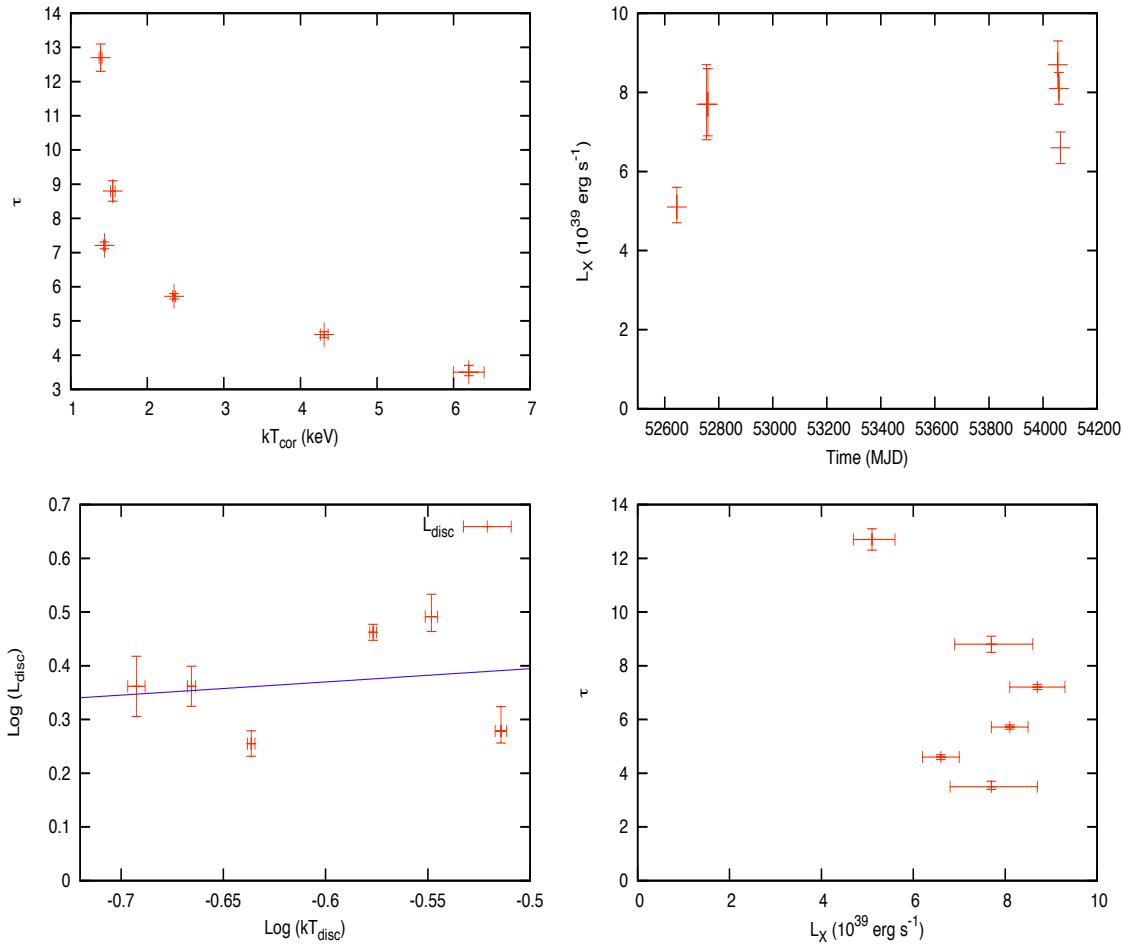

Figure 4.8: NGC 5204 X-1: *top-left*: optical depth τ versus temperature of the corona kT_{cor} (*diskbb+comptt* model); *top-right*: unabsorbed total luminosity in the 0.3-10 keV; *bottom-left*: unabsorbed luminosity vs temperature of the soft (disc) component in the 0.3-10 keV band vs the temperature of the soft component; *bottom-right*: optical depth vs unabsorbed luminosity in the 0.3-10 keV band.

Table 4.8: Fractional variability of NGC 5204 X-1.

	0142770101		**0142770301**		**0150650301**	
Energy band	counts s^{-1}	F_{var}(per cent)[a]	counts s^{-1}	F_{var}(per cent)[a]	counts s^{-1}	F_{var}(per cent)[a]
0.3-10 keV	0.667 ± 0.008	5 ± 2	0.92 ± 0.02	13[b]	1.09 ± 0.02	12[b]
0.3-2 keV	0.557 ± 0.007	5 ± 2	0.79 ± 0.02	14[b]	0.95 ± 0.02	14[b]
2.0-10 keV	0.121 ± 0.003	24[b]	0.146 ± 0.008	37[b]	0.147 ± 0.008	34[b]
	0405690101		**0405690201**		**0405690501**	
Energy band	counts s^{-1}	F_{var}(per cent)[a]	counts s^{-1}	F_{var}(per cent)[a]	counts s^{-1}	F_{var}(per cent)[a]
0.3-10 keV	1.37 ± 0.02	8[b]	1.118 ± 0.007	2[b]	0.839 ± 0.007	7[b]
0.3-2 keV	1.20 ± 0.02	9[b]	0.975 ± 0.006	5 ± 1	0.714 ± 0.006	7[b]
2.0-10 keV	0.176 ± 0.007	26[b]	0.154 ± 0.003	14[b]	0.135 ± 0.003	19[b]

[a] Calculated from the background subtracted EPIC-pn light curves, with 200 s time bins.
[b] Upper limit at 3σ

Using a single *comptt* model, in 5 out of 6 observations the column density pegged at 0. Hence, as for the other sources of the sample, we analyzed all the data of NGC 5204 X-1 with an absorbed comptonization model plus a soft component. The Galactic absorption was fixed at $1.39 \cdot 10^{20}$ cm^{-2} (Dickey & Lockman 1990). Results of the spectral fits are shown in Table 4.7 and Figure 4.7. Luminosity of the source shows only limited variability (less than a factor of 2, Figure 4.8-*top-right*) and the disc temperature varies in the range 0.2-0.3 keV; the flux of this component is a consistent percentage of the total flux (25-40%) in the $0.3 - 10$ keV energy band; the corona is always optically thick, usually with $\tau < 9$, and has a low temperature ($\sim 1 - 6$ keV; see Figure 4.8-*top-left*). Only two observations (#1,3), which have the lowest luminosity, are (marginally) located in the *very thick* state, while all the others are in the thick state. In addition, the optical depth and the total luminosity may be slightly anticorrelated, but there is no statistical significant evidence for it (Figure 4.8-*bottom-right*). We note also that the disc temperature and the unabsorbed disc luminosity are weakly correlated ($L_{disc} \propto T_{disc}^{0.9 \pm 0.5}$; Figure 4.8-*bottom-left*) even if the points are fairly scattered and the statistical significance is poor.

We tried also the *diskpbb* model. This is generally acceptable apart from the highest quality observation (#5). Therefore, it is most likely that the observations which are

described by this model are actually well fitted only because of their low counting statistics.

Notably, the short-time variability of NGC 5204 X-1 is almost suppressed in all the observations (less than 10%, see Table 4.8), with no significant differences between the hard and soft energy band. This result may be consistent with the emission from a single spectral component.

Finally, we highlight that even in the highest quality observation it is not possible to determine the metallicity in the local environment of NGC 5204 X-1 from the Oxygen edge, because the fits turn out to be rather insensitive to variations of the chemical abundances.

4.3.4 NGC 5408 X-1

The luminosity of NGC 5408 X-1 varies less than a factor of 2, showing significant stability during the ten years of observation. In the highest quality observation (#8) a broken *power-law* is always favoured to a simple *power-law* ($\chi^2/dof = 504.58/459$ against $\chi^2/dof = 539.15/461$), showing an energy break at $\sim 3-5$ keV. A simple *comptt* model is rejected in most of the observations. However, adding a soft component improves significantly the fitting statistics. We described all the spectra with an absorbed *diskbb+comptt* model, fixing the Galactic absorption at $5.67 \cdot 10^{20}$ cm^{-2} (Dickey & Lockman 1990). The results of the spectral fits are summarized in Table 4.9 and Figure 4.9.

The high energy component is usually cold ($\sim 1-2$ keV) and optically thick ($\sim 5-6$). Its parameters do not display a relation with the luminosity, which however does not vary more than a factor of ~ 1.5 (Figure 4.10-*top-right*, *bottom-right*). The source is almost always found in the thick state. On the other hand, observation #2 shows a certain degeneracy in the parameters of the corona that appears to be warm (84 keV) and marginally optically thin ($\tau \sim 0.9$), even if the improvement over a cool corona (fixing the temperature at 1.5 keV) is only marginal ($\Delta\chi^2 = 7$). For this reason, we removed this observation from the plot $\tau - kT_{cor}$ (Figure 4.10).

Table 4.9: Best fitting spectral parameters of NGC 5408 X-1 in different observations obtained with the absorbed *diskbb+comptt* model.

NGC 5408 X-1								
No.	N_H[a] (10^{21} cm^2)	kT_{disc}[b,c] (keV)	kT_{cor}[d] (keV)	τ[e]	kT_{APEC}^{f} (keV)	L_X [0.3-10 keV] [g] (10^{39} erg s^{-1})	L_{disc} [0.3-10 keV][h] (10^{39} erg s^{-1})	χ^2/dof
1	$0.11^{+0.03}_{-0.03}$	$0.180^{+0.001}_{-0.001}$	$2.00^{+0.04}_{-0.04}$	$5.0^{+0.2}_{-0.2}$	0	$10.0^{+0.2}_{-0.5}$	$6.6^{+0.5}_{-0.4}$.	280.79/271
2	$0.09^{+0.03}_{-0.03}$	$0.192^{+0.001}_{-0.001}$	84^{+2}_{-2}	$0.11^{+0.02}_{-0.01}$	0	$9.8^{+1}_{-0.9}$	$6.2^{+0.5}_{-0.5}$	235.86/273
3	$0.28^{+0.05}_{-0.05}$	$0.177^{+0.001}_{-0.001}$	$1.03^{+0.03}_{-0.03}$	$8.9^{+0.3}_{-0.3}$	0	$11.0^{+0.1}_{-0.1}$	$7.4^{+0.7}_{-0.6}$.	93.49/133
4	$0.72^{+0.07}_{-0.07}$	$0.171^{+0.001}_{-0.001}$	$1.56^{+0.04}_{-0.04}$	$6.8^{+0.3}_{-0.3}$	0	$8.2^{+1.3}_{-1.2}$	$4.7^{-0.6}_{+0.6}$	118.3/127
5	$0.62^{+0.01}_{-0.01}$	$0.1531^{+0.002}_{-0.002}$	$1.656^{+0.008}_{-0.008}$	$6.04^{+0.04}_{-0.04}$	$0.92^{+0.06}_{-0.06}$	$8.6^{+0.2}_{-0.2}$	$4.5^{+0.1}_{-0.2}$	968.60/913
6	$0.61^{+0.01}_{-0.01}$	$0.1537^{+0.003}_{-0.003}$	$1.506^{+0.009}_{-0.009}$	$6.77^{+0.05}_{-0.05}$	$0.84^{+0.04}_{-0.03}$	$7.9^{+0.3}_{-0.3}$	$3.7^{+0.1}_{-0.1}$	868.60/796
7	$0.59^{+0.01}_{-0.01}$	$0.1556^{+0.002}_{-0.002}$	$1.813^{+0.008}_{-0.008}$	$5.88^{+0.03}_{-0.03}$	$0.95^{+0.03}_{-0.03}$	$9.6^{+0.2}_{-0.2}$	$4.3^{+0.1}_{-0.1}$	1085.20/1030
8	$0.43^{+0.01}_{-0.01}$	$0.1628^{+0.0003}_{-0.0003}$	$1.882^{+0.008}_{-0.008}$	$5.73^{+0.03}_{-0.03}$	$0.96^{+0.04}_{-0.04}$	$8.9^{+0.3}_{-0.2}$	$3.8^{+0.1}_{-0.1}$	1158.99/1023
9	$0.64^{+0.01}_{-0.01}$	$0.1542^{+0.0002}_{-0.0002}$	$1.728^{+0.007}_{-0.007}$	$5.97^{+0.03}_{-0.03}$	$0.902^{+0.04}_{-0.04}$	$9.1^{+0.2}_{-0.3}$	$4.2^{+0.1}_{-0.1}$	1045.72/981
10	$0.55^{+0.01}_{-0.01}$	$0.1600^{+0.04}_{-0.03}$	$2.047^{+0.009}_{-0.009}$	$5.43^{+0.03}_{-0.03}$	$0.87^{+0.04}_{-0.03}$	$8.5^{+0.6}_{-0.3}$	$3.8^{+0.1}_{-0.1}$	1055.82/995

[a] Column density; [b] Inner disc temperature; [c] The seed photons temperature T_0 is assumed to be equal to T_{disc}. [d] Temperature of the corona; [e] Optical depth of the corona; [f] APEC temperature; [g] Unabsorbed total X-ray luminosity in the 0.3 -10 keV range; [h] Unabsorbed disc luminosity in the 0.3-10 keV range.

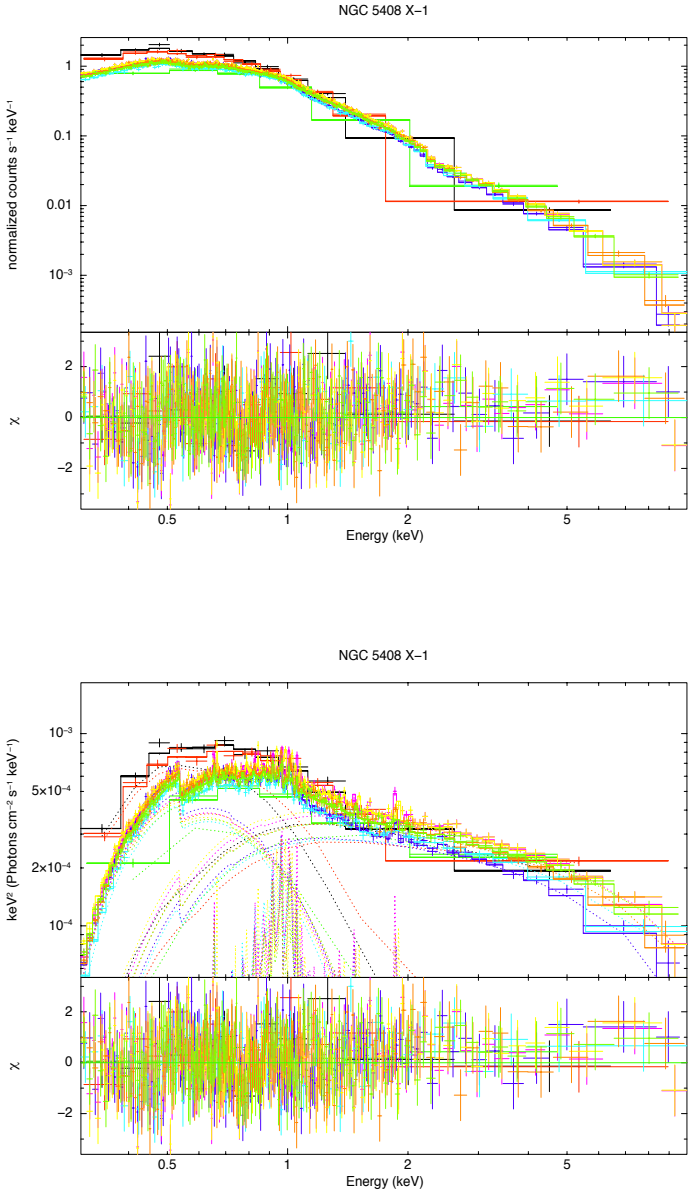

Figure 4.9: NGC 5408 X-1: comparison of all EPIC-pn spectra of NGC5408 X-1 fitted with a *diskbb+comptt* model; folded (*top*) and unfolded ($E^2 f(E)$; *bottom*) spectra. For display purposes, the spectra are rebinned at 20σ.

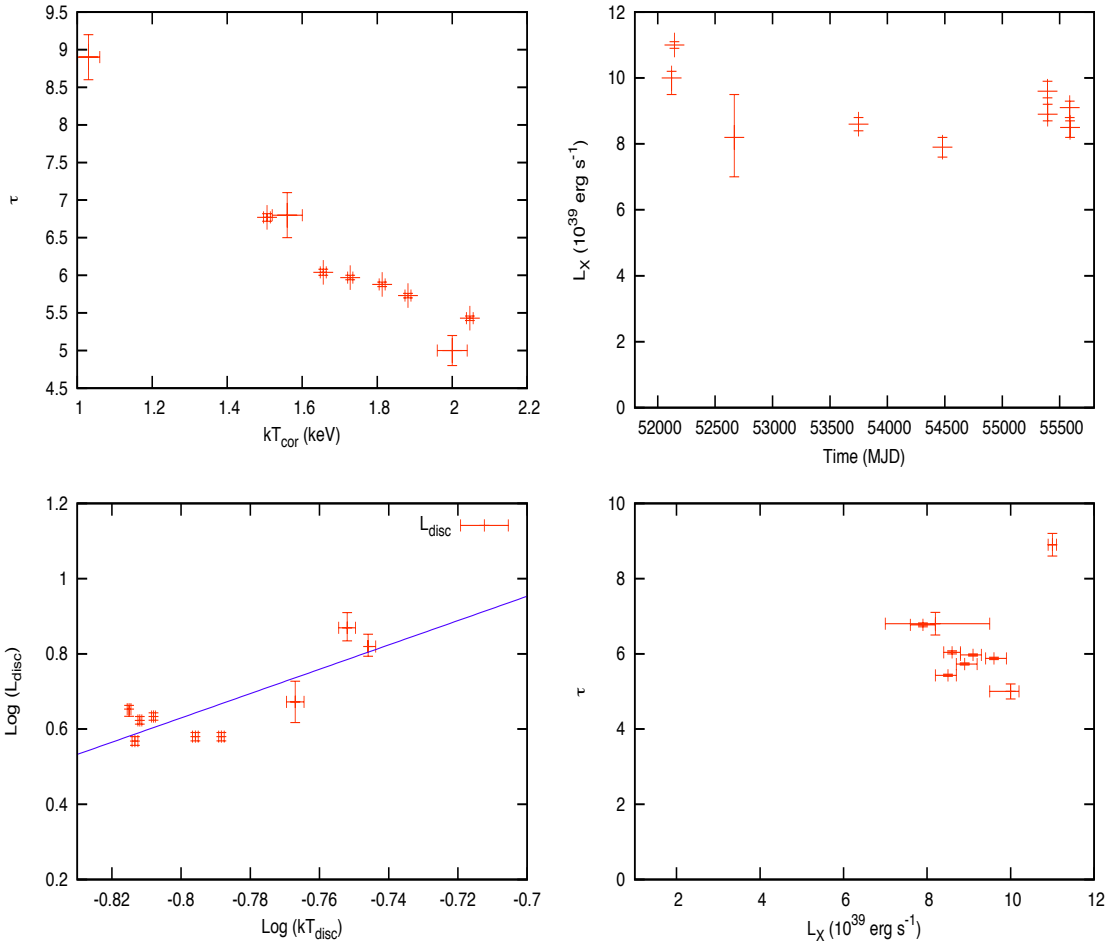

Figure 4.10: NGC 5408 X-1: *top-left*: optical depth τ versus temperature of the corona kT_{cor} (*diskbb+comptt* model); *top-right*: unabsorbed total luminosity in the 0.3-10 keV; *bottom-left*: unabsorbed luminosity vs temperature of the soft (disc) component in the 0.3-10 keV band; *bottom-right*: optical depth vs unabsorbed luminosity in the 0.3-10 keV band.

Table 4.10: Fractional variability of NGC 5408 X-1. Observation #3 is not listed as no EPIC-pn data are available.

	0112290501		**0112290601**		**0112291201**[c]	
Energy band	counts s^{-1}	F_{var}(per cent)[a]	counts s^{-1}	F_{var}(per cent)[a]	counts s^{-1}	F_{var}(per cent)[a]
0.3-10 keV	1.44 ± 0.03	17 ± 2	1.41 ± 0.02	5 ± 2	–	–
0.3-2 keV	1.37 ± 0.02	16 ± 2	1.34 ± 0.02	5 ± 2	–	–
2.0-10 keV	0.094 ± 0.007	46[b]	0.091 ± 0.006	37[b]	–	–
	0302900101		**0500750101**		**0653380201**	
Energy band	counts s^{-1}	F_{var}(per cent)[a]	counts s^{-1}	F_{var}(per cent)[a]	counts s^{-1}	F_{var}(per cent)[a]
0.3-10 keV	1.07 ± 0.004	8.8 ± 0.5	1.000 ± 0.006	12.9 ± 0.7	1.200 ± 0.004	7.0 ± 0.5
0.3-2 keV	0.995 ± 0.004	8.1 ± 0.5	0.924 ± 0.006	11.3 ± 0.8	1.110 ± 0.004	6.9 ± 0.5
2.0-10 keV	0.094 ± 0.002	24[b]	0.102 ± 0.002	25[b]	0.111 ± 0.002	20[b]
	0653380301		**0653380401**		**0653380501**	
Energy band	counts s^{-1}	F_{var}(per cent)[a]	counts s^{-1}	F_{var}(per cent)[a]	counts s^{-1}	F_{var}(per cent)[a]
0.3-10 keV	1.182 ± 0.004	6.8 ± 0.4	1.123 ± 0.004	7.7 ± 0.5	1.084 ± 0.004	9.0 ± 0.5
0.3-2 keV	1.091 ± 0.004	6.8 ± 0.5	1.038 ± 0.004	6.9 ± 0.5	0.997 ± 0.004	7.9 ± 0.5
2.0-10 keV	0.109 ± 0.001	18[b]	0.105 ± 0.002	21[b]	0.107 ± 0.002	19[b]

[a] Calculated from the background subtracted EPIC-pn light curves, with 200 s time bins;
[b] Upper limit at 3σ;
[c] Number of time bins lower than 20, too low to apply the Gaussian statistics;

The soft component is generally centered around 0.17 keV and it does not show pronounced changes during time. This component usually accounts for more than 50% of the total flux in the $0.3-10$ keV energy band, with an interesting disc temperature-luminosity correlation ($L_{disc} \propto T_{disc}^{1.8\pm0.8}$, see Figure 4.10-*bottom-left*). This result was obtained tying together the temperature of the disc and that of the seed photons, which may be questionable in these physical conditions. In fact, using a *diskbb+power-law*, the disc temperature goes as $L_X^{-3.5}$ (Kajava & Poutanen, 2009), suggesting the emission from a wind (see Chapter 1). Moreover, the fractional variability seems to be higher at higher energies although the statistics does not allow us to have constraints on the high energy component (only 3σ upper limits; see Table 4.10). If confirmed this behaviour may indicate that a clumpy wind is intersecting our line of sight to the central regions of the source, enforcing the conclusion of Middleton et al. (2011). Furthermore, in the highest quality observations, an underlying plasma component (*APEC* in XSPEC) with a temperature of ~ 0.9 keV

leads to a significant improvement in the fit. This emission can be produced either by the contamination of the diffuse emission in the host galaxy or directly from the environment around the source as a result of the wind emission at very large radii.

We estimated the metallicity of the local environment analyzing the highest quality observations (#5,7,8,9 and 10) since they can provide enough total counts to detect the Oxygen and Iron K-shell edges. No evidence of a Iron edge was found. Adding a multiplicative Oxygen *edge* component to the best fit *diskbb+comptt* model (providing particular attention to remove the APEC component which may affect our estimates) and adopting the procedure discussed in the previous chapter leads to a statistically acceptable fit (e.g. in observation #8, $\chi^2/dof = 1296.17/1030$ against $\chi^2/dof = 1267.82/1029$). We estimate that the metallicity is $[O/H] = 8.6 - 8.7$ dex and thus consistent with being sub-solar.

4.3.5 Ho II X-1

Ho II X-1 has been observed 5 times by *XMM-Newton*, displaying flux variability up to a factor of 4-5 (see Feng & Kaaret 2009). In Gladstone et al. (2009), Ho II X-1 is interpreted as one of the most extreme ULXs in which massive outflows are the origin of the important emission in the soft band. It represents the most luminous source of our sample together with NGC 5408 X-1. In the last observation (#5), the source transits from a high to a low flux regime with a decrement of $\sim 50\%$ (Kajava et al. 2012). This makes the fractional variability really high in comparison with the other observations in which, indeed, the mean fractional RMS value is $\leq 5\%$, as in NGC 5204 X-1. The fractional variability seems more pronounced at high energy even if we can place only 3σ upper limits due to the limited statistics (see Table 4.11).

We checked for the presence of curvature at high energy, finding marginal evidence of a break in two (#4,5) out of 5 observations ($\Delta\chi^2 = 22.34$ and $\Delta\chi^2 = 18.67$ for 2 additional d.o.f., respectively). We chose to describe all the spectra with the reference

Table 4.11: Fractional variability of Ho II X-1.

	0112520601		**0112520701**		**0112520901**	
Energy band	counts s^{-1}	F_{var}(per cent)[a]	counts s^{-1}	F_{var}(per cent)[a]	counts s^{-1}	F_{var}(per cent)[a]
0.3-10 keV	3.37 ± 0.03	3 ± 1	3.1 ± 0.1	21[b]	0.88 ± 0.02	2 ± 6
0.3-2 keV	2.97 ± 0.03	4 ± 1	2.6 ± 0.1	25[b]	0.81 ± 0.02	2 ± 7
2.0-10 keV	0.40 ± 0.01	14[b]	0.43 ± 0.02	22[b]	0.090 ± 0.006	40[b]
	0200470101		**0561580401**			
Energy band	counts s^{-1}	F_{var}(per cent)[a]	counts s^{-1}	F_{var}(per cent)[a]		
0.3-10 keV	3.39 ± 0.01	2.6 ± 0.9	1.33 ± 0.01	21.4 ± 0.7		
0.3-2 keV	2.98 ± 0.01	3.7 ± 0.8	1.201 ± 0.009	21.5 ± 0.8		
2.0-10 keV	0.423 ± 0.005	13[b]	0.143 ± 0.003	18[b]		

[a] Calculated from the background subtracted EPIC-pn light curves, with 200 s time bins.
[b] Upper limit at 3σ

model *diskbb+comptt*, again assuming that the seed photons temperature is equal to the inner disc temperature and fixing the local absorption at $3.4{\cdot}10^{20}$ cm^{-2} (Dickey & Lockman, 1990). Results and spectral fits are shown in Table 4.12 and Figure 4.11.

The luminosity of Ho II X-1 varies up to a factor of 4 (Figure 4.12-*top-right*) but the temperature of the disc component does not show pronounced changes, being centered around 0.19 keV. The significance of the disc component is slightly dependent on the total luminosity. Indeed it contributes almost 40-45% of the total flux when the source is in a low luminosity state and becomes less predominant when the luminosity increases ($\sim$ 25%). The luminosity of the disc is proportional to its temperature according to the relation $L_{disc} \propto T_{disc}^{3.6\pm1.4}$, although the uncertainties is high (Figure 4.12-*bottom-left*). It may be reminiscent of the standard disc relation if Ho II X-1 is hosting a IMBH accreting at sub-Eddington regime although we note again that the adopted model has some physical caveats.

The high energy component is always optically thick and cold with parameters similar to those already found for the other sources of this sample (Figure 4.12-*top-left*). The source stays predominantly in the thick state. In addition, the temperature of the high

Table 4.12: Best fitting spectral parameters of Ho II X-1 obtained with the absorbed *diskbb+comptt* model.

Ho II X-1								
No.	Date	N_H [a] (10^{21} cm^2)	kT_{disc} [b,c] (keV)	kT_{cor} [d] (keV)	τ [e]	L_X [0.3-10 keV] [f] (10^{39} erg s^{-1})	L_{disc} [0.3-10 keV] [g] (10^{39} erg s^{-1})	χ^2/dof
1	2002-04-10	$0.39^{+0.03}_{-0.03}$	$0.189^{+0.001}_{-0.001}$	$4.69^{+0.04}_{-0.04}$	$3.10^{+0.04}_{-0.04}$	21^{+1}_{-1}	$3.2^{+0.3}_{-0.3}$	576.28/629
2	2002-04-16	$0.77^{+0.04}_{-0.04}$	$0.200^{+0.004}_{-0.004}$	$2.16^{+0.03}_{-0.03}$	$6.2^{+0.1}_{-0.1}$	22^{+1}_{-1}	$7.4^{+0.3}_{0.3}$	507.21/532
3	2002-09-18	$0.75^{+0.06}_{-0.06}$	$0.167^{+0.001}_{-0.001}$	$1.00^{+0.02}_{-0.02}$	$8.4^{+0.2}_{-0.2}$	$5.7^{+0.5}_{-0.7}$	$2.5^{+0.3}_{-0.3}$	191.13/185
4	2004-04-15	$0.48^{+0.01}_{-0.01}$	$0.2031^{+0.0004}_{-0.0004}$	$2.63^{+0.01}_{-0.01}$	$4.66^{+0.02}_{-0.02}$	23^{+1}_{-1}	$5.5^{+0.1}_{-0.2}$	1326.82/1318
5	2010-03-26	$0.57^{+0.02}_{-0.02}$	$0.1999^{+0.0005}_{-0.0004}$	$1.51^{+0.01}_{-0.01}$	$7.17^{+0.07}_{-0.07}$	$8.6^{+0.2}_{-0.3}$	$3.6^{+0.2}_{-0.1}$	819.61/760

[a] Column density; [b] Inner disc temperature; [c] The seed photons temperature T_0 is assumed to be equal to T_{disc}. [d] Temperature of the corona; [e] Optical depth of the corona; [f] Unabsorbed total X-ray luminosity in the 0.3 -10 keV range; [g] Unabsorbed disc luminosity in the 0.3-10 keV range.

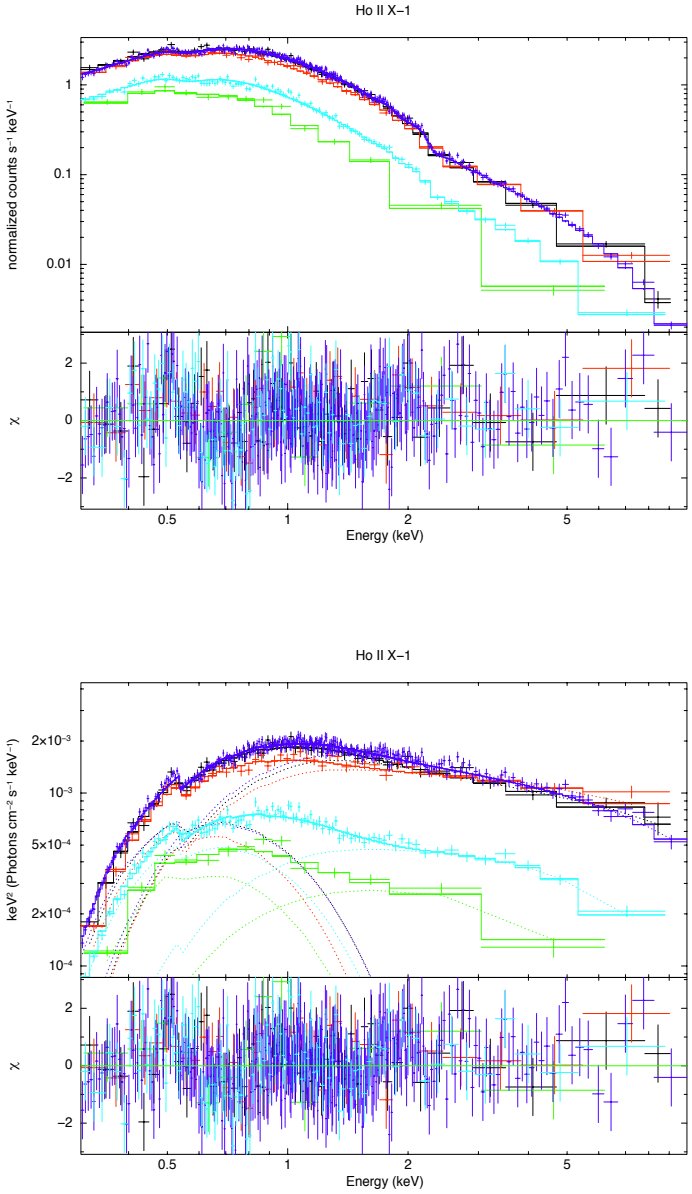

Figure 4.11: Ho II X-1: comparison of all EPIC-pn spectra of Ho II X-1 fitted with a *diskbb+comptt* model; folded (*top*) and unfolded ($E^2 f(E)$; *bottom*) spectra. For display purposes, the spectra are rebinned at 15σ.

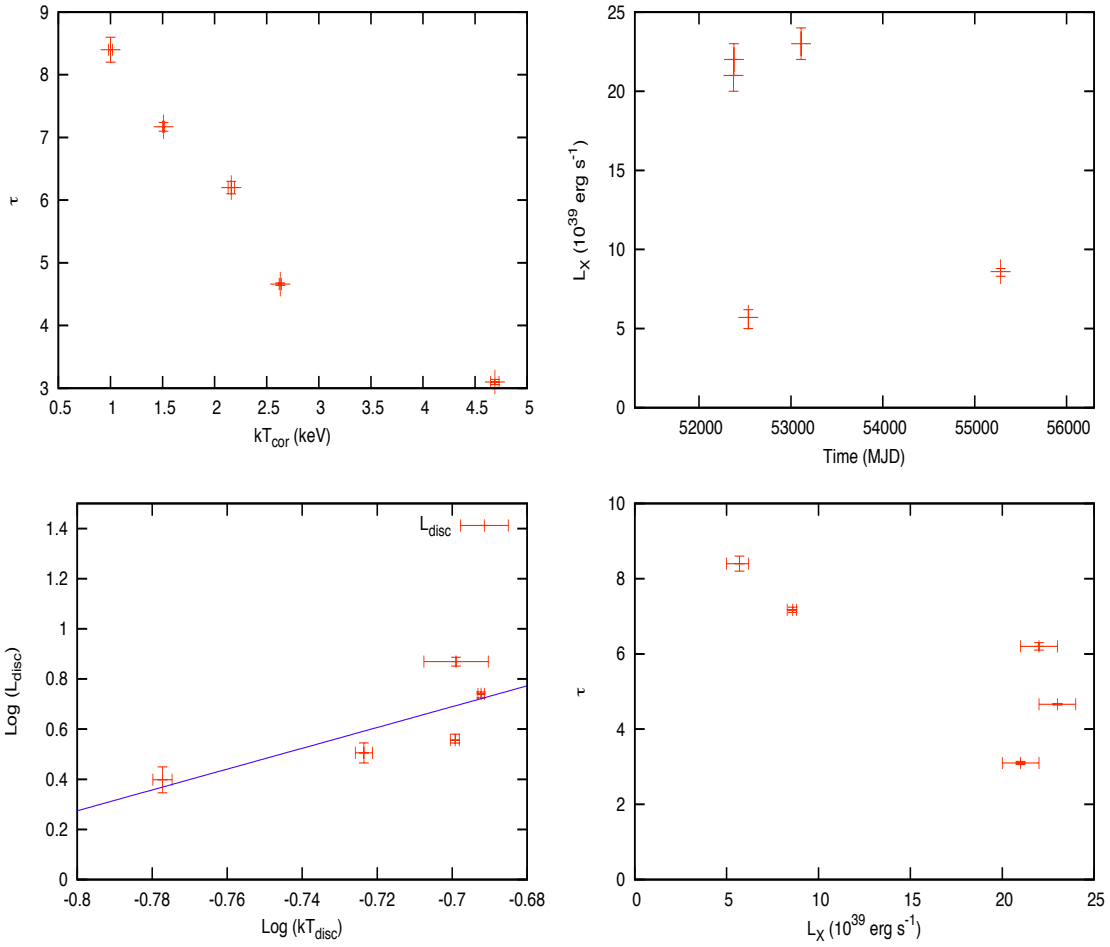

Figure 4.12: Ho II X-1: *(top-left)* optical depth τ versus temperature of the corona kT_{cor} (*diskbb+comptt* model); *top-right*: unabsorbed total luminosity in the 0.3-10 keV; *bottom-left*: unabsorbed luminosity vs temperature of the soft (disc) component in the 0.3-10 keV band; *bottom-right*: optical depth vs unabsorbed luminosity in the 0.3-10 keV band.

energy component varies with the luminosity, as found by Kajava et al. (2012). They explained this behaviour within the framework of a slim disc model with an accretion rate only slightly above the Eddington limit. However, we have also tried to fit the spectra of Ho II X-1 with the *diskpbb* model but this model is rejected in all the observations, suggesting a more complex accretion regime. Notably the optical depth seems to decrease with the total luminosity, following the same trend found in NGC 5204 X-1 (Figure 4.12-*bottom-right*). Hence, these two sources may be pretty similar since their spectral and variability properties are consistent and the different luminosities may be explained in part in terms of the different mass of the compact object.

Finally, from the O K-shell edge, we estimated an abundance of $\sim 8.8 \pm 0.1$ dex from the highest counting statistics observation (#5). This value is only marginally sub solar.

4.3.6 Holmberg IX X-1

Holmberg IX X-1 (Ho IX X-1) showed lines of evidence of a spectral curvature in 3 observations (#3, 5 and 7) out of a total of 7 *XMM-Newton* observations. In all the observations but #3, a single *comptt* model can be a good description of the data. Also the *diskpbb* model is able to fit all the spectra (except observation #3), obtaining statistically acceptable results. However, we note that the disc temperatures are unreasonably high, from $\sim$ 3.5 keV up to $\sim$ 7.5 keV. Hence we do not consider this model as a good physical description of the Ho II X-1.

As for the other sources, we adopt the *diskbb+comptt* model as reference. In Table 4.13 and Figure 4.13 we show the best fits obtained with this model. The high energy component appears always optically thick ($\sim 6.5-9$) and cold ($\sim 1.9-3$ keV, see Figure 4.14, *top-left*), and in general it represents the most important fraction of the total emission. As NGC 1313 X-2, this source populates convincingly both the thick and very thick states. Although the luminosity varies up to a factor of 3 (Figure 4.14, *top-right*), we note that the temperature

Table 4.13: Best fitting spectral parameters of Ho IX X-1 obtained with the absorbed *diskbb+comptt* model.

NGC 5204 X-1								
No.	Date	nH[a] (10^{21} cm^2)	kT_{disc}[b,c] (keV)	kT_{cor}[d] (keV)	τ[e]	L_X [0.3-10 keV] [f] (10^{39} erg s^{-1})	L_{disc} [0.3-10 keV][g] (10^{39} erg s^{-1})	χ^2/dof
1	2003-01-06	$1.26^{+0.05}_{-0.05}$	$0.240^{+0.002}_{-0.002}$	$2.75^{+0.03}_{-0.03}$	$7.2^{+0.1}_{-0.1}$	$13.8^{+1}_{-0.9}$	$2.0^{+0.2}_{-0.2}$.	685.17/706
2	2003-04-25	$1.30^{+0.05}_{-0.05}$	$0.219^{+0.002}_{-0.002}$	$2.85^{+0.03}_{-0.03}$	$6.66^{+0.08}_{-0.08}$	$15.8^{+1}_{-0.9}$	$1.3^{+0.2}_{0.1}$	749.82/817
3	2003-05-01	$1.42^{+0.02}_{-0.02}$	$0.2451^{+0.0005}_{-0.0005}$	$2.38^{+0.01}_{-0.01}$	$9.07^{+0.05}_{-0.05}$	$12.1^{+0.3}_{-0.3}$	$2.19^{+0.06}_{-0.05}$.	2182.62/2044
4	2006-11-15	$0.6^{+0.1}_{-0.1}$	$0.31^{+0.01}_{-0.01}$	$2.99^{+0.08}_{-0.07}$	$6.5^{+0.2}_{-0.2}$	22^{+2}_{-2}	$2.3^{+0.5}_{-0.5}$	159.82/195
5	2006-11-19	$1.14^{+0.04}_{-0.04}$	$0.256^{+0.003}_{-0.003}$	$1.91^{+0.01}_{-0.01}$	$8.45^{+0.08}_{-0.08}$	23^{+1}_{-2}	$1.7^{+0.2}_{-0.1}$	914.35/967
6	2006-11-25	$1.67^{+0.08}_{-0.08}$	$0.249^{+0.002}_{-0.002}$	$4.4^{+0.1}_{-0.1}$	$6.4^{+0.2}_{-0.2}$	16^{+2}_{-1}	$2.9^{0.4}_{0.3}$	340.03/350
7	2006-11-25	$1.27^{+0.04}_{-0.04}$	$0.264^{+0.002}_{-0.002}$	$1.86^{+0.01}_{-0.01}$	$8.73^{+0.07}_{-0.07}$	28^{+2}_{-1}	$2.2^{0.2}_{0.2}$	1122.68/1154

[a] Column density; [b] Inner disc temperature; [c] The seed photons temperature T_0 is assumed to be equal to T_{disc}. [d] Temperature of the corona; [e] Optical depth of the corona; [f] Unabsorbed total X-ray luminosity in the 0.3 -10 keV range; [g] Unabsorbed disc luminosity in the 0.3-10 keV range.

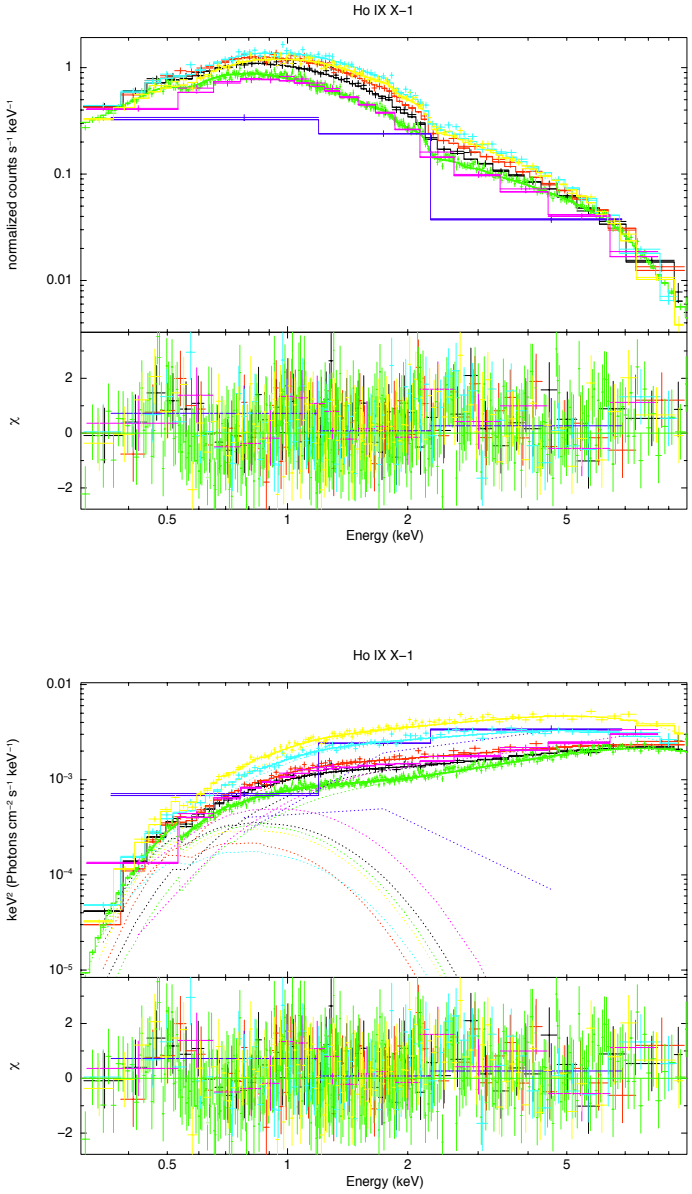

Figure 4.13: Ho IX X-1: comparison of all EPIC-pn spectra of Ho IX X-1 fitted with a *diskbb+comptt* model; folded (*top*) and unfolded ($E^2 f(E)$; *bottom*) spectra. For display purposes, the spectra are rebinned at 15σ.

and optical depth of the corona do not correlate with the luminosity (Figure 4.15 and Figure 4.14, *bottom-right*). Also the temperature of the soft component does not seem to vary markedly with the luminosity (see Figure 4.14, *bottom-left*).

Finally, we mention that the highest quality observation (#3) cannot be statistically well described by any of the adopted models (*comptt*, *diskbb+comptt* and *diskpbb* model). We note the presence of spectral features which should be further investigated.

The temporal properties of Ho IX X-1 are consistent with low variability, as already found by Heil et al. (2009). However, observation #7, in which Ho IX X-1 has the highest luminosity, shows clear evidence of a substantially higher fractional variability at high energy, supporting the hypothesis that this may be caused by two different spectral components. Such a variability may be produced by turbulences in a wind if the scale height of the wind increase with the luminosity, so that its edge may intersect our line of sight. In all the lower luminosity observations, the wind may be out of our line of sight, as proposed by Walton et al. (2012).

Finally, we estimated the chemical abundance in the local environment of Ho IX X-1, using the two highest counting statistics observations (#3, 7). It turns out to be $\sim 8.7 \pm 0.1$ dex and consistent with being sub solar.

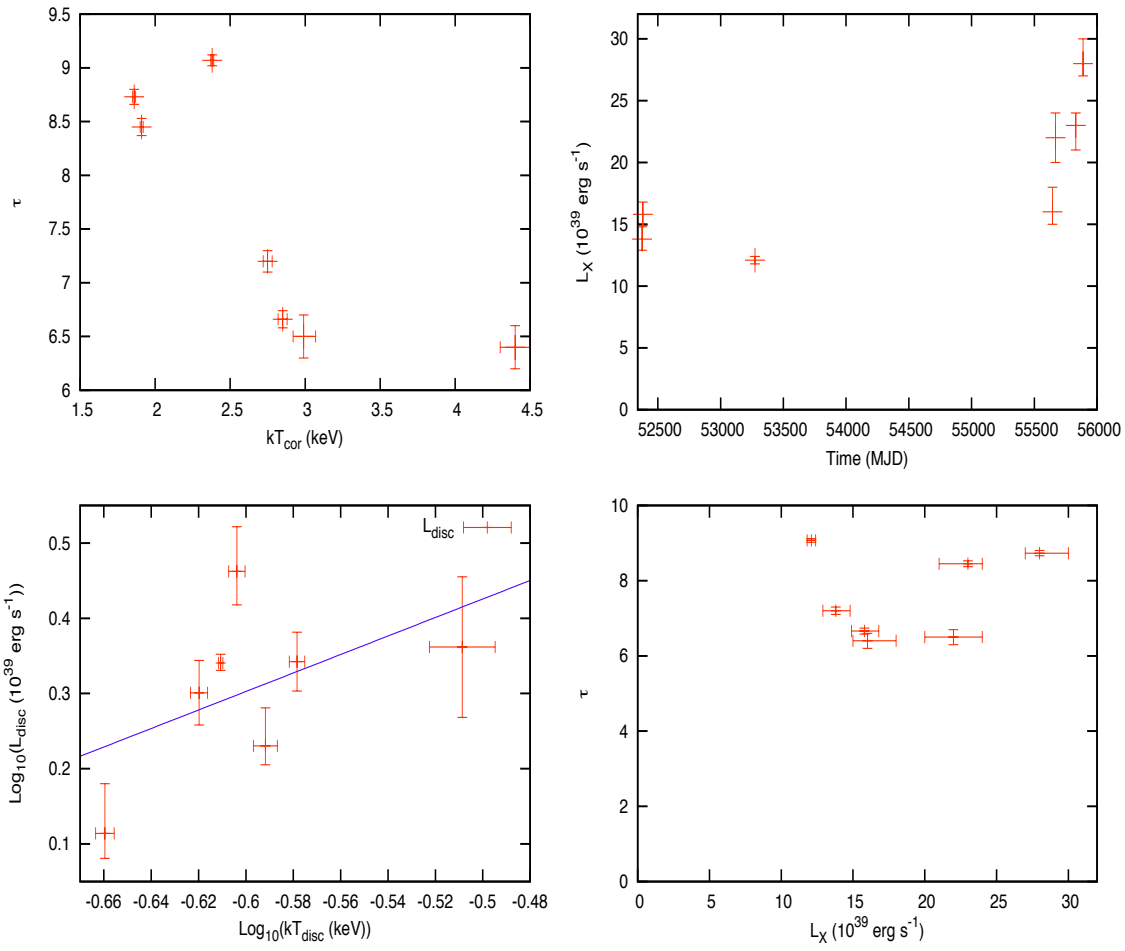

Figure 4.14: Ho IX X-1: *top-left*: optical depth τ versus temperature of the corona kT_{cor} (*diskbb+comptt* model); *top-right*: unabsorbed total luminosity in the 0.3-10 keV; *bottom-left*: unabsorbed luminosity vs temperature of the soft (disc) component in the 0.3-10 keV band; *bottom-right*: optical depth vs unabsorbed luminosity in the 0.3-10 keV band.

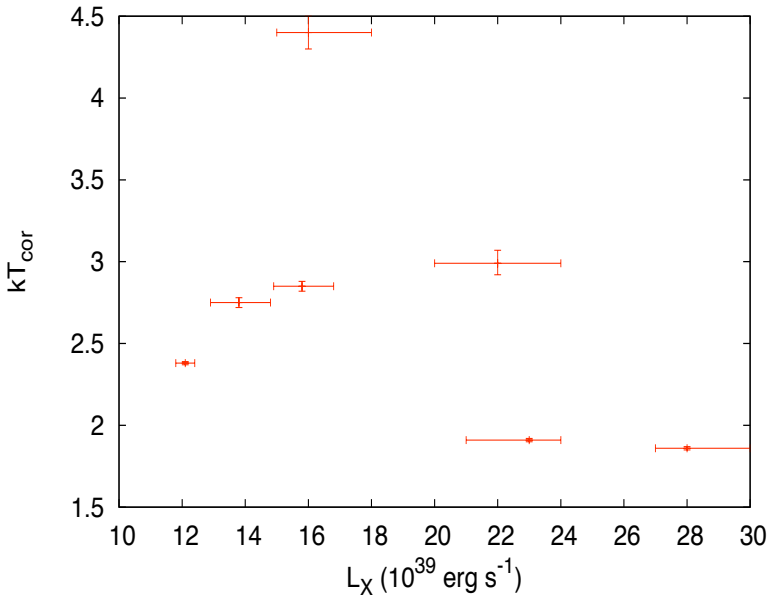

Figure 4.15: Ho IX X-1: temperature of the corona vs unabsorbed luminosity in the range 0.3-10 keV.

Table 4.14: Fractional variability of Ho IX X-1.

	0112521001		**0112521101**		**0200980101**	
Energy band	counts s^{-1}	F_{var}(per cent)[a]	counts s^{-1}	F_{var}(per cent)[a]	counts s^{-1}	F_{var}(per cent)[a]
0.3-10 keV	2.15 ± 0.02	1 ± 3	2.50 ± 0.02	5[b]	1.709 ± 0.006	2 ± 1
0.3-2 keV	1.55 ± 0.02	4 ± 2	1.78 ± 0.02	6[b]	1.185 ± 0.005	5[b]
2.0-10 keV	0.62 ± 0.01	12[b]	0.72 ± 0.01	10[b]	0.537 ± 0.004	2 ± 3
	0657801601[c]		**0657801801**		**0657802001**[c]	
Energy band	counts s^{-1}	F_{var}(per cent)[a]	counts s^{-1}	F_{var}(per cent)[a]	counts s^{-1}	F_{var}(per cent)[a]
0.3-10 keV	5.0 ± 0.1	10 ± 3	3.68 ± 0.05	8[b]	2.37 ± 0.04	9[b]
0.3-2 keV	2.6 ± 0.1	21 ± 4	2.56 ± 0.04	12[b]	1.68 ± 0.03	4 ± 3
2.0-10 keV	1.48 ± 0.07	21[b]	1.16 ± 0.03	23 ± 3	0.74 ± 0.02	15[b]
	0657802201					
Energy band	counts s^{-1}	F_{var}(per cent)[a]				
0.3-10 keV	4.77 ± 0.03	5.8 ± 0.9				
0.3-2 keV	3.25 ± 0.03	4 ± 1				
2.0-10 keV	1.56 ± 0.02	14 ± 2				

[a] Calculated from the background subtracted EPIC-pn light curves, with 200 s time bins.
[b] Upper limit at 3σ.
[c] Number of time bins lower than 20.

4.4 Colors

We have shown that almost all the spectra of the ULXs of our sample can be described by a combination of a Comptonization model and a soft component. The spectral parameters span different ranges but, if interpreted face value, indicate similar physical conditions, such as an optically thick warm corona and a cold disc. However, the counting statistics of the observations often does not allow us to find stable spectral fits because of the degeneracy of some spectral parameters. We tried to overcome this difficulty using a complementary approach based on the hardness ratios.

The method of the *hardness ratios* or *color diagrams* has been successfully adopted in the past to study the behaviour of XRBs and, more in general, of X-ray source (Maccacaro et al., 2004). Extensive monitoring of some Galactic BH binaries with *Rossi-XTE* led to the discovery of a common evolutionary path in the hardness-intensity diagram, the hysteresis cycle, that all the BH binary systems accreting at sub-Eddington rates appear to follow (see for example Remillard & McClintock 2006; Belloni 2010). This cycle describes how the X-ray spectrum changes with the source count rate. The *hardness* ratio is usually defined as $(B_2 - B_1)/(B_2 + B_1)$, in which B_1 and B_2 are the total counts in two given energy bands. This technique is very powerful for low counting statistics data and appears then particularly suitable for many observations of ULXs. In this section we will reanalyze all the observations using this approach.

Since different instruments give different *colors*, only EPIC-pn data are used and, for every observation in which EPIC-pn data are available, we selected three energy bands: $0.3-1$ keV, $1-3$ keV and $3-10$ keV, defined as Soft (S), Medium (M) and Hard (H) band, respectively. This choice is not the standard one adopted for *XMM-Newton* catalogues or surveys (e.g. the *2XMMi DR3* or the *M31 Deep XMM-Newton Survey X-Ray Source Catalog*), but it provides an adequate sampling of the spectral regions in which the soft

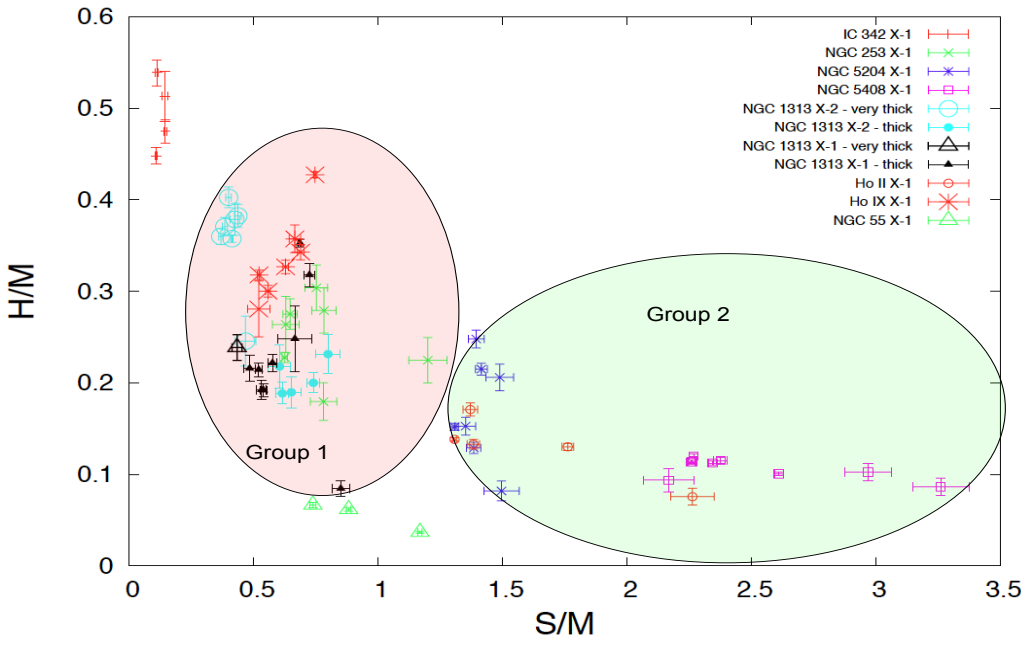

Figure 4.16: Color-color diagram (in terms of the S, H and M bands defined in the text) for the sources of our sample. Group 1 and Group 2 are marked with pink and green ellipses, respectively.

excess, spectral pivoting (see Kajava & Poutanen 2009; Pintore & Zampieri 2012) and/or the comptonizing component are usually contributing. In each energy band of interest, we added the counts of every good channel of the spectrum and subtracted the total counts of the corresponding background channels, properly scaled for the extraction areas.

Figure 4.16 shows a *color-color* diagram in which the y-axis is defined as the ratio between the counts in the hard and medium energy band (H/M) and the x-axis as the ratio between the soft and medium band (S/M). The sources are placed along a hypothetical curve starting from IC 342 X-1 and ending with NGC 5408 X-1. At least two groups of observations can be distinguished, labeled as *1* and *2* for simplicity. Group 1 is composed by the observations of NGC 1313 X-1, X-2, Holmberg IX X-1 and NGC 253 X-1 and we suggest it can be split into two sub-groups (*1a, 1b*): group *1a* contains almost all the

observations of NGC 253 X-1, Ho IX X-1 and the *very thick* state observations of NGC 1313 X-2, while group *1b* is populated by almost all the observations of NGC 1313 X-1 and those of the *thick* state of NGC 1313 X-2. Group 2 contains NGC 5204 X-1, NGC 5408 X-1 and Ho II X-1 that show similar H/M ratios (about 0.1-0.2). NGC 5204 X-1 shows variations in the ratio H/M up to a factor of 3, while S/M stays nearly constant indicating either that the high energy component is significantly variable or that the soft and medium band vary together. On the other hand, NGC 5408 X-1 shows the opposite behaviour in which the S/M ratio is modulated up to a factor of 2-3, while H/M is almost constant meaning that either the soft component has the largest changes or the medium and soft component have similar variability.

Only NGC 55 ULX1 (see the following chapter for a detailed discussion about it) and IC 342 X-1 are detached from these two groups of sources. We know that, in terms of spectral parameters, IC 342 X-1 shows similarities with the *very thick* state of NGC 1313 X-2. On the other hand, IC 342 X-1 has the largest N_H of the whole sample and hence its position on the color-color diagram is strongly affected by absorption at soft energies which distorts the hardness ratios. To test this, we chose the best *diskbb+comptt* fit of the longest observation of NGC 1313 X-2 (see previous chapter) and changed the value of N_H setting it equal to $6 \cdot 10^{21}$ cm^{-2}, consistent with the mean value of IC 342 X-1, and leaving the other parameters unchanged. Then we simulated a fake spectrum and evaluated its *colors*: as expected it fills the location occupied by the observations of IC 342 X-1, i.e. $H/S \sim 0.5$ and $S/M \sim 0.1$.

To better understand what are the effects of variations in the column density and normalization of the soft component on the position of the sources on the color-color diagram, we adopted the approach outlined below. We select two observations of NGC 1313 X-2, one in the *very thick* state (group *1b*, Obs.ID 0405090101) and one in the *thick* state (group *1b*, Obs.ID 0205230401), and one of Ho II X-1 (group *2*, Obs.ID 0200470101). We

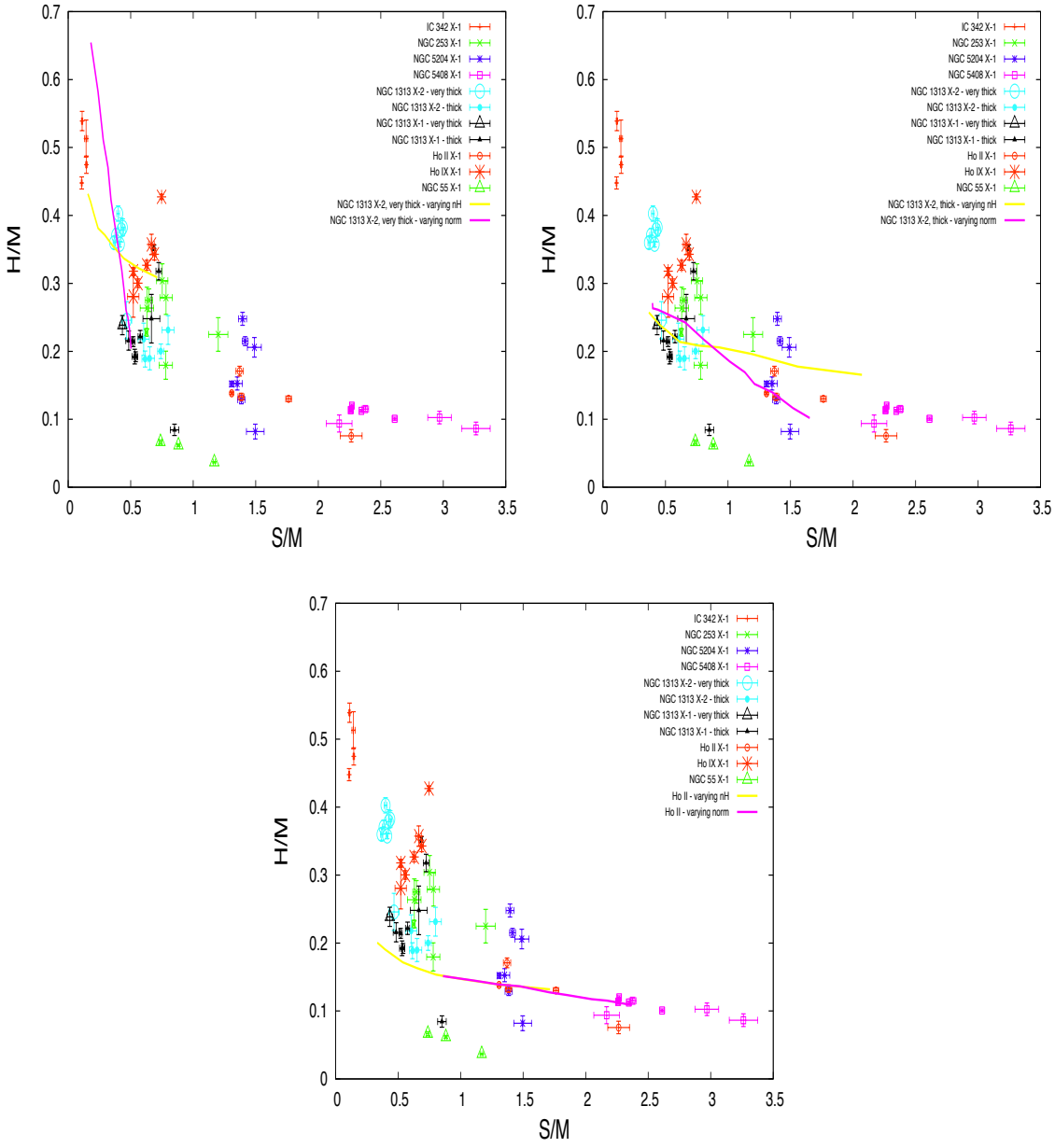

Figure 4.17: Color-color diagrams for the sources of our sample, with the tracks computed from fake spectra with varying column density and normalization of the soft component (as explained in the text). N_H decreases going from left to right while the normalization from right to left. N_H goes from 10^{20} cm^{-2} up to $6.4 \cdot 10^{21}$ cm^{-2}.

then changed the values of the column density or the normalization of the soft component and simulated a fake spectrum and finally computing its colors. We find that the main parameter driving the observed changes of position of NGC 1313 X-2 from the *very thick* to the *thick* state is likely to be the normalization of the soft component (see Figure 4.17-*top-left*), with some contribution from variations (a decrease) in N_H.

Likewise, group *1b* and group *2* can be related mostly considering variations in N_H or in the normalization of the soft component. In fact, the track of the fake spectra of NGC 1313 X-2 and that of the *thick* state of Ho II X-1 show that the groups can be directly connected, through a decrement in N_H or an increment in the normalization (Figure 4.17-*top-right,bottom*). This is consistent with the scenario proposed by Gladstone et al. (2009) in which the soft component becomes more and more significant along a certain spectral sequence which here appears to correspond to the path *1a-1b-2*. This path seems then driven mostly by changes in the importance of the soft component. Similar conclusions based on a detailed spectral analysis of a different sample of sources have been reached also by Sutton et al. (2012).

In order to better understand what part of the energy spectrum drives the observed variations in the color-color diagram, we attempted a finer sampling of the energy bands, using the intervals 0.3-0.7, 0.7-2.0, 2.0-4.0 and 4.0-10 keV (for simplicity we label them $1, 2, 3$ and 4, respectively) and we re-evaluated the hardness ratios as $(B_2 - B_1)/(B_2 + B_1)$. With this choice in the energy bands 3 and 4 the effects of N_H are essentially negligible.

Figure 4.18, shows a color-color (*top*) and a hardness-intensity (*bottom*) diagram obtained using the hardness ratios defined by the energy bands reported above. The total absorbed count rates of each source are rescaled to a distance of 1 Mpc. The color-color plot shows even more clearly the two groups of sources previously identified, characterized by values of the color $2 - 1/2 + 1$ above or below ~ 0.4.

We suggest that the ULXs follow a path on the hardness-intensity plane: low luminosity

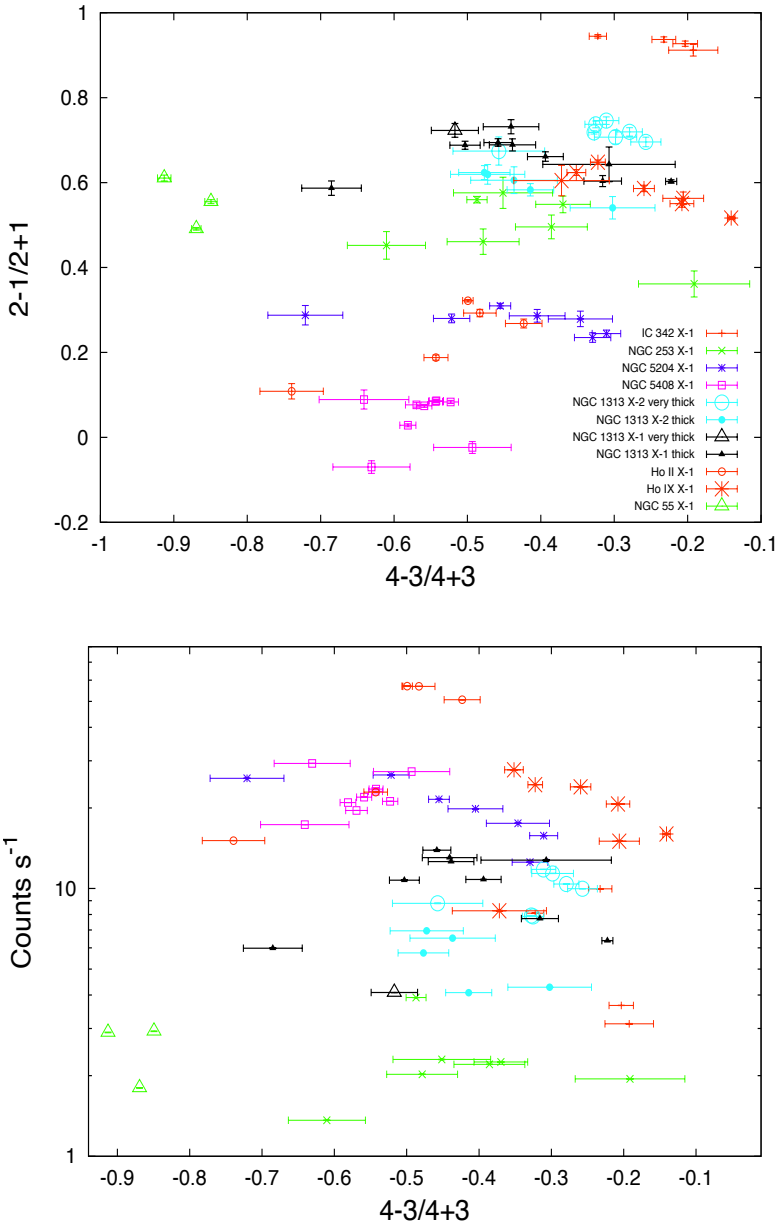

Figure 4.18: Color-color (*top*) and hardness-intensity (*bottom*) diagrams obtained using the hardness ratios defined by the energy bands 1, 2, 3 and 4 (see text).

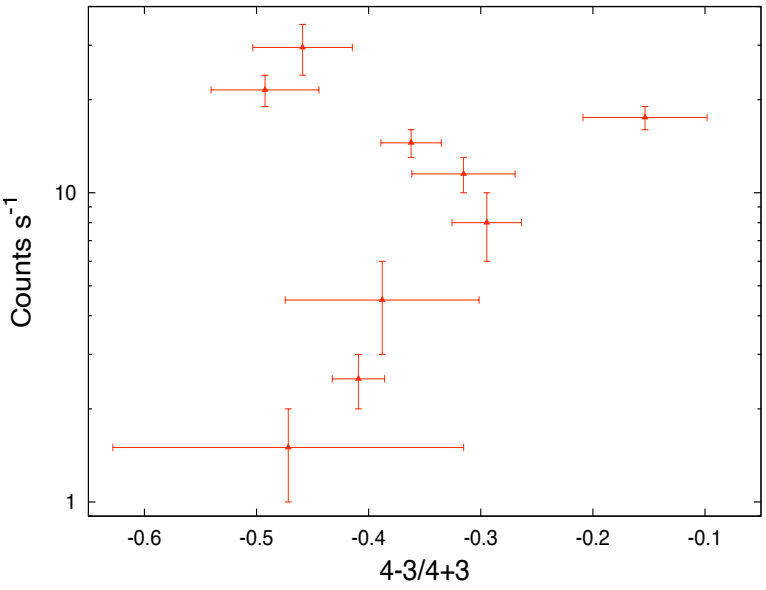

Figure 4.19: Hardness-intensity diagrams rebinned in terms of count rate to better clarify the evolutionary pattern.

sources (as NGC 253 X-1 and NGC 1313 X-2) show a tendency to harden as the count rate increases (determined by the development of a bell-shaped spectrum with a flattening below 5 keV and a pronounced curvature above this energy; see previous chapter) up to the position of the *very thick* state of NGC 1313 X-2, IC 342 X-1 and some very thick observations of Ho IX X-1. At even higher count rates, NGC 5204 X-1 and NGC 5408 X-1 show an opposite behaviour, becoming "softer" when their flux increases. To better clarify this pattern, we rebinned the observations in count rate and averaged the color of the observations in each bin. As NGC 55 ULX1 is clearly outside the region occupied by the other sources and Ho II X-1 is possibly a misplaced group 1 source, they are not included in this plot. The resulting plot is shown in Figure 4.19. The two main groups that we identified previously are still observed but, on this diagram, the situation appears clearer. A certain degeneracy is present in groups *1a* and *1b*, which is here removed.

The only sources that do not appear to conform to this picture are Ho II X-1 and NGC 55 ULX1. Ho II X-1 stays in group 2 but it shows a variability pattern reminiscent of group 1. We argue that Ho II X-1 is powered by a BH with a mass larger than that of the BHs in group 1, which implies a higher value of the luminosity at comparable accretion rates. On the other hand, NGC 55 ULX1 may be a source of group 2 but seen from a high inclination, and highy absorbed. This affects its luminosity and consequently its position on the hardness-intensity diagram.

Assuming indeed that the black hole masses are roughly similar (except possibly for Ho II X-1), the physical parameter that drives the variability along the sequence may be the accretion rate. In particular we suggest that there is a turning point after which the accretion mechanism changes and the spectral evolution turns character. From the plots, we estimate that the count rate of the turning point is ~ 10 counts s^{-1}, assuming a distance of 1 Mpc.

4.5 Discussion

We have shown that although a common spectral model can be used to describe the spectral properties of ULXs, the sources show a different spectral evolution. It is possible to describe such an evolution in terms of variations in a soft component and a hardness ratio at high energies. Changes in the soft component could be intrinsic (mostly normalization) and/or caused by variations in the column density to the source.

Because the soft component does not show the characteristic correlation between temperature and luminosity expected for a standard accretion disc, it is more likely that such a component is associated to strong and extended outflows which, at the high accretion rates expected for these sources, may set in and cover a large part of the outer regions of the disc; the expelled material expands and cools above the outer disc until it becomes neutral

and optically thin. The wind could have two different phases, an inner emitting optically thick region and an outer optically thin absorbing region (see Figure 4.20). In our scenario, the cold outer region of the wind may be responsible for the different absorption levels we observe in the sources of our sample. If the inclination angle to the source is small, our line of sight passes through the colder regions of the outflow and we should observe a higher column density with significant absorption of the soft component. On the other hand, the high energy component may be either a bare disc or a comptonized disc coupled to an optically thick corona above its inner regions (see Middleton et al. 2011).

We note that the short-term variability of these sources spans the range $\sim 5 - 20\%$ in the $0.3 - 10$ keV energy band and in most cases it seems higher at high energy. Middleton et al. (2011) proposed that the high values of variability may be due to turbulences in the wind along our line of sight if it intersects its outer edge, making the variability observed at high energy extrinsic to this component. Hence high levels of variability can be seen only when the line of sight encounters wandering blobs of optically thick matter. An intrinsic variability related to turbulences in the accretion flow itself may also be present and may explain the low level of RMS variability that is often observed and does not appear to correlate with the count rate or the spectral parameters. A combination of this two effects may be at work in the sources with high variability. In addition, if the direction of propagation of the wind is far from our line of sight we may see signatures of the optically thin phase in emission. Some evidence of this may possibly be found in NGC 5408 X-1 that seem to display improvements in the spectral fits when a plasma component is added.

In the sources of group 1, the outflow is also present but not copious enough to remove sufficient energy from the inner regions, which appear hotter when the accretion rate and the total flux increase. When the accretion rate increases further radiative forces become strong enough to blow out a larger amount of material from the disc. A fraction of internal energy in the disc is then converted in kinetic energy to power the outflow, which explains

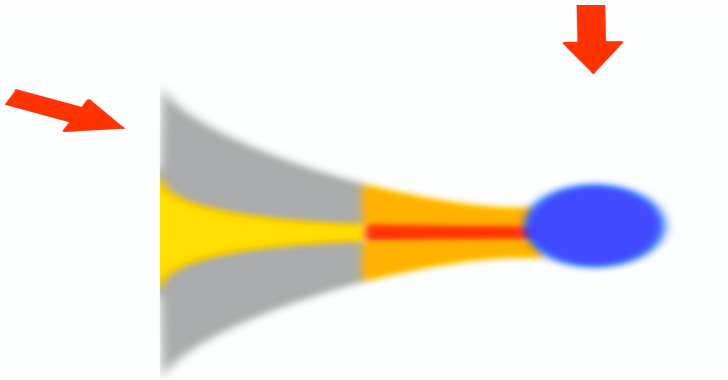

Figure 4.20: A schematic representation of the geometry of the inflow/outflow in a ULX. The yellow/red area is the accretion disc, the *gray* region is the optically thin phase of the wind while the orange area represents the region in which the wind is ejected and produces the soft emission. Finally, the blue area is the innermost region of the disc possibly coupled to an optically thick corona.

the inversion of the trend of the hardness ratio with the total count rate. We suggest that the turning point is at $\sim$ 10 count s^{-1} assuming a distance of 1 Mpc. Only NGC 1313 X-1 and possibly Ho IX X-1 and NGC 1313 X-2 seem to switch between the two accretion regimes. In addition a certain dispersion in the vertical direction in the hardness-intensity diagram may be caused by differences in the amount of absorption (inclination) and/or differences in the BH mass.

Thus, a combination of accretion rate, inclination angle and mass of the BH can explain the X-ray spectral evolution of ULXs. It is possible that most absorbed sources are seen from the largest inclination angles. We remind that the absorption component to which we refer here, is intrinsic, as the Galactic absorption in the direction of the sources has been separately taken into account. IC 342 X-1 could be the most inclined source of the sample. Instead, for NGC 1313 X-2 the inclination can be slightly smaller but the cold absorber is also along the line of sight. We can try to explain the evolutionary path from the *thick* to the *very thick* spectral state in group 1 within this scenario. As the accretion

rate increases, the wind and the corona become progressively more mass loaded and part of the disc internal energy goes into the wind, reducing the temperature of the corona. The temporal variability tends to be higher in the *very thick* state, because of either a more pronounced intrinsic activity of the corona at higher accretion rates or the increasing obscuration caused by the turbulent wind.

On the other hand, sources in group 2 show on average a smaller N_H and hence we probably see them at relatively small inclinations. This is probably caused by the small statistics of our sample more than by selection effects. In fact, in this respect, we suggest that NGC 55 ULX1 may be a group 2 source seen at a much larger inclination angle although part of the obscuration may be caused by the host galaxy, as it is placed almost edge-on.

In group 2, the soft component becomes more extended, increasing the total luminosity. In addition, when the sources are observed from low inclination angles, the scatter of the high energy photons by the funnel of the outflow makes the luminosity higher (Poutanen et al. 2007) .

NGC 1313 X-1 and possibly Ho IX X-1 seem to fill the gap between group 1 and 2. Indeed they show the same absorption level and variability of the hard component of NGC 1313 X-2.

Chapter 5

Investigating the variability of ULX1 in NGC 55

5.1 Introduction

As previously mentioned, the soft component may be the emission of a massive outflow ejected by the inner regions of the disc. Amongst the sources of our sample, NGC 55 ULX1 seems to present the most puzzling behaviour in terms of position on the hardness-intensity diagram. It may have properties which we are not observing in the other sources and thanks to its proximity we can have high quality data to investigate them. Since the source presents strong energy dependent "dips" in the lightcurve on timescales of minutes to hours which dominate the variability (see Section 2.2), we suggest that they are produced by turbulences in the outflow and the source is possibly seen from a high inclination angle. NGC 55 ULX1 is therefore an ideal candidate to explore the properties of extrinsic variability probably associated with large scale height winds from a super-critical inflow.

In this chapter we analyse how the obscuring material affects the emission along the line of sight. To obtain testable predictions for ULXs, we compare the spectral/temporal properties of NGC 55 ULX1 with those of EXO 0748-676, a well understood dipping, low

mass X-ray binary (LMXB), where material residing in the outer disc obscures our view to the inner regions (White & Swank 1982; White et al. 1995; Homan et al. 1999; Díaz Trigo et al. 2006; Cottam et al. 2002).

In the previous chapter, we showed that in poor quality data a degeneracy affects the spectral parameters, and we by-passed this issue adopting the hardness ratio analysis. It is therefore clear that, neither a spectral nor a timing analysis alone can unambiguously determine the physical nature of ULXs, however a combined approach on high quality data allows model degeneracies to be resolved. How such an approach might allow us to understand the distorting effects of extrinsic variability, inferred to be present in high luminosity/wind-dominated ULXs, is of particular importance. Contrarily to the previous chapters, here we adopted a more complex analysis to investigate both the spectral and temporal properties of NGC ULX1. Regarding the spectral analysis, we still describe the spectra using the combination of a *diskbb* and comptonizing models (*nthcomp*) but we add an ionised absorber component. In fact, if we expect that part of the central emission is absorbed by a warm and ionised optically thick medium which constitutes the wind, we should detect absorption features in the spectra. The detection of these features is difficult in poor quality data but NGC 55 ULX1 provides high counting statistics, hence allowing us to have reliable constraints on this warm component. We used the *XSTAR* model which offers an adequate description of the physical conditions of photoionised gases and their corresponding spectra, modelling the effect of a spherical gas shell surrounding the central source of ionizing radiation and evaluating how the shell absorbs and reprocesses part of this radiation. The model allows us to calculate the column density, the ionizing parameter and the redshift of the warm absorber. It is important to note that XSTAR is usually adopted for modeling of narrow absorption features

In addition, the temporal analysis can be far more complex than a simple study of the RMS variability in different energy bands. In this analysis we are helped by the high

Table 5.1: Log of the observations of EXO 0748-676 and NGC 55 ULX1.

No.	Source	Obs ID	Date	Exp[a] (ks)	Instr.[b]	Net counts
1	EXO 0748-676	0160761301	12/11/2003	62	pn	913968
2	EXO 0748-676	0212480501	27/04/2005	53	pn	12670416
1	NGC 55 ULX1	0028740201	14/11/2001	27.2	M1/M2/pn	13555, 12695, 37427
2	NGC 55 ULX1	0028740101	15/11/2001	24.5	M1/M2/pn	7455, 8210, 16355
3	NGC 55 ULX1	0655050101	24/05/2010	102	M1/M2/pn	26992, 26838, 83548

[a] GTI of EPIC-pn; [b]M1,M2= EPIC-MOS1, EPIC MOS2 camera; pn = EPIC-pn camera

counting statistics and we can perform a deep complete temporal investigation that involves time lag and covariance spectra. These particular tests cannot be done on the majority of ULXs, hence NGC 55 ULX1 is one of the best laboratory to understand the properties of super-Eddington accretion sources.

5.2 EXO 0748-676

5.2.1 X-ray spectra

As the X-ray spectrum of the first observation is well studied, we restrict our discussion to that of previous analyses. Cottam et al. (2002) investigated the presence and redshift of atomic absorption features (mainly Fe XXVI and Fe XXV) in the spectra of 28 X-ray bursts in order to constrain the NS equation of state. Unsurprisingly these features, associated with photospheric emission at the surface of the NS, were no longer observed during the steady, albeit dipping emission (Díaz Trigo et al. 2006).

The time-averaged spectrum of the 2003 observation can be well described by a hard ($\Gamma = 1.57 \pm 0.05$) power-law and a hot disc black body ($kT_{disc}\sim$1.9 keV) with strong, ionised atomic features in emission (associated to O VII and Ne IX at 0.57 keV and 0.92 keV) and absorption.

As the dips are not thought to be due to drops in the accretion rate, it is expected that

changes in the continuum should not be observed between dips and persistent spectra. Indeed when the same continuum model is applied to spectra extracted at different count rates in the dips, the main differences are due to changes in the column density of the ionised absorber (from $3.5 \cdot 10^{22}$ to $15.5 \cdot 10^{22}$ cm^{-2}) and a corresponding drop in the ionization parameter (from 2.45 ± 0.02 to 2.26 ± 0.03, see Table 7 in Díaz Trigo et al. 2006). This strongly implies that an absorbing medium, associated with the source, is obscuring the intrinsic emission during the dip phases. The implication of strong ionised absorption edges (O VIII and Ne X) and well constrained turbulent velocity broadening of these narrow features in both the dip and persistent phases, is that the source is constantly 'saturated', i.e. the line width does not change for a change in column density but increases with velocity broadening. This in turn implies that the source is constantly "dipping", a picture supported by the ionisation parameter being relatively low and the low luminosity of the source compared to others with similar orbital periods. This has led to the reasonable conclusion that the source is viewed at a high inclination angle and the obscuring medium is somewhat clumpy in nature (Díaz Trigo et al. 2006).

The X-ray spectrum of the second observation has not been studied and so we present this here for the first time. We used the EPIC-pn 0.3-10 keV energy band light curve to define the *persistent* spectrum, extracted at a count rate of 300-370 count s^{-1}, and the *dip1*, *dip2*, *dip3* and *dip4* spectra, extracted for count rates in the ranges 280-300, 250-280, 220-250 and < 220 counts s^{-1}, respectively. For consistency with the analysis of Díaz Trigo et al. (2006), we removed the eclipsing intervals of the source both from the spectral and temporal analysis and we adopted a similar approach for the spectral analysis.

Since the dips are thought to originate from obscuration by a clumpy medium, we do not expect variations in the continuum. Hence all of the spectra were fitted simultaneously, adopting an absorbed multicolor black body disc (*diskbb* in XSPEC, Mitsuda et al. 1984,) and comptonization medium (*nthcomp* in XSPEC, Zdziarski et al. 1996), leaving their

normalizations free to vary independently. The disc temperature is lower than in the previous observation ($\sim$ 0.91 keV) and the high energy component is described by a cold medium (kT_{cor} =2.8 keV) with a hard photon index of $\sim$ 1.9. However this model provides a statistically poor fit to the data ($\chi^2_\nu > 2$) and a careful inspection of the residuals shows the presence of several features in absorption and emission. In order to model them, we introduce a warm absorber (*Xstar* in XSPEC) which can vary independently between the spectra. The fit quality is now strongly improved ($\chi^2_\nu \sim 1.3$ or $\chi^2/dof = 10876.65/8395$) but some strong features are still present in the residuals: three absorption lines at 6.69 keV (possible associated to Fe XXV), 1.07 keV (possibly a Fe XXII line) and 1.45 keV (associated to Al line) and two emitting features at $\sim$ 2.2 keV (possible associated with Si XIII) and 2.82 keV (perhaps associated to S XV). Gaussian models were introduced to describe them improving the fit to $\chi^2/dof = 8789.89/8366$.

In Table 5.2 the results of the spectral fitting are shown. We found that the column density of the warm absorber seems to show a positive trend (from $0.05 \cdot 10^{22}$ to $1.5 \cdot 10^{22}$ cm^{-2}) when the count rate of the source decreases, with a slight variation of the column density of the neutral absorber. These values are lower than those obtained by Díaz Trigo et al. (2006) but we point out that the source is now more luminous and the absorption may have decreased or the absorber has become more ionised between the two observations. The comparison of the lightcurves across the two epochs appears to support this scenario; the low points of the dips may confirm it, because the bottom of the dips of the 2005 observation are consistent with the count rate of the "persistent" intervals of the 2003 observation (Figure 5.1). On the other hand, the ionization level decreases (from $\sim$ 2.5 to $\sim$ 1.5) when the count rate drops, with values consistent with those inferred by Díaz Trigo et al. (2006). The blueshift of the warm absorber may indicate an outflow from the disc. However, the shift velocities have no clear trend with the depth of the dips and most of them are consistent with a blueshift of $\sim 0.07 - 0.2$ c, which may be too high for a Galactic

Table 5.2: Best fitting spectral parameters of EXO 0748-676 obtained with an absorbed *diskbb+nthcomp* model. The error bars are evaluated at 90% confidence level.

Parameter	Component					
kT_{disc} (keV)[a]	*diskbb*			$0.91^{+0.01}_{-0.01}$		
kT_0 (keV)[b]	*Nthcomp*			$0.104^{+0.02}_{-0.02}$		
kT_{cor} (keV)[c]	*Nthcomp*			2.8^{+1}_{-1}		
Γ[d]	*Nthcomp*			$1.89^{+0.01}_{-0.01}$		
		Persistent	Dip 1	Dip 2	Dip 3	Dip 4
n_H (10^{21} cm^{-2})		$1.25^{+0.02}_{-0.02}$	$1.25^{+0.02}_{-0.02}$	$1.16^{+0.01}_{-0.02}$	$0.888^{+0.004}_{-0.02}$	$1.18^{+0.006}_{-0.02}$
n_H^{abs} (10^{21} cm^{-2})[e]	*Xstar*	$0.50^{+0.1}_{-0.1}$	$1.94^{+0.08}_{-0.2}$	$4.4^{+0.1}_{-0.4}$	$3.2^{+0.3}_{-0.3}$	$15.1^{+0.2}_{-0.1}$
$log(\xi)$ (erg cm s^{-1})[f]	*Xstar*	$1.42^{+0.06}_{-0.05}$	$2.46^{+0.02}_{-0.04}$	$2.35^{+0.01}_{-0.05}$	$1.47^{+0.06}_{-0.08}$	$2.03^{+0.07}_{-0.04}$
z[e]	*Xstar*	$-0.202^{+0.004}_{-0.003}$	$-0.075^{+0.003}_{-0.004}$	$-0.073^{+0.002}_{-0.005}$	$-0.138^{+0.004}_{-0.005}$	$-0.073^{+0.009}_{-0.004}$

[a] Column density; [a] Inner disc temperature; [b] The seed photons temperature; [c] Temperature of the electrons in the corona; [d] Photon index; [e] Column density of the warm absorber ; [f] Ionization parameter of the warm absorber; [g] Redshift of the warm absorber.

source; this will be tested in a further analysis.

Finally, the 2005 observation strongly suggests that the observed dips are mainly produced by absorption of an ionised medium which intersects our line of sight towards the central regions of the source. However, compared to the other observation, the source is now brighter, showing narrower dips and a more long lasting persistent emission. In conclusion, we note that the column density of the ionised absorber during the persistent emission is low ($\sim 5 \cdot 10^{20}$ cm^{-2}) suggesting that the source is not continuously dipping as in the previous observation.

RGS

Due to its relative proximity we have very high quality RGS spectra for EXO 0748-676, which allow us to investigate the presence and nature of features in both the dip and 'persistent' intervals at a higher energy resolution than that obtained via the EPIC CCD

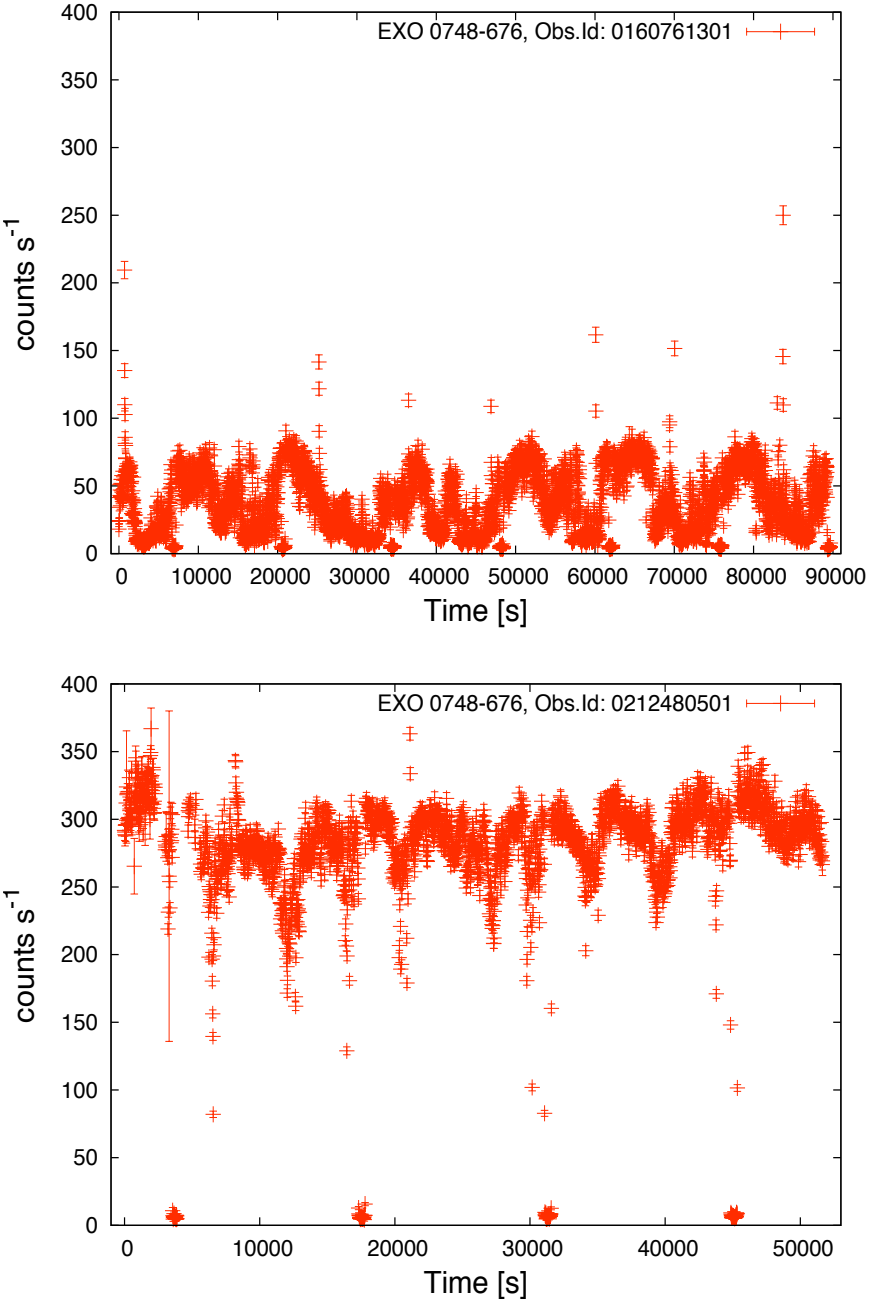

Figure 5.1: Combined EPIC-MOS and EPIC-pn background subtracted X-ray lightcurves of EXO 0748-676 of the first and second observation (*top, bottom*) sampled with time bin of 20 s. The lightcurves are obtained in the energy band 0.3-10 keV.

spectra alone.

We defined the dip intervals by selecting periods in which the total count rate was lower than 78 counts s^{-1} and $\sim$ 280 counts s^{-1} for the first and second observations, respectively. We then evaluated the spectra in the $0.3 - 2.2$ keV energy band using the line-finding algorithm of Page et al. (2003) where a line is deemed significant for $\Delta\chi^2 > 9$.

As expected, the dip spectra contain several significant features. In the first observation we find an emission line ($\Delta\chi^2$=22) at 21.8 Å ($\sim$0.57 keV) that could be associated with O VII, as seen in the CCD spectrum (although we note that this is only in the first arm as the second arm has an energy gap spanning this region) and an absorption line ($\Delta\chi^2$=10) at 11.8 Å ($\sim$1.05 keV) with a probable association with Fe XXII or Ne K edge. We note the lack of emission line at $\sim$0.92 keV, suggesting that the feature is too broad to be well resolved by the algorithm.

In the second observation, we find a slew of absorption features at 0.527 ± 0.001 keV ($\Delta\chi^2$=26, probable association with O I K_α), 0.545 ± 0.001 keV ($\Delta\chi^2$=10, probable association with O VII), 1.055 ± 0.001 keV ($\Delta\chi^2$=21, probable association with Mn XXII or Fe XXII), and 1.284 ± 0.002 keV ($\Delta\chi^2$=26, possible associated to Mg). Unlike the dip spectra, we do not find evidence for any absorption or emission features in the persistent spectra from either observation − consistent with a highly ionised absorber in the first observation and a direct line of sight to the intrinsic emission in the second or a highly ionised absorber which leaves no imprint in the spectrum, although from the spectral analysis of EPIC-pn data the latter scenario is more unlikely.

5.2.2 Power Density Spectra

We can investigate the frequency dependent variability of the emission by obtaining the power density spectrum (PDS), in units of fractional Root Mean Squared (RMS) variability. The PDS is the stochastic realisation of an underlying variability process and, for X-ray

binaries, is usually well constrained due to the high data quality yelding excellent sampling and low statistical (white) noise. If the PDS shows changes over time, then this process is deemed to be non-stationary (see Vaughan et al. 2003 for a full discussion) and indicates a change in the accretion properties. On the other hand, should variability be introduced to the PDS via extrinsic means (such as obscuration by material in the outer disc or wind) then the accretion flow may not have changed but the PDS may not be stationary. The PDS can usually be described by band limited noise approximated by a power-law shape of the form $P_\nu \propto \nu^{-\alpha}$, with alpha breaking from 0 to ~ -1 at low frequencies and ~ -1 to ~ -2 at high frequencies (e.g. Wijnands & van der Klis 1999). In addition, there are several observational effects that can distort the shape of the PDS including the effects of variability outside of the sampling range (red noise leak) and the presence of quasi-periodic oscillations (QPOs) at both low and high frequencies. We note that, although QPOs have been claimed to be present in Rossi X-ray Timing Explorer data of EXO 0748-676 in the range 0.58 - 2.44 Hz by Homan et al. (1999), this is above our highest sampled (Nyquist) frequency and will have little effect on the continuum shape.

We extract the PDS from the full lightcurves of EXO 0748-676, binned on 1 second. We model the PDS using a Bayesian maximum likelihood algorithm (Vaughan, 2010) which allows to test the presence of bends/breaks to be tested as well as providing a robust description of the power-law index.

For the first and second observations we obtain best-fitting indices of 1.22 ± 0.01 (across the 0.01 mHz $-$ 0.1 Hz bandpass with $\sim$ 42000 frequency bins) and 1.51 ± 0.02 (across the same frequency bandpass with $\sim$ 48000 frequency bins). In neither case does a model with a broken power law provide a better quality fit (as parametrised by the LRT statistic: Vaughan 2010). As we do not detect the presence of a break we cannot rule out red noise leak from frequencies below the observable bandpass.

However we note that the second observation is affected by some type 1 bursts which

can modify the power spectral density, so we remove them from the lightcurves. This produces gaps in the lightcurves that reduces the available continuum intervals. We decide to fill the gaps adding a fake count rate which is obtained by a linear interpolation between the count rate pre-gap and that post-gap (e.g. González-Martín & Vaughan, 2012). Since the gaps are narrow we can be confident that this method will not strongly affect the final PDS.

We can crudely see how the properties of the PDS are affected by the dips by excluding them from the lightcurve and obtaining the PDS for the longest continuous segment. We stress that as the frequency bandpass is smaller than that obtained from the full observation, the difference in PDS shape only provides an indication rather than a quantitative measure of the distorting effects of the dips.

For the first observation this is not strictly possible as the source is believed to be constantly dipped. However, we exclude the obvious drops in flux associated with neutral absorption and obtain a best-fitting single power-law description across the 0.2 mHz − 0.1 Hz bandpass (with $\sim$ 1060 frequency bins) with an index of 0.97±0.18. Although the index appears flatter, it is consistent with being the same as the PDS with the neutral dips (with the previously discussed caveats).

In the second observation we obtain a PDS across the 2 mHz − 0.1 Hz bandpass (with $\sim$ 300 frequency bins) with a best-fitting single power-law index of 0.75±0.30. This implies that the PDS shape is flatter but the error bars are less constrained and, although the counting statistics is low, it is consistent with the shape without dips. It can be interpreted as if the dips are still marginally affecting the persistent emission.

5.2.3 Flux dependent variability

The integrated PDS is the variance of the light curve across the frequency and energy range over which it is sampled. This variability is usually described in terms of the standard deviation (RMS or σ in the text) as a fraction of the mean count rate (F_{var}) which is a very useful measure when making a comparison across multiple objects. The RMS has been shown to scale with flux in a linear manner, ubiquitous for accretion onto compact objects (Uttley & McHardy 2001; Gleissner et al. 2004; Uttley et al. 2005; Gandhi 2009; Uttley et al. 2011; Scaringi et al. 2012). Such a relation cannot be generated by random shot noise models and instead requires the power to be a result of radially propagating flux (Lyubarskii, 1997). The most comprehensive analysis of the relations seen from BH XRBs (Heil et al., 2012) observes flat-to-positive slopes with an offset from zero intercept probably due to absorption effects. To first order, absorption should also flatten the slope of the relation (although the situation may be complicated by physical changes in ionisation and covering fraction). If the variability is dominated by absorption effects we would therefore expect a negative slope in the RMS-flux relation. In order to test for an RMS-flux relation, the PDS in each flux bin must be stationary thereby ensuring that the same process is being sampled (see Vaughan et al. 2003; Heil et al. 2012). This can be achieved by taking the ratio of the PDS between the bins of the RMS-flux relation and verifying that this is consistent with unity (via a chi-squared test).

The RMS-flux relation in XRBs or AGNs has been observed on short to long timescales (e.g. Uttley et al., 2005), meaning that it is produced by a propagating flux, explaining its ubiquitous existence in the accreting sources. Therefore, we test the RMS-flux relation choosing to sample low and high frequency ranges. The high frequency range is defined on the timescale 1s-40s while the low frequency range on the timescale 40s-1000s. In this way, we can test on what timescales the absorption component is dominating the variability.

In addition, we remove the intervals in which type I burst are observed as they introduce further variability at high fluxes.

For the first and the second observation of EXO 0748-676 we extracted EPIC-pn lightcurves across the energy ranges 0.3-2.0 keV and 2-10 keV in order to investigate the effect of absorption on the spectrum versus the hard emission which may be less affected as the absorption is energy-dependent and, for low ionization, it should be predominant in the soft band. In fact, several absorption features were found in the soft band of both observations rather than in the hard band. For each segment of the lightcurve, we determine the RMS value in the timing domain. Since its value is expected to scatter around a mean value following a gaussian distribution, we average the RMS on a number of segments which will not usually be less than 20, unless the number of total segments is small; in which case we average on at least 10 segments. We then fit these averages, using least squares, with linear trends. In Figure 5.2 we show the distribution of the RMS and flux of the first observation on the high (*left*) and low (*right*) frequency domain for the soft $0.3-2.0$ keV (*top*) and hard $2.0-10$ keV (*bottom*) bands. We note that where we expect low contribution from the absorption the RMS and flux correlate or the slope is flat. This happens in the hard energy band on both timescales. On the other hand, in the soft band we have two different slopes below and above $\sim 20-30$ count s^{-1}. In fact in the high frequency range, the RMS increases with flux (σ=0.32 $\pm$ 0.04 $\langle F\rangle$ + 0.9 $\pm$ 0.8, where $\langle F\rangle$ is the flux) and it becomes flat above the mentioned count rate. The low flux correlation slope is consistent with that of the hard band, σ=0.26 $\pm$ 0.04 $\langle F\rangle$ -1.0 $\pm$ 0.8. This may suggest that although the source in this observation is continuosly dipping, the absorption effects may be negligible on these timescales. However, at lower frequency, the RMS still correlates with the flux up to $\sim$ 25 count s^{-1} (σ=0.43 $\pm$ 0.07 $\langle F\rangle$ + 0.8 $\pm$ 0.9) but then the slope becomes negative (σ=-0.20 $\pm$ 0.03 $\langle F\rangle$ + 15 $\pm$ 1). The positive slope is still consistent with that of the hard band suggesting that we are observing the same process,

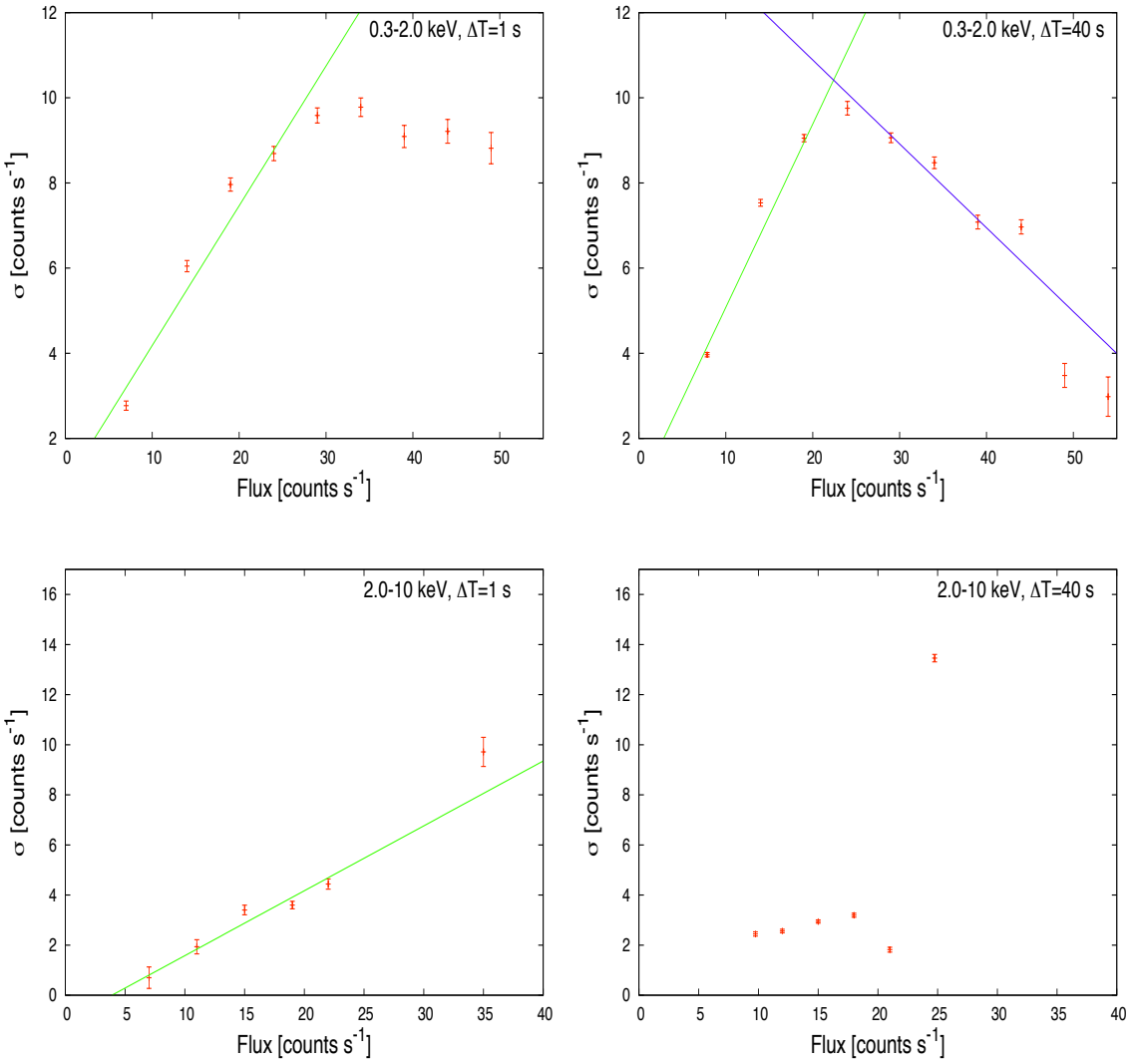

Figure 5.2: σ-flux relation sampling the EPIC-pn data on the timescales of 1s-40s (*left*) and 40s-1000s (*right*) for the first observation of EXO 0748-676 in the 0.3-2.0 keV (*top*) and 2.0-10 keV (*bottom*) energy range, respectively. The solid green and blue lines are the best fit linear relations.

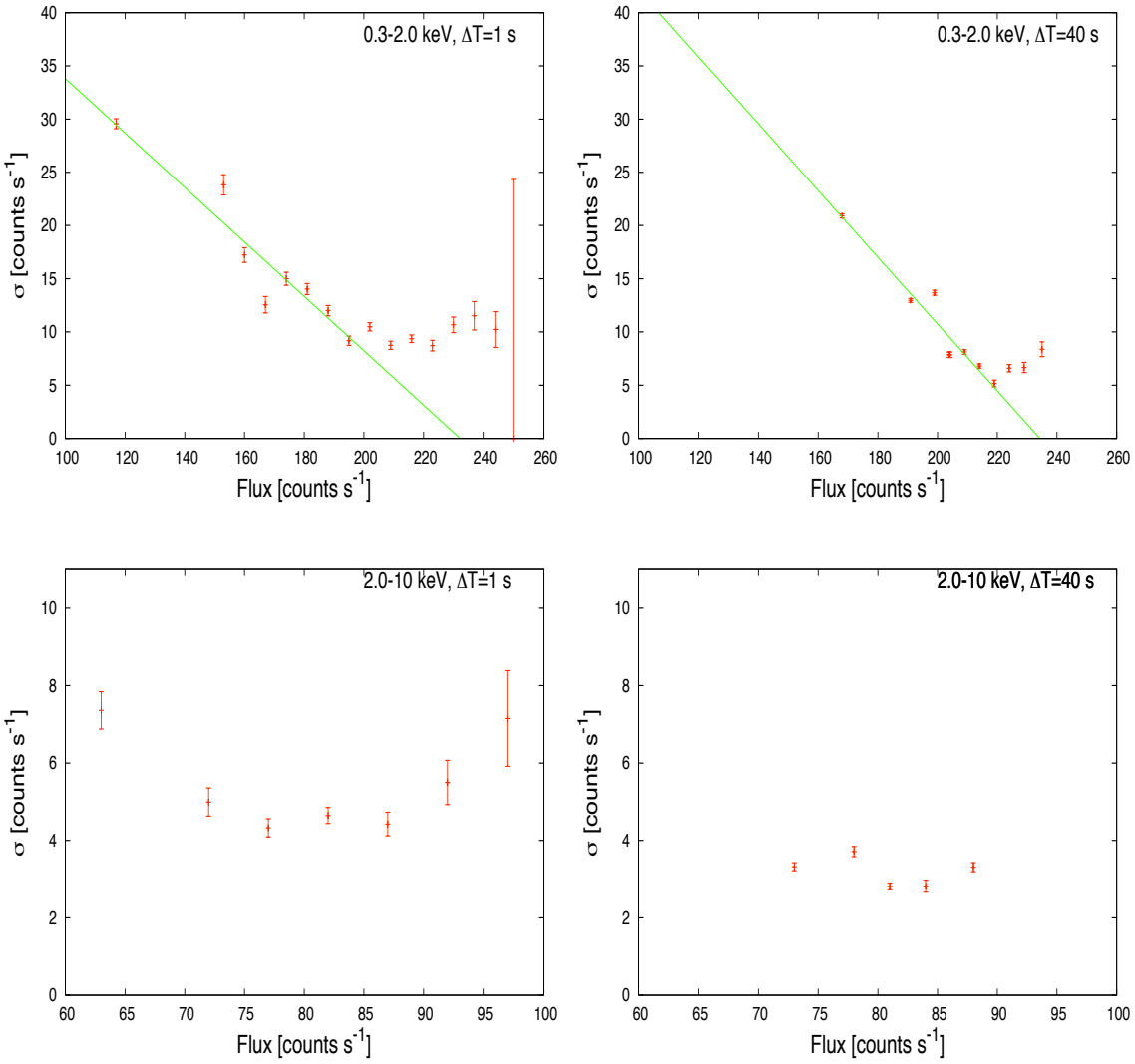

Figure 5.3: σ-flux relation sampling the EPIC-pn data on the timescales of 1s-40s (*left*) and 40s-1000s (*right*) for the second observation of EXO 0748-676 in the 0.3-2.0 keV (*top*) and 2.0-10 keV (*bottom*) energy range, respectively. The solid green line is the best fit linear relations.

i.e. the accretion flow. Therefore, since the source is continuosly dipping, we can explain the inversion of the slope in terms of a different behaviour of the ionised absorber. We propose that at low fluxes, the absorber is saturated (as found by Díaz Trigo et al. 2006) and it does not introduce additional variability since its obscuration is no longer dependent on the column density. Therefore we are only observing the intrinsic variability of the accretion flow. However, at higher fluxes, it may be unsaturated, making its variability effect on long time scales predominant on the intrinsic variability.

We tested this idea in the second observation in which we expect a more ionised or unsaturated absorber during the dips and no absorption effects during the persistent intervals. Then, we should obtain results consistent with the previous ones. In Figure 5.3, we present the distribution of the RMS and flux of the second observation in the high (*left*) and low (*right*) frequency domains for $0.3 - 2.0$ keV (*top*) and $2.0 - 10$ keV (*bottom*). As we can see, in the soft band and on both timescales, there is evidence of a linear anti-correlation below ~ 210 count s^{-1} (σ=-0.26 $\pm$ 0.02 $\langle F \rangle$ + 59 $\pm$ 4 and σ=-0.31 $\pm$ 0.03 $\langle F \rangle$ + 73 $\pm$ 7) and above this threshold the RMS is flat or with a slight indication of positive slope. The slopes are consistent with the anticorrelation found in the other observation, suggesting that the absorber shows similar properties. The result points toward the scenario of a clear line of sight to the central regions of the source at the highest fluxes and an unsaturated absorber during the lowest flux intervals. In addition, in the hard band, the RMS slope is flat as we do not expect that the absorption is highly contributing on this energy range although it may slightly change the slope of the relation.

In conclusion, we suggest that in the first observation the source is indeed continuosly dipping and the absorber is saturated except at high fluxes in which we observe the effects of an unsaturated medium on low frequency timescales. In the second observation, the source may present an unsaturated absorber during the dips phases but at high fluxes the source is no longer obscured or only marginally affected by absorption.

5.2.4 Lag and Covariance spectra

Since we found a significant contribution from an ionised absorber to the averaged spectra and a negative linear correlation between short-term RMS variability and flux, we try to find further evidence of the variability produced by an absorbing medium which obscures the central regions of the source. For this reason, we check for significant time lags between the energy ranges $0.3 - 2.0$ keV and $2.0 - 10$ keV, since in the first band we found the most important indications of absorption. The time delay (or lag) between two different energy bands is defined as the phase of their average cross correlation function. Previous studies have found out that the time lags in accreting BHs are dependent on frequency and energy (e.g. Nowak et al. 1999; McHardy et al. 2007; Zoghbi & Fabian 2011). The time lag properties of the source could be a useful tool to obtain a simple description of the obscuration mechanisms. Since the obscuring medium is closer to us and its energy supply is given by the central high energy emission, under the hypothesis that the obscuration is always present even if self-shielded/stratified, the hard emission should lead the soft energy absorption on long timescales. Hereafter, we evaluate the time lag following the standard convention in which a positive delay indicates that the hard energy band lags the soft energy band. It is important to stress that the cross correlation function must be averaged on a number of segments when handling data affected by the Poissonian noise. Indeed, the Poissonian noise adds a random component to the cross-spectrum (see Nowak et al. 1999) that could be reduced averaging on several independent measurements of the cross-spectrum. The error bars are estimated following Equation 16 in Nowak et al. (1999) which takes into account the contribution of the random noise.

We sample the lightcurves in the energy range $0.3 - 2.0$ and $2.0 - 10$ keV with different time bins of 1, 20 and 100 seconds and we investigate several frequency ranges. In none of the cases we find any robust trend of the frequency distribution of the lags. Indeed, in

both observations of EXO 0748-676, all of the points are consistent with zero delay within 3σ error bars. Actually, if the wind has a multi-phase nature, it will introduce multiple lags on the analysed timescales and this could make it harder to interpret the time lags.

Even though the time lag analysis does not offer any additional contribution, we can further investigate the variability from its energy distribution. Here we present a study of the the covariance spectra (e.g. Wilkinson & Uttley 2009; Middleton et al. 2011). This method cross-correlates narrow energy bands with a reference band which works as a filter to select the correlation. It reduces the effect of the Poisson noise, and thus reduces the error bars. Normalising the covariance for the expected variance of the reference band, we obtain a covariance spectrum in detector counts. This spectrum can be folded with a suitable binned response matrix. However, we note that the covariance spectrum is dependent on the coherence between the reference band and each energy band. In the limit of coherence equal to 1, the covariance spectrum is consistent with the RMS spectrum but with smaller error bars (e.g. Revnivtsev et al., 1999).

Using EPIC-pn data, we extract the covariance spectra of the two observations of EXO 0748-676 on the timescale $\Delta T = 20s - T_{obs}$, including dips. We choose as reference bands the energy intervals $1.0-1.6$ keV and $1.3-2.1$ keV, respectively, as they provided the most constrained RMS values. In order to avoid correlated Poisson noise, we remove from the reference bands the energy bands of interest. Furthermore we compare the RMS spectra with the covariance spectra in order to check if the reference bands are well-correlated (i.e. high coherence) with each energy band. We find that in both observations the RMS and covariance spectra are consistent within 3σ error bars.

Fig 5.4 shows the corresponding covariance spectra of the two observations in which we unfolded the continuum with a *power-law* of photon index of 0. The highest variability is found at energies of $\sim 2.0-4$ keV and $\sim 1.3-3$ keV for the first and the second observation, respectively. In particular, the variability increases with the energy but above ~ 3 or ~ 5

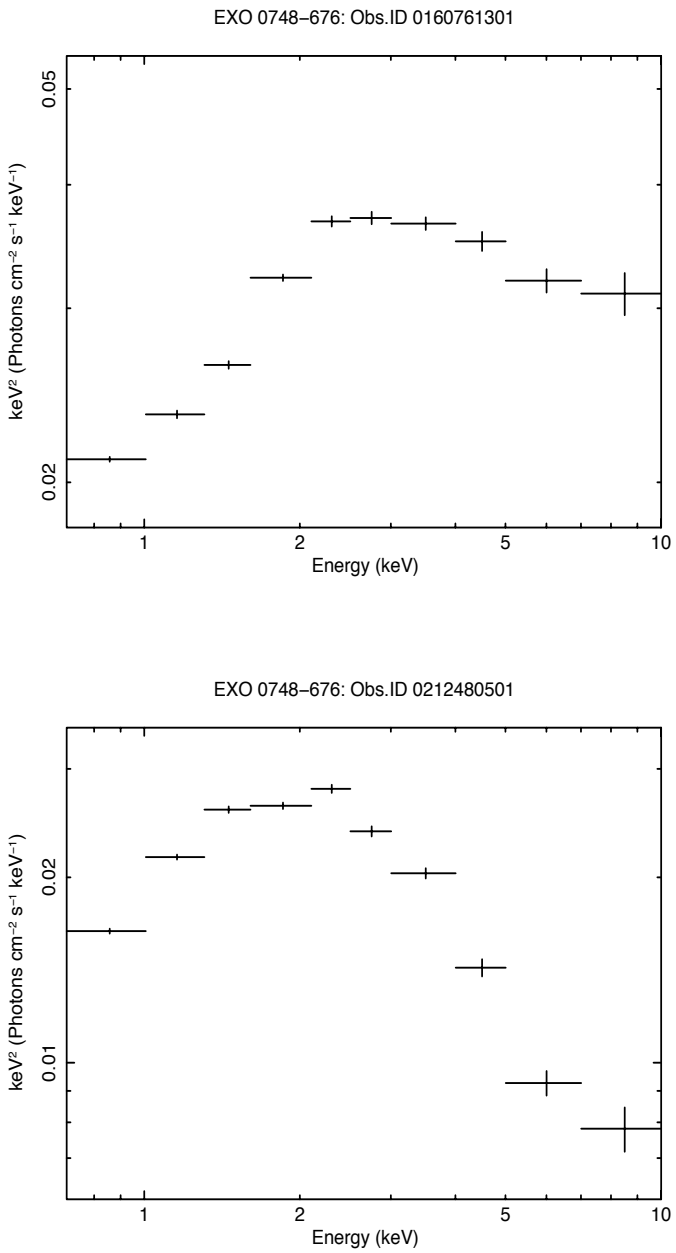

Figure 5.4: Covariance spectra of the two observations − first (*top*) and second (*bottom*) − of EXO 0748-676, unfolded with a *power-law* with photon index of 0. In both observations, the variability shows a clear peak at $\sim 2 - 3$ keV.

keV it becomes weaker, and it drops up to a factor of ~ 10 in the second observation. This clearly supports the energy dependence of the variability as found in the previous section.

5.3 Predictions for wind induced variability in ULXs

The physical nature of the obscuring material in dipping LMXBs is distinctly different to that in ULXs where the wind is predicted to originate at the sonic point of the photosphere (Dotan & Shaviv, 2011). However, we can manipulate the spectral-timing characteristics of EXO 0748-676 to accommodate a more highly ionised absorber that is probably more extended and will demonstrate some measure of self-shielding/stratification.

In the case of ULX winds we would not expect a large imprint at lower energies where the absorption opacity for moderately ionised material is low unless there is a spread of ionisation parameters (in e.g. a stratified wind). As both continuum components in ULXs are expected to be stable on observational timescales, we predict that, at energies where absorption dominates, the RMS-flux relation should be negative. At other energies there should be a flat to positive relation, although this will be of low statistical significance (as the intrinsic variability is low).

Characteristic timescales present in the lag spectra may indicate the light travel time to the absorber (as the properties of the absorbing material change upon illumination) although these may again be heavily distorted by stratification/self-shielding.

Should the variability originate from obscuration, i.e. such a high column density that there is no observed reprocessing, merely a drop in flux, then the spectrum of the variability should resemble that of the continuum component the material is blocking. Should the column be lower such that there is reprocessing, the spectrum of the variability should instead resemble the absorption features.

5.4 NGC 55 ULX1

5.4.1 X-ray Spectra

As already found by Stobbart et al. (2004), NGC 55 ULX1 shows high levels of variability on short timescales. In the first two *XMM-Newton* observations the count rate of the source undergoes decrements of a factor $\sim 3-4$ on timescale of few minutes, leading the hypothesis that such variations are produced by optically thick blobs of matter that partially and occasionally obscures the central regions of the source. The "dips" of NGC 55 ULX1 do not show a definite periodicity that could be associated to the orbital motion. However the emission is not completely obscured as the source still remains in the Ultraluminous regime. Therefore such effect could be owing to a very thick medium obscuring or absorbing only part of the central emission. However, the third *XMM-Newton* observation seems extremely intriguing because dips have disappeared and the source experiences a long period ($\sim$ 120 ks) in a low flux regime (see Figure 5.5). Under the hypothesis of a stellar mass BH accreting at super-Eddington rate, it is reasonable that the absorption is almost completely due to a turbulent wind thrown out by the accretion disc. If this hypothesis is correct, we should find imprints of the wind/obscuring medium in the spectral and temporal properties of the source in a version similar but not equal of the absorber that we already found for EXO 0748-676.

As shown in Table 5.3, the averaged spectrum of the first/second observations can be adequately fitted by an absorbed *diskbb+nthcomp* model (χ^2/dof = 897.83/839 and χ^2/dof = 705.39/689). The high energy component is cold (kT_{cor} = 0.84/0.98 keV) and optically thick (the optical depth is not a parameter of the fit but can be evaluated by the combination of the electron temperature kT_e and the photon index Γ, see equation 2.5 in Section 2.3) and the soft component is cold ($\sim$ 0.23/0.20 keV), as observed in the ULXs of our sample and other ULX sources (e.g. Miller et al. 2003; Stobbart et al. 2006; Feng

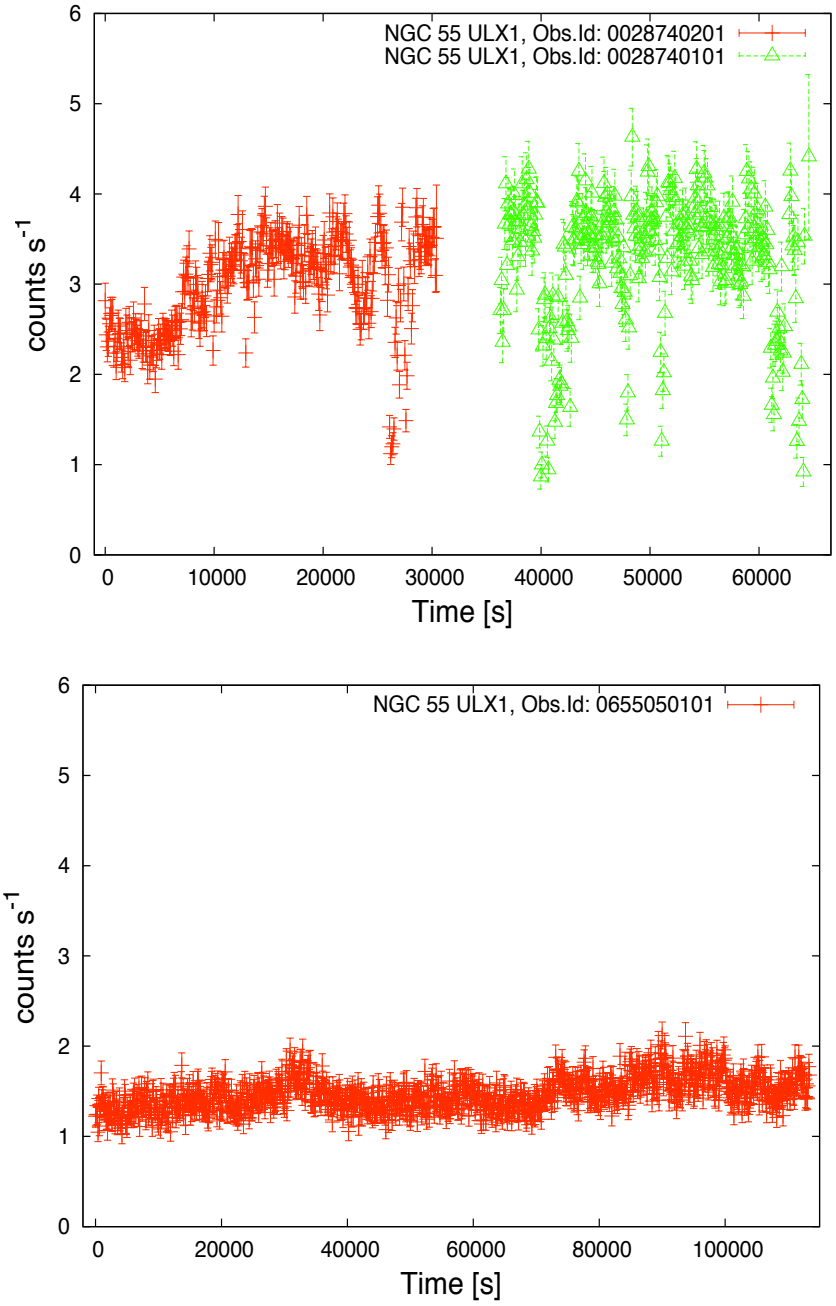

Figure 5.5: Combined EPIC-MOS and EPIC-pn background subtracted X-ray lightcurves of NGC 55 ULX1 in the first and second observations (*top*) and third observation (*bottom*), sampled with time bin of 100s. The lightcurves are evaluated in the 0.3-10 keV energy band
.

Table 5.3: Best fitting spectral parameters of NGC 55 ULX1 obtained with an absorbed *diskbb+nthcomp* model. The error bars are evaluated at 90% for each parameter of interest.

	$N_H{}^a$ (10^{21} cm^{-2})	$kT_{disc}{}^{b,c}$ (keV)	Γ^d	$kT_{cor}{}^e$ (keV)	$f_X{}^f$	$f_{soft}{}^g$	$f_{nthcomp}{}^g$	$\chi^2/d.o.f.$
Dip (Obs.Id: 0028740201)	$3.20^{+0.04}_{-0.04}$	$0.239^{+0.001}_{-0.001}$	$1.90^{+0.02}_{-0.02}$	$0.69^{+0.01}_{-0.01}$	$5.84^{+0.06}_{-0.05}$	$3.32^{+0.06}_{-0.05}$	$2.52^{+0.05}_{-0.04}$	638.87/636
Persistent (Obs.Id: 0028740201)	$3.03^{+0.04}_{-0.04}$	$0.246^{+0.002}_{-0.002}$	$2.15^{+0.02}_{-0.02}$	$0.90^{+0.02}_{-0.02}$	$7.81^{+0.07}_{-0.08}$	$2.19^{+0.08}_{-0.08}$	$5.62^{+0.08}_{-0.04}$	638.16/677
Total (Obs.Id: 0028740201)	$3.15^{+0.03}_{-0.03}$	$0.234^{+0.001}_{-0.001}$	$2.20^{+0.01}_{-0.01}$	$0.84^{+0.01}_{-0.01}$	$6.76^{+0.04}_{-0.06}$	$2.47^{+0.05}_{-0.05}$	$4.27^{+0.04}_{-0.04}$	897.83/839
Dip (Obs.Id: 0028740101)	$3.5^{+0.01}_{-0.01}$	$0.168^{+0.007}_{-0.008}$	$2.46^{+0.05}_{-0.05}$	$0.92^{+0.08}_{-0.07}$	$4.9^{+0.08}_{-0.2}$	$0.79^{+0.17}_{-0.16}$	$4.2^{+0.1}_{-0.1}$	186.34/173
Persistent (Obs.Id: 0028740101)	$3.16^{+0.05}_{-0.05}$	$0.219^{+0.003}_{-0.004}$	$2.25^{+0.02}_{-0.02}$	$1.01^{+0.03}_{-0.03}$	$6.82^{+0.07}_{-0.08}$	$0.89^{+0.7}_{-0.7}$	$5.92^{+0.07}_{-0.07}$	694.65/644
Total (Obs.Id: 0028740101)	$3.48^{+0.04}_{-0.04}$	$0.193^{+0.002}_{-0.002}$	$2.23^{+0.002}_{-0.02}$	$0.98^{+0.03}_{-0.03}$	$6.71^{+0.06}_{-0.06}$	$1.25^{+0.07}_{-0.07}$	$5.46^{+0.06}_{-0.06}$	705.39/689
Total (Obs.Id: 0655050101)	$4.26^{+0.02}_{-0.02}$	$0.186^{+0.0003}_{-0.0003}$	$2.23^{+0.01}_{-0.01}$	$0.590^{+0.006}_{-0.006}$	$6.30^{+0.02}_{-0.02}$	$3.81^{+0.03}_{-0.02}$	$2.47^{+0.02}_{-0.02}$	280.42/253
	Xstar							
	$N_{H}{}^i_{abs}$	$13.1^{+0.6}_{-0.6}$						
	ξ^l	$3.33^{+0.01}_{-0.01}$						
	z^m	$0.250^{+0.01}_{-0.01}$						

[a] Column density; [b] Inner disc temperature; [c] The seed photons temperature T_{bb} is assumed to be equal to T_{disc} ; [d] Photon index; [e] Temperature of the electron in the corona; [f] Unabsorbed total x-ray flux in the 0.3 -10 keV range in unity of 10^{-12} erg s^{-1} cm^{-2}; [g] Unabsorbed flux emitted by the soft component in the 0.3-10 keV range in unity of 10^{-12} erg s^{-1} cm^{-2}; [h] Unabsorbed flux emitted by the high energy component in the 0.3-10 keV range in unity of 10^{-12} erg s^{-1} cm^{-2}; [i] Column density of the warm absorber in unity of 10^{22} cm^{-2} ; [l] Ionization parameter of the warm absorber; [m] Redshift of the warm absorber.

& Kaaret 2006, 2009; Gladstone et al. 2009; Vierdayanti et al. 2010; Pintore & Zampieri 2011, Middleton et al. 2011b). From the residuals, in the first observation only, an excess in emission is observed at 1 keV with a probable association to Fe XXI. We note that adding a *gaussian* component to the best fit model gives an improvement of $\Delta\chi^2$=42.16 for 3 d.o.f., in which the energy of the line is 1.00 ($\pm$0.02) keV with an equivalent width (EW) of 0.014 keV.

On the other hand, the third observation cannot be fitted using this model (Figure 5.6, *bottom*) but a more careful analysis allows us to find indications of some features. In order to model the features in absorption, we add an ionised absorber (*XSTAR*). The best fit parameters are reported in Table 5.3. However, three emission features are still present in the spectrum at $\sim 0.91 \pm 0.01$ (possibly associated to Ne IX), $\sim 2.01 \pm 0.04$ (possibly associated to Si XIV) and $\sim 4.21 \pm 0.06$ keV (which nature is still unclear). We describe them adopting a gaussian component which results in a marginal detection.

From a direct comparison between the results of the three observations, the spectral properties of the source seem to change with time. First of all, the (absorbed) luminosity has changed almost by a factor of 3, suggesting or a significant drop in the accretion rate or an increment of the absorption between us and the central region of the source. In particular, the longest observation is modeled by an optically thick corona with a lower temperature than in the first and second observations. Notably, the temperature of the disc component does not display a strong variation but the soft emission becomes more important when the total luminosity decreases ($\sim$ 70% of the total luminosity in the longest observation). If the soft component is due to the wind emission, this could be an indication of an increase of its size during time, with a subsequent increment of the absorption. In addition, during the longest observation the low flux may be explained or in terms of an important absorbing medium, or of an intrinsic drop of the accretion rate.

In the light of this results, we follow a similar analysis to that adopted for EXO 0748-

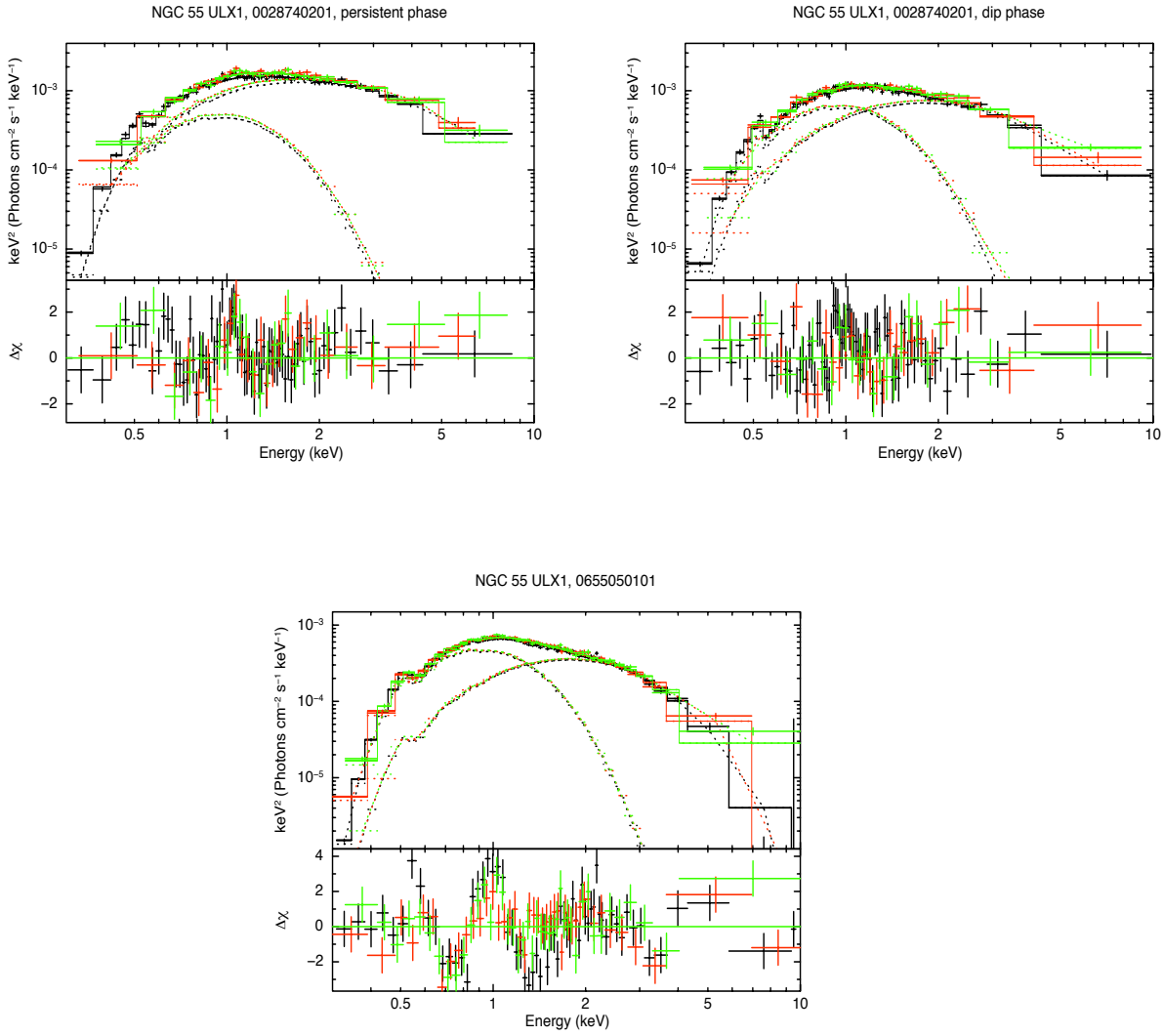

Figure 5.6: (*top-left, top-right*): unfolded EPIC-pn(black) and EPIC-MOS (*red* and *green*) spectra from the first observation (in the *persistent* and *dip* phase) and the third observation (*bottom*) of NGC 55 ULX1; all of the spectra were analyzed in the 0.3-10 keV and were rebinned for display purpose only.

676, studying the spectral properties during the "obscured" intervals. Since for ULX1 we do not have enough statistics to select several intervals of count rate, we select only one dip spectrum. The spectrum is obtained by the averaged temporal intervals in which the count rate of the combined EPIC-pn+EPIC-MOS lightcurve is lower than 3 counts s^{-1} (we used this criterion hereafter). As shown in Tabel 5.3, the *diskbb+nthcomp* model well describes the data – χ^2/dof= 638.87/636 and χ^2/dof= 186.34/173 for the dip (Figure 5.6, *top-right*) and χ^2/dof= 638.16/677 and χ^2/dof= 694.65/644 for the persistent (Figure 5.6, *top-left*) intervals of the first and second observations, respectively – with a cold disc component and an optically thick comptonizing medium. More interestingly the temperature of the corona in the dip phase is lower than in the persistent one (0.69/0.92 keV against 0.90/1.01 keV in the first and second observation, respectively), indicating a thicker medium in the former state. A strong emission line is again found at 1.04 (±0.03) keV in the persistent spectrum of the first observation and it could be associated to Ne X or Fe XX, with an improvement of $\Delta\chi^2$=25.29 for 3 d.o.f. and an EW of 0.017 keV. In the dip spectrum of the same observation there is just marginal evidence of this additional emission feature ($\Delta\chi^2$=12.99 for 3 additional d.o.f., EW= 0.011 keV). Also in this case the temperature of the soft component does not dramatically change, but in the dip spectrum it represents a big fraction of the total emission (e.g. $\sim$ 60% in the first observation). It is important to mention that the neutral column density is higher at low luminosity. Therefore, the spectral results give us strong indications that an optically thick medium is intersecting our line of sight and that its physical properties are changing during time.

RGS

In the previous section we found evidence of absorption features in the spectra of NGC 55 ULX1. Therefore we tentatively try to analyse the RGS spectra of the two observations in order to take advantage of the high spectral resolution of this instrument. In the first

and second observation, the source was outside the field of view and no information can be obtained for its high flux state. On the other hand, in the third observation the source was too faint to find evidence of any features in the RGS spectra adopting the line-finding algorithm of Page et al. (2003).

5.4.2 Flux dependent variability

The previous finding seems to slightly suggest that ULX1 could be affected by periods of obscurations, so we may compare its temporal properties with those obtained for EXO 0748-676, in particular the negative dependence of RMS and flux. Similarly to the analysis of EXO 0748-676, we study the RMS-flux relations on two timescales.

For the third observation of NGC 55 ULX1, we create 12 averaged EPIC-pn and EPIC-MOS spectra on intervals of 10 ks. The spectra associated to every interval are subsequently fitted simultaneously using an absorbed *diskbb+nthcomp* model. For each spectra we estimate the absorbed flux in the 0.3-10 keV band and we find that it spans an interval of values between $1.27{\cdot}10^{-12}$ erg s^{-1} cm^{-2} and $1.65{\cdot}10^{-12}$ erg s^{-1} cm^{-2}. The intervals are then grouped in terms of flux in three bins in order to have a total of 40 ks in every bin and the RMS variability is calculated from the lightcurves associated to these periods. In Figure 5.7, we present the RMS-flux relation in the $0.3-10$ keV range of the three bins, fitting the points with a linear model. We selected two different timescales: 20s-400s and 400s-T_{obs}. In the first timescale, we can obtain hints of a positive linear correlation ($\sigma = 0.17{\pm}0.03\,\langle F\rangle{+}0.3{\pm}0.3$). Interestingly, the relation is also seen in the other frequency range ($\sigma = 0.6 \pm 0.1\,\langle F\rangle + 0.5 \pm 0.1$). Although the statistics is limited and the number of bins is small, this result may suggest we are observing or the effects of the accretion flow or a strong saturated absorption component which does not introduce additional variability to the intrinsic one.

We check for a similar relation in the soft and hard bands, i.e. the energy bands $0.3-2.0$

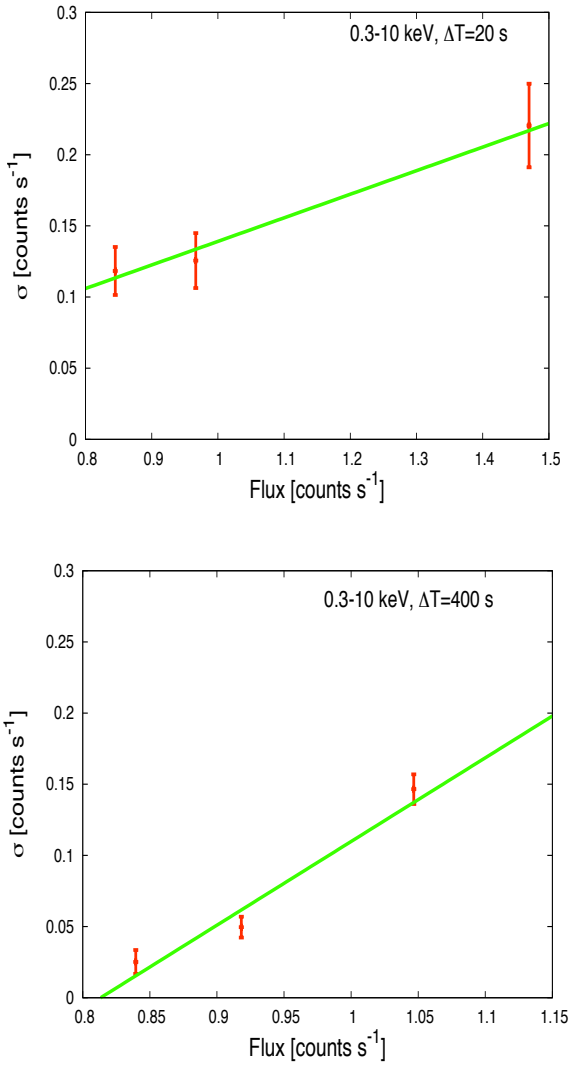

Figure 5.7: σ-flux relation sampling the third NGC 55 ULX1 observation using EPIC-pn data on timescales 20s-400s (*top*), and 400s-T_{obs} (*bottom*) in the energy range $0.3-10$ keV; best fit correlation (*green*): $\sigma = 0.17 \pm 0.03 \langle F \rangle + 0.3 \pm 0.3$ and $\sigma = 0.6 \pm 0.1 \langle F \rangle + 0.5 \pm 0.1$ (see text).

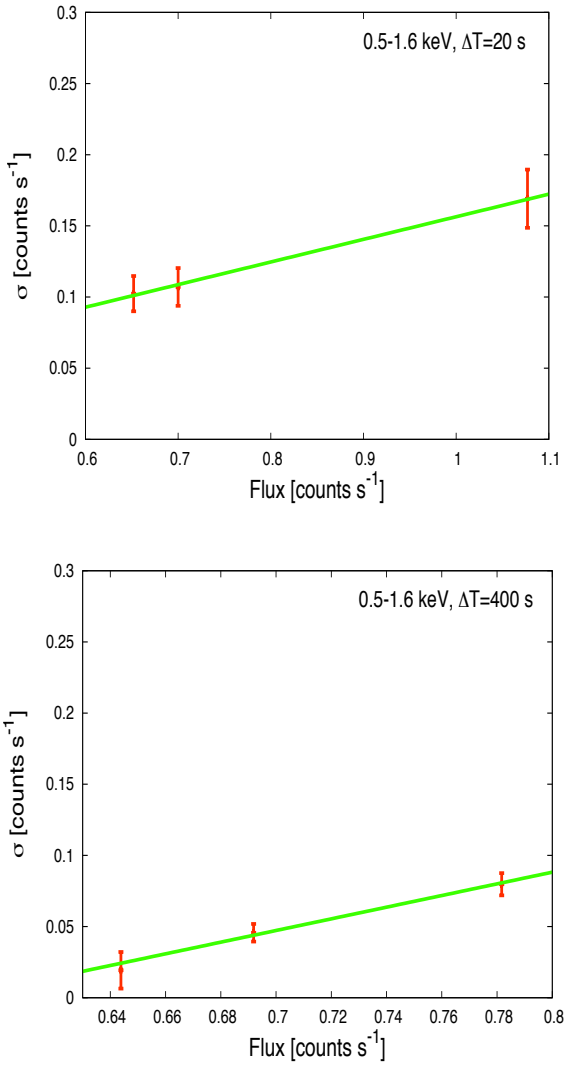

Figure 5.8: σ-flux relation sampling the third NGC 55 ULX1 observation using EPIC-pn data on timescales 20s-400s (*top*) and 400s-T_{obs} (*bottom*) in the energy range $0.5-1.6$ keV; best fit correlation (*green*): $\sigma = 0.159 \pm 0.009 \langle F \rangle + 0.002 \pm 0.007$ and $\sigma = 0.41 \pm 0.04 \langle F \rangle + 0.24 \pm 0.03$ (see text).

and $2.0 - 10$ keV, but also in inter-bands of the $0.3 - 2.0$ keV range. We find evidence of a linear relation in the $0.3 - 2.0$ keV; however the most constrained linear RMS-flux relation is obtained in the range $0.5 - 1.6$ keV in which we found the main absorption features in the time averaged spectrum. In this energy range, on the two timescales, we have the following positive linear relations: $\sigma = 0.159 \pm 0.009 \langle F \rangle + 0.002 \pm 0.007$ and $\sigma = 0.41 \pm 0.04 \langle F \rangle + 0.24 \pm 0.03$ for 20s-400s and 400s-T_{obs}, respectively (Figure 5.8) and this further confirms the aforementioned scenario. On the other hand, in the $2 - 10$ or $1.6 - 10$ keV energy bands, because of the limited statistics, we obtain only upper limits and no well-defined slope can be claimed. We note that co-adding the EPIC-pn and EPIC-MOS data may improve the signal-to-noise ratio but in this particular case the results are still consistent with the previous ones.

For the remaining observations of NGC 55 ULX1 in which the variation of the count rate is wider, a slightly different and easier approach is adopted: we evaluate the fractional RMS variability of a number of continuos segments of fixed length of the lightcurves in the energy band of interest. The RMS points are randomly scattered by the stochastic nature of the lightcurves around a mean value (see e.g. Van der Klis, 1989), therefore in order to remove this effect, the continuous segments are grouped in terms of mean count rate. In the first observation, we study the energy range $0.3 - 10$ and $1 - 10$ keV in which there is the highest counting statistics, and on timescales of 20s-400s and 100s-T_{obs}. In Figure 5.9 the RMS-flux relation in the $0.3 - 10$ keV band in the two timescales is shown. In this energy range, we find indication of a linear anticorrelation on the timescale 20s-400s ($\sigma = 0.27 \pm 0.05 \langle F \rangle + 1.1 \pm 0.1$) and only marginally on the other timescale ($\sigma = -0.18 \pm 0.09 \langle F \rangle + 0.8 \pm 0.2$). We propose that such an anticorrelation is the effect of an obscuring and unsaturated absorber which dominates the variability, as observed in EXO 0748-676. This absorber shows its effects only on short timescales as for long timescales its variability is diluted by the variability of the accretion flow.

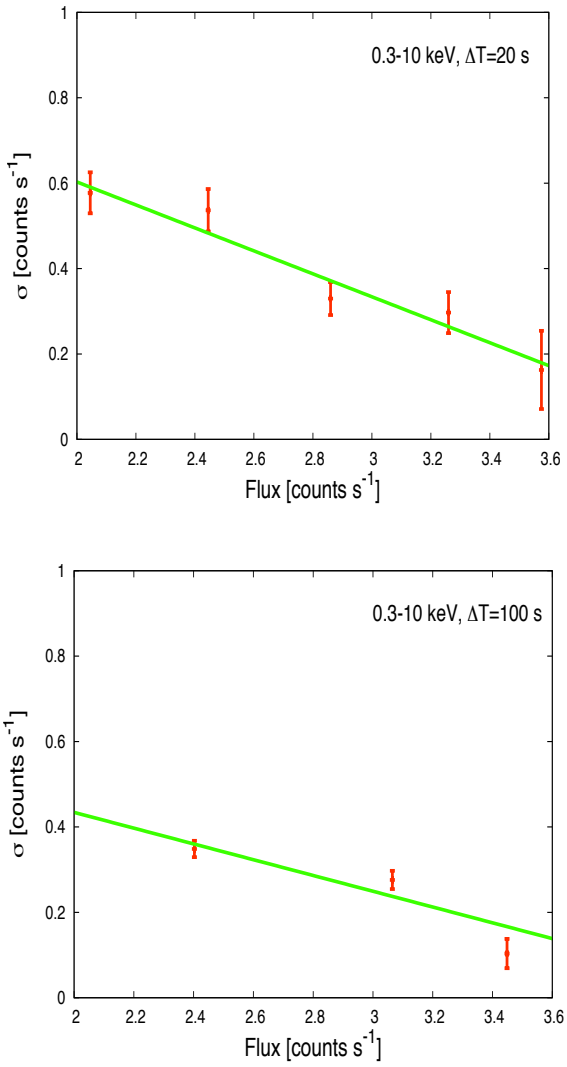

Figure 5.9: σ-flux relation sampling the first NGC 55 ULX1 observation using EPIC-pn data on timescales 20s-400s (*top*) and 100s-T_{obs} (*bottom*) in the energy range $0.3-10$ keV; best fit correlation (*green*): $\sigma = 0.27\pm0.05\,\langle F\rangle + 1.1\pm0.1$ and $\sigma = -0.18\pm0.09\,\langle F\rangle + 0.8\pm0.2$ (see text).

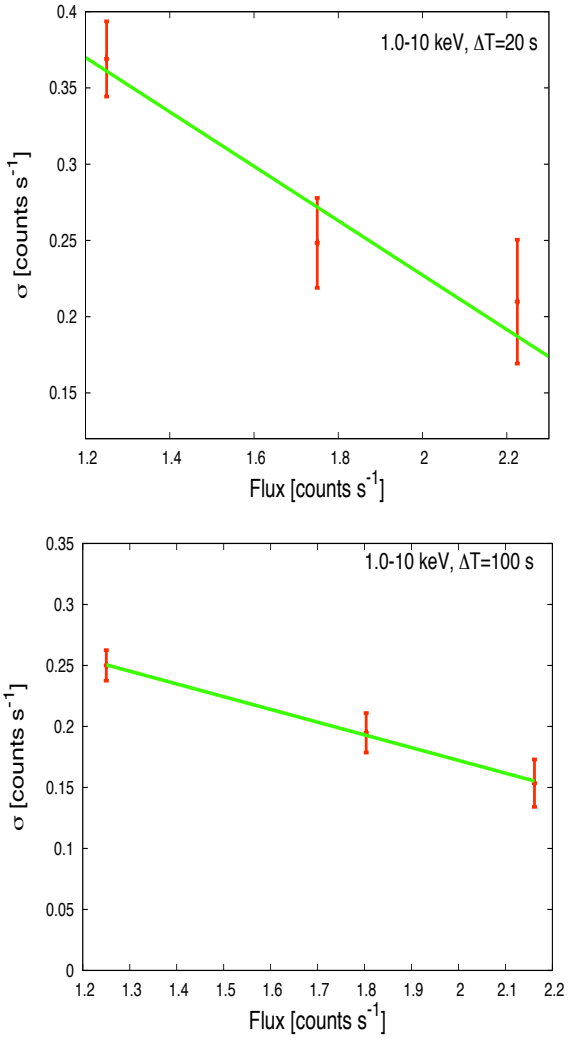

Figure 5.10: σ-flux relation sampling the first NGC 55 ULX1 observation using EPIC-pn data on timescales 20s-400s (*top*), and 100s-T_{obs} (*bottom*) in the energy range $1.0-10$ keV; best fit correlation (*green*) of the short and long timescales are $\sigma = -0.18 \pm 0.05 \langle F \rangle + 0.58 \pm 0.08$ and $\sigma = -0.104 \pm 0.004 \langle F \rangle + 0.381 \pm 0.006$, respectively (see text).

Since from Stobbart et al. (2004) we know that the dips are energy dependent, we expect to find more pieces of evidence of the anticorrelation in the high energy band as the absorber may be less ionised and saturated than in the soft energy band. In Figure 5.10 the RMS-flux relation in the $1.0 - 10$ keV band in the two timescales is shown. We note that for short timescales (20s-400s) and long timescales (100s-T_{obs}) the anticorrelation is observed ($\sigma = -0.18 \pm 0.05 \langle F \rangle + 0.58 \pm 0.08$ and $\sigma = -0.104 \pm 0.004 \langle F \rangle + 0.381 \pm 0.006$).

On the other hand, in the second observation we find only marginal evidence of anticorrelation in the $1 - 10$ keV energy band. Possibly the statistics is affected by the position of the source in the EPIC-pn CCD gap. It is important to notice that we checked the stationarity in each bin of the RMS-flux relations mentioned above, and the stationarity was achieved for all the analysed bins. The PDS shapes, on the same timescales of the RMS points, do not change within 3σ error bars in any of the observations, further supporting the reliability of these results.

Therefore, our findings seem to suggest that in the first two observations the variability is mainly driven by the absorption of a unsaturated medium while in the third observation the source could have experienced either a real drop of the accretion rate or an increment of the obscuration. In the second case, the obscuring medium may highly cover the source and it may be saturated: in such a condition no further variability is introduced by the absorber as it is no longer depending on the column density.

5.4.3 Lag and Covariance spectra

We study the time lags of NGC 55 ULX1 in order to make a connection with the previous RMS-flux relations and understand if they can be associated to the aforementioned obscuring medium.

Here, we compare the time lag properties of all of the observations between the $0.3 - 2.0$ and $2 - 10$ keV energy bands, computing the time delays on EPIC-pn data.

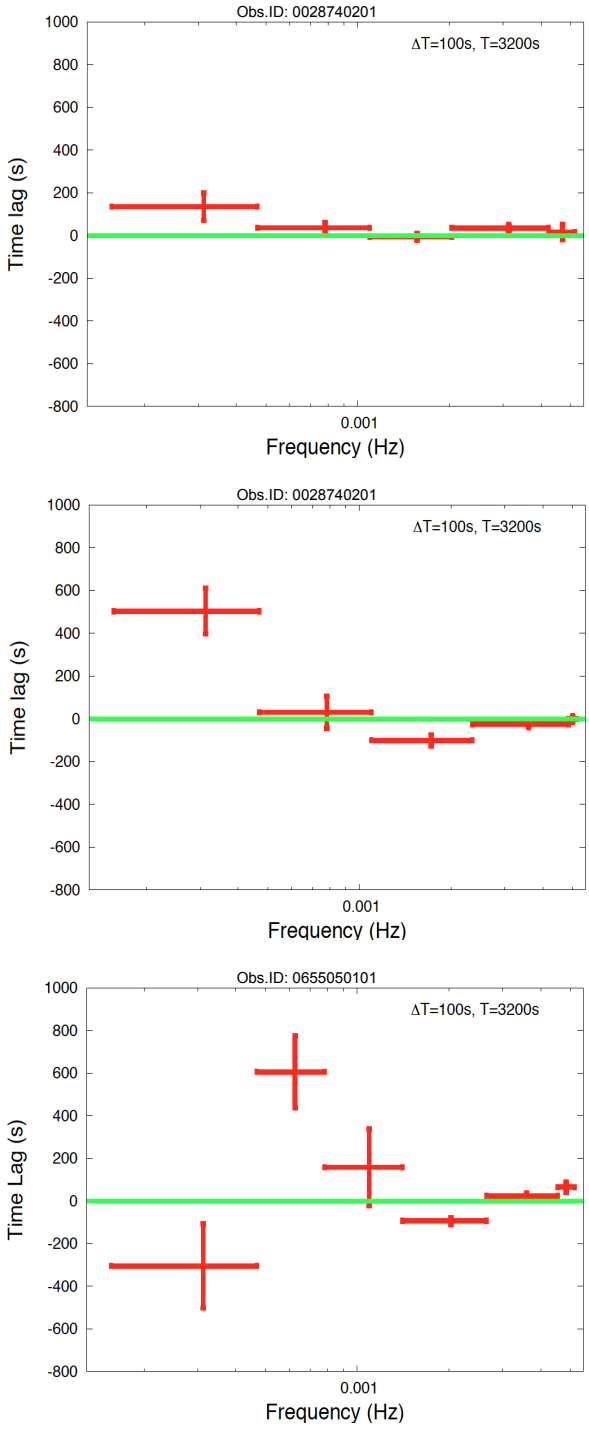

Figure 5.11: Time lag frequency distribution of NGC 55 ULX1 in the first observation with dips (*top*) and without dips (*center*), and the third observation (*bottom*). The delay was evaluated between the 0.3-2.0 and 2.0-10 keV energy bands, sampling the light curves with $\Delta T = 100$s and averaging on segments of 3200 s, with the error bars evaluated at 1σ.

Since this analysis is sensitive to counting statistics, in order to have small error bars, we make use of the first and the third observation. We sample the lightcurves of both observations with ΔT=100s and averaging 9 and 18 intervals of 3.2 ks, respectively. In this way we can be confident that we are investigating the overlap of the timescales in which the RMS-Flux relation was found. As shown in Figure 5.11 (*top*), in the first observation, we find a positive lag at ~ 0.0003 Hz with a value of 136 ± 64 seconds even if it is consistent with zero within 3σ error bars. Also the third observation shows a strong positive lag at a slightly higher frequency ($\sim 0.0006 \div 0.0007$ Hz) and larger value (606 ± 170 seconds). The positive lag can be due to the intrinsic delay between the soft energy emission and the hard emission of the accretion flow. On the other hand, a significant negative point at 0.002 Hz with a value of 92 ± 16 seconds is found in the time lag frequency distribution of the third observation. This could be associated to an optically thick medium that intersects our line of sight, obscuring and reprocessing the high energy emission of the source. We suggest that such an absorbing medium may be the coolest region/remnant of the wind ejection. This scenario can be enforced by the emission line at $\sim$1 keV observed in the spectra of both observations which may be emitted by the wind remnant. The remnant should be fed during the high accretion rate phases in which the intensity of the wind is stronger, i.e. during the first observation, but indications of it (or in other words, a negative delay) are not observed and the time lag seems to be consistent with zero at all frequencies of our interval. Actually, the dip phases can confuse the picture, introducing a random variability that can mask the absorption effects. Although this reduces the counting statistics, in Figure 5.11(*center*) we show the time lag frequency distribution of the first observation removing the dip intervals. As expected, the shape of the time lag does not show the same trend of that of the third observation (Figure 5.11-*bottom*) but we can find statistically significant evidence of a negative point consistent in value and frequency position with that observed in the third observation. This clearly indicates that the dips have affected

the variability.

We further prove our assumptions with the analysis of the covariance spectra (excluding the second observation as no clear timing indications were obtained in the previous sections). The covariance spectra of the observations of NGC 55 ULX1 are obtained adopting the $0.7 - 1.3$ keV interval as reference band for the first observation and $0.5 - 0.7$ keV for the third. We choose these energy ranges because in these intervals the RMS value is well constrained. The spectra are extracted on the timescale $\Delta T = 700s - T_{obs}$ and subsequently unfolded with a *power-law* with photon index of 0. In Figure 5.12, we show the energy distribution of the variability: in the first observation (*top*) the peak of the variability is between $1 - 10$ keV, further suggesting, as for EXO 0748-676, that the high energy component is more variable than the soft component. In fact, there is a clear trend of an increase of the variability with the energy, in which the variability increases by a factor of 10 from 0.3 keV to ~ 2 keV.

On the other hand, this trend is not observed, on the same timescales, in the third observation (Figure 5.12-*bottom*) in which the variability is consistent with a constant within 3σ error bars. However we observe that the reference band has a high coherence with each energy band only in the first observation (RMS and covariance points are consistent) while in the third observation the coherence is low also adopting different reference bands.

Finally, since in the longest observation the RMS-flux correlation is positive, the spectral parameters indicate a strong soft component and several features are present. These results allow us to advance the hypothesis of a transition of the accretion regime between the first two observations and the third one. In the next section we will discuss the implications regarding the physical processes that can explain such a result for ULX1.

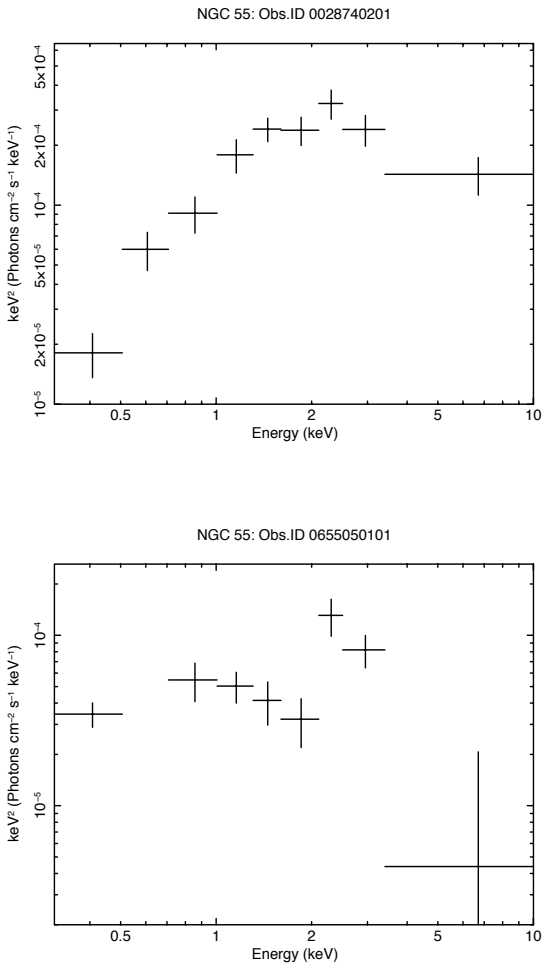

Figure 5.12: Covariance spectra of two observations of NGC ULX1, unfolded with a single *power-law* of photon index of 0. In the first observation (*top*), the variability peaks at $1 - 10$ keV while in the third (*bottom*) it is consistent with a constant within 3σ error bar over the whole energy range.

5.5 Discussion

NGC 55 ULX1 reveals intriguing spectral and temporal properties which are not commonly found in other ULXs. The source was observed mainly in two different flux levels with a drop of about a factor of 2. In the first two observations, the EPIC instruments detected a mean count rate of ~ 3 counts s^{-1} but with high variations up to a factor of three. As noticed by Stobbart et al. (2004), deep decrements (dips) of the total count rate occur on short timescales of minutes/hours and do not show periodical variability. They are more likely associated to obscuring matter that intercepts our line of sight rather than quick changes in the accretion rate. On the other hand in the low flux state, which is persistent for at least 100 ks, the source reaches approximately ~ 1.5 counts s^{-1} and the dips are no longer clearly visible. The spectral properties indicate that a comptonization model plus a multicolor black body disc can describe the source spectra. The latter component has a temperature of ~ 0.23 keV which changes with flux and, in particular, it reaches the lowest value during the lowest flux levels. However the prominence of the soft component anti-correlates with the temperature: indeed the lower is the flux (and the lower is the temperature), the higher is the fraction of the total emission carried by the soft component, ranging from $\sim 50\%$ (during the dip phases) up to $\sim 70\%$ (during the low flux state). Instead the high energy component becomes optically thicker and cooler when the source is in the low flux state. These spectral properties seem inconsistent with the scenario in which the emission is due to an accretion disc coupled with a inner region compact corona. In particular, in the longest observation, we found indications of an ionised medium interposed between us and the inner region of the source which can partially obscure its central emission. Signatures of this medium could also be present in the first two observations but the high flux can hide them and only a marginal detection can be found. Some ULXs have shown an anti-correlation between disc temperature and total luminosity and it was

associated to emission of a wind. Also in this case we have pieces of evidence that this trend is significant, even if this assumption is affected by some caveats regarding the adopted model. Ejection of winds during jet-free accretion phases was observed in several Galactic BH XRBs (Lee et al. 2002; Miller et al. 2004, 2006) indicating that it is a common feature in their accretion processes. In particular the source GRS 1915+105, known to have accreted above the Eddington limit, has shown the ejection of a massive wind (e.g. Neilsen & Lee 2009) during the softer X-ray phases. Furthermore, it was found that also NGC 5408 X-1 has shown indications of outflows (Middleton et al. 2011) and for this reason it is more likely that the production of wind is a common mechanism also in the systems accreting above the Eddington limit. As already found in NGC 5408 X-1, in the first two observations the variability of NGC 55 ULX1 increases with the energy and it seems to be higher at $1 - 10$ keV where the ionised absorber may be important. Middleton et al. (2011) interpreted this behaviour in terms of an extrinsic variability of the high energy component due to turbulences in the wind which intersects our line of sight. The variability introduced by an ionised absorber on the temporal properties was investigated using the source EXO 0748-676 and we found that the RMS and flux anti-correlate in the energy range in which an absorber is not negligible. The clear roll-over observed in the RMS-flux relation of the first observation suggests a transition between two different phases of the absorber. In fact, at low fluxes, the absorber may be completely saturated and an increment of its column density does not affect the equivalent width of the absorption lines, making its effect negligible and allowing us to find the imprint of the intrinsic propagating variability of the accretion flow. On the other hand, at higher fluxes, the situation is reversed and the absorber may be unsaturated and it may strongly affect the variability. In the first observation of NGC 55 ULX1, the RMS-flux relation is negative in the $1 - 10$ keV band and it could be interpreted as if a shield of unsaturated optically thick matter, obscuring the high energy regions, carries the most important imprint on the variability.

At low flux in the third observation when the dip episodes have disappeared, the variability is almost suppressed. In addition, we found that in the $0.3 - 10$ keV energy band there is a linear correlation between RMS and flux, covering a wide range of timescales. The correlation is observed on the same timescales even in the soft energy band, especially at $0.5 - 1.6$ keV. The interpretation of such a RMS-flux correlation may be twofold: 1) in the third observation the source may have experienced a real drop in the accretion rate and the higher column density of the neutral absorber is mainly due to the cold remnant of the wind, which is now less fed by the disc, yelding an almost negligible variability; 2) the source is highly covered by an ionised and saturated absorber and only the intrinsic variability of the accretion flow is seen.

Therefore, on the basis of these results, we suggest that in NGC 55 ULX1 the soft emission is produced by a massive, optically thick and turbulent wind emitted by the accretion disc. The wind drains part of the material from the accretion disc (first and second observation) and the absorption is unsaturated. Consequently, the wind may also or reduce the accretion rate (third observation) or highly obscure the inner regions and become saturated. However, we note that the wind may also produce a drop in the energy reservoir of the comptonizing component (that appears colder). We are possibly seeing the source from a high inclination angle, close to the edge of the wind, and encountering both an unsaturated, optically thick and quickly variable medium (in the first observation) and a more saturated absorbing medium during the longest observation.

Our interpretation may also describe the properties of NGC 5408 X-1 which has shown a positive RMS-flux relation, although it was proved that a turbulent absorber is encountering our line of sight. In fact, in this source, the absorber may be fully saturated and not introduce further variability in the soft energy band.

A common point for at least two observations of NGC 55 ULX1 is the presence of several features in the spectra as a strong Fe XXI and Ne X or Fe XXII emission lines. In the

first observation the feature at ~ 1 keV is only marginally observed and it is statistically significant only during the persistent regime. In the third observation, the continuum emission is deeply reduced allowing us to observe the absorption features and the emission features of Ne IX and Si XIV. The emission features may be due to reprocessed emission from the colder regions of the wind which is expanding into the local environment.

The time lag analysis of NGC 55 ULX1 provides useful information regarding the soft component and its obscuring/absorbing behaviour. In both the first and the third observation, we found that, at the frequency of ~ 0.002 Hz, the hard band leads the soft band and the delay is surprisingly not changed between the two observations (if the dips are removed since they confuse the picture because of their random variability). Indeed, in the hypothesis of an obscuring material surrounding the source, the negative lag represents the temporal distance between the source and the absorber. In case of accretion onto a 10 $M_{\odot}$ BH, we estimated this distance to be $\sim (1.9 \pm 0.4) \cdot 10^6\ R_g$.

Chapter 6

Swift observations of the transient ULX XMMU J004243.6+412519 in M31

6.1 Introduction

Despite the substantial body of work that has been done in the last decade, transient ULXs still represent a poorly know population. Only few ULXs with transient behaviour have been detected so far and only a handful of them have been studied in detail. Examples of well-studied genuine ULX transients are CXOM31 J004253.1+411422 in M31 (hereafter M31 ULX-1), CXOU 133705.1–295207 in M83 and CXOU J132518.2–430304 in NGC 5128 (Kaur et al. 2012; Soria et al. 2012; Sivakoff et al. 2008). In 2012 January a new X-ray source with a luminosity of $\sim 10^{38}$ erg s^{-1} was discovered by *XMM-Newton* in M31 (XMMU J004243.6+412519; Henze et al. 2012b). Seven days after its discovery, it reached a luminosity of $\sim 2 \times 10^{39}$ erg s^{-1}, which made it the second most luminous ULX in M31 (Henze et al., 2012c). During the outburst the source was repeatedly observed by *Swift* and other instruments. Here we present the analysis of the several *Swift* XRT and UVOT observations performed between 2012 March and August with the aim to explore the nature of this source. We also present the results of deep optical observations taken

on 2012 July 18 with the 1.8-m Copernico Telescope at Cima Ekar (Asiago, Italy) and the analysis of serendipitous observations of the source region collected in recent years by *Swift* and *CHANDRA*.

In Section 6.2 we describe the *Swift* observations used in our study and we present the results of the spectral and timing analysis of the X-ray data in Section 6.3. In Section 6.4 we report on the *Swift*/UVOT and Copernico optical and ultraviolet observations of the source. In Section 6.5 we present the upper limits on the pre-outburst X-ray flux of XMMU J004243.6+412519 obtained from our inspection of *CHANDRA* and *Swift* archival observations. Discussion follows in Section 6.6.

6.2 *Swift* observations and data reduction

The *Swift* payload includes a wide-field instrument, the coded-mask gamma-ray Burst Alert Telescope (BAT, Barthelmy et al. 2005), and two narrow-field instruments, the X-Ray Telescope (XRT, Burrows et al. 2005) and the Ultra-Violet/Optical Telescope (UVOT, Roming et al. 2005). In this work we made use of only the narrow-field instruments data.

The XRT uses a front-illuminated CCD detector sensitive to photons between 0.2 and 10 keV. Two main readout modes are available: photon counting (PC) and windowed timing (WT). PC mode provides two dimensional imaging information and a 2.507-s time resolution; in WT mode only one-dimensional imaging is preserved, achieving a time resolution of 1.766 ms. The UVOT is a 30-cm modified Ritchey-Chrétien reflector using a microchannel-intensified CCD detector which operates in photon counting mode. A filter wheel accommodates a set of optical and ultraviolet (UV) filters and the wavelength range is 1700–6000 Å. The data were processed and filtered with standard procedures and quality cuts[1] using FTOOLS tasks in the HEASOFT software package (v. 6.12) and the calibration files in the 2012-02-06 CALDB release.

[1]See http://*Swift*.gsfc.nasa.gov/docs/*Swift*/analysis/ for more details.

Following the discovery of XMMU J004243.6+412519 (2012 January; Henze et al. 2012b), the source was observed by *Swift* ten times in about three weeks, until it came out of visibility in 2012 March. At the end of 2012 May, XMMU J004243.6+412519 became visible again for *Swift* and the monitoring was resumed with many further pointings, mostly off-axis (see also Henze et al. 2012). Around mid 2012 August, the source flux became too low for the typical sensitivity of a ∼2-ks XRT snapshot. For this reason, after the visibility gap we consider only the sixteen observations taken up to 2012 September 01. A summary of the observations used in this work is given in Table 6.1.

6.3 X-ray data analysis

We extracted the PC source events from a circle with a radius of 20 pixels (1 XRT pixel corresponds to about 2,36 arcseconds) and the WT data from a 40 × 40 pixels box along the image strip. To estimate the background, we extracted PC and WT events from regions far from the position of XMMU J004243.6+412519. The ancillary response files (arf) were generated with XRTMKARF, and they account for different extraction regions, vignetting and point spread function corrections. We used the latest available spectral redistribution matrix (rmf) in CALDB. The spectral channels were grouped so as to have bins with a minimum number of 20 photons. The spectral analysis was performed with the XSPEC 12.7 fitting package (Arnaud, 1996); the abundances used are those of anders89 and photoelectric absorption cross-sections are from Balucinska-Church & McCammon (1992).

Initially we focus our analysis on the 2012 February–March data (see Table 6.1). For a preliminary look at the data, we fit all spectra simultaneously (in the 0.5–10 keV energy range) with the hydrogen column density tied between all observations using a simple power law (e.g. Henze et al. 2012c). While this simultaneous modelling yields a rather

Table 6.1: *Swift* observations used for this work.

Observation	XRT mode	UVOT filter[a]	Start / end time (UT) (YYYY-MM-DD hh-mm-ss)		Exposure (ks)
00032286002	PC	u	2012-02-19 00:47:34	2012-02-19 23:23:57	3.9
00032286003	PC	u	2012-02-23 18:49:39	2012-02-23 22:13:56	3.3
00032286004	WT	–	2012-02-24 13:54:21	2012-02-24 15:35:02	0.5
00032286005	WT	$uvw2$	2012-02-28 04:50:00	2012-02-28 08:17:00	3.0
00032286009	WT	$uvw2$	2012-03-02 03:02:59	2012-03-02 03:45:40	2.5
00032286006	PC	u	2012-03-02 04:54:08	2012-03-02 14:58:57	6.3
00032286007	PC	$uvw2$	2012-03-03 00:09:07	2012-03-03 16:37:58	7.1
00032286008	WT	$uvw2$	2012-03-03 01:41:44	2012-03-03 06:57:00	2.7
00032286010	PC	$uvm2$	2012-03-04 04:52:27	2012-03-04 21:21:57	4.3
00032286011	WT	$uvw2$	2012-03-07 10:00:31	2012-03-07 12:01:00	3.1
00035336052	PC	$uvw1$	2012-05-24 14:55:42	2012-05-24 21:36:56	4.3
00032286012	WT	$uvw1$	2012-05-28 11:55:26	2012-05-28 15:37:59	4.1
00035336053	PC	–	2012-06-01 18:28:39	2012-06-01 23:43:57	4.0
00035336054	PC	$uvw1$	2012-06-09 06:20:09	2012-06-09 11:22:57	2.0
00035336055	PC	–	2012-06-17 03:17:31	2012-06-17 08:14:56	2.1
00035336056	PC	$uvw1$	2012-06-25 00:42:19	2012-06-25 18:40:57	1.9
00035336058	PC	$uvw1$	2012-07-09 16:01:04	2012-07-09 19:30:55	1.1
00035336059	PC	–	2012-07-11 06:36:01	2012-07-11 06:37:49	0.1
00035336060	PC	$uvw1$	2012-07-15 11:37:32	2012-07-15 11:55:55	1.1
00035336061	PC	$uvw1$	2012-07-19 02:11:18	2012-07-19 15:23:56	2.1
00035336062	PC	$uvw1$	2012-07-27 18:33:47	2012-07-27 20:25:54	2.3
00035336063	PC	–	2012-08-05 03:03:49	2012-08-05 11:19:53	2.0
00035336064	PC	–	2012-08-12 11:32:21	2012-08-12 21:20:56	0.9
00035336065	PC	$uvw1$	2012-08-20 21:29:05	2012-08-20 23:24:55	2.1
00035336066	PC	$uvw1$	2012-08-28 13:49:33	2012-08-28 14:05:53	1.0
00035336067	PC	$uvw1$	2012-09-01 13:58:43	2012-09-01 14:24:55	1.6

[a] u: central wavelength 3465 Å, FWHM 785 Å; $uvw1$: central wavelength 2600 Å, FWHM 693 Å; $uvm2$: central wavelength 2246 Å, FWHM 498 Å; $uvw2$: central wavelength 1928 Å, FWHM 657 Å.

high reduced χ^2 of 1.37 for 553 degrees of freedom (dof), the test shows that, as can be seen in Fig. 6.1, the spectra of XMMU J004243.6+412519 are all very similar in this set of XRT observations (see also Henze et al. 2012a).

Thus, in order to achieve better statistics and higher signal-to-noise ratio, we merged the data from all the observations and accumulated combined PC and WT spectra. In the following, we concentrate on the PC total spectrum (24.9 ks, about 7900 counts, 99.4% of which are attributable to XMMU J004243.6+412519), because of the intrinsically higher signal-to-noise ratio of the PC data with respect to the WT ones. The combined spectrum was fit adopting several phenomenological models frequently used in literature for ULXs (e.g. Roberts 2007; Feng & Soria 2011): a DISKBB, a POWER-LAW, a DISKBB+POWER-LAW, and a DISKBB+COMPTT, all corrected for interstellar absorption. All these models but the power law provide statistically good fits. However, the improvement given by the combination of two models is not significant in comparison with a single DISKBB model ($\chi^2_\nu = 1.07$ for 231 d.o.f. against, for instance, $\chi^2_\nu = 1.03$ for 229 for the DISKBB+POWER-LAW). We also tried to fit more sophisticated Comptonization models (COMPTT and SIMPL in XSPEC) to the data, but the count statistics of the spectrum is not sufficient to provide good-enough constraints on the model parameters. Hence, it seems appropriate to describe the pre-gap PC spectrum of XMMU J004243.6+412519 in terms of a simple DISKBB model. The best fitting parameters show that the disc is relatively hot (0.86 ± 0.02 keV) and the luminosity is quite high ($\sim 1.1 \times 10^{39}$ erg s^{-1} for a distance of 780 kpc; Holland 1998; Stanek & Garnavich 1998). The results are summarised in Table 6.2.

Similarly, for the second batch of data (collected starting from 2012 May; see Table 6.1) we extracted a cumulative PC spectrum (23.7 ks, about 1600 counts, 99.2% of which are attributable to XMMU J004243.6+412519). We tested the same single-component[2] spectral

[2]Owing to the lower count statistics, this time we did not consider more complicated (two-component) models.

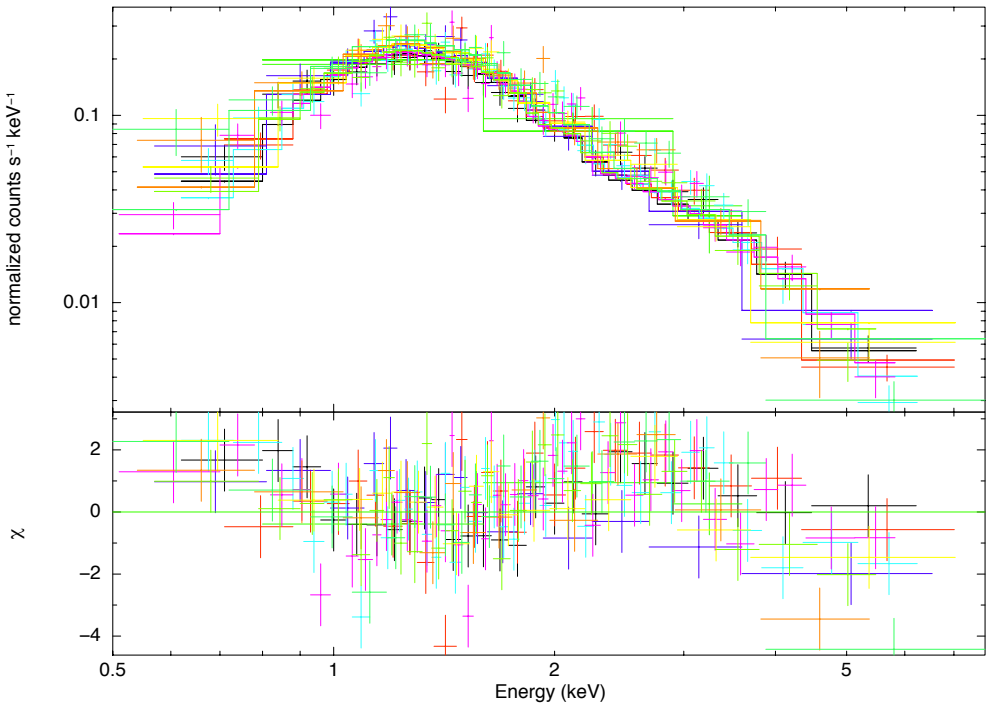

Figure 6.1: Simultaneous modelling of all the 2012 February–March PC and WT spectra using an absorbed power-law model. Bottom panel: the residuals of the fit (in units of standard deviations). Each color of this plot represents a specific observation.

Table 6.2: Spectral analysis of XMMU J004243.6+412519 (2012 February–March, PC data). Errors are at a 1σ confidence level for a single parameter of interest.

Model[a]	$N_{\rm H}$ (10^{21} cm^{-2})	Γ_1	$E_{\rm cut/break}$ (keV)	kT_{in} (keV)	Γ_2 / Norm.[b]	Observed flux[c] (10^{-11} erg cm^{-2} s^{-1})	Luminosity[c] (10^{39} erg s^{-1})	χ^2_ν (dof)
PHABS*POWERLAW	6.7 ± 0.2	2.91 ± 0.04	–	–	–	1.12 ± 0.02	2.33 ± 0.09	1.46 (231)
PHABS*DISKBB	2.9 ± 0.1	–	–	0.86 ± 0.02	1.4 ± 0.1	1.04 ± 0.02	$1.04^{+0.02}_{-0.01}$	1.07 (231)
PHABS*CUTOFFPL	3.5 ± 0.3	$0.7^{+0.2}_{-0.3}$	$1.4^{+0.1}_{-0.2}$	–	–	$1.06^{+0.02}_{-0.01}$	$1.15^{+0.07}_{-0.06}$	1.03 (230)
PHABS*BKNPOWER	4.5 ± 0.3	$2.1^{+0.1}_{-0.2}$	$2.6^{+0.2}_{-0.1}$	–	$3.6^{+0.2}_{-0.1}$	1.10 ± 0.02	$1.44^{+0.09}_{-0.08}$	1.00 (229)
PHABS*(POWERLAW+DISKBB)	$3.2^{+0.4}_{-0.2}$	$1.6^{+0.6}_{-1.8}$	–	$0.79^{+0.04}_{-0.02}$	1.8 ± 0.2	1.10 ± 0.02	$1.12^{+0.03}_{-0.02}$	1.03 (229)
PHABS*(CUTOFFPL+DISKBB)	9^{+1}_{-2}	1.4 ± 0.5	$1.7^{+0.5}_{-0.3}$	$0.12^{+0.02}_{-0.01}$	$1.1^{+4.3}_{-0.9} \times 10^5$	$1.07^{+0.01}_{-0.02}$	$1.15^{+0.07}_{-0.06}$	1.00 (228)

[a] XSPEC model.

[b] DISKBB normalisation: $(R[\mathrm{km}]/D[10\ \mathrm{kpc}])^2 \cos\theta$, $\theta = 0$ corresponding to a face-on disc.

[c] In the 0.5–10 keV energy range; for the luminosity we assumed a distance to M31 of 780 kpc (Holland 1998; Stanek & Garnavich 1998).

models reported in Table 6.2, obtaining the parameters shown in Table 6.3. In general, they appear to have values of the column density consistent with those of the pre-gap state and significantly lower fluxes/luminosities. In particular the post-gap average spectrum is well described by a DISKBB component with an (average) temperature (∼0.6 keV) smaller than that of the pre-gap combined spectrum. In Fig. 6.2 we show the PHABS*DISKBB model fit to the pre- and post-visibility gap combined PC spectra. The softening suggested by the spectral parameters and Fig. 6.2 is apparent from the contour plots shown in Fig. 6.3.

In order to study the source flux evolution over time, we fit all the PC spectra from the individual observations or from small groups of observations. When the source flux dropped below 2×10^{-12} erg cm^{-2} s^{-1}, around mid 2012 July, in order to accumulate sufficient statistics for meaningful spectral fits, we combined data from a few contiguous observations; namely, we obtained a spectrum from observations 00035336058–61 and another one from observations 00035336062–64. We fit all the spectra simultaneously adopting the PHABS*DISKBB model with the hydrogen column density (which is consistent with a single value in both the pre- and post-gap cumulative spectra) tied between observations ($\chi^2_\nu = 1.10$ for 676 dof). We plot the resulting long-term light curve and the inferred temperatures kT in Fig. 6.4. We show both the absorbed and unabsorbed fluxes. As can be seen from Fig. 6.4 the effect of the interstellar absorption is larger on the softer spectra from the post-gap observations. Progressive spectral softening and flux decay are evident during the post-gap observations. The flux decreased by a factor of ≈5 over ∼70 days (by a factor of ≈10 over ∼150 days with respect to the pre-gap flux), while the disc temperature changed from $kT \sim 0.7$ keV to ∼0.4 keV.

Although, owing to the long visibility gap, the available data do not allow us to perform an accurate modelling of the decay shape, we tried a number of simple models to fit the light curve of XMMU J004243.6+412519. We fixed $t = 0$ at the time the source was observed for the first time to exceed the ULX threshold (MJD 55947.51; Henze et al.

Table 6.3: Spectral analysis of XMMU J004243.6+412519 (2012 May–August, PC data). Errors are at a 1σ confidence level for a single parameter of interest.

Model[a]	$N_{\rm H}$ (10^{21} cm^{-2})	Γ_1	$E_{\rm cut}$ (keV)	kT_{in} (keV)	Γ_2 / Norm.[b]	Observed flux[c] (10^{-12} erg cm^{-2} s^{-1})	Luminosity[c] (10^{39} erg s^{-1})	χ^2_ν (dof)
PHABS*POWERLAW	6.9 ± 0.5	3.6 ± 0.1	–	–	–	2.04 ± 0.07	$0.71^{+0.10}_{-0.08}$	1.45 (66)
PHABS*DISKBB	2.7 ± 0.3	–	–	0.62 ± 0.02	1.2 ± 0.2	1.95 ± 0.06	0.22 ± 0.01	0.98 (66)
PHABS*CUTOFFPL	$1.5^{+1.0}_{-0.8}$	$-1.0^{+0.8}_{-0.6}$	0.6 ± 0.1	–	–	1.95 ± 0.06	$0.17^{+0.04}_{-0.02}$	0.98 (65)
PHABS*BKNPOWER	$3.8^{+0.7}_{-0.9}$	$2.2^{+0.3}_{-0.5}$	$2.3^{+0.1}_{-0.3}$	–	$4.6^{+0.4}_{-0.5}$	$2.01^{+0.06}_{-0.07}$	0.29 ± 0.05	0.99 (64)

[a] XSPEC model.

[b] DISKBB normalisation: $(R[\mathrm{km}]/D[10\ \mathrm{kpc}])^2 \cos\theta$, $\theta = 0$ corresponding to a face-on disc.

[c] In the 0.5–10 keV energy range; for the luminosity we assumed a distance to M31 of 780 kpc (Holland 1998; Stanek & Garnavich 1998).

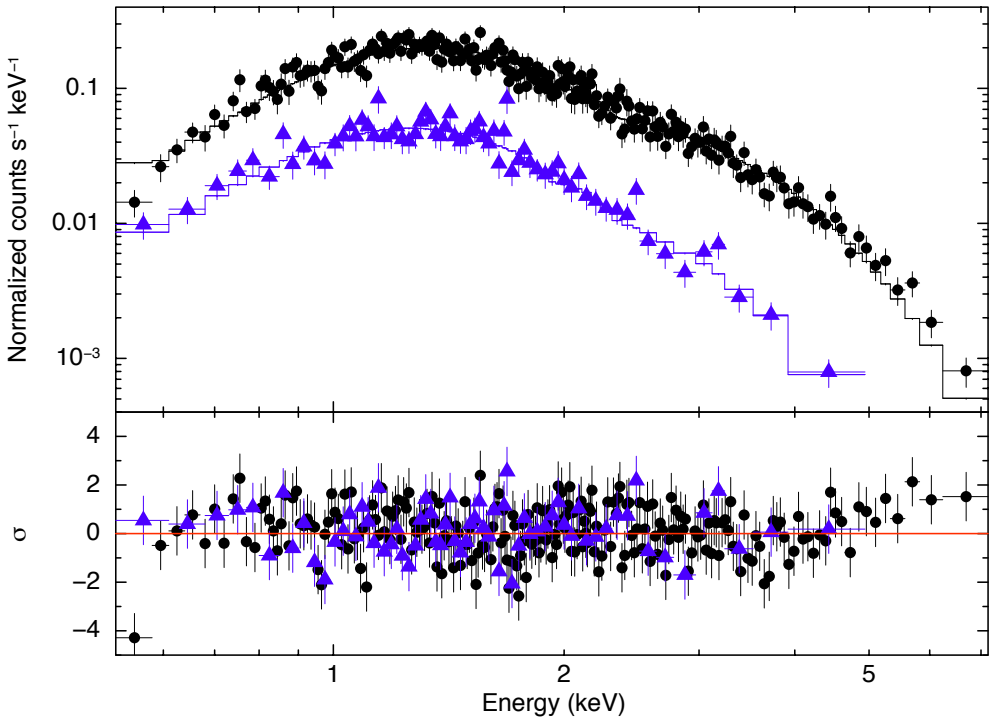

Figure 6.2: Comparison of the pre- (black circles) and post-visibility gap (blue triangles) cumulative PC spectra for the PHABS*DISKBB model (see Section 6.3 for details). Bottom panel: the residuals of the fit (in units of standard deviations).

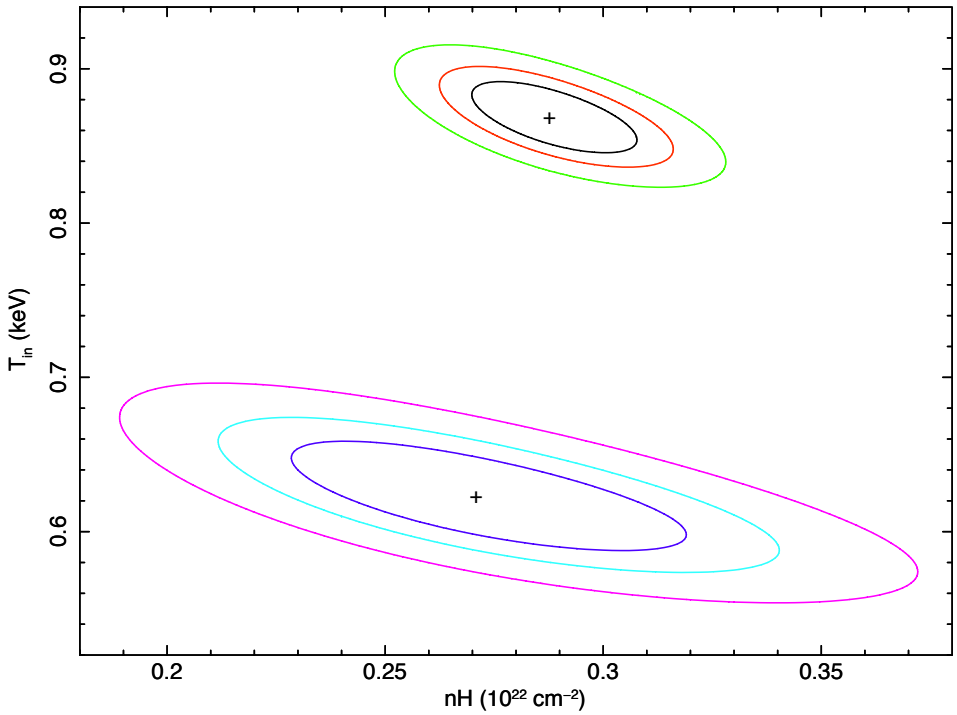

Figure 6.3: Contour plots of temperature versus column density (adopting the PHABS*DISKBB model) for the pre-gap (black/red/green upper contours) and post-gap (blue/cyan/violet lower contours) PC data. The crosses indicate the best fits. Lines mark 1, 2 and 3σ confidence levels.

2012c). An exponential function of the form $F(t) = A\exp(-t/\tau)$ gives a rather poor fit ($\chi^2_\nu = 11.58$ for 10 dof). The best-fitting parameters for the observed (absorbed) flux are $A = (2.00 \pm 0.05) \times 10^{-11}$ erg cm^{-2} s^{-1} and e-folding time $\tau = (63.9 \pm 1.3)$ d.

Among the other models tested, a broken-power-law model provides the better fits for the evolution of both the absorbed ($\chi^2_\nu = 4.33$ for 8 dof) and unabsorbed fluxes ($\chi^2_\nu = 3.65$ for 8 dof). Assuming as $t = 0$ MJD 55947.51, for the observed flux, the break occurs at (111.4 ± 6.4) d, when the index changes from $\alpha_1 = -0.41 \pm 0.18$ to $\alpha_1 = -4.03 \pm 0.19$; the flux at the break time is $(6.9 \pm 1.5) \times 10^{-12}$ erg cm^{-2} s^{-1}. For the unabsorbed flux, the best-fitting parameters are: $\alpha_{\circ,1} = -0.26 \pm 0.15$, $\alpha_{\circ,2} = -3.06 \pm 0.19$ and (104.5 ± 6.4) d for the break epoch (with an unabsorbed flux of $(1.1 \pm 0.2) \times 10^{-11}$ erg cm^{-2} s^{-1}). The steeper decay of the absorbed flux is due to the fact that the absorption affects the softer (later) spectra more. We stress that the fit parameters depend on the assumed time origin. The uncertainties introduced by making different (reasonable) assumptions can be larger than the statistical errors reported here. For instance, assuming $t = 0$ at MJD 55942 (the day after the discovery of the source at a luminosity of $\approx 2 \times 10^{38}$ erg s^{-1}; Henze et al. 2012b), we find for the observed flux: $\alpha'_1 = -0.19 \pm 0.12$, $\alpha'_2 = -4.18 \pm 0.19$, (110.3 ± 3.6) d for the break epoch and flux at the break time of $(8.8 \pm 1.0) \times 10^{-12}$ erg cm^{-2} s^{-1}.

In the last observations (segments 00035336065, 00035336066 and 00035336067), XMMU J004243.6+412 was not detected. The 3σ upper limits on the XRT count rate derived from the deeper observations (6065 and 6067) are of $\sim$0.1 counts s^{-1} (0.3–10 keV, following Kraft et al. 1991). Assuming the spectrum of the closest observations (6062–6064, $kT \simeq 0.4$ keV), this corresponds to upper limits on the observed flux of $\sim 4 \times 10^{-13}$ erg cm^{-2} s^{-1} and of $\sim 6 \times 10^{37}$ erg s^{-1} on the luminosity (for 780 kpc).

For the timing analysis we concentrate on the data in WT mode (total exposure: 16.0 ks; see Table 6.1), since their time resolution of $\sim$1.7 ms (corresponding to a Nyquist frequency of $\sim$280 Hz) makes it possible to search for fast time variability. For each observation we

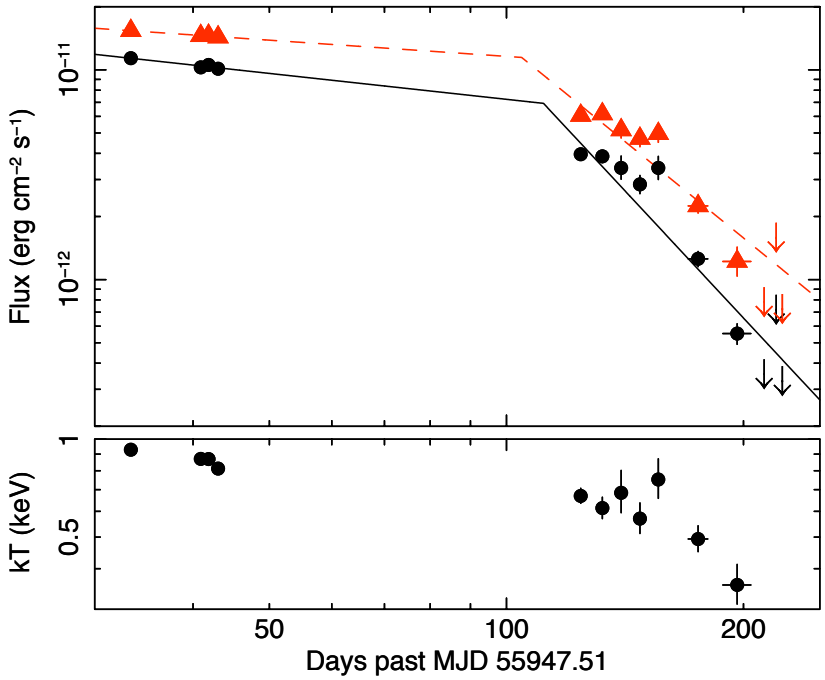

Figure 6.4: The top panel shows time evolutions of the absorbed (black circles) and unabsorbed (red triangles) fluxes in the 0.5–10 keV energy range for the PHABS*DISKBB model (see Section 6.3 for details); the down-arrows indicate upper limits at the 3σ confidence level. The broken-power-law models describing the decays are also plotted (black solid line for the observed flux and red dashed line for the unabsorbed flux). Bottom panel: evolution of the characteristic temperature of the DISKBB model inferred from the spectral fitting. We assumed as $t = 0$ the date the source was observed for the first time to exceed the ULX threshold (Henze et al., 2012c).

computed a power density spectrum (PDS) in the energy band 0.3–10 keV by using intervals up to ∼925-s long and averaging the individual spectra for each observation. The PDS did not reveal any significant variability from XMMU J004243.6+412519: neither broad-band components nor narrow features were detected; no significant evolution of the PDS in time could be detected as well.

To improve the statistics, we produced a single PDS averaging all the WT data. The PDS was normalised according to Leahy et al. (1983), so that powers due to Poissonian counting noise have an average value of 2. Since PDS created from data taken in WT mode show a drop-off at high frequencies[3] and since also the averaged PDS from all the WT observations did not show any significant feature, we rebinned our data at a Nyquist frequency of ∼17 Hz (rebin factor of 16) using data stretches 925-s long to obtain a new average PDS. The PDS is well fit by a constant component equal to 2.286 ± 0.006 (reasonably describing the Poissonian noise) with a best-fitting $\chi^2 = 169.56$ for 152 dof. Hence we conclude that no significant variability is detected from the source. It is not possible, however, to exclude that the emission from the source has a certain level of variability hidden by photon counting statistics or on time-scales not accessible to our data ($\leq 10^{-4}$ Hz).

Apart from the flux decay on the scale of weeks, the emission from XMMU J004243.6+412 does not show signs of strong aperiodic variability either. There is only some evidence of moderate variability on the 1-ks-scale, with a rms variance of (20 ± 5) percent in the WT data. This is probably related to some level of variability of the local astrophysical background and could account for the fact that the Poissonian noise level observed in the PDS is slightly higher than the expected value (2 with the Leahy normalisation). For the pre-gap PC light curves (a similar analysis of the post-gap data is hampered by the low count

[3]This effect is mostly visible above ~ 50 Hz and is related to the read-out method of the XRT detector, see http://www.*Swift*.ac.uk/analysis/xrt.

rates) the 3σ upper limits on the rms variability range from approximately 12 percent to 20 percent.

6.4 Optical and ultraviolet observations

The *Swift*/UVOT observed XMMU J004243.6+412519 simultaneously with the XRT. The data were taken with the u, $uvw1$, $uvm2$ and $uvw2$ filters (see Table 6.1). The analysis was performed on the individual and stacked (for each filter) images with the UVOTSOURCE task, which calculates the magnitude through aperture photometry within a circular region (we used a 3-arcsec radius) and applies specific corrections due to the detector characteristics.

No source was detected at the position of XMMU J004243.6+412519 in any of the UVOT observations and filters, before or after the visibility gap. The 3σ limits before the visibility gap are in the stacked images $u > 23.2$ mag (total exposure: 13.4 ks), $uvm2 > 23.7$ mag (total exposure: 5.6 ks) and $uvw2 > 24.5$ (total exposure: 18.2 ks). After the gap, XMMU J004243.6+412519 was observed only with the $uvw1$ filter; the 3σ limit from the stacked image is $uvw1 > 24.4$ (total exposure: 23.2 ks) All magnitudes are in the AB system (Oke & Gunn, 1983); see Poole et al. (2008) for more details on the UVOT photometric system and Breeveld et al. (2011) for the most updated zero-points and count rate to flux conversion factors.

The above magnitudes have not been corrected for extinction. At the position of XMMU J004243.6+412519, the total line-of-sight optical extinction estimated from background infrared emission is $A_V = 0.05$ mag (Schlegel et al., 1998), while the X-ray fits, adopting the relation $N_{\rm H} = 1.79 \times 10^{21} A_V$ cm^{-2} by Predehl & Schmitt (1995), yield higher values in the range $A_V \approx 1.7$–5.0. Indicatively, $A_V = 1$ mag corresponds to $A_u \simeq 1.8$ mag, $A_{uvw1} \simeq 2.2$ mag , $A_{uvm2} \simeq 3.2$ mag, and $A_{uvw2} \simeq 2.8$ mag (Fitzpatrick & Massa, 2007).

The field of XMMU J004243.6+412519 was also observed with the 1.8-m Copernico

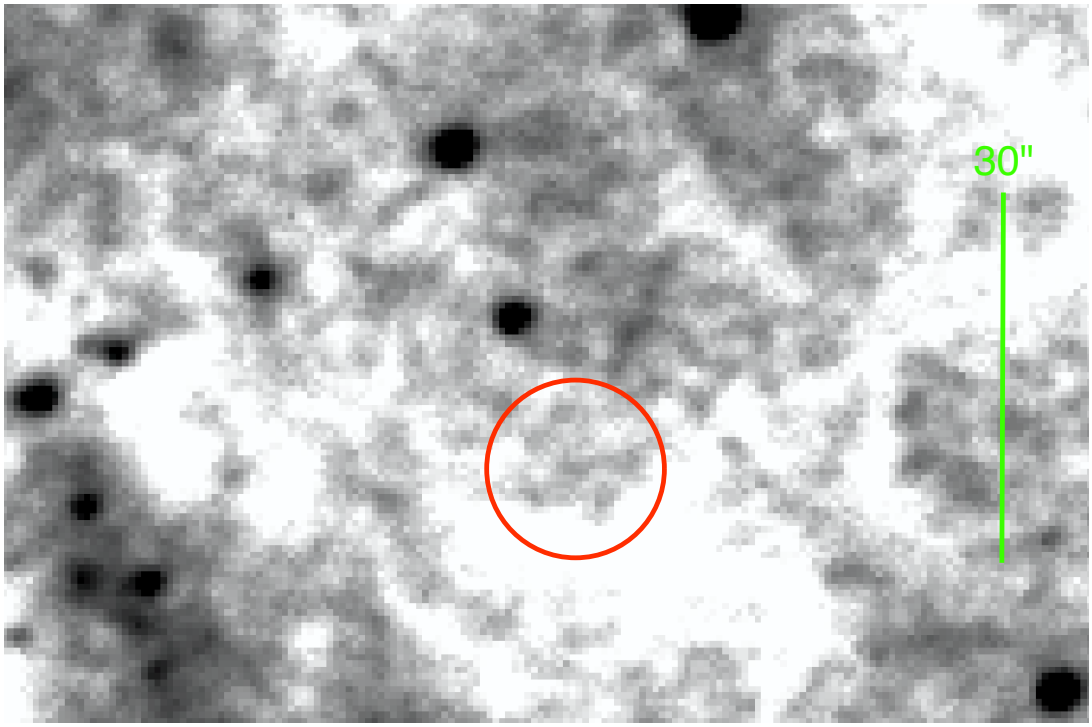

Figure 6.5: V-band image of the field of XMMU J004243.6+412519 taken on 2012 July 18 at the 1.8-m Copernico Telescope at Cima Ekar in Asiago. North is up, East to the left. The red circle ($7'', 2,\ 3\sigma$) is centred on the *CHANDRA* position of XMMU J004243.6+412519 (Barnard et al., 2012).

Telescope at Cima Ekar in Asiago (Italy) on 2012 July 18. Three images of 20 minutes were taken in both the V and B band filters. The data were reduced following standard prescriptions. After removal of the detector signature (bias and flat field corrections), the images were astrometrically calibrated performing a polynomial interpolation starting from the positions of the NOMAD star catalogue (Zacharias et al., 2005). The accuracy is $0''.2$. The three calibrated frames in each filter were then averaged and the resulting V band image is shown in Fig. 6.5.

Instrumental magnitudes were measured on the images through the point-spread function (PSF) fitting technique. The photometric calibration was performed using reference stars from the catalogue of M31 compiled by Magnier et al. (1992), homogeneously distributed around the source position. The internal accuracy of this calibration is 0.1 mag in both bands. No source at the position of XMMU J004243.6+412519 was detected in any of the two filters down to a limiting magnitude of 21.7 and 22.2 in the V and B band filters, respectively (see Fig. 6.5). In fact, the background emission from M31 is highly variable inside the error box, so that the actual limiting magnitude varies from 21.5 to 21.9 in V and from 21.6 to 22.8 in B, depending on the position.

6.5 Pre outburst observations

As noted by Henze et al. (2012b,c), no source compatible with the position of XMMU J004243.6+412519 was listed in any X-ray catalogue. We have searched the *XMM-Newton*, *CHANDRA*, and *Swift* public archives for possible previous bright states of XMMU J004243.6+412519 in recent years, but the source was never detected. Since the *XMM-Newton* observations are rather sparse, in the following we summarise only the upper limits obtained from the much more intense coverage (from 1999 November to 2012 January) with *CHANDRA* and *Swift*.

6.5.1 *CHANDRA*

The distribution of the 93 *CHANDRA* observations (from 1999 November 30 to 2011 August 25) covering the field of XMMU J004243.6+412519 can be seen in Fig. 6.6; 54 observations were carried out with the HRC-I instrument (Murray et al., 2000), 39 with the ACIS (I or S; Garmire et al. 2003). Typical exposures are for the HRC-I ∼1–5 ks in the 1999–2011 observations and ∼20 ks in the more recent ones, and ∼5 ks for the ACIS pointings; the deepest upper limit (see Fig. 6.6) was obtained from a 38-ks ACIS-I observation carried out on 2001 October 05 (obs. ID: 1575; MJD 52187).

For each observation, an upper limit on the count rate from XMMU J004243.6+412519 was computed using the CIAO tool APRATES and taking into account the point-spread function fraction in the apertures within which the counts were extracted. In order to convert limits on the count rates from the different detectors into upper limits on the unabsorbed flux, we used the NASA/HEASARC PIMMS tool assuming a soft power-law spectrum with photon index $\Gamma \sim 3$ and absorption $N_{\rm H} \sim 7 \times 10^{21}$ cm^{-2}. The corresponding upper limits on the luminosity (assuming a distance of 780 kpc) range from $\sim 6 \times 10^{35}$ to 5×10^{37} erg s^{-1} and are shown in Fig. 6.6.

6.5.2 *Swift*

In the period between 2006 September 01 and 2012 January 01, *Swift* serendipitously imaged with the XRT (in PC mode) the position of XMMU J004243.6+412519 119 times for a total exposure of ∼370 ks. The spread of the observations can be seen in Fig. 6.7 while the exposure time for each year is given in Table 6.4.

We examined each observation, but the source was never detected, nor it was detected in the total and yearly total images. For each year and for the total data set, we computed 3σ upper limits on the count rate (following Kraft et al. 1991). These upper limits (Table 6.4) can be directly compared with the average (and fairly constant) PC rate observed in 2012

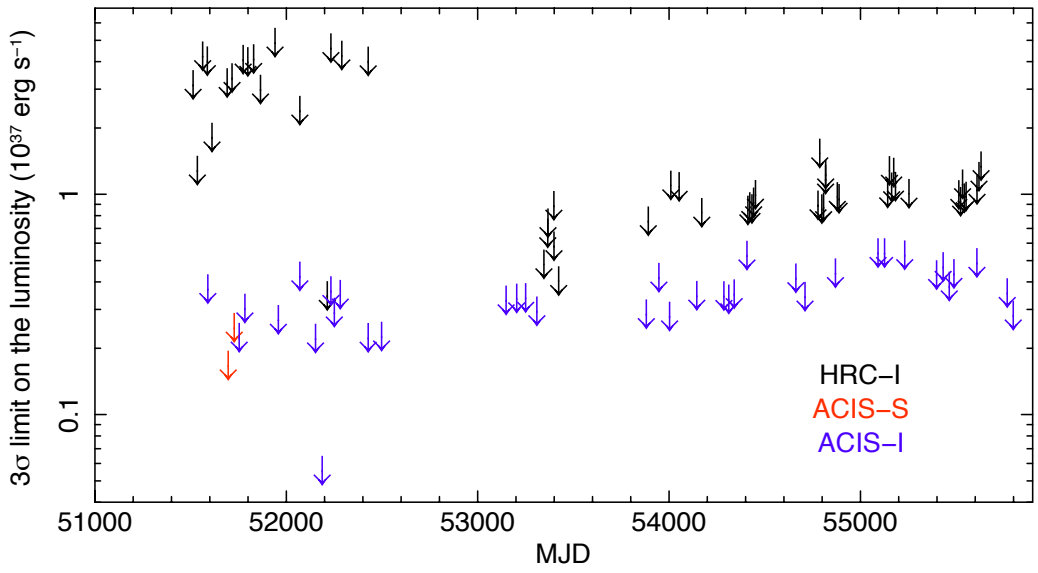

Figure 6.6: *CHANDRA* 3σ upper limits on the 0.5–10 keV luminosity (for a distance of 780 kpc; Holland 1998; Stanek & Garnavich 1998).

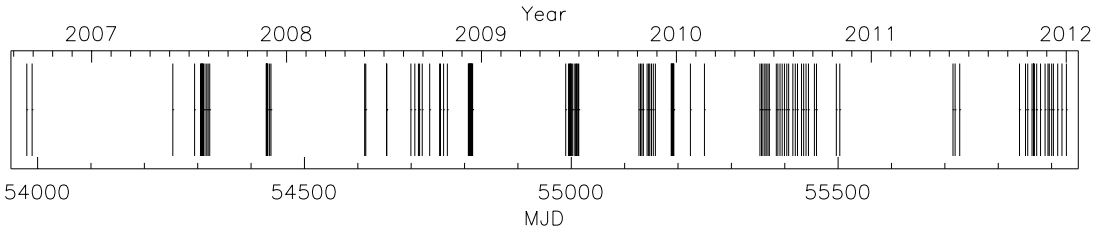

Figure 6.7: Epochs of the *Swift*/XRT serendipitous observations of the position of XMMU J004243.6+412519.

Table 6.4: Pre-outburst upper limits from *Swift*/XRT serendipitous observations of the position of XMMU J004243.6+412519.

Year	Observations	Total exposure (ks)	Flux upper limit[a] (erg cm^{-2} s^{-1})
2006	2	9.9	3.5e-14
2007	19	58.3	1.3e-14
2008	23	65.3	8.0e-15
2009	28	86.2	9.8e-15
2010	27	98.5	1.1e-14
2011	19	47.9	2.3e-14
2012	1	4.1	8.7e-14
2006–2012	119	369.5	5.6e-15

[a] At a confidence level of 3σ.

February–March, (0.370 ± 0.007) counts s^{-1}. In particular, the last *Swift* observation performed before the discovery of XMMU J004243.6+412519 (obs. ID: 00035336051; 2012 January 01) yields an upper limit of 2.5×10^{-3} counts s^{-1}, implying for the source a flux increase of 150 or more during 2012 January/February.

6.6 Discussion: spectral states in transient ULXs

XMMU J004243.6+412519 is a transient X-ray source in M31 that, at its maximum, reached luminosity in the ULX range. Undetected in all previous X-ray observations, in February 2012 it suddenly started to show powerful X-ray emission. After reaching the maximum, the source luminosity remained fairly constant at $\geq 10^{39}$ erg s^{-1} for at least $\sim$40 days, then it faded below $\approx 10^{38}$ erg s^{-1} in the following $\sim$200 days. The decay, accompanied by a spectral softening, can be described by a broken power-law with a break time of $\approx$100 days. No broad components nor narrow features (in the form of quasi-periodic oscillations) were detected in the power density spectra up to $\sim$280 Hz. We searched also for optical and near-UV emission from XMMU J004243.6+412519, but no no source was detected at its

position down to a sensitivity limit of ∼22 in the V and B bands, and of 23–24 in the near UV.

In the following, we discuss the properties of XMMU J004243.6+412519 only in the context of an accreting black hole in M31. The large absorption column and the lack of an optical counterpart exclude a foreground object. In terms of a background object, the best candidates are an active galactic nucleus or a tidal disruption event. However, no active galactic nucleus has been observed to vary in X-rays by more than two orders of magnitude, while a tidal disruption event is ruled out by the flux evolution, that does not follow the characteristic decay of such events (Burrows et al., 2011).

Our spectral analysis of the *Swift* PC data showed that the energy spectrum of XMMU J004243.6+412 can be fit using a disc component, and that the combination of a disc component and a power law that is commonly used to describe both the spectra of some ULXs and of Galactic BH binaries is not statistically needed (see also Barnard et al. 2012). However, because of the low counting statistics, we cannot definitely exclude the possibility that a *power-law* tail is present at high energy. Indeed, in Figure 6.2, the residuals show lines of evidence of a tail above 5 keV (adding a *power-law*, $\Delta\chi^2 = 10$ for 2 additional d.o.f., $\Gamma \sim 1.75$). Along its outburst XMMU J004243.6+412519 showed only moderate and slow spectral changes in contrast with what is usually seen in transient BH binaries in outburst (see e.g. Motta et al. 2009).

The transient ULXs observed so far appear to have rather different properties and XMMU J004243.6+412519 is not an exception in this picture. The source presents similarities with other transients, but it cannot be definitely associated to any of them.

M31 ULX-1 was observed to reach a peak luminosity of 5×10^{39} erg s^{-1} (Kaur et al., 2012) followed by a decrement in flux with an e-folding time-scale of ∼40 days (Middleton et al., 2012). A blue optical counterpart to M31 ULX-1 was detected during the outburst, but not in quiescence, pointing towards emission from an irradiated accretion disc. This

suggests a low mass companion star transferring matter via Roche lobe overflow. The spectral properties of M31 ULX-1 are roughly described by a single disc component around a 10-$M_{\odot}$ BH with a spin of $a \sim 0.4$.[4] On the other hand, contrarily to what we observed in XMMU J004243.6+412519, the best description of the spectra is obtained with the addition of a second component which represents an optically thick medium (namely a low temperature corona described by a COMPTT) close to the BH. It can be associated to the photosphere of a wind ejected by the inner regions of the disc, that is expected to set in at super-Eddington accretion rate. Indeed, the softer component of the spectrum can be also described by a slim disc model, indicating that advection may be important. The disc component becomes more important when the total luminosity decreases, suggesting that the wind unveils progressively the inner regions of disc when the accretion rate drops.

Also M83 ULX-1 (Soria et al., 2012) showed a long term evolution similar to XMMU J004243.6+412 but, as in the case of M31 ULX-1, the energy spectrum is significantly different from XMMU J004243.6+412519. Undetected ($L_{\rm X} < 10^{36}$ erg s^{-1}) before 2011, M83 ULX-1 was discovered by *CHANDRA* and it was seen to reach a peak luminosity comparable to that of M31 ULX-1 ($\sim 4 \times 10^{39}$ erg s^{-1}). Its spectral properties are modelled by a cold disc plus a power law without evidence of curvature at high energy, opposite to what is commonly seen in ULXs. In addition, the source does not show hints of a decline of the emission for at least 100 days after discovery and no spectral transitions were observed. Again contrarily to XMMU J004243.6+412519, a blue optical counterpart is observed, but only during the outburst, pointing to reprocessed emission from the outer accretion disc and the companion star, a red giant or AGB star with mass $M < 4\ M_{\odot}$ (Soria et al., 2012).

Finally, the ULX in NGC 5128, discovered by *CHANDRA* in the 2009, was observed at a luminosity of (2–3) $\times 10^{39}$ erg s^{-1}. The outburst lasted for at least 70 days, but the

[4]The dimensionless spin parameter $a = cJ/(GM^2)$, where J and M are the angular momentum and mass of the black hole, respectively.

source was no longer observed. It is an intriguing ULX because it experienced spectral state variations between a *very high state*, dominated by a power law with a photon index higher than 2.2, and a *high/soft* state, dominated by an accretion disc of ∼1 keV, consistent with the behaviour of the Galactic BH XRBs (Sivakoff et al. 2008).

XMMU J004243.6+412519 may be hardly associated to the behaviour of the first two transients, both in terms of spectral and timing properties. However, it may show similarities with the ULX in NGC 5128 because a possible spectral transition between a *low/hard* and a *high/soft* state may have occured. In fact, during the raising part of the outburst, the spectrum of XMMU J004243.6+412519 can be well fitted by a single *power-law* model (see ATel #3890), while at maximum luminosity and during the decay it is adequately described by a disc component. In addition, the duration of the outburst of NGC 5128 ULX1 is consistent with that of the outburst of XMMU J004243.6+412519 .

One possible interpretation of the spectra-timing properties of XMMU J004243.6+412519 can be given by making an hypothesis on the nature of the source. If it is a stellar-mass BH transient, we can assume that most of the outburst evolution of the source could not be observed due to its distance from the observer. In this scenario, the source would be visible from Earth only during its brightest phases, which for many BH transients (e.g. H 1743–322, XTE J1650–754, GRO J1655–40) is encountered during the soft spectral states (Belloni et al., 2011). In the soft states the energy spectrum is strongly dominated by a soft disc component (that sometimes is the only component visible in the X-ray spectrum) while the fast time variability is usually consistent with zero. These properties are consistent with what we reported on XMMU J004243.6+412519. The duration of this high-luminosity phase in a Galactic BH transient is variable depending on the source and on the properties of the single outburst. However, the average length of such periods (few months) is absolutely consistent with the duration of the outburst of XMMU J004243.6+412519 (see e.g. the case of the Galactic BH transients XTE J1550–754, Kubota & Done 2004 and

GRO J1655–40, Motta et al. 2012).

Assuming that at maximum luminosity XMMU J004243.6+412519 was in a disc dominated state and that it was radiating at a significant fraction of $L_{\rm Edd}$ (say $\sim$0.6), the mass of the BH would be $\sim$12 $M_{\odot}$. For small inclinations ($\leq 45^{\circ}$), a similar value is obtained from the normalisation of the disc component obtained from the fit of the combined pre-gap PC spectrum. In fact, if we assume that the inner disc radius is truncated at 6 gravitational radii ($R_{in_{BB}} = 2.6 R_{in}$, where $R_{in_{BB}}$ is the diskbb inner radius and R_{in} is the true inner radius) and that the disc spectrum has a standard color correction factor, the BH mass is defined as:

$$\frac{M_{BH}}{M_{\odot}} = f^2 \frac{67.5}{b} \left(\frac{D}{1 Mpc} \right) \left(\frac{K_{BB}}{\cos i} \right)^{1/2} \tag{6.1}$$

where f assumes the value 1.7 (see eq. [2] in Zampieri & Roberts 2009; see also Lorenzin & Zampieri 2009 and references therein). This is consistent with the hypothesis that XMMU J004243.6+412519 could be indeed an accreting stellar-mass black-hole binary observed in its soft state.

The upper limits in optical bands are sufficiently deep to place interesting constraints on the donor mass. Assuming no extinction and a distance modulus of 24.47 mag for M31 (from the NASA/IPAC Extragalactic Database),[5] the upper limit in the V band translates into an upper limit on the absolute magnitude $M_V > -2.8$. Taking binary evolution effects and X-ray irradiation into account, a stellar-mass BH accreting through Roche lobe overflow is consistent with this upper limit if the donor is a main sequence star of 8–10 $M_{\odot}$ or a giant of $<$8 $M_{\odot}$ (Patruno & Zampieri, 2010). In fact, for a donor below 5 $M_{\odot}$, the disc is no longer stable (Dubus et al., 1999; Patruno & Zampieri, 2008b), in agreement with the transient nature of the source.

[5] See http://ned.ipac.caltech.edu/.

Chapter 7

Conclusions

The main goal of this PhD thesis is to try to tidy up the manifold spectral variability properties of ULXs. This was achieved through the detailed analysis of a selected sample of ULXs. In this concluding section, we provide a summary of the results obtained through the thesis and presented in the previous chapters. They are grouped in three subsections, containing our main findings related to the characterization of ULX spectral states, to the lines of evidence supporting the existence of winds, and to the investigation of the behaviour of transient sources.

7.1 Spectral states

Modeling the spectra of the ULXs of our sample we have shown that a combination of a multicolor blackbody disc plus a comptonization component can be used to obtain a satisfactory description of the spectral behaviour of both poor and high quality observations. Although in the poor quality data the fits are sometimes unstable, nevertheless it is possible to use them to assess the overall spectral evolution of both components during time. This allowed us to draw a phenomenological picture of the spectral variability of the sources of our sample, finding that the high energy spectra can often be modelled with an optically

thick ($\tau \geq 2$) and warm comptonizing medium, with a temperature usually in the range 0.5-9 keV. Furthermore, there is a possible evolutionary path on the $kT_{cor} - \tau$ plane along which the temperature of the corona decreases and the optical depth becomes higher.

ULXs seem to populate preferentially two regions on this plane, that correspond to what we labeled as very thick and thick state; the very thick state is typically seen in the high luminosity observations of NGC 1313 X-2, and in all the spectra of IC 342 X-1. In this state, the optical depth correlates with the total luminosity. We suggest that, at the presumably high accretion rates occurring in this state, a progressively larger amount of material is injected from the inner disc regions into the corona/wind, which then appears more and more optically thick as the luminosity and accretion rate increase. On the other hand, Ho II X-1, NGC 5408 X-1, NGC 5204 X-1 and NGC 1313 X-1 do not enter (or only marginally) in the very thick state and populate in most of the cases the thick state in which a (weak) anticorrelation between optical depth and luminosity may be observed, likely indicating a different accretion regime.

An important caveat concerning the interpretation of the soft component and its consequence for the spectral analysis should be mentioned here. As typically assumed (especially for low counting statistics spectra for which the convergence of the spectral fits is more difficult), we set the temperature of the seed photons for Comptonization equal to that of the soft component. However, if the corona/wind is optically thick, in principle we cannot observe the underlying disc. Hence the usual assumption that the two temperature are equal is not fully justified, unless the corona is very compact. Even more so if we assume that the soft component is the emission of a wind. Its photons cannot be the seed of the high energy component and then the two temperatures (that of the seed photons and of the soft component) are not equal. Therefore this assumption may affect our analysis and only a sequence of comparable high quality observations for each source can allow us to play with the two temperatures (as shown in Section 3.4.1) and try to constrain them.

To better characterise the spectral states, we analyzed also the short-term variability of the ULXs of our sample. In some sources, the short-term variability at high energies seems to be more pronounced than that at low energies. On the other hand, some sources have small levels of variability both in the soft and in the high energy band. We interpret the existence of significant variability as caused mainly by an extrinsic factor, like blobs of matter that intersects our line of sight (Middleton et al., 2011). When the variability is lower or absent, our line of sight probably does not intersect the turbulences of the wind because the inclination is lower, and we see only the intrinsic variability related to the accretion engine.

If the wind is the main source of absorbing gas and is mostly equatorial, the different levels of absorption inferred from the spectral fits may also be related to the varying inclination angle. Sources with high values of the local absorption are probable seen at high inclination angles, i.e. IC 342 X-1, NGC 1313 X-1 and X-2, NGC 55 ULX1, while sources with lower average value of the column density are probably observed at smaller inclinations.

As the spectral parameters are sometimes degenerate or not so well constrained, we tried to study the spectral evolution of our sample of ULXs using also the hardness ratios. We suggest the existence of at least two groups of sources on the color-color and hardness-intensity diagrams, possibly with different average luminosity. The sources of the first group have an average count rate below $\sim$ 10 count s^{-1} in the EPIC-pn (assuming a distance of 1 Mpc), are more significantly absorbed and their hard colors seem to correlate with the count rate. On the other hand the sources of the second group have an average count rate above $\sim$ 10 count s^{-1}, are less absorbed and appear to show a possibly opposite trend in which they become less hard as the count rate increases. We note also that the color analysis supports the conclusion of Gladstone et al. (2009) that the soft component becomes systematically more important as the luminosity increases.

Assuming that the hard spectral component represents emission from the inner disc (possibly Comptonized), the correlation hard color-count rate observed in group 1 is consistent with our expectations. Indeed, as the accretion rate increases, more energy per unit mass is released and hence the temperature becomes higher. On the other hand, the anti-correlation hard color-count rate observed in group 2 may be an indication that an effective mechanism that removes energy from the inner disc (as the accretion rate increases) is at work. It is reasonable to think that this could be a strong outflow whose inner parts are sufficiently dense to form a photosphere, originating the observed soft emission.

Only NGC 253 X-1 and NGC 55 ULX1 do not clearly fit into this picture. At low luminosities the spectra of NGC 253 X-1 can be described by a standard disc, while a single slim disc solution seems to be a suitable description of the states at $L_{tot} \geq 10^{39}$ erg s^{-1}. We then suggest that NGC 253 X-1 could be a stellar mass BH accreting at around Eddington and, occasionally, at slightly super-Eddington rates without the onset of significant outflows. On the other hand, NGC 55 ULX1 appears quite faint and soft. Its faintness is mostly caused by the strong intrinsic absorption to which it is subject. This is a clue which may allow us to reconsider its position on the hardness-intensity diagram. In fact, while the parameters of the high energy component inferred from the spectral fits are consistent with a very thick state, the position of the source on the hardness-intensity diagram is not. Indeed from the spectral parameters, we know that the soft component contributes significantly to the total emission. Assuming to correct the position of NGC 55 ULX1 for absorption, it turns out to be essentially located close to the sources of group 2. Therefore, it is likely to be one of those sources but possibly observed at larger inclination angles.

7.2 Wind

As mentioned above, the level of short-term variability at high energy found in a number of observations can be explained in terms of obscuring material intersecting our line of sight to the source. This has been interpreted as originating from a turbulent outflow or wind (Middleton et al., 2011), which is expected to form at super-Eddington accretion rates (Kajava & Poutanen, 2009). With the exception of NGC 253 X-1, all the other sources show more variability at high energies at least in some observations and may then produce from time to time turbulent outflows/winds.

Therefore if the outflows/winds are the cause of the absorption and the existence of the soft component in the spectra of the sources in our sample, we suggest that they may have two different phases: an ionised phase, close to the ejection regions, where the density is sufficiently high that a photosphere may form, and another phase, in the outer regions, where the gas is recombined. If our line of sight intersects the outer neutral and cool layers of the wind, we may observe significant absorption. Clumpiness in the wind may induce the observed variability.

The most direct comparison of this scenario can be done with the properties of the obscuring medium seen in the dipping Galactic X-ray binaries. It is widely accepted that the dips are episodes in which the central emission is obscured by material expelled from the outer disc. For comparison, we then analyzed in detail the well-known dipping source EXO 0748-676, finding that the dips are associated to an increment in the column density and a corresponding decrement in the ionization level (e.g. Díaz Trigo et al. 2006). The intervals in which the obscuration is significant are characterised by high short-term variability. In addition we suggest that RMS and flux are anticorrelated when the absorber is unsaturated, which is the opposite of what expected for non-dipping X-ray binaries in which only the intrinsic accretion flow variability is observed.

Amongst the whole sample, NGC 55 ULX1 is the only one to show a similar phenomenology. Although its luminosity is only marginally above 10^{39} erg s^{-1}, it has narrow drops of minute/hours which can be compared to the dips observed in XRBs. In addition, it shows also short-term variability, more pronounced at high energy, in at least two XMM-Newton observations. In the first XMM-Newton observation we found an anticorrelation between RMS and flux in the energy band which is mostly affected by the dips, between 1 and 10 keV. In the second observation, the statistics is not sufficient to draw any conclusion. On the other hand, in the third observation, RMS and flux are correlated, meaning that the variability is driven by the accretion flow. Finally, we note also that the column density is larger when the flux is lower, suggesting that the observed flux decreases because of obscuration. Since the dips do not seem to show long-term periodicities and they are relatively short lived, they may be the effect of blobs of unsaturated matter that from time to time obscure the central regions of the source. The low flux level detected in the third observation may be due to a saturated remnant of the outflows which absorbs the central emission but does not introduce any further level of variability to the intrinsic one.

In conclusion, we tried to insert the ULXs of our sample within a common framework. Our results confirm that many ULXs may be accreting at or above Eddington. They can be stellar mass or massive stellar BHs whose properties are determined by their BH masses, accretion rates and viewing angles. Even if there are differences from source to source, there is evidence for a characteristic spectral evolutionary sequence which deserve further future investigations with higher quality observations.

7.3 Transient sources

As for Galactic BH binaries, a test-bed for investigating different accretion regimes in ULXs are transient sources. Till now, only a handful of transient ULXs have been discovered,

including XMMU J004243.6+412519 in M31.

Our multi-wavelength study of this source, based on data collected with *Swift* and the 1.8-m Copernico Telescope at Cima Ekar in Asiago (Italy) provided some interesting results. The source, undetected in all previous observations, suddenly turned on, showing powerful X-ray emission with a luminosity of 10^{38} erg s^{-1} (assuming a distance of 780 kpc) and it reached a luminosity higher than 10^{39} erg s^{-1} in the following weeks. The source luminosity remained fairly constant for at least 40 days and then it faded below 10^{38} erg s^{-1} in the following 200 days. From the phase of maximum onwards, the spectrum of XMMU J004243.6+412519 could be well described by a multicolor disc blackbody model which progressively softened during the decay (the temperature changed from 0.9 keV to 0.4 keV). The available observations suggest the existence of a BH of 12-15 $M_{\odot}$, accreting at 60% of the Eddington limit. Transient, low-luminosity ULXs may simply by BHs of this size accreting at maximum close to the Eddington limit.

7.4 Some future perspectives

The work presented in this thesis shows that a lot needs still to be done in order to characterize the X-ray spectral variability and, hence, the accretion regime of ULXs. We are simply at the beginning of this path and are starting to have some understanding of it. Future work in this area is definitely needed, collecting more high quality *XMM-Newton, Chandra* and *Swift* observations of a larger sample of sources.

As long exposures ($>$ 100 ks) with *XMM-Newton* and *Chandra* are difficult to obtain, in order to improve the quality of the spectra, another possibility may be to stack all the available observations of a single source in terms of flux. If important spectral changes (for example variations in the column density of the neutral absorber) at comparable fluxes do not occur, this method may be highly successful. This can be performed more easily

with *Swift* which provides a large number of relatively short observations. With the high counting statistics obtained in this way, it would possible to look for the imprints of the wind in terms of absorption features, which till now have been elusive, and characterise the short-term variability possibly introduced by them. We emphasize also that new X-ray missions, as the recently launched NASA's Nuclear Spectroscopic Telescope Array (*NuSTAR*), will be able to provide high quality data on a larger energy band, allowing to probe different spectral models.

Another very important future activity is to study in a systematic way the almost unknown population of transient ULXs. *Swift* can be a good candidate instrument to periodically observe some nearby galaxies in order to detect them. This approach follows the successful root that has led to the recent discovery of the transient ULXs in M31.

Finally, it is of crucial importance to understand if the brightest ULXs, with luminosities higher than few times 10^{40} erg s^{-1}, can host IMBHs. The confirmation of the existence of such BHs would definitely open new scenarios for the initial seeding and subsequent growth of nuclear BHs in galaxies. The identification of very bright ULXs with more usual XRB-like spectral transitions would be a crucial piece of information to pinpoint them.

Bibliography

Abolmasov P. K., Swartz D. A., Fabrika S., Ghosh K. K., Sholukhova O., Tennant A. F., 2007, ApJ, 668, 124

Abramowicz M. A., Czerny B., Lasota J. P., Szuszkiewicz E., 1988, ApJ, 332, 646

Arnaud K. A., 1996, in Jacoby, G. H. and Barnes, J., eds., Astronomical Data Analysis Software and Systems V. Vol. 101 of ASP Conf. Ser., San Francisco CA, XSPEC: The First Ten Years. p. 17

Arnett 1996, Space Sci. Rev., 78, 559

Balucinska-Church M., McCammon D., 1992, ApJ, 400, 699

Barnard R., 2010, MNRAS, 404, 42

Barnard R., Garcia M. R., Murray S. S., 2012, Astron. Tel., 3937

Barthelmy S. D., et al., 2005, Space Science Reviews, 120, 143

Bauer M., Pietsch W., 2005, A&A, 442, 925

Begelman M. C., 2002, ApJ, 568, L97

Begelman M. C., King A. R., Pringle J. E., 2006, MNRAS, 370, 399

Belczynski K., Bulik T., Fryer C. L., Ruiter A., Valsecchi F., Vink J. S., Hurley J. R., 2010, ApJ, 714, 1217

Belloni T. M., 2010, in Belloni T., ed., Lecture Notes in Physics, Berlin Springer Verlag Vol. 794 of Lecture Notes in Physics, Berlin Springer Verlag, States and Transitions in Black Hole Binaries. p. 53

Belloni T. M., Motta S. E., Muñoz-Darias T., 2011, Bulletin of the Astronomical Society of India, 39, 409

Berghea C. T., Weaver K. A., Colbert E. J. M., Roberts T. P., 2008, ApJ, 687, 471

Breeveld A. A., Landsman W., Holland S. T., Roming P., Kuin N. P. M., Page M. J., 2011, in J. E. McEnery, J. L. Racusin, & N. Gehrels ed., Gamma Ray Bursts 2010. Vol. 1358 of AIP Conf. Proc., Melville NY, An Updated Ultraviolet Calibration for the Swift/UVOT. pp 373–376

Bregman J. N., Cox C. V., Tomisaka K., 1993, ApJ, 415, L79

Bureau M., Carignan C., 2002, AJ, 123, 1316

Burrows D. N., et al., 2005, Space Science Reviews, 120, 165

Burrows D. N., et al., 2011, Nature, 476, 421

Caballero-García M. D., Fabian A. C., 2010, MNRAS, 402, 2559

Carpano S., Pollock A. M. T., King A. R., Wilms J., Ehle M., 2007, A&A, 471, L55

Casella P., Belloni T., Stella L., 2005, ApJ, 629, 403

Casella P., Ponti G., Patruno A., Belloni T., Miniutti G., Zampieri L., 2008, MNRAS, 387, 1707

Colbert E. J. M., Mushotzky R. F., 1999, ApJ, 519, 89

Colbert E. J. M., Ptak A. F., 2002, ApJS, 143, 25

Coppi P. S., 2000, in AAS/High Energy Astrophysics Division #5 Vol. 32 of Bulletin of the American Astronomical Society, EQPAIR: A Hybrid Thermal/Non-Thermal Model for the Spectra of X-Ray Binaries. p. 1217

Cottam J., Paerels F., Mendez M., 2002, Nature, 420, 51

Cseh D., Corbel S., Kaaret P., Lang C., Grisé F., Paragi Z., Tzioumis A., Tudose V., Feng H., 2012, ApJ, 749, 17

Davis D. S., Mushotzky R. F., 2004, ApJ, 604, 653

de Vaucouleurs G., de Vaucouleurs A., Corwin Jr. H. G., Buta R. J., Paturel G., Fouque P., 1992, VizieR Online Data Catalog, 7137, 0

Dewangan G. C., Misra R., Rao A. R., Griffiths R. E., 2010, MNRAS, 407, 291

Dewangan G. C., Titarchuk L., Griffiths R. E., 2006, ApJ, 637, L21

Dheeraj P. R., Strohmayer T. E., 2012, ApJ, 753, 139

Di Stefano R., Primini F. A., Liu J., Kong A., Patel B., 2010, Astronomische Nachrichten, 331, 205

Díaz Trigo M., Parmar A. N., Boirin L., Méndez M., Kaastra J. S., 2006, A&A, 445, 179

Dickey J. M., Lockman F. J., 1990, ARA&A, 28, 215

Done C., Kubota A., 2006, MNRAS, 371, 1216

Dotan C., Shaviv N. J., 2011, MNRAS, 413, 1623

Dubus G., Lasota J.-P., Hameury J.-M., Charles P., 1999, MNRAS, 303, 139

Ebisawa K., Życki P., Kubota A., Mizuno T., Watarai K.-y., 2003, ApJ, 597, 780

Edelson R., Turner T. J., Pounds K., Vaughan S., Markowitz A., Marshall H., Dobbie P., Warwick R., 2002, ApJ, 568, 610

Esin A. A., McClintock J. E., Narayan R., 1997, ApJ, 489, 865

Fabbiano G., 1989, ARA&A, 27, 87

Fabbiano G., Kim D.-W., Trinchieri G., 1992, ApJS, 80, 531

Fabbiano G., King A. R., Zezas A., Ponman T. J., Rots A., Schweizer F., 2003, ApJ, 591, 843

Fabian A. C., Ward M. J., 1993, MNRAS, 263, L51

Farrell S. A., Servillat M., Oates S. R., Heywood I., Godet O., Webb N. A., Barret D., 2010, X-ray Astronomy 2009; Present Status, Multi-Wavelength Approach and Future Perspectives, 1248, 93

Farrell S. A., Webb N. A., Barret D., Godet O., Rodrigues J. M., 2009, Nature, 460, 73

Feng H., Kaaret P., 2005, ApJ, 633, 1052

Feng H., Kaaret P., 2006, ApJ, 650, L75

Feng H., Kaaret P., 2007, ApJ, 668, 941

Feng H., Kaaret P., 2008, ApJ, 675, 1067

Feng H., Kaaret P., 2009, ApJ, 696, 1712

Feng H., Rao F., Kaaret P., 2010, ApJ, 710, L137

Feng H., Soria R., 2011, New Astronomy Reviews, 55, 166

Fitzpatrick E. L., Massa D., 2007, ApJ, 663, 320

Foschini L., Ho L. C., Masetti N., Cappi M., Dadina M., Bassani L., Malaguti G., Palazzi E., Di Cocco G., Martini P., Ravindranath S., Stephen J. B., Trifoglio M., Gianotti F., 2002, A&A, 396, 787

Foster D. L., Charles P. A., Holley-Bockelmann K., 2010, ApJ, 725, 2480

Freedman W. L., Hughes S. M., Madore B. F., Mould J. R., Lee M. G., Stetson P., Kennicutt R. C., Turner A., Ferrarese L., Ford H., Graham J. A., Hill R., Hoessel J. G., Huchra J., Illingworth G. D., 1994, ApJ, 427, 628

Fryer C. L., 1999, ApJ, 522, 413

Gandhi P., 2009, ApJ, 697, L167

Garmire G. P., Bautz M. W., Ford P. G., Nousek J. A., Ricker Jr. G. R., 2003, in X-Ray and Gamma-Ray Telescopes and Instruments for Astronomy. Edited by Truemper, J. E. and Tananbaum, H. D. Vol. 4851 of Proceedings of the SPIE. SPIE, Bellingham WA, Advanced CCD imaging spectrometer (ACIS) instrument on the Chandra X-ray Observatory. pp 28–44

Gladstone J. C., Roberts T. P., Done C., 2009, MNRAS, 397, 1836

Gleissner T., Wilms J., Pottschmidt K., Uttley P., Nowak M. A., Staubert R., 2004, A&A, 414, 1091

Goad M. R., Roberts T. P., Knigge C., Lira P., 2002, MNRAS, 335, L67

Goad M. R., Roberts T. P., Reeves J. N., Uttley P., 2006, MNRAS, 365, 191

Gonçalves A. C., Soria R., 2006, MNRAS, 371, 673

González-Martín O., Vaughan S., 2012, A&A, 544, A80

Grisé F., Kaaret P., Feng H., Kajava J. J. E., Farrell S. A., 2010, ApJ, 724, L148

Grisé F., Kaaret P., Pakull M. W., Motch C., 2011, ApJ, 734, 23

Grisé F., Pakull M., Motch C., 2006a, in Wilson A., ed., The X-ray Universe 2005 Vol. 604 of ESA Special Publication, The Ultraluminous X-ray Source IC 342 X-1 and its Environment. p. 451

Grisé F., Pakull M. W., Motch C., 2006b, in Meurs E. J. A., Fabbiano G., eds, Populations of High Energy Sources in Galaxies Vol. 230 of IAU Symposium, The Ultraluminous X-ray Source in Holmberg IX and its Environment. pp 302–303

Grisé F., Pakull M. W., Soria R., Motch C., Smith I. A., Ryder S. D., Böttcher M., 2008, A&A, 486, 151

Hadfield L. J., Crowther P. A., 2007, MNRAS, 381, 418

Heger A., Fryer C. L., Woosley S. E., Langer N., Hartmann D. H., 2003, ApJ, 591, 288

Heger A., Woosley S. E., 2002, ApJ, 567, 532

Heil L. M., Vaughan S., 2010, MNRAS, 405, L86

Heil L. M., Vaughan S., Roberts T. P., 2009, MNRAS, 397, 1061

Heil L. M., Vaughan S., Uttley P., 2012, MNRAS, 422, 2620

Helfand D. J., Becker R. H., 1984, Nature, 307, 215

Henze M., Pietsch W., Haberl F., 2012a, Astron. Tel., 3959

Henze M., Pietsch W., Haberl F., 2012b, Astron. Tel., 3890

Henze M., Pietsch W., Haberl F., 2012c, Astron. Tel., 3921

Henze M., Pietsch W., Haberl F., Greiner J., 2012, Astron. Tel., 4125

Hirano A., Kitamoto S., Yamada T. T., Mineshige S., Fukue J., 1995, ApJ, 446, 350

Holland S., 1998, AJ, 115, 1916

Holmberg E. B., Lauberts A., Schuster H.-E., West R. M., 1974, A&AS, 18, 463

Homan J., Jonker P. G., Wijnands R., van der Klis M., van Paradijs J., 1999, ApJ, 516, L91

Immler S., Brown P. J., Milne P. e. a., 2007, ApJ, 664, 435

Impiombato D., Zampieri L., Falomo R., Grisé F., Soria R., 2011, Astronomische Nachrichten, 332, 375

Jin J., Feng H., Kaaret P., Zhang S.-N., 2011, ApJ, 737, 87

José J., Iliadis C., 2011, Reports on Progress in Physics, 74, 096901

Kaaret P., Corbel S., 2009, ApJ, 697, 950

Kaaret P., Feng H., 2009, ApJ, 702, 1679

Kaaret P., Feng H., Wong D. S., Tao L., 2010, ApJ, 714, L167

Kaaret P., Ward M. J., Zezas A., 2004, MNRAS, 351, L83

Kajava J. J. E., Poutanen J., 2009, MNRAS, 398, 1450

Kajava J. J. E., Poutanen J., Farrell S. A., Grisé F., Kaaret P., 2012, MNRAS, 422, 990

Karachentsev I. D., Grebel E. K., Sharina M. E., Dolphin A. E., Geisler D., Guhathakurta P., Hodge P. W., Karachentseva V. E., Sarajedini A., Seitzer P., 2003, A&A, 404, 93

Kaur A., Henze M., Haberl F., Pietsch W., Greiner J., Rau A., Hartmann D. H., Sala G., Hernanz M., 2012, A&A, 538, A49

King A. R., 2009, MNRAS, 393, L41

King A. R., Davies M. B., Ward M. J., Fabbiano G., Elvis M., 2001, ApJ, 552, L109

Kong A. K. H., Di Stefano R., 2005, ApJ, 632, L107

Kong A. K. H., Yang Y. J., Yen T.-C., Feng H., Kaaret P., 2010, ApJ, 722, 1816

Körding E., Falcke H., Markoff S., 2002, A&A, 382, L13

Kraft R. P., Burrows D. N., Nousek J. A., 1991, ApJ, 374, 344

Kubota A., Done C., 2004, MNRAS, 353, 980

Kubota A., Done C., Makishima K., 2002, MNRAS, 337, L11

Kubota A., Ebisawa K., Makishima K., Nakazawa K., 2005, ApJ, 631, 1062

Kubota A., Mizuno T., Makishima K., Fukazawa Y., Kotoku J., Ohnishi T., Tashiro M., 2001, ApJ, 547, L119

Kubota A., Tanaka Y., Makishima K., Ueda Y., Dotani T., Inoue H., Yamaoka K., 1998, PASJ, 50, 667

La Parola V., Peres G., Fabbiano G., Kim D. W., Bocchino F., 2001, ApJ, 556, 47

Lang C. C., Kaaret P., Corbel S., Mercer A., 2007, ApJ, 666, 79

Leahy D. A., Darbro W., Elsner R. F., Weisskopf M. C., Kahn S., Sutherland P. G., Grindlay J. E., 1983, ApJ, 266, 160

Lee J. C., Reynolds C. S., Remillard R., Schulz N. S., Blackman E. G., Fabian A. C., 2002, ApJ, 567, 1102

Lehmann I., Becker T., Fabrika S., Roth M., Miyaji T., Afanasiev V., Sholukhova O., Sánchez S. F., Greiner J., Hasinger G., Costantini E., Surkov A., Burenkov A., 2005, A&A, 431, 847

Liang E. P. T., Price R. H., 1977, ApJ, 218, 247

Linden T., Kalogera V., Sepinsky J. F., Prestwich A., Zezas A., Gallagher J. S., 2010, ApJ, 725, 1984

Liu J., Bregman J. N., McClintock J. E., 2009, ApJ, 690, L39

Liu J.-F., 2008, ApJS, 177, 181

Liu J.-F., Bregman J., Miller J., Kaaret P., 2007, ApJ, 661, 165

Liu J.-F., Bregman J. N., 2005, ApJS, 157, 59

Liu J.-F., Bregman J. N., Seitzer P., 2002, ApJ, 580, L31

Liu J.-F., Bregman J. N., Seitzer P., 2004, ApJ, 602, 249

Long K. S., van Speybroeck L. P., 1983, in Lewin W. H. G., van den Heuvel E. P. J., eds, Accretion-Driven Stellar X-ray Sources, Cambridge University Press, Cambridge. Very Bright Non-Nuclear Sources. p. 141

Lorenzin A., Zampieri L., 2009, MNRAS, 394, 1588

Lyubarskii Y. E., 1997, MNRAS, 292, 679

Maccacaro T., Della Ceca R., Braito V., Caccianiga A., Severgnini P., Wolter A., 2004, Ap&SS, 294, 89

Madau P., Rees M. J., 2001, ApJ, 551, L27

Madhusudhan N., Justham S., Nelson L., Paxton B., Pfahl E., Podsiadlowski P., Rappaport S., 2006, ApJ, 640, 918

Madhusudhan N., Rappaport S., Podsiadlowski P., Nelson L., 2008, ApJ, 688, 1235

Magnier E. A., Lewin W. H. G., van Paradijs J., Hasinger G., Jain A., Pietsch W., Truemper J., 1992, A&AS, 96, 379

Makishima K., Kubota A., Mizuno T., Ohnishi T., Tashiro M., Aruga Y., Asai K., Dotani T., Mitsuda K., Ueda Y., Uno S., Yamaoka K., Ebisawa K., Kohmura Y., Okada K., 2000, ApJ, 535, 632

Makishima K., Maejima Y., Mitsuda K., Bradt H. V., Remillard R. A., Tuohy I. R., Hoshi R., Nakagawa M., 1986, ApJ, 308, 635

Mapelli M., Colpi M., Zampieri L., 2009, MNRAS, 395, L71

Mapelli M., Ripamonti E., Zampieri L., Colpi M., Bressan A., 2010, MNRAS, 408, 234

Markoff S., Falcke H., Fender R., 2001, A&A, 372, L25

Masetti N., Foschini L., Ho L. C., Dadina M., Di Cocco G., Malaguti G., Palazzi E., 2003, A&A, 406, L27

Matsumoto H., Tsuru T. G., Koyama K., Awaki H., Canizares C. R., Kawai N., Matsushita S., Kawabe R., 2001, ApJ, 547, L25

McClintock J. E., Remillard R. A., 2006, in Compact stellar X-ray sources, ed. W. H. G. Levin and M. van der Klis. Cambridge: Cambridge University Press, p. 157

McHardy I. M., Arévalo P., Uttley P., Papadakis I. E., Summons D. P., Brinkmann W., Page M. J., 2007, MNRAS, 382, 985

Merloni A., Heinz S., di Matteo T., 2003, MNRAS, 345, 1057

Middleton M., Uttley P., Done C., 2011, MNRAS, 417, 250

Middleton M. J., Roberts T. P., Done C., Jackson F. E., 2011, MNRAS, 411, 644

Middleton M. J., Sutton A. D., Roberts T. P., 2011, MNRAS, 417, 464

Middleton M. J., Sutton A. D., Roberts T. P., Jackson F. E., Done C., 2012, MNRAS, 420, 2969

Miller B. W., 1995, ApJ, 446, L75

Miller J. M., Fabian A. C., Miller M. C., 2004, ApJ, 614, L117

Miller J. M., Raymond J., Fabian A., Steeghs D., Homan J., Reynolds C., van der Klis M., Wijnands R., 2006, Nature, 441, 953

Miller J. M., Raymond J., Fabian A. C., Homan J., Nowak M. A., Wijnands R., van der Klis M., Belloni T., Tomsick J. A., Smith D. M., Charles P. A., Lewin W. H. G., 2004, ApJ, 601, 450

Miller J. M., Wijnands R., Méndez M., Kendziorra E., Tiengo A., van der Klis M., Chakrabarty D., Gaensler B. M., Lewin W. H. G., 2003, ApJ, 583, L99

Miller M. C., Hamilton D. P., 2002, MNRAS, 330, 232

Miller N. A., Mushotzky R. F., Neff S. G., 2005, ApJ, 623, L109

Mineshige S., Hirano A., Kitamoto S., Yamada T. T., Fukue J., 1994, ApJ, 426, 308

Mitsuda K., Inoue H., Koyama K., Makishima K., Matsuoka M., Ogawara Y., Suzuki K., Tanaka Y., Shibazaki N., Hirano T., 1984, PASJ, 36, 741

Miyaji T., Lehmann I., Hasinger G., 2001, AJ, 121, 3041

Mizuno T., Kubota A., Makishima K., 2001, ApJ, 554, 1282

Motta S., Belloni T., Homan J., 2009, MNRAS, 400, 1603

Motta S., Homan J., Muñoz-Darias T., Casella P., Belloni T. M., Hiemstra B., Mèndez, M. 2012, MNRAS, in press (eprint: astro-ph.HE/1209.0327)

Mucciarelli P., Casella P., Belloni T., Zampieri L., Ranalli P., 2006, MNRAS, 365, 1123

Mucciarelli P., Zampieri L., Falomo R., Turolla R., Treves A., 2005, ApJ, 633, L101

Mucciarelli P., Zampieri L., Treves A., Turolla R., Falomo R., 2007, ApJ, 658, 999

Mukai K., Still M., Corbet R. H. D., Kuntz K. D., Barnard R., 2005, ApJ, 634, 1085

Murray S. S., Austin G. K., Chappell J. H., Gomes J. J., Kenter A. T., Kraft R. P., Meehan G. R., Zombeck M. V., Fraser G. W., Serio S., 2000, in Truemper J. E., Aschenbach B., eds, Proc. SPIE Vol. 4012, X-Ray Optics, Instruments, and Missions III In-flight performance of the Chandra high-resolution camera. p. 68

Neilsen J., Lee J. C., 2009, Nature, 458, 481

Nowak M. A., Vaughan B. A., Wilms J., Dove J. B., Begelman M. C., 1999, ApJ, 510, 874

Ohsuga K., Mineshige S., 2007, ApJ, 670, 1283

Ohsuga K., Mineshige S., Mori M., Kato Y., 2009, PASJ, 61, L7

Oke J. B., Gunn J. E., 1983, ApJ, 266, 713

Page M. J., Soria R., Wu K., Mason K. O., Cordova F. A., Priedhorsky W. C., 2003, MNRAS, 345, 639

Pakull M. W., Angebault L. P., 1986, Nature, 322, 511

Pakull M. W., Grisé F., 2008, in Bandyopadhyay R. M., Wachter S., Gelino D., Gelino C. R., eds, A Population Explosion: The Nature & Evolution of X-ray Binaries in Diverse Environments Vol. 1010 of American Institute of Physics Conference Series, Ultraluminous X-ray Sources: Beambags and Optical Counterparts. pp 303–307

Pakull M. W., Grisé F., Motch C., 2006, in Meurs E. J. A., Fabbiano G., eds, Populations of High Energy Sources in Galaxies Vol. 230 of IAU Symposium, Ultraluminous X-ray Sources: Bubbles and Optical Counterparts. pp 293–297

Pakull M. W., Mirioni L., 2002, ArXiv Astrophysics e-prints

Pakull M. W., Mirioni L., 2003, in Arthur J., Henney W. J., eds, Revista Mexicana de Astronomia y Astrofisica Conference Series Vol. 15 of Revista Mexicana de Astronomia y Astrofisica, vol. 27, Bubble Nebulae around Ultraluminous X-Ray Sources. pp 197–199

Patruno A., Zampieri L., 2008a, MNRAS, 386, 543

Patruno A., Zampieri L., 2008b, MNRAS, 386, 543

Patruno A., Zampieri L., 2010, MNRAS, 403, L69

Pence W. D., Snowden S. L., Mukai K., Kuntz K. D., 2001, ApJ, 561, 189

Pilyugin L. S., 2001, A&A, 369, 594

Pintore F., Zampieri L., 2011, Astronomische Nachrichten, 332, 337

Pintore F., Zampieri L., 2012, MNRAS, 420, 1107

Poole T. S., et al., 2008, MNRAS, 383, 627

Portegies Zwart S. F., Baumgardt H., Hut P., Makino J., McMillan S. L. W., 2004, Nature, 428, 724

Portegies Zwart S. F., McMillan S. L. W., 2002, ApJ, 576, 899

Poutanen J., Lipunova G., Fabrika S., Butkevich A. G., Abolmasov P., 2007, MNRAS, 377, 1187

Predehl P., Schmitt J. H. M. M., 1995, A&A, 293, 889

Puche D., Westpfahl D., Brinks E., Roy J.-R., 1992, AJ, 103, 1841

Ramsey C. J., Williams R. M., Gruendl R. A., Chen C.-H. R., Chu Y.-H., Wang Q. D., 2006, ApJ, 641, 241

Rao F., Feng H., Kaaret P., 2010, ApJ, 722, 620

Read A. M., Ponman T. J., Strickland D. K., 1997, MNRAS, 286, 626

Remillard R. A., McClintock J. E., 2006, ARA&A, 44, 49

Revnivtsev M., Gilfanov M., Churazov E., 1999, A&A, 347, L23

Ripamonti E., Mapelli M., Zampieri L., Colpi M., 2011, Astronomische Nachrichten, 332, 418

Roberts T. P., 2007, Ap&SS, 311, 203

Roberts T. P., Gladstone J. C., Goulding A. D., Swinbank A. M., Ward M. J., Goad M. R., Levan A. J., 2011, Astronomische Nachrichten, 332, 398

Roberts T. P., Goad M. R., Ward M. J., Warwick R. S., 2003, MNRAS, 342, 709

Roberts T. P., Goad M. R., Ward M. J., Warwick R. S., O'Brien P. T., Lira P., Hands A. D. P., 2001, MNRAS, 325, L7

Roberts T. P., Kilgard R. E., Warwick R. S., Goad M. R., Ward M. J., 2006, MNRAS, 371, 1877

Roberts T. P., Levan A. J., Goad M. R., 2008, MNRAS, 387, 73

Roberts T. P., Warwick R. S., 2000, MNRAS, 315, 98

Roberts T. P., Warwick R. S., Ward M. J., Goad M. R., 2004, MNRAS, 349, 1193

Roberts T. P., Warwick R. S., Ward M. J., Goad M. R., Jenkins L. P., 2005, MNRAS, 357, 1363

Roming P. W. A., et al., 2005, Space Science Reviews, 120, 95

Sabbi E., Gallagher J. S., Smith L. J., de Mello D. F., Mountain M., 2008, ApJ, 676, L113

Saha A., Claver J., Hoessel J. G., 2002, AJ, 124, 839

Scaringi S., Körding E., Uttley P., Knigge C., Groot P. J., Still M., 2012, MNRAS, 421, 2854

Schlegel D. J., Finkbeiner D. P., Davis M., 1998, ApJ, 500, 525

Servillat M., Farrell S. A., Lin D., Godet O., Barret D., Webb N. A., 2011, ApJ, 743, 6

Shakura N. I., Sunyaev R. A., 1973, A&A, 24, 337

Shimura T., Takahara F., 1995, ApJ, 445, 780

Sivakoff G. R., et al., 2008, ApJ, 677, L27

Sivakoff G. R., Kraft R. P., Jordán A., Juett A. M., Evans D. A., Forman W. R., Hardcastle M. J., Sarazin C. L., Birkinshaw M., Brassington N. J., Croston J. H., Harris W. E., Jones C., Murray S. S., Raychaudhury S., Woodley K. A., Worrall D. M., 2008, ApJ, 677, L27

Socrates A., Davis S. W., 2006, ApJ, 651, 1049

Soria R., 2007, Ap&SS, 311, 213

Soria R., Cropper M., Pakull M., Mushotzky R., Wu K., 2005, MNRAS, 356, 12

Soria R., Ghosh K. K., 2009, ApJ, 696, 287

Soria R., Kuntz K. D., Winkler P. F., Blair W. P., Long K. S., Plucinsky P. P., Whitmore B. C., 2012, ApJ, 750, 152

Soria R., Motch C., Read A. M., Stevens I. R., 2004, A&A, 423, 955

Stanek K. Z., Garnavich P. M., 1998, ApJ, 503, L131

Stewart S. G., Fanelli M. N., Byrd G. G., Hill J. K., Westpfahl D. J., Cheng K.-P., O'Connell R. W., Roberts M. S., Neff S. G., Smith A. M., Stecher T. P., 2000, ApJ, 529, 201

Stobbart A.-M., Roberts T. P., Warwick R. S., 2004, MNRAS, 351, 1063

Stobbart A.-M., Roberts T. P., Wilms J., 2006, MNRAS, 368, 397

Stocke J. T., Wurtz R., Kuehr H., 1991, AJ, 102, 1724

Strohmayer T. E., Mushotzky R. F., 2003, ApJ, 586, L61

Strohmayer T. E., Mushotzky R. F., 2009, ApJ, 703, 1386

Strohmayer T. E., Mushotzky R. F., Winter L., Soria R., Uttley P., Cropper M., 2007, ApJ, 660, 580

Sunyaev R. A., Titarchuk L. G., 1985, A&A, 143, 374

Sutton A. D., Roberts T. P., Walton D. J., Gladstone J. C., Scott A. E., 2012, MNRAS, 423, 1154

Svensson R., Zdziarski A. A., 1994, ApJ, 436, 599

Swartz D. A., Ghosh K. K., Suleimanov V., Tennant A. F., Wu K., 2002, ApJ, 574, 382

Swartz D. A., Ghosh K. K., Tennant A. F., Wu K., 2004, ApJS, 154, 519

Swartz D. A., Soria R., Tennant A. F., 2008, ApJ, 684, 282

Swartz D. A., Soria R., Tennant A. F., Yukita M., 2011, ApJ, 741, 49

Tao L., Feng H., Grisé F., Kaaret P., 2011, ApJ, 737, 81

Titarchuk L., 1994, ApJ, 434, 570

Tully R. B., Fisher J. R., 1988, Catalog of Nearby Galaxies

Uttley P., McHardy I. M., 2001, MNRAS, 323, L26

Uttley P., McHardy I. M., Vaughan S., 2005, MNRAS, 359, 345

Uttley P., Wilkinson T., Cassatella P., Wilms J., Pottschmidt K., Hanke M., Böck M., 2011, MNRAS, 414, L60

Vaughan S., 2010, MNRAS, 402, 307

Vaughan S., Edelson R., Warwick R. S., Uttley P., 2003, MNRAS, 345, 1271

Vesperini E., McMillan S. L. W., D'Ercole A., D'Antona F., 2010, ApJ, 713, L41

Vierdayanti K., Done C., Roberts T. P., Mineshige S., 2010, MNRAS, 403, 1206

Vierdayanti K., Mineshige S., Ebisawa K., Kawaguchi T., 2006, PASJ, 58, 915

Walton D. J., Miller J. M., Reis R. C., Fabian A. C., 2012, MNRAS, 426, 473

Walton D. J., Roberts T. P., Mateos S., Heard V., 2011, MNRAS, 416, 1844

Watarai K.-y., Fukue J., Takeuchi M., Mineshige S., 2000, PASJ, 52, 133

Watarai K.-y., Mizuno T., Mineshige S., 2001, ApJ, 549, L77

Webb N., Cseh D., Lenc E., Godet O., Barret D., Corbel S., Farrell S., Fender R., Gehrels N., Heywood I., 2012, Science, 337, 554

White N. E., Nagase F., Parmar A. N., 1995, X-ray Binaries, pp 1–57

White N. E., Swank J. H., 1982, ApJ, 253, L61

Wijnands R., van der Klis M., 1999, ApJ, 514, 939

Wilkinson T., Uttley P., 2009, MNRAS, 397, 666

Winter L. M., Mushotzky R. F., Reynolds C. S., 2006, ApJ, 649, 730

Winter L. M., Mushotzky R. F., Reynolds C. S., 2007, ApJ, 655, 163

Wong D. S., Chornock R., Filippenko A. V., 2008, PASP, 120, 266

Yuan F., 2001, MNRAS, 324, 119

Zacharias N., Monet D. G., Levine S. E., Urban S. E., Gaume R., Wycoff G. L., 2005, VizieR Online Data Catalog, 1297, 0

Zampieri L., Impiombato D., Falomo R., Grisé F., Soria R., 2012, MNRAS, 419, 1331

Zampieri L., Mucciarelli P., Falomo R., Kaaret P., Di Stefano R., Turolla R., Chieregato M., Treves A., 2004, ApJ, 603, 523

Zampieri L., Patruno A., 2011, Astronomische Nachrichten, 332, 422

Zampieri L., Roberts T. P., 2009, MNRAS, 400, 677

Zdziarski A. A., Johnson W. N., Magdziarz P., 1996, MNRAS, 283, 193

Zezas A. L., Georgantopoulos I., Ward M. J., 1999, MNRAS, 308, 302

Zoghbi A., Fabian A. C., 2011, MNRAS, 418, 2642

Życki P. T., Done C., Smith D. A., 1999, MNRAS, 309, 561

Ringraziamenti

Dopo aver affrontato le fatiche di scrivere un'intera tesi basata su un lavoro lungo 3 anni, la parte dei ringraziamenti sembra essere ancora più difficile visto che tiene conto di 27 anni di vita. Infatti il mio più grosso ringraziamento va sicuramente alla mia famiglia per tutto quello che ha fatto e farà per me. Se sto raggiungendo questo importante traguardo lo devo a loro, per aver fatto di me il ragazzo che sono ora. Nei momenti di difficoltà mi sono sempre stati vicino cercando di offrirmi i consigli che ritenevano più giusti. Il loro apporto non è mai mancato e mi hanno sempre assicurato tutta la tranquillità di cui potevo aver bisogno. Non ci sono parole per esprimere quanto voglio bene a mamma, papà e Federico e questo lavoro è dedicato interamente a loro.

Ovviamente, non posso non considerare il mio supervisore che io ho sempre chiamato "Prof." in tono un po' scherzoso, visto che non sono mai riuscito a chiamarlo Luca ma inizierò a farlo da questi ringraziamenti. Luca è stato sicuramente stata la persona più importante che ho avuto modo di incontrare in questi tre anni di attività di ricerca. Aveva accettato di prendermi sotto la sua ala praticamente a scatola chiusa ma mi ha sempre dato fiducia e stimoli per migliorare giorno per giorno. Anche quando in certi momenti mi sentivo scoraggiato perchè mi accorgevo di avere ancora tantissimo da imparare. Grazie a lui penso di aver migliorato il "mio occhio scientifico" e mi ha insegnato a capire come funziona il mondo della ricerca. Voglio però dire in tutta onestà che tutte le sue dritte non sarebbero sicuramente state recepite allo stesso modo se lui non fosse stato una persona

incredibilmente umana e di grandi valori morali come poche se ne incontrano lungo la propria vita. Quindi a lui va un enorme ringraziamento per tutto.

Un ringraziamento va anche a Padova e alle persone che ho incontrato grazie ad essa. Io ero un piccolo sardo mai stato nel "continente" se non per delle gite, che non aveva mai vissuto fuori da casa sua neppure durante il periodo dell'Università e che si trovava immerso in una realtà completamente diversa da quella a cui era abituato. Eppure sono stato accolto benissimo e ho scoperto un mondo bellissimo, pieno di persone interessanti e a cui va tutto il mio più grande affetto. A partire dai miei coinquilini con cui ho condiviso momenti splendidi e di felicità. In particolare a Giorgio e Corinne: senza di loro probabilmente avrei avuto mille volte più difficoltà ad inserirmi in società, seppure i nostri stili di vita non fossero esattamente simili.

Infine vorrei ringraziare le mie ex colleghe di ufficio Sagretta Bottiglietta e Marcella, Alessandro B., Il Parroco Matteo B., Simonza, Maria B., Maria Di Cucciolo., Annina F., Anna S., Valentina, Elisa, Franzetta, Lucia, Luca Borsello, Alice pugno di ferro, Letizia Cassarancia, Fiorangela, Il Bello e il Berry, gli inglesi "J, Han" , "Nessie" con il suo mega aiuto di rilettura e tutti gli altri miei amici dottorandi e non di cui non posso parlare ad uno ad uno visto che avrei bisogno di altre 200 pagine ma con cui ho condiviso splendidi momenti che porterò sempre nel cuore e a cui chiedo venia per aver assegnato cosi tanti nomignoli. E infine chiedo scusa a Lamentina per averla fatta impazzire ogni volta che sono stato portato via dalla tesi! :)

Un enorme "grazie" anche a Lucia e Roberto che mi hanno offerto l'unico rifugio familiare in Veneto, facendomi sentire a casa!

Senza tutte queste persone che ho citato, il mio lavoro sarebbe stato molto più triste e con molto meno amore di quello che ho messo per completarlo. Grazie a tutti.